

Bending and Stretching:
A Practical Examination
of Molecules at Aqueous Interfaces



Carolyn Jil Moll

**Bending and Stretching: A Practical
Examination of Molecules at Aqueous Interfaces**

ISBN 978-94-92323-60-6

© 2022, C.J. Moll. All rights reserved.

Photographs and Cover: Bernhard Moll (www.moll-fotografie.de)

Print: Ridderprint

Bending and Stretching: A Practical Examination of Molecules at Aqueous Interfaces

ACADEMISCH PROEFSCHRIFT

ter verkrijging van de graad van doctor
aan de Universiteit van Amsterdam
op gezag van de Rector Magnificus
prof. dr. ir. K.I.J. Maex
ten overstaan van een door het College voor Promoties ingestelde
commissie,
in het openbaar te verdedigen in de Agnietenkapel
op donderdag 24 maart 2022, te 10:00 uur

Carolyn Jil Moll

geboren te Neuss

PROMOTIECOMMISSIE

Promotor:	prof. dr. H. J. Bakker	Universiteit van Amsterdam
Copromotor:	dr. K. K. Meister	University of Alaska Southeast
Overige leden:	prof. dr. W. J. Buma	Universiteit van Amsterdam
	prof. dr. W. L. Noorduyn	Universiteit van Amsterdam
	prof. dr. E. H. G. Backus	Universiteit van Amsterdam
	prof. dr. I. K. Voets	Technische Universiteit Eindhoven
	prof. dr. P. Petersen	Ruhr-Universität Bochum
	dr. ir. M. A. van der Veen	Technische Universiteit Delft

Faculteit der Natuurwetenschappen, Wiskunde en Informatica

PUBLICATIONS COVERED IN THIS THESIS

Carolyn J. Moll, Jan Versluis, Huib J. Bakker. Direct Evidence for a Surface and Bulk Specific Response in the Sum-Frequency Generation Spectrum of the Water Bend Vibration. *Phys. Rev. Lett.* *127*,116001, 2021.

- *chapter 4*

Carolyn J. Moll, Jan Versluis, Huib J. Bakker. Direct Observation of the Orientation of Urea Molecules at Charged Interfaces. *J. Phys. Chem. Lett.* *12*, 12, 10823-10828, 2021.

- *chapter 5*

Carolyn J. Moll, Alexander A. Korotkevich, Jan Versluis, Huib J. Bakker. Molecular orientation of small carboxylates at the water-air interface. *submitted*.

- *chapter 6*

Carolyn J. Moll, Jan Versluis, Huib J. Bakker. Bulk response of carboxylic acid solutions observed with surface sum-frequency generation spectroscopy. *J. Phys. Chem. B* *126*, 1, 270-277, 2022. - *chapter 7*

Carolyn J. Moll, Konrad Meister, Jan Versluis, Huib J. Bakker. Freezing of Aqueous Carboxylic Acid Solutions on Ice. *J. Phys. Chem. B* *124*, 25, 5201–5208, 2020.

- *chapter 8*

Konrad Meister, Carolyn J. Moll, Sandipan Chakraborty, Biman Jana, Arthur L. DeVries, Hans Ramløv, Huib J. Bakker. Molecular structure of a hyperactive antifreeze protein adsorbed to ice. *J. Chem. Phys.* *150*,25, 131101, 2019.

- *chapter 9*

Carolyn J. Moll, Giulia Giubertoni, Jan Versluis, Gijsje H. Koenderink, Huib J. Bakker. The molecular structure and surface accumulation dynamics of hyaluronan at the water/air interface. *Macromolecules* *54*, 18, 8655–8663, 2021.

- *chapter 10*

OTHER PUBLICATIONS

Carolyn J. Moll, Konrad Meister, Johannes Kirschner, Huib J. Bakker. Surface Structure of Solutions of Poly (vinyl alcohol) in Water. *J. Phys. Chem. B* *122*, 47, 10722-10727, 2018.

Rahul Gera, Carolyn J. Moll, Aditi Bhattacharjee, Huib J. Bakker. Water-Induced Restructuring of the Surface of a Deep Eutectic Solvent. *J. Phys. Chem. Lett.* *13*, 2, 634-641, 2022.

This work is part of the research program of the Netherlands Organization for Scientific Research (NWO) and was performed at the research institute AMOLF. This project has received funding from the European Research Council (ERC) under the European Union's Horizon 2020 research and innovation program (grant agreement No. 694386).

CONTENTS

1	Introduction	11
1.1	Interfaces	11
1.1.1	Aqueous Interfaces	11
1.1.2	Ice Interfaces	13
1.1.3	Biological Interfaces	14
1.2	Outline of this Thesis	15
2	Theory of Vibrational Sum-Frequency Generation	19
2.1	The Origin of VSFG	19
2.2	Geometry Dependence of the Nonlinear Susceptibility	22
2.3	Hyperpolarizability	23
2.4	Fresnel Factors	25
2.4.1	Interfacial Dielectric Constant ϵ' in the Microscopic Regime	28
2.5	Quadrupolar Contributions	29
2.6	$\chi^{(3)}$ Effect at Charged Interfaces	35
3	Experimental Methods	39
3.1	Optical VSFG Setup	39
3.2	Noise Reduction and Improved Measurement Procedure	42
3.3	Fabrication and Sample Handling of Monocrystalline Ice	45
4	The VSFG Response of the Water Bend Vibration	49
4.1	Introduction	50
4.2	Experimental Methods	51
4.3	Results and Discussion	51
4.4	Conclusions	57
4.5	Appendix	58
5	Orientation of Urea Molecules at Charged Interfaces	67
5.1	Introduction	68
5.2	Experimental Methods	68
5.3	Results and Discussion	69
5.4	Conclusion	74
5.5	Appendix	75
6	Small Carboxylates at the Water-Air Interface	81
6.1	Introduction	82
6.2	Experimental Methods	82
6.3	Results and Discussion	83

6.4	Conclusions	88
6.5	Appendix	88
7	VSG Response of Carboxylic Acid Solutions	95
7.1	Introduction	96
7.2	Experimental Methods	97
7.3	Results and Discussion	97
7.4	Conclusions	105
7.5	Appendix	106
8	Freezing of Aqueous Carboxylic Acid Solutions on Ice	113
8.1	Introduction	114
8.2	Experimental Methods	114
8.3	Results	115
8.4	Conclusion	121
8.5	Appendix	121
9	Hyperactive Antifreeze Protein Adsorbed to Ice	129
9.1	Introduction	130
9.2	Experimental Methods	130
9.3	Results and Discussion	131
9.4	Conclusion	136
9.5	Appendix	137
9.5.1	Molecular Dynamics Simulations	137
9.5.2	Modeling of RmAFP Structure	137
9.5.3	Docking of RmAFP and α -Lactalbumin to the Basal Plane	138
9.5.4	Calculation of the Binding Free Energy for the Protein Adsorption to the Basal Plane	138
10	Hyaluronan at the Water/Air Interface	143
10.1	Introduction	144
10.2	Experimental Methods	145
10.3	Results and Discussion	145
10.3.1	Effect of the Hyaluronan Concentration on its Accumulation at the Surface	148
10.3.2	Effect of Hyaluronan Molecular Weight on its Accumulation at the Surface	150
10.3.3	Effect of pH on the Surface Accumulation of Hyaluronan .	150
10.4	Conclusions	154
10.5	Appendix	156
10.5.1	Effect of the Salt Concentration in the Solvent on the Accumulation of Hyaluronan at the Surface	156
10.5.2	Surface Tension	159
	Bibliography	167
	Summary	193

Samenvatting	197
Acknowledgements	201



1 INTRODUCTION

"God made the bulk; the surface was invented by the devil." - Wolfgang Pauli

1.1 INTERFACES

Pauli described that the devilish characteristics of the surface were due to the simple fact that surface atoms are interacting with three different types of atoms: with the atoms within the surface and with the atoms located right above or below. Thus, the properties of the surface atoms can vary strongly from the ones in the bulk and cannot be described in the same manner. Therefore, obtaining detailed descriptions of physical and chemical processes at the surface on a molecular level is a huge challenge. As surfaces are ubiquitous, in the past numerous theoretical and experimental techniques were developed to get a fundamental understanding of important interfacial processes,¹⁻⁶ such as molecular recognition at bio-membranes, protein folding, and energy conversion and storage, corrosion and lubrication.⁷⁻¹³ The research field of surface science deals with many different surfaces ranging from well-defined metal surfaces to complex biomembranes in living cells. The investigation of surfaces is not only driven by the urge for fundamental understanding, but also by technological, pharmaceutical, and medical development. In this thesis, we use surface-specific vibrational sum-frequency generation spectroscopy (VSFG) to study surfaces on a molecular level ranging from simple surfaces as the neat water/air interface (Chapter 4) to more complex surfaces as the ice/air interface doped with antifreeze proteins (Chapter 9).

1.1.1 AQUEOUS INTERFACES

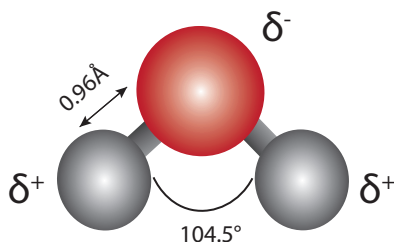


FIGURE 1.1. Schematic of a water molecule consisting of one oxygen atom (red) and two hydrogen atoms (gray).

Water is a chemical compound that consists of two hydrogen atoms that are covalently bonded to one oxygen atom with an angle of 104.45° between the bonds 1.1. At room temperature water appears as a colorless, odorless, and tasteless liquid. One of the most important properties of the water molecule is its polar nature. As the oxygen atom has a higher electronegativity than the hydrogen atoms, the oxygen atom is slightly negatively charged, and the hydrogen atoms are slightly positively charged. A molecule with such a charge difference is called a dipole. The positively charged hydrogen atoms of the water molecules are attracted by negatively charged oxygen atoms of other water molecules, resulting in the formation of a hydrogen bond between the water molecules. Each water molecule can form in total four hydrogen bonds: two donating hydrogen bonds from the two hydrogen atoms, and two accepted hydrogen bonds from the oxygen lone pairs. This leads to a three-dimensional hydrogen bond network, in which the ideal arrangement would be tetrahedral. In liquid water, however the hydrogen-bonded network is more disordered and each water molecule is forming on average 3.5 hydrogen-bonds.^{14,15}

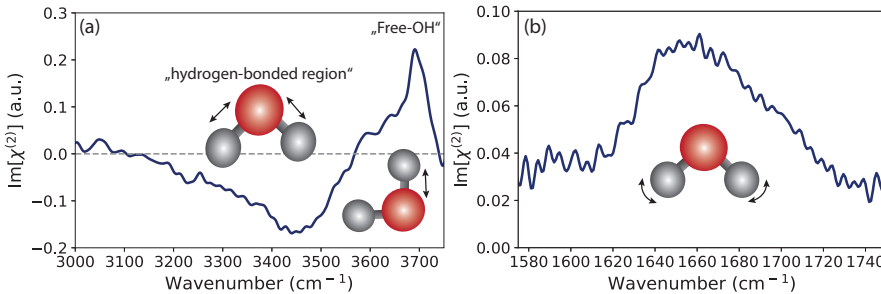


FIGURE 1.2. The heterodyne detected VSGF spectrum of the water/air interface in (a) the water stretching region and (b) the water bending region.

Even though water appears a rather simple molecule, it is one of the most abundant molecules and essential to all life on earth. As water is so omnipresent undoubtedly many important interfacial processes take place at aqueous interfaces. As Pauli mentioned molecules at the interface interact not only with each other but with additionally two different kinds of molecules, which means for water that its nearly tetrahedral arrangement will be broken at the interface. VSGF spectroscopy is a surface selective technique that can give direct molecular information about the vibrational modes at the surface, therefore VSGF is perfectly suited to investigate aqueous interfaces. The first VSGF intensity spectrum of the neat water surface was taken by Du *et al.*¹⁶ in 1993. As for other spectroscopic techniques like Raman^{17,18} or linear IR spectroscopy¹⁹ the broad band of the OH stretch vibrations of the hydrogen-bonded water molecules could be observed. Beside this broad feature additionally a sharp feature assigned to the non hydrogen-bonded water molecules with a free OH sticking out of the surface was observed, that manifests the surface selective capabilities of VSGF spectroscopy. Over the following years the technique of VSGF was de-

veloped further and more advanced VSFG techniques like heterodyne-detected VSFG (HD-VSFG)²⁰⁻²², time-resolved VSFG²³⁻²⁶ and even two-dimensional VSFG^{27,28} gave additional information about the orientation and the dynamics of molecules at aqueous interfaces. Despite its apparent simplicity the VSFG spectrum of the neat water surface is probably the most studied and discussed spectrum over the last decades. In the frequency region of the water OH stretch vibrations, the water/air interface^{16,29} has been extensively studied with VSFG spectroscopy resulting in a comprehensive understanding of the structural properties of water molecules at the surface.^{8,30-32} The frequency region of the water bending vibrations on the other hand has been much less investigated, even though this region can provide unique information on the hydrogen-bond structure. As in contrast to the stretching mode, the water bending mode is hardly influenced by intermolecular coupling due to its small transition dipole moment.³³⁻³⁵ Furthermore, there is only one water bending mode per water molecule, thus strongly decreasing the effects of intramolecular coupling on the spectrum. One reason why the bending mode at the interface was less studied is because of its small transition dipole moment that yields to a ~ 5 times smaller signal than the OH stretching modes. Therefore, the measurement of a clean VSFG response of the water bending mode is very challenging. Nevertheless, Vinaykin and Benderskii reported VSFG spectrum of the water bending mode measured with intensity VSFG.³⁴ Up to date, the origin of the response of the bending mode is highly debated and has been assigned to either surface-specific or to bulk effects. In chapter 4 of this thesis, we discuss the origin of the water bending mode in detail and clear up the existing inconsistencies between earlier reports.^{12,33,34,36,37}

1.1.2 ICE INTERFACES

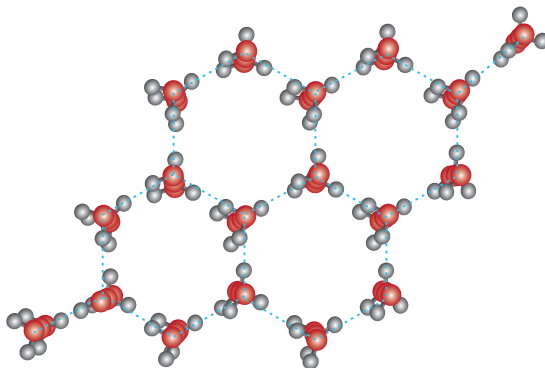


FIGURE 1.3. Schematic of the hexagonal structure of ice (I_h). The orientation is shown in the basal plane.

As many people would see it, ice is just frozen water by overlooking the tremendous differences between water and ice starting from the state of aggregation. At atmospheric pressure, the hydrogen-bonded network in ice has a fixed and ordered tetrahedral structure, which means that all water molecules form 4 hydrogen bonds with their neighboring water molecules. Another unique difference between liquid water and ice is that upon freezing the density decreases, which is the reason why ice is floating on liquid water.³⁸ The structure of hexagonal ice is presented in Figure 1.3 and shows that an ice crystal in basal plane orientation has a hexagonal structure. Also at the ice surface occur various chemical processes which are in particular of great interest to the field of atmospheric chemistry.³⁹⁻⁴² Ice surfaces for instance are known to act as sinks for pollutants, a process that considerably changes the properties of the ice surface.⁴³ Further, the formation of ice is devastating for biological systems, therefore some organisms in arctic regions developed strategies to survive, as for instance antifreeze proteins (AFPs). AFPs are a unique class of proteins that can bind to the surface of ice crystals and arrest their growth. Understanding the working mechanism of these proteins at the ice surface is of great interest for medicine, pharmacy, and industry.⁴⁴⁻⁴⁷

1.1.3 BIOLOGICAL INTERFACES

Nowadays the necessity of water in the functioning of bio-molecules is inarguable. Without water bio-molecules would not acquire their structure and therefore their function. It is well known that proteins as well as the carrier of our genetic information, deoxyribonucleic acid (DNA) need to be surrounded by water to be functional.^{48,49} Further, it is known that lipids form in an aqueous environment lipid bilayers in order to shield their hydrophobic tails from the water, these lipid bilayers are the basis of every cell membrane (Figure 1.4).⁵⁰ Cell membranes form the boundary of every living cell, which makes it the most essential interface in biological systems. Surrounded by the cell membrane are the cell's constituents, such as proteins, nucleic acids, carbohydrates, and substances involved in cellular metabolism. The most important function of the cell membrane is to be a barrier, which means keeping the constituents in and unwanted substances that are toxic for the cell out. Another essential function is to control the transport of necessary nutrients into the cell and the waste products out of the cell. Undoubtedly cell membranes and their constituents have been studied intensively with various techniques.⁵¹⁻⁵⁴ Along with these studies also the role of water related to bio-molecules got more into focus and investigated with techniques including spectroscopic approaches as FTIR^{55,56}, Raman⁵⁷⁻⁵⁹, dielectric relaxation^{60,61}, pump-probe^{62,63} and two-dimensional infrared spectroscopy^{64,65}. However, up to date the study of interfacial water molecules that are directly in contact with a bio molecules stays a challenge. In the recent past, it was proven that VSFG is one of the promising techniques that can give more information about the function of water surrounding biomolecules.^{7,66-68}

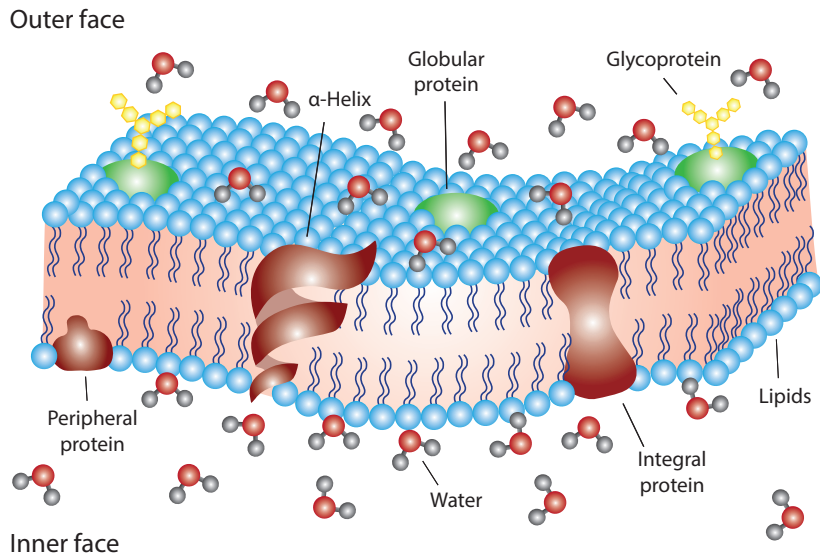


FIGURE 1.4. Schematic of a cell membrane surrounded by water molecules.

1.2 OUTLINE OF THIS THESIS

In this thesis we investigate different aqueous interfaces, from simple surfaces as the neat water/air interface (Chapter 4) to more complex surfaces as ice/air interface doped with antifreeze proteins (Chapter 9). First we introduce in chapter 2 the theoretical background of VSFG to give a good understanding of the theoretical origin of the measured VSFG response. Therefore, we discuss first the dependence of the nonlinear susceptibility on the experimental geometry and its molecular origin by introducing molecular hyperpolarizabilities. Further, we discuss the effect of the Fresnel factors on the VSFG response and the origin of the quadrupolar contribution. Finally, we briefly describe the $\chi^{(3)}$ effect at charged interfaces. Chapter 3 covers a description of the optical VSFG setup, that was used throughout the following chapters in this thesis, and how to improve our measurements by reducing the noise with a new measurement procedure. Furthermore, chapter 3 describes the fabrication and sample handling of monocrystalline ice. In chapter 4 we discuss the origin of the VSFG response of the water bending mode in pure water and at charged interfaces. Further, in chapter 5 we describe the molecular orientation of urea molecules in water at charged interfaces. In chapter 6 we study the vibrational response and the molecular orientation of small carboxylate ions at the water/air interface. Further, chapter 7 discusses the origin of the VSFG signal of small carboxylic acids at the water/air interface, while chapter 8 describes the different freezing behavior of aqueous solutions of small carboxylic acids on ice. Chapter 9 gives insights into the molecular structure of hyperactive antifreeze proteins adsorbed to the ice surface. We show that the water molecules in the hydration

layer around the antifreeze proteins are not changing their orientation upon interacting with the ice surface. In the final chapter, chapter 10, we discuss the molecular structure and surface accumulation dynamics of hyaluronan at the water/air interface in dependence of the molecular weight, the concentration, and the properties of the solvent.

(2) P SFG = €0X (2) EIR E VIS

2 THEORY OF VIBRATIONAL SUM-FREQUENCY GENERATION

In this thesis surface-specific vibrational sum-frequency generation (VSFG) spectroscopy was used to investigate different aqueous surfaces. While the experimental findings of these studies are described in chapter 4-10, this chapter will give a general description of the theory of VSFG to provide an overall understanding. A more detailed description of the theoretical background can be found in textbooks.⁶⁹⁻⁷³

2.1 THE ORIGIN OF VSFG

NON-RESONANT SUM-FREQUENCY GENERATION SFG is a nonlinear process involving the interaction between light and matter. While most linear and nonlinear processes provide information about the molecular structure and properties of material systems in bulk, SFG gives insights into the molecular structure at the surface. To generate a light-induced optical response of a material that will also include higher-order terms, the applied electric field needs to have a sufficiently high intensity. By interacting with charges within the material the applied electric field induces electric dipole moments. As a result, the material gets polarized. In the non-resonant case the polarization response to the applied field is instantaneous and has no memory effect. In this limit, the induced polarization $\mathbf{P}(t)$ can be written as a power series in terms of the applied electric field $\mathbf{E}(t)$:

$$\mathbf{P}(t) = \epsilon_0(\chi^{(1)}\mathbf{E}(t) + \chi^{(2)}\mathbf{E}^2(t) + \chi^{(3)}\mathbf{E}^3(t) + \dots) \quad (2.1)$$

where ϵ_0 is the vacuum permittivity and $\chi^{(1)}$ the linear susceptibility, $\chi^{(2)}$ the second-order, and $\chi^{(3)}$ the third-order susceptibility. The higher-order polarizations are typically smaller than the linear polarization. Thus, if the applied electric field is weak, all nonlinear terms in Eq. 2.1 are negligible. The induced nonlinear polarization leads to the emission of an electric field that is combined with the incident electric field. For a non-magnetic medium without free charges and current the electromagnetic fields are described by the Maxwell wave equation:

$$\nabla^2\mathbf{E}(\mathbf{x}, t) = \frac{1}{c^2} \frac{\partial^2}{\partial t^2}\mathbf{E}(\mathbf{x}, t) + \frac{1}{\epsilon_0 c^2} \frac{\partial^2}{\partial t^2}\mathbf{P}(\mathbf{x}, t) \quad (2.2)$$

where \mathbf{E} is the electric field and \mathbf{P} the linear and nonlinear polarization. The derivation of the wave equations can be found elsewhere.^{69,72} The wave

equation describes the propagation of the electric field through the material. The solutions of the wave equation provide us with transverse plane waves dependent on the time t with an angular frequency ω and in space \mathbf{x} with a spatial frequency $\mathbf{k}(\omega)$. For $\mathbf{E}(\mathbf{x}, t)$ it can be written:

$$\mathbf{E}(\mathbf{x}, t) = \frac{1}{2\pi} \int d\omega \mathbf{E}(\omega) e^{i(\mathbf{k}(\omega)\mathbf{x} - \omega t)} \quad (2.3)$$

where $\mathbf{E}(\omega)$ is the complex frequency component that incorporates both the phase and the amplitude. The polarization $\mathbf{P}(\mathbf{x}, t)$ can be written as:

$$\mathbf{P}(\mathbf{x}, t) = \frac{1}{2\pi} \int d\omega \mathbf{P}(\omega) e^{i(\mathbf{k}(\omega)\mathbf{x} - \omega t)} \quad (2.4)$$

Considering the interaction of two incident electric fields E_1 and E_2 the frequencies ω_1 and ω_2 interacting with a material with a non-zero $\chi^{(2)}$, for a monochromatic wave the total electric field can be described as:

$$\mathbf{E}(t) = \mathbf{E}_1(e^{-i\omega_1 t} + e^{i\omega_1 t}) + \mathbf{E}_2(e^{-i\omega_2 t} + e^{i\omega_2 t}) + c.c. \quad (2.5)$$

The resulting second-order nonlinear polarization response is:

$$\mathbf{P}^{(2)}(t) = \epsilon_0 \chi^{(2)} \mathbf{E}(t) \mathbf{E}(t) \quad (2.6)$$

Substituting the sum of the electric field, we obtain various components of the nonlinear polarization, leading to:

$$\begin{aligned} \mathbf{P}^{(2)}(t) = \epsilon_0 \chi^{(2)} [& \mathbf{E}_1^2 (e^{-i2\omega_1 t} + e^{i2\omega_1 t}) && (SHG) \\ & + \mathbf{E}_2^2 (e^{-i2\omega_2 t} + e^{i2\omega_2 t}) && (SHG) \\ & + 2\mathbf{E}_1 \cdot \mathbf{E}_2 (e^{-i(\omega_1 + \omega_2)t} + e^{i(\omega_1 + \omega_2)t}) && (SFG) \\ & + 2\mathbf{E}_1 \cdot \mathbf{E}_2 (e^{-i(\omega_1 - \omega_2)t} + e^{i(\omega_1 - \omega_2)t}) && (DFG) \\ & + 2(\mathbf{E}_1^2 + \mathbf{E}_2^2)] && (OR) \end{aligned} \quad (2.7)$$

The two incident electric fields give rise to second-harmonic generation (SHG) at frequencies $2\omega_1$ and $2\omega_2$, sum frequency generation (SFG) $\omega_1 + \omega_2$, difference-frequency generation (DFG) $\omega_1 - \omega_2$ and optical rectification (OR). The nonlinear processes are displayed in Figure 2.1.

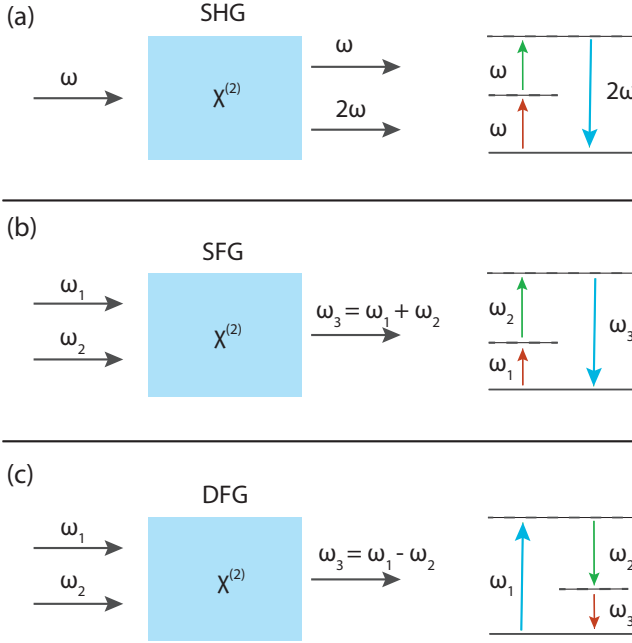


FIGURE 2.1. The nonlinear processes described in Eq. 2.7 (a) second-harmonic generation (SHG), (b) sum frequency generation (SFG) $\omega_1 + \omega_2$ and (c) difference-frequency generation (DFG) $\omega_1 - \omega_2$. The right side shows the energy-level description of the second-order conversion processes.

RESONANT VIBRATIONAL SUM-FREQUENCY GENERATION SPECTROSCOPY In the case of resonant vibrational sum-frequency generation spectroscopy, the frequency of one of the incident beams is chosen to be in resonance with the vibrational modes of the probed material (ω_{IR}) to enhance the second-order susceptibility $\chi^{(2)}$, while the second beam is fixed at a visible frequency (ω_{VIS}), and is usually not in resonance with the probed system. In the frequency domain the induced polarization can be described as:

$$\mathbf{P}(\omega) = \epsilon_0 \{ \chi^{(1)}(\omega) \mathbf{E}(\omega) + \chi^{(2)}(\omega) [\mathbf{E}]^2(\omega) + \chi^{(3)}(\omega) [\mathbf{E}]^3(\omega) + \dots \}, \quad (2.8)$$

where the brackets in the nonlinear terms indicate that the frequency ω corresponds to the higher powers of the E field and not to the E field itself. The second-order polarization coefficient $\mathbf{P}^{(2)}$ of the sum frequency process can be expressed as follows:

$$\mathbf{P}^{(2)}(\omega_{SFG}) = \epsilon_0 \chi^{(2)}(\omega_{SFG}) \mathbf{E}(\omega_{IR}) \mathbf{E}(\omega_{VIS}) \quad (2.9)$$

Further the second-order susceptibility $\chi^{(2)}$ consists of a resonant (R) and non-resonant (NR) term and can be written as:

$$\chi^{(2)} = \chi_{NR}^{(2)} + \chi_R^{(2)} = A_{NR} + \sum_n \frac{A_R}{\omega_n - \omega_{IR} - i\Gamma_n} \quad (2.10)$$

In this equation, $\chi_{NR}^{(2)}$ and $\chi_R^{(2)}$ represent the effective non-resonant and resonant second-order susceptibilities. Further, A_{NR} and A_R are the amplitudes of the non-resonant and resonant susceptibility and ω_n and Γ_n represent the resonant frequency and the width of the n -th vibrational mode.

2.2 GEOMETRY DEPENDENCE OF THE NONLINEAR SUSCEPTIBILITY

In chapter 2.1 the theoretical origin of the nonlinear second-order susceptibilities in the SFG process is described, which can finally be expressed with equation 2.10. Nevertheless, the absolute probed $\chi^{(2)}$ is dependent on the experimental geometry and thus dependent on the incident angles and the polarization of the beams. Furthermore, as mentioned at the beginning of chapter 2.1 VSFG is a surface-specific technique, which can be explained by the fact that due to symmetry reasons the SFG process is bulk forbidden for isotropic materials. In a centrosymmetric material, all directions are identical and therefore also the physical response of the material, here the $\chi^{(2)}$ should be equivalent in opposing directions.

$$\chi^{(2)} = -\chi^{(2)} \quad (2.11)$$

This expression only holds if, $\chi^{(2)} = 0$. This is the case for centrosymmetric media, and only at positions with broken symmetry, i.e. surfaces or interfaces SFG light can be generated. The second-order susceptibility $\chi^{(2)}$ can be described as a third-rank tensor that contains 27 components in the laboratory coordinate system, $\chi_{ijk}^{(2)}$. However, due to symmetry constraints at isotropic surfaces the number of non-zero components is reduced to seven. Here, we define the laboratory coordinates with the z-axis parallel to the surface normal and the x- and y-axis as spanning the surface plane (Figure 2.2). Further, for isotropic surfaces the x- and y-axis are equivalent, thus there are only four independent $\chi_{ijk}^{(2)}$ components, that can be written as follows:

$$\chi_{xxz}^{(2)} = \chi_{yyz}^{(2)}, \chi_{xzx}^{(2)} = \chi_{yzy}^{(2)}, \chi_{zxx}^{(2)} = \chi_{zyy}^{(2)}, \chi_{zzz}^{(2)} \quad (2.12)$$

Experimentally the four different $\chi_{ijk}^{(2)}$ components can be determined by varying the polarization combinations of the incident beams and the reflected SFG signal. S-polarization denotes a polarization of the optical field entirely parallel to the surface (along the y axis), whereas P-polarization has both parallel and perpendicular components (along the x and z axis) (Figure 2.2). The four different polarization combinations are SSP (S polarized VSFG, S polarized VIS and P polarized IR), SPS, PSS, and PPP. In this thesis only the SSP-polarization combination was used, therefore in the following chapters, only this polarization configuration will be discussed.

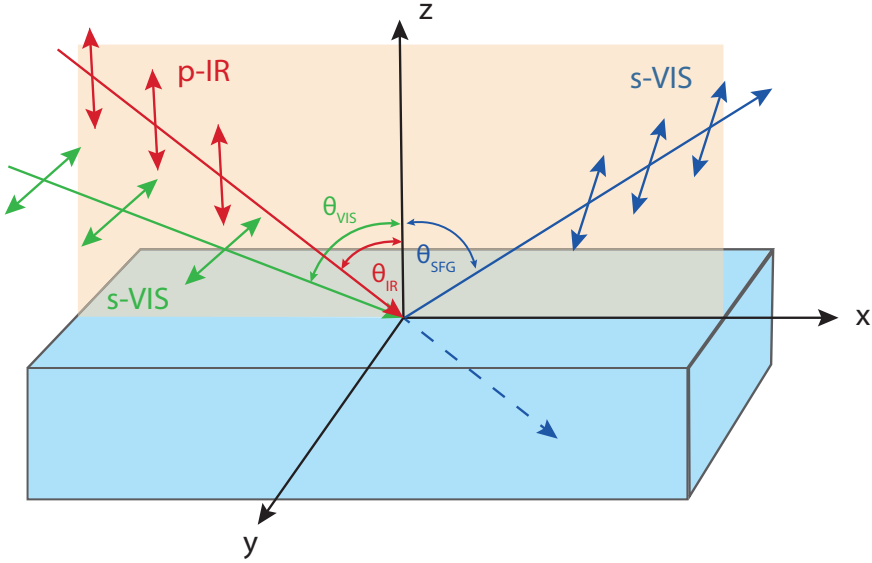


FIGURE 2.2. The geometry of VSFG including the incident angles and polarization of the electric fields. Here, a SSP-polarization configuration (S polarized VSFG (blue), S polarized VIS (green) and P polarized IR (red)) is shown.

2.3 HYPERPOLARIZABILITY

The $\chi_{ijk}^{(2)}$ is the average of the molecular hyperpolarizabilities β of the molecules at the interface (Eq. 2.13). As described in the previous chapter 2.2 the $\chi_{ijk}^{(2)}$ component is defined in laboratory coordinates. The hyperpolarizabilities β however are defined in molecular coordinates ($\beta_{i'j'k'} = \beta_{abc}$). The molecular coordinates do not in general coincide with the laboratory coordinates. This is for instance the case if the probed molecules at the surface are tilted with respect to the z-axis (surface normal). However, the tensor elements of $\chi_{ijk}^{(2)}$ and the hyperpolarizabilities $\beta_{i'j'k'}$ are directly related through the transformation of the Euler angles (Figure 2.3).

$$\chi_{ijk}^{(2)} = \frac{N_S}{\epsilon_0} \sum_{i'j'k'} \langle R_{ii'} R_{jj'} R_{kk'} \rangle \beta_{i'j'k'} \quad (2.13)$$

where N_S is the number density of probed molecules at the surface and $R_{ii'} R_{jj'} R_{kk'}$ are the rotation matrices using all three Euler angles to project the molecular coordinates to the laboratory coordinates. A detailed description of the Euler transformation can be found elsewhere.^{74,75}

Further, it is important to mention that the hyperpolarizabilities $\beta_{i'j'k'}$ of a particular vibrational mode q are proportional to the derivatives of the Raman

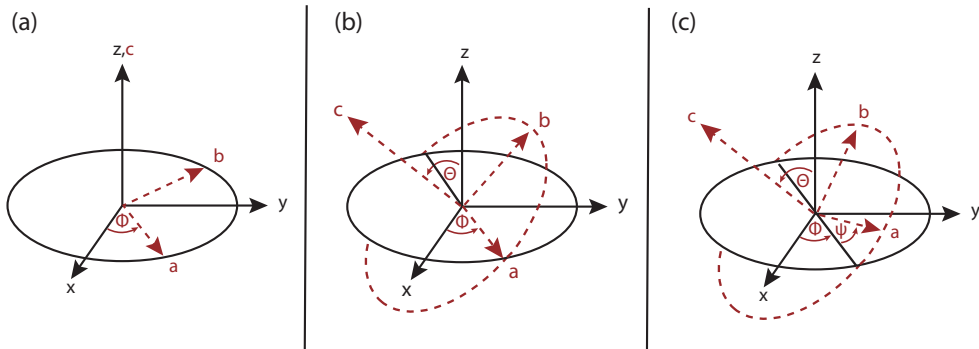


FIGURE 2.3. Schematic of the Euler transformation between the laboratory coordinates x, y, z and the molecular coordinates a, b, c through the three Euler angles Φ , Θ and Ψ .

polarizability $\alpha_{i'j'}$ and the dipole moment $\mu_{k'}$.

$$\beta_{i'j'k'}(Q_q) \propto \frac{1}{2\epsilon_0\omega_q} \frac{\partial\alpha_{i'j'}}{\partial Q_q} \frac{\partial\mu_{k'}}{\partial Q_q} \quad (2.14)$$

where ω_q is the resonant frequency and Q_q is the normal coordinate of the vibrational mode q . Thus, it can be concluded that a vibrational mode has to be Raman and IR active to be VSFG active.

Also $\beta_{i'j'k'}$ consists in total of tensor 27 elements. In order to find the elements that contribute for a particular molecular group, we need to consider not only the geometry of the experiment but the symmetry of the molecular group (C_{nv}). In this thesis all experiments are performed in SSP-polarization configuration, therefore it follows: $\chi^{(2)} \propto \chi_{xxx}^{(2)} = \chi_{yyy}^{(2)}$. Further, we will describe in more detail the non-vanishing molecular hyperpolarizability tensor elements of the C_{2v} symmetry group, as it is of great importance for the understanding of the vibrational response of the carboxyl group of small carboxylates in chapter 6. A description of other symmetry groups can found elsewhere.^{33,74,76-80}

HYPERPOLARIZABILITY OF C_{2v} SYMMETRY GROUP For C_{2v} symmetry groups, such as the carboxyl group, water or the methylene (CH_2) group there are in total seven non-vanishing molecular hyperpolarizability tensor elements:

$$\beta_{aac}, \beta_{bbc}, \beta_{ccc}, \beta_{aca} = \beta_{caa}, \beta_{bcb} = \beta_{cbb} \quad (2.15)$$

For the symmetric stretching and bending modes the transition dipole moment changes along the c -axis. Therefore, only three of these hyperpolarizability tensor elements ($\beta_{aac}, \beta_{bbc}, \beta_{ccc}$) contribute to the measured VSFG response, hence only the hyperpolarizability tensor elements with the last subindex c are nonzero.

As the transition dipole moment of the antisymmetric stretching modes is changing along the a - or b - axis, only the hyperpolarizability tensor elements

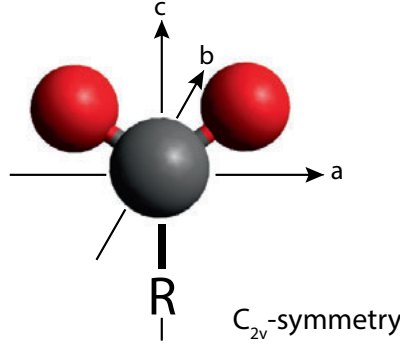


FIGURE 2.4. Schematic of the C_{2v} symmetry of the carboxyl group in the molecular axes frame. The c-axis coincides with the rotation axis.

with the last subindex a or b are active. Thus, for the antisymmetric modes four elements contribute (β_{aca} , β_{caa} , β_{bcb} , β_{cbb}). In the case of the C_{2v} symmetry group $\beta_{bcb} = 0$.⁸⁰ Further, performing the Euler transformation and assuming free rotation of the molecule around the molecular axis c (uniform distribution in the azimuthal angle ϕ), the $\chi_{ijk}^{(2)}$ components can be described with the following expressions:^{74,80}

$$\chi_{xxz}^{(2),ss} = \chi_{yyz}^{(2),ss} = \frac{1}{4}N_s(\beta_{aac} + \beta_{bbc} + 2\beta_{ccc})\langle \cos\Theta \rangle + \frac{1}{4}N_s(\beta_{aac} + \beta_{bbc} - 2\beta_{ccc})\langle \cos^3\Theta \rangle \quad (2.16)$$

for the symmetric stretch vibrational mode,

$$\chi_{xxz}^{(2),as} = \chi_{yyz}^{(2),as} = -\frac{1}{2}N_s\beta_{aca}(\langle \cos\Theta \rangle - \langle \cos^3\Theta \rangle) \quad (2.17)$$

for the antisymmetric stretch vibrational mode, where θ is the tilt angle between the c-axis and the surface normal z.

2.4 FRESNEL FACTORS

The dielectric constants of the air and the bulk are different. While passing from one *medium_a* (air) into another *medium_b* (bulk) the electric field passes through a boundary of two different dielectric constants, which influences the electric field and its wave vector. At the boundary, the electric field can be either reflected or transmitted (Figure 2.5). Here, we consider that *medium_b* is not resonant with the electric field, which means that we assume its dielectric function to be real. The effect of the different dielectric constants on the electric fields can be described with the Fresnel factors ($\mathbf{F}^{a \rightarrow b}$), which can be expressed with two different models the two-layer model and the three-layer model. First, we will describe the Fresnel factors described with the two-layer model. Within this model we assume two bulk media that have a dielectric constant of ϵ_a and

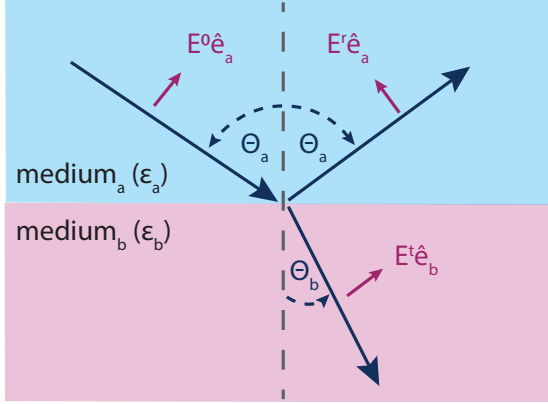


FIGURE 2.5. Change of the electric field passing from *medium_a* (air) to *medium_b* (bulk) described with the two-layer model, considering p-polarization.

ϵ_b , and therefore the refractive indices of $n_a = \sqrt{\epsilon_a}$ and $n_b = \sqrt{\epsilon_b}$ (Figure 2.5). Further, we denote the incident and transmitted angle with Θ_a and Θ_b , respectively. Accordingly, Snell's law can be written as follows,

$$n_a \sin \Theta_a = n_b \sin \Theta_b \quad (2.18)$$

and therefore $\cos \Theta_b$ can be expressed as:

$$\cos \Theta_b = \sqrt{1 - \sin^2 \Theta_b} = \sqrt{1 - \frac{n_a^2}{n_b^2} \sin^2 \Theta_a} \quad (2.19)$$

As shown in Figure 2.5 the incident, transmitted and reflected beams are labeled as E^0, E^r and E^t . The ratios of the reflected and transmitted amplitudes of the electric fields ($r = E^r/E^0$ and $t = E^t/E^0$) are extracted from the ordinary boundary conditions of electric fields at a plane interface.⁸¹ Further, these ratios are dependent on the polarization and can be written as follows:

(a) For P-polarization

$$t_P = \frac{2n_a \cos \Theta_a}{n_b \cos \Theta_a + n_a \cos \Theta_b}, r_P = \frac{n_b \cos \Theta_a - n_a \cos \Theta_b}{n_b \cos \Theta_a + n_a \cos \Theta_b} \quad (2.20)$$

(b) For S-polarization

$$t_S = \frac{2n_a \cos \Theta_a}{n_a \cos \Theta_a + n_b \cos \Theta_b}, r_S = \frac{n_a \cos \Theta_a - n_b \cos \Theta_b}{n_a \cos \Theta_a + n_b \cos \Theta_b} \quad (2.21)$$

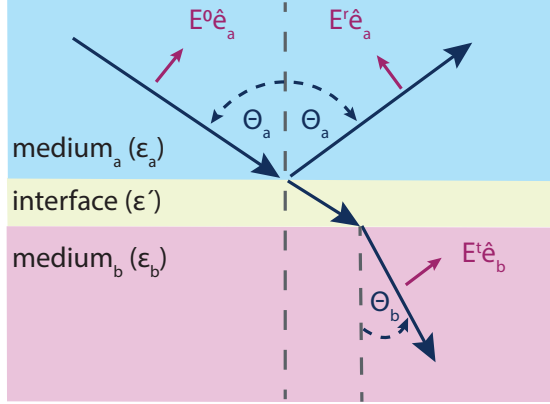


FIGURE 2.6. Change of the electric field passing from *medium_a* (air) to *medium_b* (bulk) described with the three-layer model, considering p-polarization .

Further, the electric field amplitudes for P-polarization are

$$E^0 e_a = E^0 \begin{pmatrix} \cos\Theta_a \\ 0 \\ \sin\Theta_a \end{pmatrix}, E^t e_b = E^t \begin{pmatrix} \cos\Theta_b \\ 0 \\ \sin\Theta_b \end{pmatrix} = t_p E^0 \begin{pmatrix} \cos\Theta_b \\ 0 \\ \sin\Theta_b \end{pmatrix} \quad (2.22)$$

and consequently

$$\mathbf{F}_{zz}^{a \rightarrow b} = t_p \frac{\sin\Theta_b}{\sin\Theta_a}, \mathbf{F}_{xx}^{a \rightarrow b} = t_p \frac{\cos\Theta_b}{\cos\Theta_a} \quad (2.23)$$

For S-polarization the electric field amplitudes can be written as:

$$E^0 e_a = E^0 \begin{pmatrix} 0 \\ 1 \\ 0 \end{pmatrix}, E^t e_b = E^t \begin{pmatrix} 0 \\ 1 \\ 0 \end{pmatrix} = t_s E^0 \begin{pmatrix} 0 \\ 1 \\ 0 \end{pmatrix}, \quad (2.24)$$

and consequently

$$\mathbf{F}_{yy}^{a \rightarrow b} = t_s. \quad (2.25)$$

$\mathbf{F}^{a \rightarrow b}$ can be written as:

$$\mathbf{F}^{a \rightarrow b} = \begin{pmatrix} \frac{2n_a \cos\Theta_b}{n_b \cos\Theta_a + n_a \cos\Theta_b} & & \\ & \frac{2n_a \cos\Theta_a}{n_a \cos\Theta_a + n_b \cos\Theta_b} & \\ & & \frac{2n_a^2 \cos\Theta_a}{n_b^2 \cos\Theta_a + n_a n_b \cos\Theta_b} \end{pmatrix} \quad (2.26)$$

The two-layer model can be extended to the three-layer model in which we assume that the electric fields pass also through an interface layer by entering from *medium_a* into *medium_b*. As described in the two-layer model by passing from one medium into the other with different dielectric constants the electric field and its wavevectors can be modified. In the three-layer model the electric field is passing instead of one boundary through two boundaries (Figure 2.6). Here, we denote the dielectric constant in the interface layer as ϵ' . Considering $\epsilon' \neq \epsilon^a, \epsilon^b$, $\mathbf{F}^{a \rightarrow b}$ can be written as:

$$\mathbf{F}^{a \rightarrow b} = \begin{pmatrix} \frac{2n_a \cos \Theta_b}{n_b \cos \Theta_a + n_a \cos \Theta_b} & & \\ & \frac{2n_a \cos \Theta_a}{n_a \cos \Theta_a + n_b \cos \Theta_b} & \\ & & \left(\frac{n_a}{n'}\right)^2 \frac{2n_b \cos \Theta_a}{n_b \cos \Theta_a + n_a \cos \Theta_b} \end{pmatrix} \quad (2.27)$$

2.4.1 INTERFACIAL DIELECTRIC CONSTANT ϵ' IN THE MICROSCOPIC REGIME

Importantly, the dielectric constant of the interfacial layer ϵ' is unknown. To get an approximation of the dielectric constant of the interfacial layer ϵ' we have to implement a microscopic formulation based on the molecular theory of the local field. First, we assume that the interfacial layer is infinitely small ($z \approx 0$). For simplicity we further assume that *medium_a* is vacuum, and thus $\epsilon_a = 1$. In the microscopic regime we distinguish the incident field \mathbf{E}_I , the external field \mathbf{E}_{ext} and the local field \mathbf{E}_{loc} . Next we suppose a plane wave $\mathbf{E}_I^a(\omega)$ is entering from *medium_a* into the interface layer, the interface near $z \approx 0$ feels now the external field $\mathbf{E}_{ext}(\omega)$. The external field is now related to the incident field through the optical factor $\mathbf{L}_I(\omega)$.

$$\mathbf{E}_{ext}(\omega) = \mathbf{L}_I(\omega) \mathbf{E}_I^a(\omega) \quad (2.28)$$

Considering $\epsilon^a = \epsilon' = 1$, $\mathbf{F}^{a \rightarrow b}$ coincides with \mathbf{L}_I and can be described as:

$$\mathbf{L}_I = \begin{pmatrix} \frac{2n_a \cos \Theta_b}{n_b \cos \Theta_a + n_a \cos \Theta_b} & & \\ & \frac{2n_a \cos \Theta_a}{n_a \cos \Theta_a + n_b \cos \Theta_b} & \\ & & \frac{2n_a^2 \cos \Theta_a}{n_b^2 \cos \Theta_a + n_a \cos \Theta_b} \end{pmatrix} \quad (2.29)$$

Here, we omit the z dependence, as we treat the field near the interface ($z \approx 0$) much shorter than the wavelength. Nevertheless, due to the local field correction the external field is not equal to the local field that is felt by each individual molecule. Therefore, the local field \mathbf{E}_{loc} near the interface is related with \mathbf{E}_{ext} through the local field factor $\mathbf{f}(\omega, z)$,

$$\mathbf{E}^{loc}(z, \omega) = \mathbf{f}(\omega, z) \mathbf{E}_{ext}(\omega) = \mathbf{f}(\omega, z) \mathbf{L}_I(\omega) \mathbf{E}_I^a(\omega) \quad (2.30)$$

Further, we consider the inhomogeneous structure of the interfacial layer, therefore \mathbf{E}_{loc} and thus $\mathbf{f}(\omega, z)$ depend on the z coordinate. The implemented z -dependence of $\mathbf{f}(\omega, z)$ is related to the dielectric constant of the interfacial layer, thus different models can be applied to get an approximation for ϵ' . One of this models is the Lorentz model for which the derivation of ϵ' can be found in Morita *et. al.*⁷⁰. Next, we take the z -dependence of the nonlinear polarization into account,

$$\mathbf{P}^{(2)}(z, \omega_{SFG}) = \chi^{D0}(z, \omega_{SFG}, \omega_{IR}, \omega_{VIS}) : \mathbf{E}^{loc}(z, \omega_{IR}) \mathbf{E}^{loc}(z, \omega_{VIS}) \quad (2.31)$$

where $\chi^{D0}(z, \omega_{SFG}, \omega_{IR}, \omega_{VIS})$ second-order susceptibility affected by the local fields. In SSP-polarization configuration the effect of the optical factor L on the measured $\chi^{(2)}$ can be expressed as:

$$\chi^{(2)} = L_{yy}(\omega_{SFG}) L_{yy}(\omega_{VIS}) L_{zz}(\omega_{IR}) \sin \Theta_{IR} \chi_{yyz}^{(2)} \quad (2.32)$$

At last, it would be accurate if all experimentally obtained VSG spectra would be corrected with the Fresnel factors. However, Feng *et. al* has shown that the difference in the corrected and uncorrected VSG spectra of the water/air interface is negligible.⁸² Therefore in this thesis we only account for the Fresnel factors in chapter 6 and 7 in which the refractive index is sufficient changed and the Fresnel factors have a visible effect on the experimental VSG spectra. Importantly, in the case of VSG, we need to consider that the electric field is in resonance with medium, therefore to calculate the Fresnel factors we need to consider the complex refractive index.⁸³

2.5 QUADRUPOLAR CONTRIBUTIONS

Up to now, we have described the theory of VSG spectroscopy alone based on the induced dipole contribution of the material χ^{ID} that exclusively arises from the region where the symmetry is broken. Accurately, within the theory of VSG we also have to take higher-order contributions into consideration, as the electric quadrupole contribution and the magnetic dipole contribution. These higher-order contributions are not necessarily forbidden in isotropic media. In this chapter, we focus on the electric quadrupolar contribution by closely following the description by Morita *et al.*⁷⁰ To describe the second-order polarization including the quadrupolar contributions we need to consider the configuration of the electric field gradient within the interfacial layer on a molecular scale. First, we need to extend the description of nonlinear polarization including the dependence on z and the phase factor.

$$\mathbf{P}_i^{(2)}(\mathbf{r}, \omega_{SFG}, t) = \sum_{j,k} \chi_{ijk}^{D0}(z, \omega_{SFG}, \omega_{IR}, \omega_{VIS}) E_j^{loc}(\mathbf{r}, \omega_{IR}, t) E_k^{loc}(\mathbf{r}, \omega_{VIS}, t) \quad (2.33)$$

where i, j, k represent the cartesian coordinates x, y, z , and $\chi^{D0}(z, \omega_{SFG}, \omega_{IR}, \omega_{VIS})$ is the second-order susceptibility affected by the local fields ($E_j^{loc}(\mathbf{r}, \omega_{IR}, t)$ and

$E_k^{loc}(\mathbf{r}, \omega_{VIS}, t)$). Further, we extend the description of the nonlinear polarization including the quadrupolar contributions.

$$\begin{aligned}
\mathbf{P}_i^{(2)}(\mathbf{r}, \omega_{SFG}, t) = & \\
& \sum_{j,k} \chi_{ijk}^{D0}(z, \omega_{SFG}, \omega_{IR}, \omega_{VIS}) E_j^{loc}(\mathbf{r}, \omega_{IR}, t) E_k^{loc}(\mathbf{r}, \omega_{VIS}, t) \\
& + \sum_{jkl} [\chi_{ijkl}^{D1}(z, \omega_{SFG}, \omega_{IR}, \omega_{VIS}) \frac{\partial E_j^{loc}(\mathbf{r}, \omega_{IR}, t)}{\partial l} E_k^{loc}(\mathbf{r}, \omega_{VIS}, t) \\
& + \chi_{ijkl}^{D2}(z, \omega_{SFG}, \omega_{IR}, \omega_{VIS}) E_j^{loc}(\mathbf{r}, \omega_{IR}, t) \frac{\partial E_k^{loc}(\mathbf{r}, \omega_{VIS}, t)}{\partial l} \\
& - \frac{\partial}{\partial l} \{ \chi_{ijkl}^Q(z, \omega_{SFG}, \omega_{IR}, \omega_{VIS}) E_j^{loc}(\mathbf{r}, \omega_{IR}, t) E_k^{loc}(\mathbf{r}, \omega_{VIS}, t) \}] \quad (2.34)
\end{aligned}$$

The first term including χ_{ijk}^{D0} does not indicate any quadrupolar components and is completely interface specific. The middle lines of eq. 2.34 on the other hand including χ_{ijkl}^{D1} , χ_{ijkl}^{D2} describe in particular the polarization induced by the electric field and the field gradient. The last term including χ_{ijkl}^Q is the derivative of the induced polarization and is describing the induced quadrupolar contribution. General, a quantity that couples with the field gradient has quadrupolar character and is not necessarily bulk forbidden. Furthermore, χ^{D1} , χ^{D2} and χ^Q are fourth rank tensors (even-rank) and χ^{D0} is a third rank tensor (odd-rank). This difference is important as for symmetry reasons the material properties of even rank tensors are not necessarily vanishing in centrosymmetric media. The local electric field at the interface and in the bulk E_{tot}^{loc} can be written as follows:

$$\mathbf{E}_{tot}^{loc}(\mathbf{r}, \omega, t) = \mathbf{E}^{loc}(z, \omega) \exp(i\mathbf{k}_T^b(\omega) \cdot \mathbf{r} - i\omega t) \quad (2.35)$$

The nonlinear polarization induced in the interface ($z \approx 0$) and the bulk *medium_b* ($z > 0$) can be extended accordingly.

$$\begin{aligned}
& \mathbf{P}_i^{(2)}(\mathbf{r}, \omega_{SFG}, t) \\
&= \sum_{j,k} f_i(z, \omega_{SFG}) \chi_{ijk}^{D0}(z, \omega_{SFG}, \omega_{IR}, \omega_{VIS}) f_j(z, \omega_{IR}) L_{I,j}(\omega_{IR}) E_{I,j}^a(\omega_{IR}) \\
& \exp(i\mathbf{k}_T^b(\omega_{IR}) \cdot \mathbf{r} - i\omega_{IR}t) \cdot f_k(z, \omega_{VIS}) L_{I,k}(\omega_{VIS}) E_{I,k}^a(\omega_{VIS}) \\
& \exp(i\mathbf{k}_T^b(\omega_{VIS}) \cdot \mathbf{r} - i\omega_{VIS}t) \\
&+ \sum_{j,k,l} f_i(z, \omega_{SFG}) [\chi_{ijkl}^{D1}(z, \omega_{SFG}, \omega_{IR}, \omega_{VIS}) \frac{\partial}{\partial l} \{f_j(z, \omega_{IR}) L_{I,j}(\omega_{IR}) E_{I,j}^a(\omega_{IR}) \\
& \exp(i\mathbf{k}_T^b(\omega_{IR}) \cdot \mathbf{r} - i\omega_{IR}t)\} \cdot f_k(z, \omega_{VIS}) L_{I,k}(\omega_{VIS}) E_{I,k}^a(\omega_{VIS}) \\
& \exp(i\mathbf{k}_T^b(\omega_{VIS}) \cdot \mathbf{r} - i\omega_{VIS}t) \\
&+ \sum_{j,k,l} f_i(z, \omega_{SFG}) [\chi_{ijkl}^{D2}(z, \omega_{SFG}, \omega_{IR}, \omega_{VIS}) f_j(z, \omega_{IR}) L_{I,j}(\omega_{IR}) E_{I,j}^a(\omega_{IR}) \\
& \exp(i\mathbf{k}_T^b(\omega_{IR}) \cdot \mathbf{r} - i\omega_{IR}t) \cdot \frac{\partial}{\partial l} \{f_k(z, \omega_{VIS}) L_{I,k}(\omega_{VIS}) E_{I,k}^a(\omega_{VIS}) \\
& \exp(i\mathbf{k}_T^b(\omega_{VIS}) \cdot \mathbf{r} - i\omega_{VIS}t)\} \\
&- \sum_{j,k,l} f_i(z, \omega_{SFG}) \frac{\partial}{\partial l} \{\chi_{ijkl}^Q(z, \omega_{SFG}, \omega_{IR}, \omega_{VIS}) f_j(z, \omega_{IR}) L_{I,j}(\omega_{IR}) E_{I,j}^a(\omega_{IR}) \\
& \exp(i\mathbf{k}_T^b(\omega_{IR}) \cdot \mathbf{r} - i\omega_{IR}t) f_k(z, \omega_{VIS}) L_{I,k}(\omega_{VIS}) E_{I,k}^a(\omega_{VIS}) \\
& \exp(i\mathbf{k}_T^b(\omega_{VIS}) \cdot \mathbf{r} - i\omega_{VIS}t)\} \\
\end{aligned} \tag{2.36}$$

Equation 2.36 shows that on all quadrupolar terms the spatial derivative $\frac{\partial}{\partial l}$ ($l = x, y, z$) is implied. The derivative of the local field factor $f(z, \omega)$ and the phase factor $\exp(i\mathbf{k}(\omega) \cdot \mathbf{r} - i\omega t)$ correspond to definite mechanisms in the SFG process. The value of the derivative of the local field depends on the inhomogeneous structure of the interfacial layer and thus is part of the interfacial nonlinear polarization. However, the derivative of the phase factor does not vanish in homogeneous media and can therefore be assumed to be the bulk nonlinear polarization. Further, we divide the total nonlinear polarization in an interfacial part $\mathbf{P}^{(2),I}$ and a bulk part $\mathbf{P}^{(2),B}$, to discuss measured SFG response including dipolar and quadrupolar contribution in more detail.

$$\mathbf{P}^{(2),tot} = \mathbf{P}^{(2),I} + \mathbf{P}^{(2),B} \tag{2.37}$$

INTERFACE CONTRIBUTION The interface nonlinear polarization is derived from Eq. 2.36. The derivative $\frac{\partial}{\partial l}$ arises along the normal direction $l=z$. Thus, the nonlinear polarization at the the interface $P^{(2),I}$ can be written as:

$$\begin{aligned}
& P^{(2),I} \exp(ik_x(\omega_{SFG})x - i\omega_{SFG}x) \\
&= \int_{z_b}^{\infty} dz \left[\sum_{j,k} f_i(z, \omega_{SFG}) \chi_{ijk}^{D0}(z, \omega_{SFG}, \omega_{IR}, \omega_{VIS}) f_j(z, \omega_{IR}) f_k(z, \omega_{VIS}) \right. \\
&+ \sum_{j,k} f_i(z, \omega_{SFG}) \chi_i^{D1} jkz(z, \omega_{SFG}, \omega_{IR}, \omega_{VIS}) \frac{\partial f_j(z, \omega_{IR})}{\partial z} f_k(z, \omega_{VIS}) \\
&+ \sum_{k,l} f_i(z, \omega_{SFG}) \chi_i^{D2} jkz(z, \omega_{SFG}, \omega_{IR}, \omega_{VIS}) f_j(z, \omega_{IR}) \frac{\partial f_k(z, \omega_{VIS})}{\partial z} \\
&- \left. \sum_{j,k} f_i(z, \omega_{SFG}) \frac{\partial}{\partial z} \{ \chi_{ijkz}^Q(z, \omega_{SFG}, \omega_{IR}, \omega_{VIS}) f_j(z, \omega_{IR}) f_k(z, \omega_{VIS}) \} \right] \\
&\cdot L_{I,j}(\omega_{IR}) E_{I,j}^a(\omega_{IR}) \exp(ik_x(\omega_{IR})x - i\omega_{IR}t) \\
&\cdot L_{I,k}(\omega_{VIS}) E_{I,k}^a(\omega_{VIS}) \exp(ik_x(\omega_{VIS})x - i\omega_{VIS}t)
\end{aligned} \tag{2.38}$$

Here, the lower boundary z_b is an arbitrary position in the bulk, that covers the whole inhomogeneous interfacial layer in *medium_b*. Consequently, χ^{D0} and $\frac{\partial f}{\partial z}$ vanish outside the integral. Further, within the integral, the phase factor along z can be assumed to be negligible as the interfacial layer is much shorter than the wavelength of the electric fields. However, by altering the fifth line of Eq. 2.38 using integration in parts:

$$\begin{aligned}
& - \int_{z_b}^{\infty} dz \sum_{j,k} f_i(z, \omega_{SFG}) \frac{\partial}{\partial z} \{ \chi_{ijkz}^Q(z, \omega_{SFG}, \omega_{IR}, \omega_{VIS}) f_j(z, \omega_{IR}) f_k(z, \omega_{VIS}) \} \\
&= \int_{z_b}^{\infty} dz \sum_{j,k} \frac{\partial f_i(z, \omega_{SFG})}{\partial z} \{ \chi_{ijkz}^Q(\omega_{SFG}, \omega_{IR}, \omega_{VIS}) f_j(z, \omega_{IR}) f_k(z, \omega_{VIS}) \} \\
&+ \sum_{j,k} f_i^b(\omega_{SFG}) \chi_{ijkz}^{Q,b}(\omega_{SFG}, \omega_{IR}, \omega_{VIS}) f_i^b(\omega_{SFG}) f_j^b(\omega_{IR}) f_k^j(\omega_{VIS})
\end{aligned} \tag{2.39}$$

In the last term of Eq. 2.39 all variables with the superscript b describe quantities of *medium_b*, which originate from the lower bond $z = z_b$. The upper bond $z = \infty$ however corresponds to *medium_a* (air), for which all material quantities vanish. The total interface contribution of the nonlinear polarization can be expressed as follows:

$$\begin{aligned}
P^{(2),I} &= \sum_{j,k} (\chi_{ijk}^{ID}(\omega_{SFG}, \omega_{IR}, \omega_{VIS}) \chi_{ijk}^{IQ}(\omega_{SFG}, \omega_{IR}, \omega_{VIS})) \\
&\chi_{ijk}^{IQB}(\omega_{SFG}, \omega_{IR}, \omega_{VIS}) \cdot L_{I,j}(\omega_{IR}) E_{I,j}^a(\omega_{IR}) \exp(ik_x(\omega_{IR})x - i\omega_{IR}t)
\end{aligned} \tag{2.40}$$

where

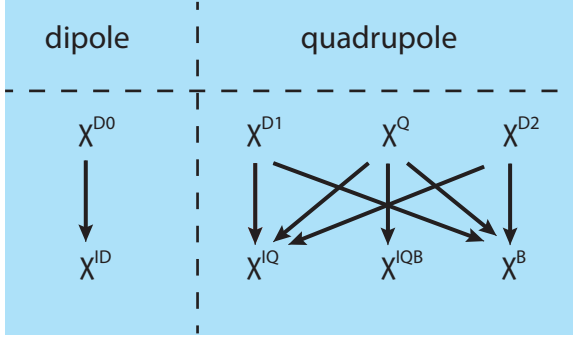


FIGURE 2.7. Schematic of the quadrupolar and dipolar nonlinear susceptibility terms.

$$\chi_{ijk}^{ID}(\omega_{SFG}, \omega_{IR}, \omega_{VIS}) = \int_{z_b}^{\infty} dz \chi_{ijk}^{D0}(z, \omega_{SFG}, \omega_{IR}, \omega_{VIS}) f_i(z, \omega_{SFG}) f_j(z, \omega_{IR}) f_k(z, \omega_{VIS}), \quad (2.41)$$

$$\begin{aligned} \chi_{ijk}^{IQ}(\omega_{SFG}, \omega_{IR}, \omega_{VIS}) = & \int_{z_b}^{\infty} dz \{ \chi_{ijkz}^{D1}(z, \omega_{SFG}, \omega_{IR}, \omega_{VIS}) f_i(z, \omega_{SFG}) \frac{\partial f_j(z, \omega_{IR})}{\partial z} f_k(z, \omega_{VIS}) \\ & + \chi_{ijkz}^{D1}(z, \omega_{SFG}, \omega_{IR}, \omega_{VIS}) f_i(z, \omega_{SFG}) f_j(z, \omega_{IR}) \frac{\partial f_k(z, \omega_{VIS})}{\partial z} \\ & + \chi_{ijkz}^Q(z, \omega_{SFG}, \omega_{IR}, \omega_{VIS}) \frac{\partial f_i(z, \omega_{SFG})}{\partial z} f_j(z, \omega_{IR}) f_k(z, \omega_{VIS}) \}, \end{aligned} \quad (2.42)$$

$$\begin{aligned} \chi_{ijk}^{IQB}(\omega_{SFG}, \omega_{IR}, \omega_{VIS}) = & \chi_{ijkz}^{Q,b}(\omega_{SFG}, \omega_{IR}, \omega_{VIS}) f_i^b(\omega_{SFG}) f_j^b(\omega_{IR}) f_k^b(\omega_{VIS}), \end{aligned} \quad (2.43)$$

BULK CONTRIBUTION The remaining part of the non-linear polarization from Eq. 2.36 is the term including the derivative over the phase factor. This term describes the bulk part of the total non-linear polarization $\mathbf{P}^{(2),B}$ and can be written as:

$$\begin{aligned}
P^{(2),B} = & \sum_{j,k,l} f_i^b(\omega_{SFG}) \chi_{ijkl}^{D1,j} f_j^b(\omega_{IR}) L_{I,j}(\omega_{IR}) E_{I,j}^a(\omega_{IR}) \left\{ \frac{\partial}{\partial l} \exp(i\mathbf{k}_T^b(\omega_{IR}) \cdot \mathbf{r} - i\omega_{IR}t) \right\} \\
& f_k^b(\omega_{VIS}) L_{I,k}(\omega_{VIS}) E_{I,k}^a(\omega_{VIS}) \exp(i\mathbf{k}_T^b(\omega_{VIS}) \cdot \mathbf{r} - i\omega_{VIS}t) \\
& + \sum_{j,k,l} f_i^b(\omega_{SFG}) \chi_{ijkl}^{D2,j} f_j^b(\omega_{IR}) L_{I,j}(\omega_{IR}) E_{I,j}^a(\omega_{IR}) \exp(i\mathbf{k}_T^b(\omega_{IR}) \cdot \mathbf{r} - i\omega_{IR}t) \\
& f_k^b(\omega_{VIS}) L_{I,k}(\omega_{VIS}) E_{I,k}^a(\omega_{VIS}) \left\{ \frac{\partial}{\partial l} \exp(i\mathbf{k}_T^b(\omega_{VIS}) \cdot \mathbf{r} - i\omega_{VIS}t) \right\} \\
& - \sum_{j,k,l} f_i^b(\omega_{SFG}) \chi_{ijkl}^{Q,j} f_j^b(\omega_{IR}) L_{I,j}(\omega_{IR}) E_{I,j}^a(\omega_{IR}) f_k^b(\omega_{VIS}) L_{I,k}(\omega_{VIS}) E_{I,k}^a(\omega_{VIS}) \\
& \cdot \left\{ \frac{\partial}{\partial l} \exp(i\mathbf{k}_T^b(\omega_{IR}) \cdot \mathbf{r} - i\omega_{IR}t) \exp(i\mathbf{k}_T^b(\omega_{VIS}) \cdot \mathbf{r} - i\omega_{VIS}t) \right\}
\end{aligned} \tag{2.44}$$

By performing the derivative and integrating along z it can be observed that $\mathbf{P}^{(2),B}$ and therefore χ^B is dependent on the geometry of the experiment. The derivation can be found in Morita *et al.*⁷⁰ It is known that for the experimental geometry used in this thesis with SSP polarization combination χ^B is estimated to be negligible.^{37,70,84} Finally, the total quadrupolar contribution of the VSG response can be classified in three different contributions, namely χ^{IQ} , χ^{IQB} and χ^B . Therefore, the total second-order response including both the bulk and the surface can be written as:

$$\chi_{total} = \chi^{ID} + \chi^{IQ} + \chi^{IQB} + \chi^B \tag{2.45}$$

Both the χ^{ID} and χ^{IQ} reflect purely interface properties, while χ^{IQB} and χ^B are determined entirely from bulk properties. Theoretical studies show that the χ^{IQ} component for the systems measured in this thesis is small, therefore we do not account for this component in the following interpretation of our measurements,^{37,85} in particular in chapter 4 and 7. As the χ^B component the χ^B is dependent on the experimental geometry and thus negligible for the SSP polarization, at last we assign the observed quadrupole contribution in our measurements only to the χ^{IQB} component.

Origin/Properties	χ^{ID}	χ^{IQ}	χ^{IQB}	χ^B
Dipole vs Quadrupole	Dipole	Quadrupole	Quadrupole	Quadrupole
Surface vs Bulk	Surface	Surface	Bulk	Bulk

2.6 $\chi^{(3)}$ EFFECT AT CHARGED INTERFACES

In this section, we describe the so-called $\chi^{(3)}$ effect at charged interfaces, which can have a substantial effect on the measured VSG spectra.^{70,86–89} In this thesis we work mostly with aqueous solutions, thus we consider in this chapter a charged water/air interface. Charges located at the interface produce a static electric field E_0 that penetrates into the interface and bulk of the solution and thereby can form an additional contribution to the non-linear polarization. Here, it needs to be noticed that the $\chi_{ijkl}^{(3)}$ is a fourth-rank tensor, consequently the $\chi^{(3)}$ component is not necessarily zero in an isotropic material. Considering the influence of an additional static electric field Eq. 2.9 can be extended as follows:

$$\mathbf{P}_{SFG}^{(2)} = \epsilon_0 \chi^{(2)} \mathbf{E}_{IR} \mathbf{E}_{VIS} + \epsilon_0 \chi^{(3)} \mathbf{E}_{IR} \mathbf{E}_{VIS} \mathbf{E}_0 \quad (2.46)$$

The second term in Eq. 2.46 includes the electrostatic field dependence of the nonlinear polarization. The $\chi^{(3)}$ contribution of the measured nonlinear polarization can result from an orientational and an electronic mechanism, while in an aqueous solution the orientational mechanism is confirmed to be dominant.^{86,88} Within the orientational mechanism the static electric field is perturbing the orientation of the water molecules. Water molecules have a static electric dipole moment, which allows the molecules to align within the electric field even beyond the first molecular layers. The induced alignment of the water molecules allows more water molecules to contribute to the nonlinear polarization. Without an applied static electric field the water molecules are expected to have no net orientation below a few water layers and thus not contributing to the nonlinear polarization. This principle holds not only for water but also for other polar molecules as for instance urea (Chapter 5). As the applied static electric field changes in the direction perpendicular to the

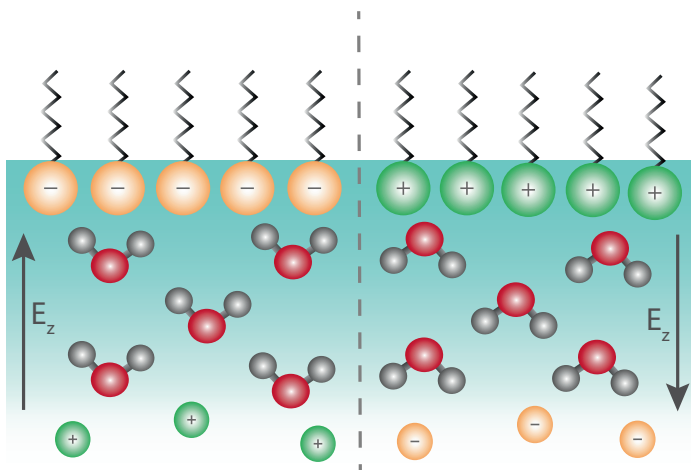


FIGURE 2.8. Water structure near positive and negative charged surfactants.

interface, the total $P_{SFG}^{(3)}$ polarization can be obtained by integration over z .

$$P_{SFG}^{(3)} = \epsilon_0 \chi^{(3)} E_{IR} E_{VIS} \int_0^\infty E_0(z) dz = \epsilon_0 \chi^{(3)} E_{IR} E_{VIS} \Phi_0 \quad (2.47)$$

Where Φ_0 is the surface potential. In Eq. 2.47 we plainly integrate over z with omitting the phase of the electric field. This is only possible if the range of $E_0(z)$ is sufficiently shorter than the wavelength of the incident and emitted electric fields. In the case that the range of $E_0(z)$ penetrates longer in the bulk than the wavelength of the electric fields we additionally have to consider the phase factor in the integral.

$$P_{SFG}^{(3)} = \epsilon_0 \chi^{(3)} E_{IR} E_{VIS} \int_0^\infty E_0(z) e^{i\Delta k_z z} dz \quad (2.48)$$

Where Δk_z is the wavevector difference of VSFG. Further, it needs to be mentioned that $E_0(z)$ and its penetration depth are related to the charge density of the system near the surface. The range over which $E_0(z)$ varies in electrolyte solutions can be approximated with the Debye lengths (λ_D). Therefore, we give in table I λ_D at different concentrations for a 1:1 electrolyte solution. Table I shows that with increasing ion concentration λ_D is decreasing, which subsequently means that the range of $E_0(z)$ is becoming shorter. From this, it can be concluded that with decreasing concentration and the increase of the range of $E_0(z)$ we have to consider and correct for phase distortions in the experimental obtained HD-VSFG spectra. Furthermore, both the quadrupolar contribution described in section 2.5 and the $\chi^{(3)}$ component are fourth rank tensors. Thus, both components are not necessarily forbidden in bulk. Therefore, it is important to mention that the $\chi^{(3)}$ component only arises in the case an electrostatic field is imposed to the system, while the quadrupolar contribution arises independently from an imposed electrostatic field.

Concentration	Debye length (λ_D)
100 mM	1 nm
10 mM	3 nm
1 mM	9.6 nm
0.1 mM	30 nm

TABLE I. Estimation of λ_D with respect to the concentration for a 1:1 electrolyte solution.



3 EXPERIMENTAL METHODS

The following chapter describes the experimental methods that were used to obtain the results presented in this thesis. We first describe the optical VSG setup and second a new measurement procedure to improve the quality of the data. Lastly, we explain the fabrication and sample handling of monocrystalline ice.

3.1 OPTICAL VSG SETUP

The setup used for the VSG experiments is based on a commercial Ti:sapphire laser source, which consists of an oscillator (Coherent “Mantis”) and an amplifier. The oscillator delivers 35 fs pulses centered at 800 nm that are amplified by using chirped pulse amplification. The resulting pulses have an energy of 3.5 mJ and a repetition rate of 1 kHz. Approximately two-thirds of the laser output is used to pump an optical parametric amplifier (OPA) and a difference-frequency mixing (DFG) stage. The resulting mid-infrared pulses are tunable from 2.5 to 10 μ with a bandwidth of 400 cm^{-1} . These pulses have an energy of 10–20 μ J. The other one-third of the 800 nm laser output is narrowed down to a bandwidth of $\sim 15 \text{ cm}^{-1}$. The resulting narrow-band 800 nm visible light pulses (VIS) and the mid-infrared pulses (IR) are combined at the sample surface in spatial and temporal overlap. The VIS and IR beams are sent onto the sample surface at angles of incidence of $\sim 50^\circ$ and $\sim 55^\circ$ and focused with lenses with focal lengths of 200 and 100 mm, respectively. The generated and reflected SFG light is directed into a spectrometer and detected by a thermo-electrically cooled electron multiplied charged-coupled device (EMCCD). We also perform a reference measurement in which we replace the sample with a z-cut quartz crystal. The intensity VSG spectrum $|\chi^{(2)}(\omega)|^2$ is then obtained by dividing the spectrum measured with the sample by the spectrum measured with the reference crystal. With this division, we corrected the VSG spectrum for the frequency dependence of the intensity of the input infrared beam. Furthermore, we performed a background subtraction.

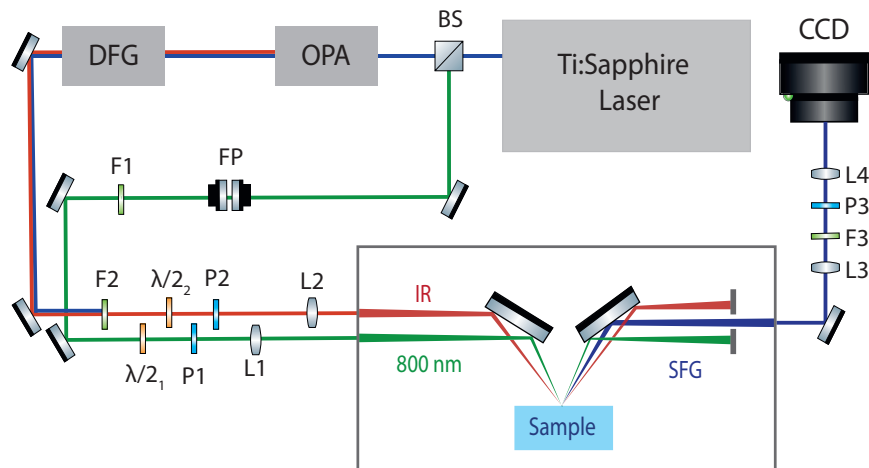


FIGURE 3.1. Experimental lay-out of the VSF optical setup. Abbreviations: BS - beam splitter; FP - Fabry-Pérot etalon; $\lambda/2$ - $\lambda/2$ plate; P - polarizer; L - lens, F - filter.

VSF provides information about the spectral dependence of the absolute square of the second-order susceptibility $|\chi^{(2)}(\omega)|^2$. To obtain the imaginary and real parts of $\chi^{(2)}(\omega)$, the SFG signal of the sample is combined with that of a local oscillator (LO) with the same frequency spectrum. The LO is created by focusing the VIS and IR beams on a gold metal surface that leads to the non-resonant generation of a strong broadband SFG signal. This broadband SFG signal and the reflected VIS and IR beams are then all three directed to the sample surface. Before reaching the sample surface, the LO-SFG signal is time delayed by ~ 1.6 ps with respect to the IR and VIS beam by passing this beam through a silica plate with a thickness of ~ 1 mm. All beams are focused by a spherical mirror on the sample surface, where the VIS and IR beam will generate the VSF signal. Subsequently, the delayed LO-SFG and sample VSF light are sent into a spectrometer and on the EMCCD, where the interference spectrum of the two SFG signals is recorded. From the interference spectrum, the real (Re) and the imaginary (Im) spectra can be extracted, providing direct information on the orientation of the vibrational transition dipole moments at the sample surface. Thus the HD-VSF spectrum provides unique information on the absolute orientation of molecules at the surface.²⁰ The typical acquisition time of an HD-VSF spectrum is 120 s.

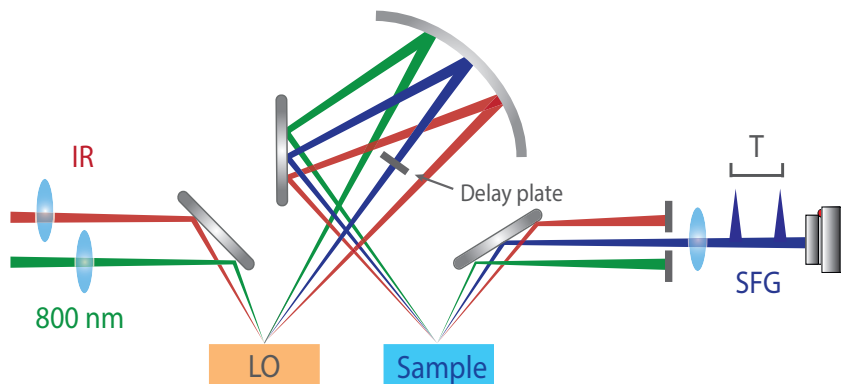


FIGURE 3.2. Schematic representation of HD-VSFG.

The measured spectral response is corrected for the spectral dependence of the input IR beam by dividing the HD-VSFG spectrum of the sample by the HD-VSFG spectrum of a reference *z*-cut quartz crystal. In this normalization, it is important to make sure that the surface of the *z*-cut quartz crystal is at the same height as the sample, as a difference in height will lead to an error in the determination of the phase of the VSG light and thus of the real and imaginary parts of $\chi^{(2)}(\omega)$. By monitoring the position of the VSG-signal on the EMCCD, we can control the height of the reference *z*-cut quartz crystal to such an extent that the overall phase uncertainty is $\sim \pi/10$. The lateral spatial resolution of the technique is defined by the size of the foci and is approximately $100 \mu\text{m}$.

In this thesis two different experimental VSG setups for the 3 μm and the 6 μm region were used. The following table enlightens the technical differences of the two setups:

Frequency Region	3 μm	6 μm
Laser system	Coherent "Legend USP"	Coherent "Duo Legend USP"
Oscillator	Coherent Mantis	Coherent Mantis
Camera	Andor Technologies "Newton"	Princeton Instruments "Pixis 100"
OPA	home-built	Light Conversion HE-TOPAS
spectral narrowed 800 nm	Fabry-Pèrot etalon	pulse shaper

TABLE I. Specification of the different VSG systems.

3.2 NOISE REDUCTION AND IMPROVED MEASUREMENT PROCEDURE

In a typical VSG experiment, the signal to noise ratio is determined by photon shot noise⁹⁰. However, at very high photon counts (long integration times) a systematic error will limit the sensitivity in HD-VSG experiments prohibiting the analysis of small signals like that of the water bending mode. The origin of the systematic error is the high-frequency spectral noise introduced in the detection path. This high-frequency spectral noise mixes with the heterodyne signal and cannot be removed by post-processing or averaging more. The main reason for the spectral noise is the structural noise on the CCD camera, which results from an etaloning effect. This phenomenon degrades the performance of thinned, back-illuminated CCD cameras. The effect is caused by light waves passing through the camera and getting reflected at the rear surface, producing interference fringes when they interact with incoming waves. Even though new cameras have many strategies to reduce this effect and improving the data quality, it is not possible to suppress it completely. The signal-to-noise ratio particular in the 6 μm region is low which makes it difficult to analyze the data if we would not reduce the structural noise resulting from the etaloning effect.

We developed a measurement procedure to determine the structural noise and to remove it from the data. We perform two independent measurements of z-cut quartz with a different orientation of 180 degrees (Figure 3.3 (a)). By doing so we change the phase of our reference measurement exactly by 180 degrees. If we now add up the two quartz spectra, the interference induced by the SFG signal of the local oscillator and the quartz crystal is removed (Figure 3.3 (b)). The remaining modulation largely represents the structural noise of the etaloning effect and can now be used as a scaling factor to remove the structural noise from the data. In the following Figure, we show the experimental spectrum

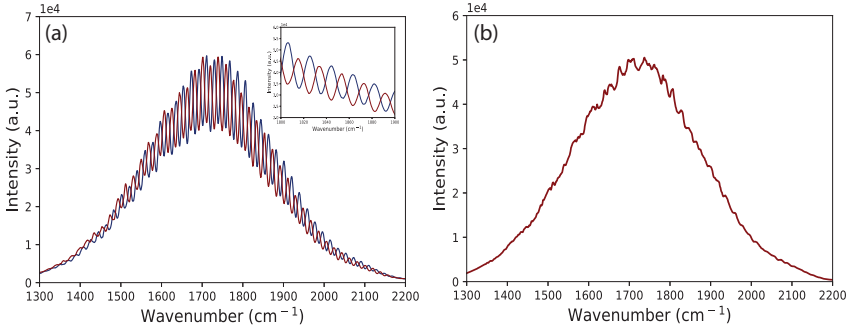


FIGURE 3.3. (a) Two independent measurements of z-cut quartz using different orientations that differ by 180 degrees. (b) The remaining modulation obtained by adding up the two z-cut quartz spectra of Fig. (a). This signal represents the structural noise of the etaloning effect.

of the $\text{Im}[\chi^{(2)}]$ of the water bending mode data before and after this structural noise removal. The observed improvement of the sensitivity is at least one order of a magnitude (Figure 3.4 (a)-(b)). The efficiency of the above method will vary for different experimental setups and wavelength ranges of interest, but in all cases this method will improve the sensitivity limit of broadband HD-VSFG setups.

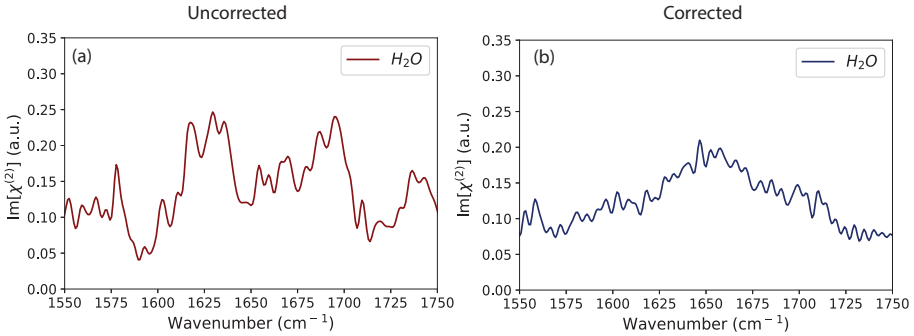
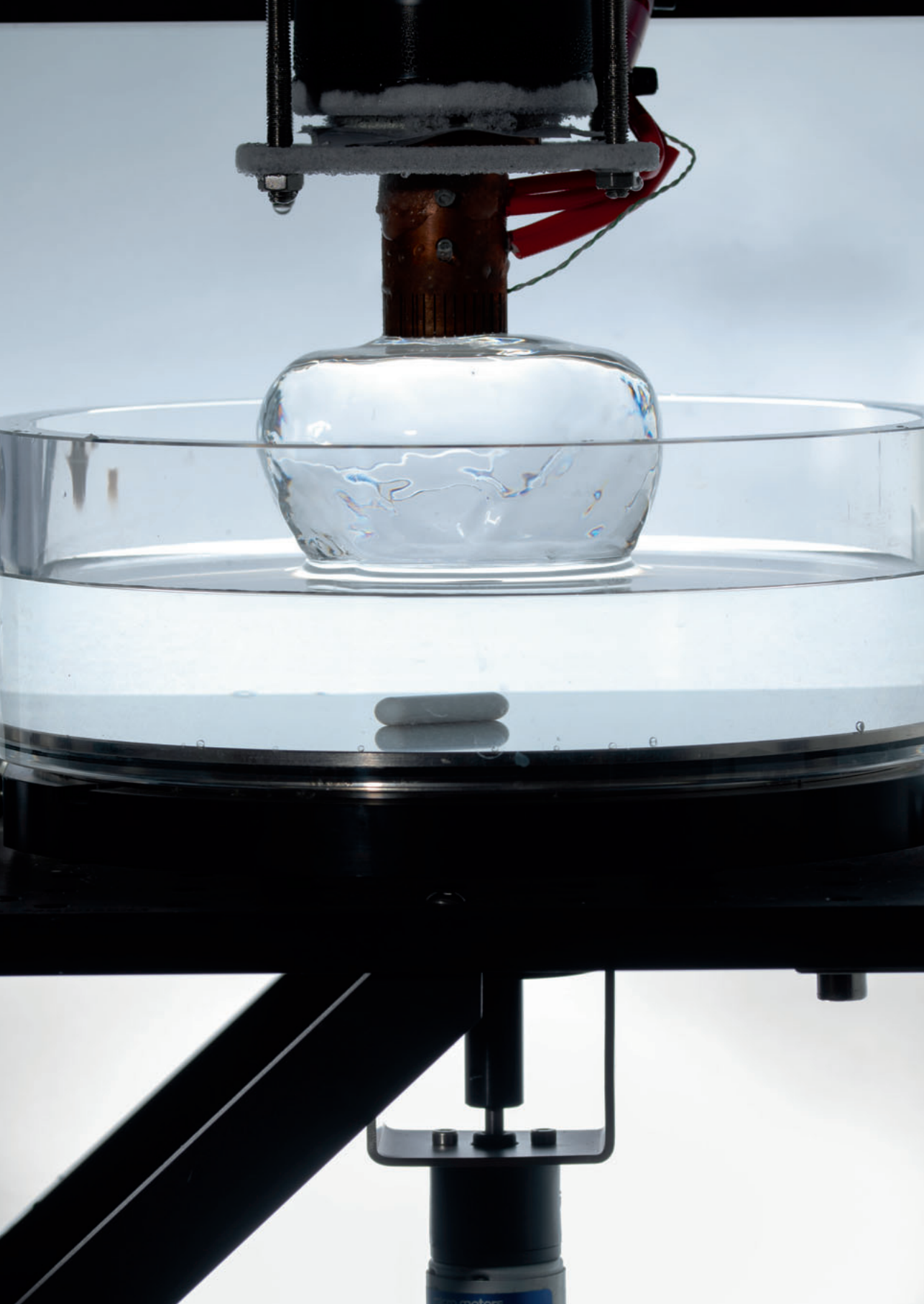


FIGURE 3.4. $\text{Im}[\chi^{(2)}]$ spectra of the neat water/air interface (a) before and (b) after removing the structural noise from the experimental data.



3.3 FABRICATION AND SAMPLE HANDLING OF MONOCRYSTALLINE ICE

Monocrystalline ice is grown using the method of seed extraction from a melt. A single monocrystalline seed crystal is frozen to a copper pin which is cooled to 272 K by a processor cooler (LD PC-V2). The seed is dipped into ultrapure water (273 K) and is allowed to grow in the melt. The seed is slowly pulled from the melt after ~ 60 minutes with a speed of ~ 5 mm/hour. Then the temperature of the copper pin is gradually lowered to 233 K. After 10 h a ~ 50 mm high and ~ 70 mm wide crystal is produced which is stored in a freezer before further handling. The ice crystal is cut into smaller pieces using a band saw (Proxxon MBS 240/E) with a nickel-plated blade. The orientation of the basal face of the ice piece is determined with a Rigsby stage following the routine described by Fairbrain.⁹¹ The ice is then cut in a way that its optical axis is oriented perpendicular to the surface. The ice is smoothened by repeatedly shaving the ice using a heated blade of cemented carbide.

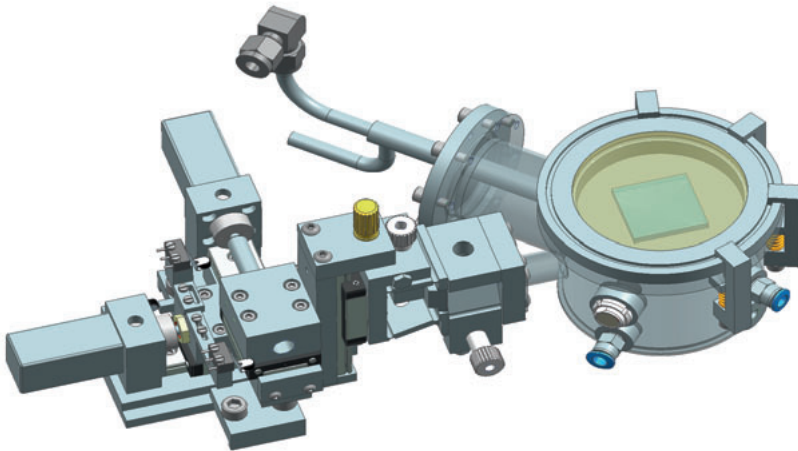


FIGURE 3.5. Mechanical drawing of the nitrogen cooled temperature cell. "The drawing was made by Dirk Jan Spaanderman."

In the VSFG measurements on ice, the ice sample is placed in a liquid nitrogen-cooled temperature cell (Figure 3.5). The temperature cell is closed with a CaF_2 window that allows the transmittance of the two laser beams. To regulate the temperature in the cell, a heating foil on the bottom of the cell is used that is covered by a copper plate. The ice sample is directly placed on this

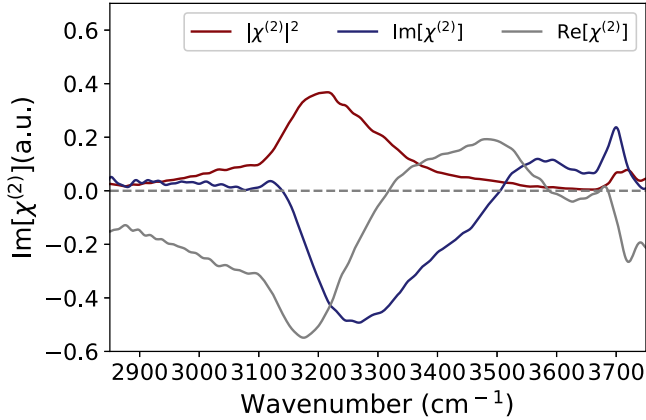


FIGURE 3.6. HD-VSFG spectrum of monocrystalline basal plane ice at 255 K.

copper plate. To accurately control the temperature of the sample surface, the sensor is glued directly onto the ice crystal with a droplet of water. After the ice sample is placed inside the sample cell, the cell is flushed with N_2 gas in order to remove the evaporated and condensed water produced during the positioning of the sample. Subsequently, the cell is put under vacuum that remains during the measurements. To prevent heat damage of the ice sample by the two laser beams, the temperature cell can be moved in the horizontal plane by using two motorized stepper motors.

In Figure 3.6 we present the HD-VSFG spectrum of the basal plane of monocrystalline ice at a temperature of 255 K, including the $|\chi^{(2)}|^2$, the $\text{Im}[\chi^{(2)}]$ and the $\text{Re}[\chi^{(2)}]$ responses. The $\text{Im}[\chi^{(2)}]$ spectrum shows a broad negative signal between 3200 cm^{-1} and 3500 cm^{-1} which is assigned to the OH stretch vibrations of crystalline ice and a quasi-liquid layer.⁹² The sharp feature at 3700 cm^{-1} is attributed to the stretch vibration of non-hydrogen bonded OH groups of water molecules sticking out of the ice surface ('free-OH').



4 DIRECT EVIDENCE FOR A SURFACE AND BULK SPECIFIC VSFG RESPONSE OF THE WATER BEND VIBRATION

Spectroscopic studies of aqueous surfaces can provide a fundamental understanding of interfacial processes. These studies have largely focused on the OH stretch vibrations of water, which is unfortunate as the bending mode is an attractive feature to probe as it is relatively free of inter- and intramolecular couplings. However, the origin of the response of the bending mode is highly debated and has been assigned to either surface-specific or to bulk effects. We study the bending mode of pure water and charged aqueous surfaces using heterodyne-detected vibrational sum frequency generation spectroscopy (HD-VSFG). We observe a low - (1626 cm^{-1}) and a high - (1656 cm^{-1}) frequency component which can be unambiguously assigned to an interfacial dipole and a bulk quadrupolar response, respectively. We thus demonstrate that probing the bending mode provides structural and quantitative information on both the surface and the bulk.

4.1 INTRODUCTION

The structure and dynamics of aqueous interfaces is of high relevance for many different scientific fields.^{93–101} Many important chemical and biological processes take place at aqueous interfaces, like for instance molecular recognition at bio-membranes, protein folding, and energy conversion and storage.^{7–12} The structural properties of the neat water/air interface^{16;29} and charged aqueous interfaces have been extensively studied with vibrational sum-frequency generation spectroscopy (VSFG) in the frequency region of the water OH stretch vibrations.^{8,30–32} The frequency region of the water bending vibrations has been much less investigated, even though this region can provide unique information on the hydrogen-bond structure, because, in contrast to the stretching mode, the water bending mode is hardly influenced by intermolecular coupling due to its small transition dipole moment.^{33–35} Furthermore, there is only one water bending mode per water molecule, thus strongly decreasing the effects of intramolecular coupling on the spectrum. Vinaykin and Benderskii were the first to study the water bending mode of the neat water/air interface with conventional VSFG, for which the response is proportional to the modulo squared of the second-order susceptibility ($|\chi^{(2)}|^2$).³⁴ These authors reported the observation of an inhomogeneously broadened line shape centered at 1650 cm^{-1} . They assigned the low- and high-frequency wing of this band to weakly hydrogen bonded water molecules sticking out of the surface, and to fully hydrogen-bonded interfacial water molecules, respectively. Furthermore, they found evidence for the presence of a large orientational inhomogeneity.³⁴ These findings have been confirmed by recent computational studies by Nagata *et al.*,³⁵ and Ni and Skinner.³³

Kundu *et al.* reported the first heterodyne detected VSFG (HD-VSFG) measurements of the neat water/air interface in the bending mode region.³⁷ In this technique the real and imaginary part of the second-order susceptibility $\chi^{(2)}$ are determined. The measured $\text{Im}[\chi^{(2)}]$ showed a single positive peak centered at 1650 cm^{-1} . In the same work it was also reported that charging the interface negative with iodide ions leads to an enhancement of this signal. This observation strongly contrasts with observations in the OH stretching mode region, for which a change of the sign of the band is observed when the surface gets negatively charged.^{30,32} The accompanying calculations indicated that the observed $\text{Im}[\chi^{(2)}]$ signal would originate mainly from a quadrupole response from the bulk.³⁷ In the most recent intensity VSFG measurements of Benderskii¹² it was found that the interfacial water molecules orient in different directions depending on the charge of the surface, which suggests that the observed signal primarily results from a surface dipolar response. This explanation is consistent with the $|\chi^{(2)}|^2$ measurements of the group of Bonn and Nagata, and thus strongly disagrees with the interpretation of the $\text{Im}[\chi^{(2)}]$ measurements by Kundu *et al.*^{36,37} Here we perform HD-VSFG measurements to investigate the sum-frequency response of the bending mode of aqueous systems. By measur-

ing the effect of surface charge on the signal, we demonstrate the presence of both a dipolar contribution of the surface and a quadrupolar contribution of the bulk to the signal and we clear up the existing inconsistencies between earlier reports.^{12,33,34,36,37}

4.2 EXPERIMENTAL METHODS

SAMPLE PREPARATION The solutions are prepared by dissolving different concentrations of dodecyltrimethylammonium bromide (DTAB) or sodium dodecyl sulfate (SDS) in in H₂O. For all solutions we used H₂O from a Millipore Nanopure system (18,2 MΩ cm). Both DTAB and SDS are purchased from Sigma Aldrich with a purification of 99% and are used without further purification.

SPECTROSCOPY The VSFG measurements described in this chapter are performed with the setup described in section 3.1.

4.3 RESULTS AND DISCUSSION

In Figure 4.1 we present $|\chi^{(2)}|^2$ (intensity VSFG) spectra of the neat water surface water/air (dark blue), the water/ Dodecyltrimethylammonium bromide (DTAB)/air (darkcyan) interface and the water/ Sodium dodecyl sulfate (SDS)/air interface (magenta) in the frequency region of the water bend vibration. For pure water we observe that the $|\chi^{(2)}|^2$ spectrum has the shape of a step function, in agreement with previous findings.³⁴ The addition of a charged surfactant leads to strong changes of the response. Adding the positively charged DTAB leads to an enhancement and a redshift of the response, adding the negatively charged SDS leads to a redshift of the maximum of the SFG intensity. These findings are in line with previous intensity VSFG measurements performed by Dutta *et al.*¹² The solid cyan curves in Figure 4.1 are the result of model calculations, as described in the text below and in the Appendix.

In Figure 4.2 (a) the experimental $\text{Im}[\chi^{(2)}]$ spectra of neat water (dark blue) in the frequency region of the water bend vibration is presented. We observe a symmetric positive peak centered at 1656 cm^{-1} that we assign to the water bending mode. The observed spectrum agrees with previous HD-VSFG measurements of Kundu *et al.*³⁷ We find that this $\text{Im}[\chi^{(2)}]$ response can be fitted well with a single Lorentzian curve (cyan). In Figure 4.2 (b) we show a comparison of the calculated $\text{Im}[\chi^{(2)}]$ spectrum of neat water over a broad frequency region (cyan) combined with the experimental data (dark blue) in the frequency region of the water bending mode. In addition to the water bending mode, the model includes the resonances of the OH stretch vibrations of hydrogen-bonded and non-hydrogen-bonded water molecules (red dotted line, $\chi_{\sigma,OH}$). The OH stretch band of the hydrogen-bonded water molecules is modeled with two Lorentzian curves with maxima at 3250 cm^{-1} and 3450 cm^{-1} , and the response of the non-hydrogen-bonded water molecules is modeled with a single Lorentzian centered at 3700 cm^{-1} . In addition to the resonances in

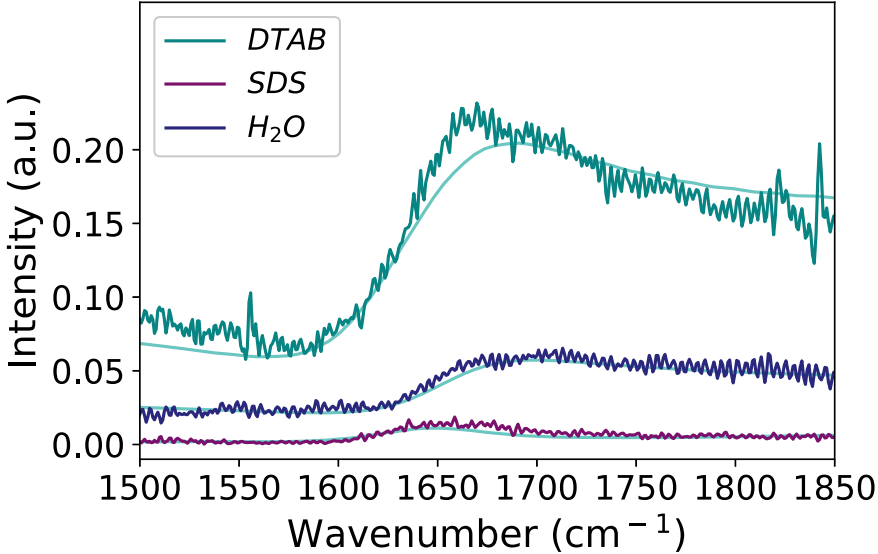


FIGURE 4.1. $|\chi^{(2)}|^2$ spectra of the neat water surface water/air (dark blue), the water/DTAB/air interface (darkcyan) and the water/SDS/air interface (magenta) in the frequency region of the water bend vibration. The concentration of the SDS and DTAB solution is 10 mM. Note that the spectra are not offset with respect to each other, the signal observed for the DTAB solution is much stronger than that of pure water and the SDS solution.

the stretching mode region, we included a frequency-independent non-resonant background χ_{NR} (orange dotted). The comparison of the model and the experimental data shows that the resonances of the OH stretch band have a negligible influence on the observed $\text{Im}[\chi^{(2)}]$ in the bending mode region. However, the $\text{Re}[\chi^{(2)}]$ in the bending mode region does show significant contributions from both the different OH stretch vibrations $\chi_{\sigma,OH}$ and the non-resonant background χ_{NR} , as illustrated in Figure 4.2 ((c-d)). The low-frequency wing of the real response of the stretching band (red dotted) adds a negative value to the real part of the response of the bending mode χ_{δ} (green dotted). In Figure 4.2 (d) we show the $\text{Re}[\chi^{(2)}]$ over a broad frequency range. This figure clearly shows that the χ_{σ} contribution also induces a slight tilt of the total $\text{Re}[\chi^{(2)}]$ in the frequency region of the bending mode. From the analysis of Figure 4.2 it is clear that the observed step in the intensity SFG spectrum of pure water of Figure 4.1 can be well explained from the interference with the stretch vibrations. The $\text{Re}[\chi_{\sigma}^{(2)}]$ of the stretch vibrations compensates the positive $\text{Re}[\chi_{\delta}^{(2)}]$ of the bending vibration at frequencies $<1650 \text{ cm}^{-1}$, and enhances the negative $\text{Re}[\chi_{\delta}^{(2)}]$ of the bending vibration at frequencies $>1650 \text{ cm}^{-1}$. As a result, the total intensity ($|\chi^{(2)}|^2$) shows a steplike shape.

In Figure 4.3, we present experimental $\text{Im}[\chi^{(2)}]$ spectra of (a) the water/DTAB/air interface (dark-cyan) and (b) the water/SDS/air interface (ma-

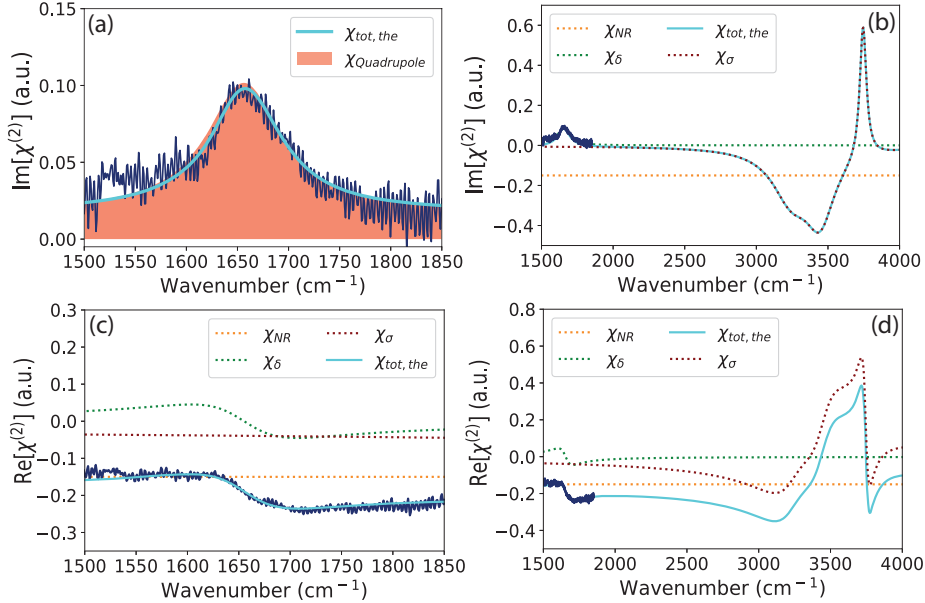


FIGURE 4.2. (a) $\text{Im}[\chi^{(2)}]$ spectrum of neat water (dark blue) in the frequency region of the bending mode. The solid line represents the result of a fit, explained in the text. (b)-(d) modeled $\text{Im}[\chi^{(2)}]$ and $\text{Re}[\chi^{(2)}]$ spectra of neat water ($\chi_{tot,the}$, cyan) compared to the experimental data (dark blue). The figures also show the decomposition of the total response $\chi_{tot,the}$ in different contributions: the non-resonant background χ_{NR} (dotted orange), the bending mode response χ_{δ} (dotted green), and the response of the OH stretch vibrations χ_{σ} (dotted red).

genta) in the frequency region of the water bend vibration. The $\text{Im}[\chi^{(2)}]$ spectrum of the water/DTAB/air interface shows a positive band centered at 1640 cm^{-1} . This band is stronger, broader and somewhat redshifted in comparison to the $\text{Im}[\chi^{(2)}]$ spectrum of water/air. The $\text{Im}[\chi^{(2)}]$ spectrum of the water/SDS/air interface shows a clear negative feature at lower frequencies. At this point it should be noted that we can exclude phase distortions in the HD-VSFG spectra, as the electric double layer (EDL) has a thickness $<10\text{ nm}$ for ionic strengths $>1\text{ mM}$.^{87,88,102} The spectra observed for water/DTAB/air and water/SDS/air can be well explained from the presence of an additional low-frequency band in the $\text{Im}[\chi^{(2)}]$ spectra that is negligibly present for neat water/air, and that has a different sign for the water/DTAB/air and the water/SDS/air interface. To substantiate that the lower-frequency band depends on the sign of the surface charge, we also performed measurements with a different negatively charged surfactant sodium monododecyl phosphate (SMP) (Appendix Figure 4.5). These measurements also show the presence of a negative band centered at 1626 cm^{-1} , thus confirming that this band results from the bending mode of water and that its sign is determined by the sign of the surface charge. To quantify the different contributions to the $\text{Im}[\chi^{(2)}]$ spectra

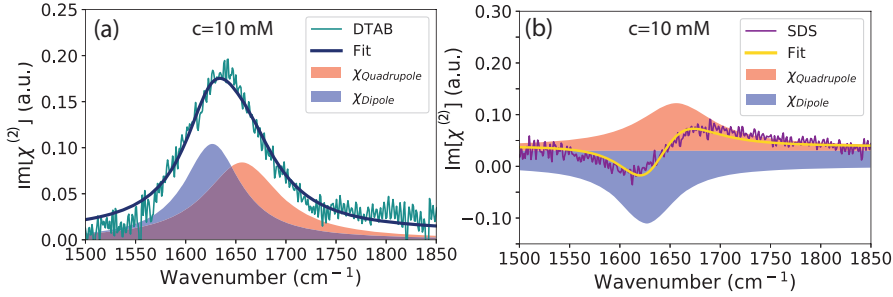


FIGURE 4.3. Spectral decomposition of the $\text{Im}[\chi^{(2)}]$ spectra of (a) the water/DTAB/air interface (dark cyan) and (b) the water/SDS/air interface (magenta), each modeled with two Lorentzian-shaped spectral components. The two Lorentzian-shaped components are assigned to the quadrupolar contribution of the bulk (red, centered at 1656 cm^{-1}), and to the surface dipolar contribution (blue, centered at 1626 cm^{-1}), of the water bending mode.

we decompose the spectra observed for the water/DTAB/air interface and the water/SDS/air interface into Lorentzian-shaped bands centered at 1656 cm^{-1} (blue) and 1626 cm^{-1} (red). The band at 1656 cm^{-1} does not depend on the charge of the surface and is assigned to the quadrupolar response of the bulk. This assignment is consistent with the notion that the quadrupolar contribution of the water bending mode does not depend on the orientation of the water molecules, and is thus not strongly affected by the surface electric field.⁷⁰ The sign and amplitude of the 1626 cm^{-1} band are determined by the charge at the surface and can therefore be assigned to a dipolar surface contribution. This assignment is further supported by studying the effect of adding 0.5 M NaCl to the water/DTAB and the water/SDS solutions. The addition of salt leads to screening of the electric field of the charged surfactants. We observe that the addition of salt leads to a vanishing of the 1626 cm^{-1} band (Appendix Figure 4.6).

For the positively charged DTAB/air surface the interfacial water molecules are oriented with their hydrogen atoms toward the bulk. For the stretch vibration this orientation leads to a negative contribution to $\text{Im}[\chi^{(2)}]$, because for the stretch vibration the dipole and the polarizability have the same dependence on the phase of the stretch vibration (when the hydrogen atoms move away from the oxygen atom, the dipole moment increases and the size and polarizability of the water molecules also increase). For the bending vibration the dipole moment and polarizability have an opposite dependence on the phase of the bending vibration (when the atoms move together, the dipole moment increases while the size and polarizability of the water molecule decreases). As a result, the surface dipolar contribution to the $\text{Im}[\chi^{(2)}]$ of the bending mode is positive for water molecules with their hydrogen atoms oriented toward the bulk, and negative for water molecules that have their hydrogen atoms oriented toward the surface.

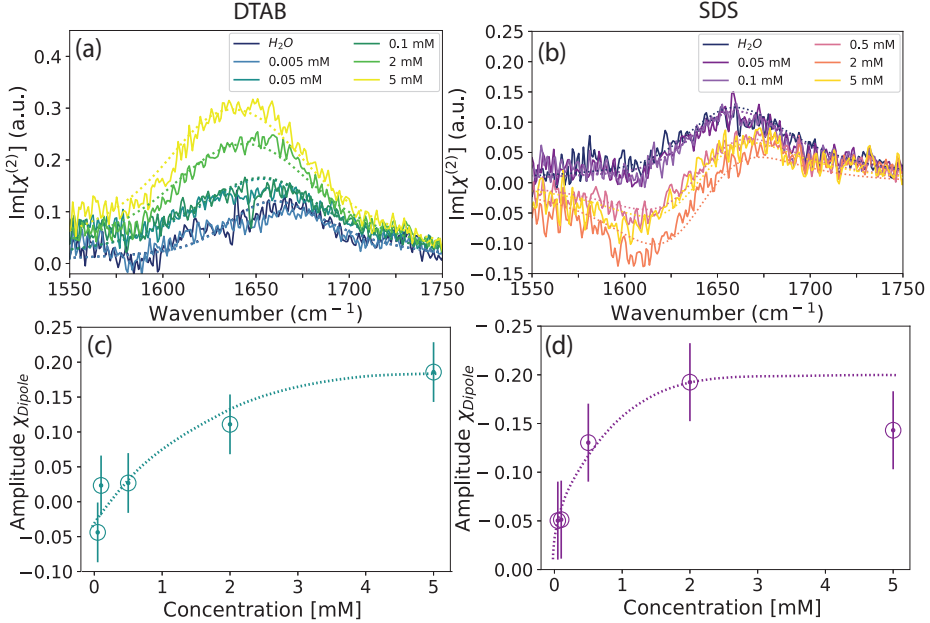


FIGURE 4.4. The $\text{Im}[\chi^{(2)}]$ spectra of the water/DTAB/air (a) and the water/SDS/air (b) interface at different concentrations in the range of 0.05 to 5 mM including fits presented with dashed lines. (c-d) show the absolute amplitude of the dipole contribution extracted from the fitting procedure in respect to the concentration of DTAB (c) and SDS (d).

For neat water we find that the experimental data can be well described with a single Lorentzian line that only represents the quadrupolar contribution of the bulk (Figure 4.2). In our fitting procedure for the water/DTAB/air and water/SDS/air (10 mM) interfaces presented in Figure 4.3 (a-b) we use the same description for the quadrupolar contribution. In the Appendix we show the measured $\text{Re}[\chi^{(2)}]$ responses of the water/DTAB/air interface and the water/SDS/air interface, and the decomposition of the $\text{Im}[\chi^{(2)}]$ and $\text{Re}[\chi^{(2)}]$ spectra (Appendix Figures 4.7 and 4.8), as was done for neat water/air, which was shown in Figure 4.2. In this analysis we include the interference effect between the quadrupolar bulk and dipolar interface responses of the bending mode, and the interference effect between the water bending mode responses and the response of the OH stretch vibrations and the nonresonant background response. We find that for the water/DTAB/air interface and the water/SDS/air interface, the $\text{Re}[\chi^{(2)}]$ response and the intensity spectrum ($\sim |\chi^{(2)}|^2$) are strongly affected by the interference with the response of the OH stretch vibrations, as was the case for neat water.

In Figure 4.4 we present the $\text{Im}[\chi^{(2)}]$ spectra of (a) water/DTAB/air and (b) water/SDS/air at different concentrations in the range of 0 mM to 5 mM. For water/DTAB/air we observe that the positive peak centered at 1656 cm^{-1} assigned to the water bending mode is increasing with increasing DTAB con-

centration. Furthermore, we observe a broadening and a slight red shift of the $\text{Im}[\chi^{(2)}]$ spectra. Increasing the SDS concentration leads to an ingrowth of a negative peak at lower frequencies. These observations confirm the assignment of the band at 1626 cm^{-1} to a surface dipolar contribution. In the case of DTAB, the positive surface charge is increasing with increasing concentration, thus causing an enhanced ordering of the interfacial water molecules with their hydrogen atoms toward the bulk, which leads to an increase of a positive dipolar band at 1626 cm^{-1} . The increase of the concentration of SDS increases the negative charge density at the surface, thereby inducing an enhanced orientation of the water molecules with their hydrogen atoms toward the surface, and thus to an increase of a negative dipolar contribution at 1626 cm^{-1} . The concentration-dependent increase of the dipolar contribution of the water bending mode is also observed for the OH stretch vibration of aqueous solutions of DTAB and SDS (Appendix Figure 4.9).

To quantify the results, we decompose the responses measured at different concentrations of DTAB and SDS in two Lorentzian bands centered at 1626 cm^{-1} and 1656 cm^{-1} , for the dipole and quadrupole contribution, respectively. As the quadrupolar contribution is not expected to depend on the orientation of the water molecules, we keep the quadrupolar contribution constant at all concentrations. We also keep the width of the dipolar contribution constant, and we only allow the amplitude of this contribution to change with the surfactant concentration. The fits are shown in Figure 4.4 (a-b) with dashed lines. The decompositions for the different concentrations are presented in the Appendix (Figure 4.10 and 4.11). In Figure 4.4 (c-d) we present the amplitude of the dipolar band extracted from the fitting procedure as a function of the surfactant concentration. For both DTAB and SDS, the amplitude of the dipolar band increases nonlinearly with concentration, showing saturation behavior at a bulk concentration of a few mM. This saturation behavior can be explained from the saturation of the surface density of surfactant molecules, the resulting decrease of the water density at the surface, and the enhanced screening effect of the counter ions of the surfactant molecules. A similar saturation effect is observed for the OH stretching mode of water (Appendix Figure 4.9). The combination of these effects can even lead to a decrease of the dipolar response at higher SDS concentrations. From the fitting procedure we find that at a surfactant concentration of 10 mM the absolute ratio of the amplitudes of the dipolar interfacial and the quadrupolar bulk contribution is 1:0.7, both for the water/DTAB/air interface and the water/SDS/air interface. It is also seen that at zero surfactant concentration the dipolar contribution is negligible.

Recently Ahmed et al.⁸⁴ reported HD-VSFG measurements of water with charged surfactants and lipid monolayer/water interfaces in which they did not find evidence for an interfacial dipole contribution of the water bending mode. Their $\text{Im}[\chi^{(2)}]$ spectra show a positive band, independent on the sign of the charge of the headgroup. Therefore, Ahmed et al. argued that the $\text{Im}[\chi^{(2)}]$ response of the water bending mode arises only from a quadrupolar response, even for charged surfaces.⁸⁴ At first sight this finding appears to disagree with the results of Figure 4.3. However, the measurements of Ahmed et al. were performed with a surfactant concentration of only 0.1 mM, while the measure-

ments shown in Figure 4.3 are performed with a surfactant concentration of 10 mM. As is clearly illustrated in Figure 4.4, for a surfactant concentration of 0.1 mM, the dipolar contribution is negligibly small. To detect the dipolar contribution of the OH bending mode, a sufficiently high surface charge density is needed. The absence of a dipolar contribution in the SFG spectrum of the water bending mode for a 2.1 M NaI solution in the work of Kundu et al.³⁷, can thus be explained from the relatively low negative surface charge density of NaI solutions in comparison to SDS solutions.

An interesting observation is that the dipolar contribution has a significantly lower frequency than the quadrupolar contribution. The lower frequency of the dipolar contribution indicates that the hydrogen bonds of the contributing water molecules are weaker than those of the water molecules giving rise to the quadrupolar contribution.³⁴ This finding agrees with the fact that the molecules giving rise to the quadrupolar contribution are predominantly located in the bulk of the liquid, whereas the molecules giving rise to the dipolar contribution will be located at the surface.

4.4 CONCLUSIONS

In summary, we performed HD-VSFG measurements of pure water, and of aqueous solutions of ionic surfactants. We find that the $\text{Im}[\chi^{(2)}]$ response in the frequency region of the bending mode of water is strongly affected by the interference with the low-frequency wing of the OH stretch vibrations of water. By comparing the measured $\text{Im}[\chi^{(2)}]$ spectra of differently charged water surfaces, we demonstrate the presence of a surface-specific dipolar response of the water bending mode centered at 1626 cm^{-1} . This response changes sign when the sign of the surface charge changes, and increases with increasing surface charge, i.e. increasing concentration of ionic surfactant. In addition to this dipolar surface contribution, the bending mode of water shows a quadrupolar bulk contribution centered at 1656 cm^{-1} . This contribution is not surface-charge dependent and dominates the $\text{Im}[\chi^{(2)}]$ response of neat water in the frequency region of the bending mode. The water bending vibrations form an excellent probe of the (hydrogen-bonded) environment of the water molecule, as they are much less affected by intra- and intermolecular couplings than the stretch vibrations. Therefore, small changes in frequency and amplitude of the bending mode spectrum can be directly connected to changes in the environment of the water molecules. We thus demonstrate that HD-VSFG involving the bending mode of the water molecules can provide important information on the hydrogen-bond structure of both the surface and the bulk of aqueous solutions.

4.5 APPENDIX

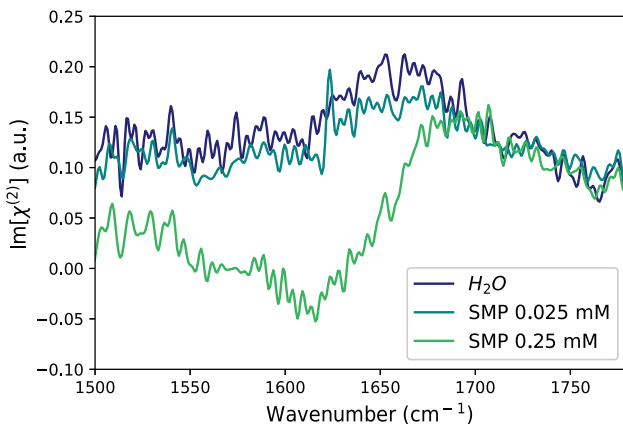


FIGURE 4.5. The $\text{Im}[\chi^{(2)}]$ spectra of the neat water surface (blue) and the water/sodium monododecyl phosphate (SMP)/air interface at different concentrations of 0.025 mM (darkcyan) and 0.25 mM (green).

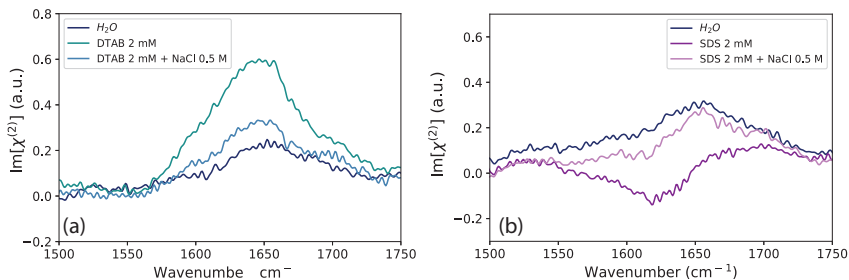


FIGURE 4.6. The $\text{Im}[\chi^{(2)}]$ spectra of the neat water surface (blue) and (a) the water/DTAB/air interface with a concentration of 2 mM (darkcyan) including NaCl with a concentration of 0.5 M (light blue) and (b) the water/SDS/air interface with a concentration of 2 mM (dark magenta) including NaCl with a concentration of 0.5 M (violet).

From previous studies it is well known that the response of the OH stretch band can be well explained from a purely dipolar contribution, which implies that this response is dominated by oriented water molecules in the electric dipole layer (EDL). By adding NaCl to the surfactant solution, the intensity of the OH stretch band substantially decreases, due to screening of the electric field of the

surfactants and the resulting decrease of the degree of orientation of the water molecules within the EDL.^{84,103,104} For the response of the bending vibration of water the situation is somewhat more complex. We observe two bands in the $\text{Im}[\chi^{(2)}]$ response, at 1626 cm^{-1} and at 1656 cm^{-1} . The lower-frequency band at 1626 cm^{-1} changes sign when the charge of the surfactant changes, which constitutes strong evidence for the assignment of this band to a dipolar contribution. In figure 4.6 we support this assignment further with the $\text{Im}[\chi^{(2)}]$ measurements of the neat water surface (blue) and (a) the water/DTAB/air interface with a concentration of 2 mM (darkcyan) including NaCl with a concentration of 0.5 M (light blue) and (b) the water/SDS/air interface with a concentration of 2 mM (dark magenta) including NaCl with a concentration of 0.5 M (violet). We observe that the addition of 0.5 M NaCl to aqueous solutions of DTAB and SDS (2mM), leads to a substantial decrease of the band at 1626 cm^{-1} . This indicates that the amplitude of this band is strongly influenced by screening of the electric field of the surfactant and the resulting decrease of the degree of orientation of the water molecules. This finding supports the assignment of the low-frequency band at 1626 cm^{-1} to a dipolar surface contribution. The higher frequency peak at 1656 cm^{-1} is neither changing sign upon charging the surface nor decreasing its amplitude upon the addition of salt, and can therefore be assigned to a quadrupolar bulk contribution.

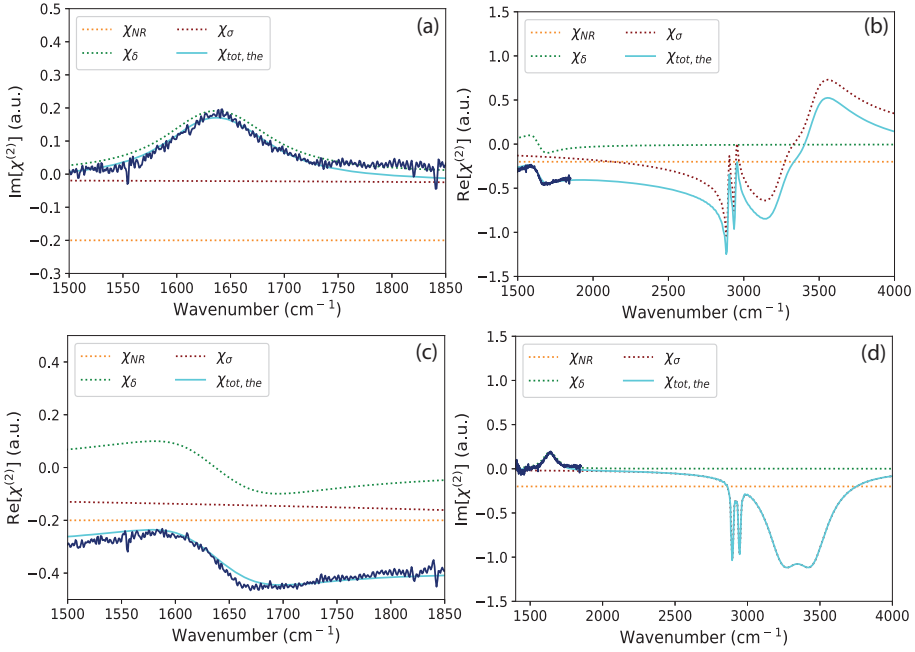


FIGURE 4.7. (a-d) present the modeled $\text{Im}[\chi^{(2)}]$ and $\text{Re}[\chi^{(2)}]$ spectra of the water/DTAB/air interface ($\chi_{tot,the}$, cyan) combined with the experimental data (dark blue). The model shows additionally a decomposition of the total response $\chi_{tot,the}$ in different contributions: the non-resonant background χ_{NR} (dotted orange), the bending mode response χ_{δ} (dotted green), and the response of the OH stretch vibrations χ_{σ} (dotted red).

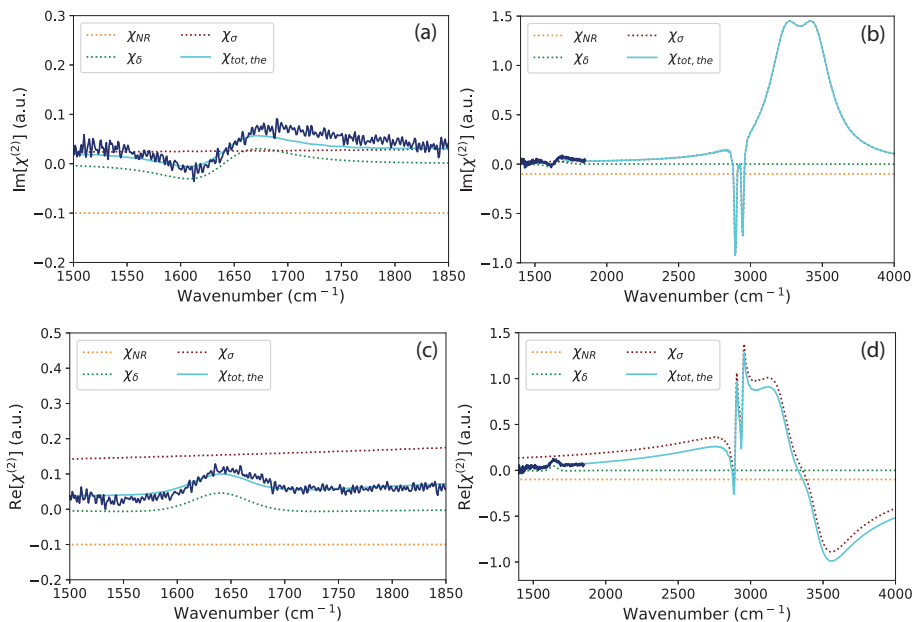


FIGURE 4.8. (a-d) present the modeled $\text{Im}[\chi^{(2)}]$ and $\text{Re}[\chi^{(2)}]$ spectra of the water/SDS/air interface ($\chi_{tot,the}$, cyan) combined with the experimental data (dark blue). The model shows additionally a decomposition of the total response $\chi_{tot,the}$ in different contributions: the non-resonant background χ_{NR} (dotted orange), the bending mode response χ_{δ} (dotted green), and the response of the OH stretch vibrations χ_{σ} (dotted red).

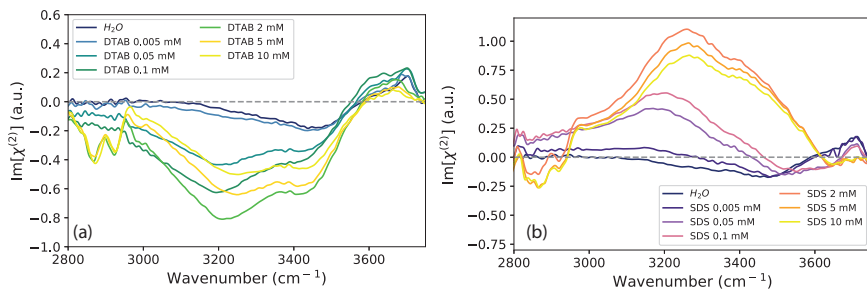


FIGURE 4.9. The $\text{Im}[\chi^{(2)}]$ spectra of (a) the water/DTAB/air interface and (b) the water/SDS/air interface with different concentrations in a range of $5 \mu\text{M}$ - 10 mM .

In Figure 4.9 we show the $\text{Im}[\chi^{(2)}]$ spectra of (a) water/DTAB solutions and (b) water/SDS solutions at different concentrations in a range of $5 \mu\text{M}$ - 10 mM . The $\text{Im}[\chi^{(2)}]$ spectrum of the water/DTAB/air interface shows a negative peak centered at $3000 - 3500 \text{ cm}^{-1}$ that can be assigned to the OH stretch band. The negative sign of the OH stretch band implies that the interfacial water molecules have a net orientation with their hydrogen atoms pointing towards the bulk. The amplitude of this response increases with increasing concentration of DTAB, reaching a maximum at a concentration of 2 mM . These results indicate that the observed response of the OH stretch band can be well explained from a purely dipolar contribution, which implies that this response results from oriented water molecules in the electric double layer (EDL). The amount of oriented water molecules within the EDL is dependent on the charge density at the surface, and therefore on the concentration of charged surfactant molecules. The increase of the amplitude of the OH stretch band at low surfactant concentrations ($< 2 \text{ mM}$) can thus be explained from the increased alignment resulting from the increase of the positive surface charge density. For higher concentrations ($> 2 \text{ mM}$) a small decrease of the OH stretch band is observed, which can be explained from the saturation of the surface density of surfactant molecules, and the enhanced screening effect of the negative counter ions of the surfactant molecules.¹⁰⁵ For the negatively charged SDS/air surface the interfacial water molecules are oriented with their hydrogen atoms towards the surface, leading to a positive OH stretch band in the $\text{Im}[\chi^{(2)}]$ spectrum. The concentration dependence of the amplitude of the OH stretch band at the water/SDS/air interface is similar to that at the water/DTAB/air interface. For both DTAB and SDS two additional negative features at 2880 cm^{-1} and 2940 cm^{-1} arise at higher concentrations ($> 2 \text{ mM}$). The 2880 cm^{-1} band is assigned to the symmetric stretch vibration of the terminal methyl group ($\nu_{\text{CH}_3, \text{SS}}$) of the hydrocarbon chain of the surfactant molecules, while the 2940 cm^{-1} band represents the overlapping responses of the symmetric stretch vibrations of the methylene groups ($\nu_{\text{CH}_2, \text{SS}}$) and the Fermi resonance of the symmetric stretch vibration of the terminal methyl group ($\nu_{\text{CH}_3, \text{SS}}$). The sharp positive peak at 2970 cm^{-1}

can be assigned to the antisymmetric stretch vibration of the methyl group ($\nu_{CH_3,AS}$).³² We also observe that with increasing DTAB and SDS concentration the peak centered at 3700 cm^{-1} , assigned to the OH stretch vibrations of non-hydrogen bonded OH-groups that stick out of the surface, decreases, due to the increased surface coverage by the surfactant molecules.

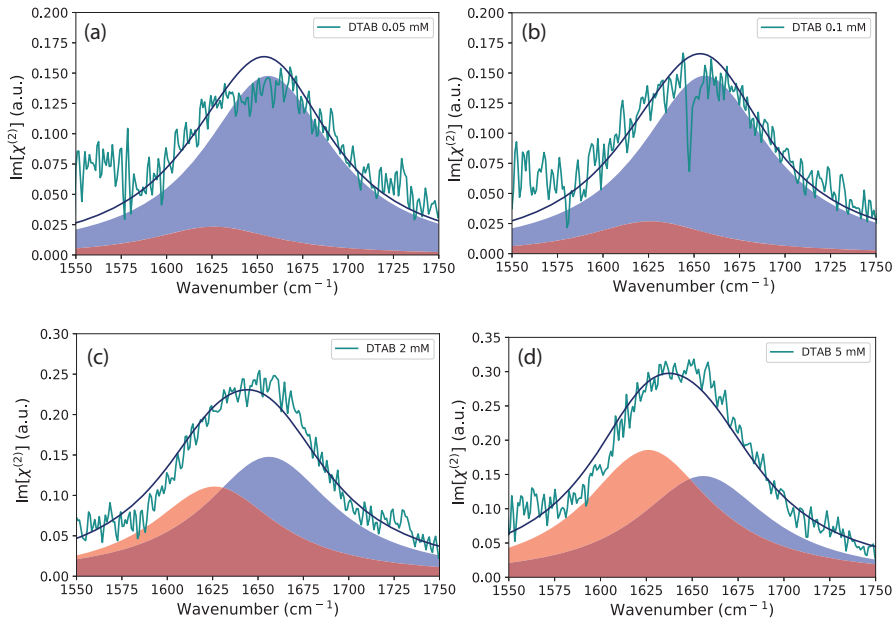


FIGURE 4.10. Spectral decomposition of experimental obtained $\text{Im}[\chi^{(2)}]$ spectra of the water/DTAB/air (cyan) with two Lorentzian-shaped spectral components of different concentrations (a) 0.05 mM (b) 0.1 mM (c) 2 mM and (d) 5 mM. The two Lorentzian-shaped spectral components are assigned to the quadrupole contribution of the bulk (blue) and to the interfacial dipole contribution (red) of the water bending mode centered at 1656 cm^{-1} and 1626 cm^{-1} respectively.

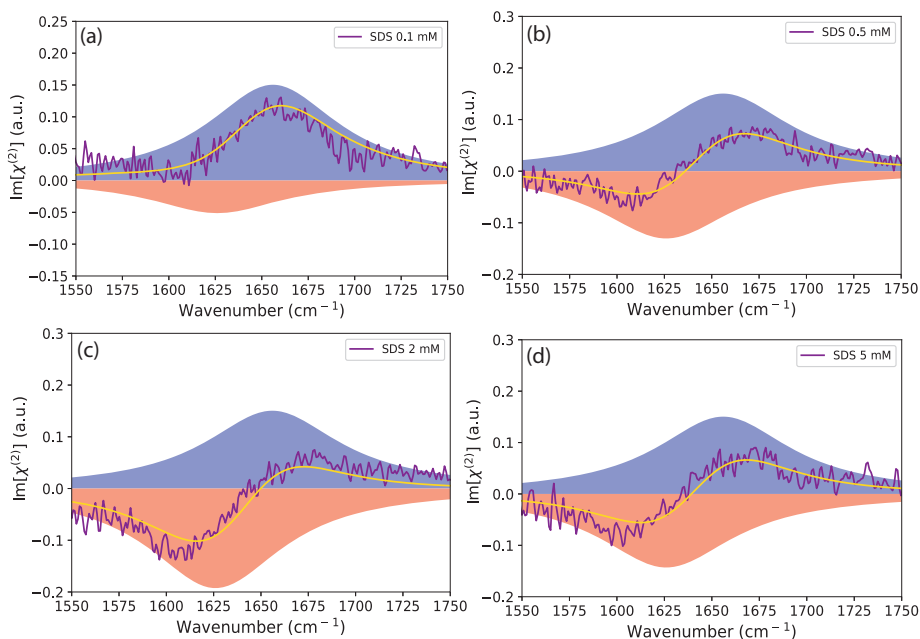


FIGURE 4.11. Spectral decomposition of experimental obtained $\text{Im}[\chi^{(2)}]$ spectra of the water/SDS/air (magenta) with two Lorentzian-shaped spectral components of different concentrations (a) 0.1 mM (b) 0.5 mM (c) 2 mM and (d) 5 mM. The two Lorentzian-shaped spectral components are assigned to the quadrupole contribution of the bulk (blue) and to the interfacial dipole contribution (red) of the water bending mode centered at 1656 cm^{-1} and 1626 cm^{-1} respectively.



5 DIRECT OBSERVATION OF THE ORIENTATION OF UREA MOLECULES AT CHARGED INTERFACES

Dissolving urea in water induces special solvation properties that play a crucial role in many biological processes. Here, we probe the properties of urea molecules at charged aqueous interfaces using heterodyne-detected vibrational sum-frequency generation (HD-VSFG) spectroscopy. We find that at the neat water/air interface urea molecules do not yield to a significant sum-frequency generation. However, upon the addition of ionic surfactants, we observe two vibrational bands at 1660 cm^{-1} and 1590 cm^{-1} in the HD-VSFG spectrum assigned to mixed bands of the C=O stretch and NH_2 bend vibrations of urea. The orientation of the urea molecules depends on the sign of the charge localized at surface, and closely follows the orientation of the neighboring water molecules. We demonstrate that urea is an excellent probe of the local electric field at aqueous interfaces.

5.1 INTRODUCTION

Aqueous solutions of urea show most striking properties, like the inhibition of micellar aggregation of surfactants and the enhancement of the solubility of hydrocarbons.^{106–109} Furthermore urea plays a key role in many biological processes, of which the best known is the denaturation of proteins.^{110–113} Due to these remarkable properties aqueous solutions of urea have been the subject of many experimental and theoretical studies over the past decades.^{106,114–118} A great deal of these studies focused on the question to what extent the hydrogen bonding network of water gets perturbed by adding urea molecules. The answer to this question is of great importance to understand the denaturation process of proteins by urea. In previous nuclear magnetic resonance (NMR) and molecular dynamics (MD) simulations studies, it has been proposed that urea breaks the hydrogen bond structure of water and thereby enhances the solvation of the hydrophobic groups of the protein.^{116–118} However, the result of recent pump-probe Infra-red (IR) -measurements, nuclear magnetic resonance (NMR) and terahertz (THz) absorption spectroscopy studies contradict this hypothesis by showing that urea has no significant effect on the hydrogen bond network of water.^{107,119,120} These latter studies indicate that the protein denaturation is driven by a direct mechanism in which the urea molecules interact with the amide groups of the backbone of the protein.¹¹⁹ Up to now, primarily the properties of urea in the bulk of aqueous solutions have been studied, and little work has been done addressing the properties of urea at aqueous surfaces. Recently, surface tension measurements supported by MD-simulations showed that the surface tension increases proportionally with the urea concentration.^{121–125} Previous vibrational sum-frequency generation (VSFG) spectroscopy studies of solutions containing α -lactalbumin and urea showed, that the orientation of the amide groups of the protein at the surface is independent from that of the urea molecules. This observation suggests that there are no strong direct interactions between the amide groups of the protein and the urea molecules, and points at an indirect denaturation process of the protein.^{7,126} In this work we perform HD-VSFG measurements to investigate the molecular response of urea molecules at charged aqueous interfaces, by measuring the effect of surface charge on the vibrational response of urea. Our results demonstrate that urea orients within in the hydrogen bonded network of water and that its absolute orientation is dependent on the sign of the charged surface.

5.2 EXPERIMENTAL METHODS

SAMPLE PREPARATION The solutions are prepared by dissolving different concentrations of dodecyltrimethylammonium bromide (DTAB), sodium dodecyl sulfate (SDS), urea and sodium chloride (NaCl) in H₂O. For all solutions we used H₂O from a Millipore Nanopure system (18.2 M Ω cm). DTAB, SDS, urea

and NaCl are purchased from Sigma Aldrich with a purification of 99% and are used without further purification.

SPECTROSCOPY The VSFG measurements described in this chapter are performed with the setup described in section 3.1.

5.3 RESULTS AND DISCUSSION

In Figure 5.1 we present the experimental $\text{Im}[\chi^{(2)}]$ spectra of neat water (dark blue) and aqueous urea solutions with a concentration of 1 M (cyan) and 6 M (magenta) in the frequency region of 1550 - 1750 cm^{-1} . For pure water we observe a symmetric positive peak centered at 1656 cm^{-1} that we assign to the water bending mode. The observed spectrum of the neat water surface agrees well with the results of previous HD-VSFG studies.^{37,84,127} The $\text{Im}[\chi^{(2)}]$ spectra of the aqueous urea solutions with concentrations of 1 M and 6 M both show a symmetric peak at 1656 cm^{-1} , identical to what is observed for the neat water surface, and that we assign to the water bending mode. This observation suggests that even at a high urea concentration of 6 M no characteristic vibrational modes of urea are observed. This implies that urea is either not located in the vicinity of the surface and/or does not show a net orientation near an uncharged water surface. This observation is consistent with the results of VSFG experiments in the OH and NH stretch vibrational region by Stratzdaite et al.⁷

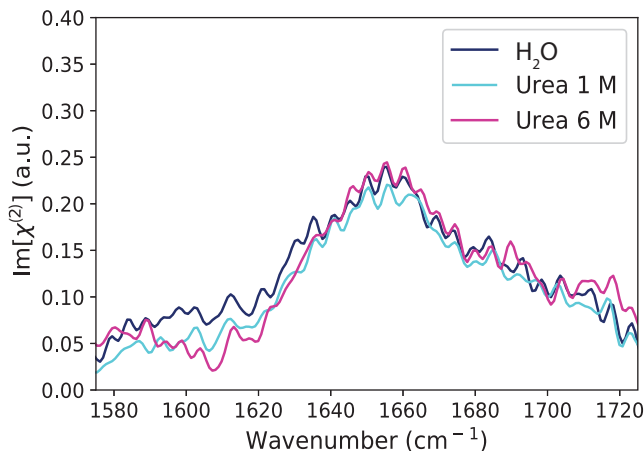


FIGURE 5.1. The $\text{Im}[\chi^{(2)}]$ spectra of the neat water surface (dark blue) and aqueous urea solutions with a concentration of 1 M (cyan) and 6 M (magenta) within the frequency region of 1550 - 1750 cm^{-1} .

Figure 5.2 (a) shows the $\text{Im}[\chi^{(2)}]$ spectrum of an aqueous Sodium dodecyl sulfate (SDS) solution (dotted magenta) with a concentration of 2 mM, and the $\text{Im}[\chi^{(2)}]$ spectrum of the same solution of SDS with 1 M of urea added (solid dark magenta). We used a concentration of 2 mM of SDS. With this concentration

the expected phase distortion effects are expected to be negligible in the HD-VSFG spectra, as the electrical double layer (EDL) has a thickness <10 nm for ionic strengths >1 mM.^{87,88,102} To verify this notion, we modeled the expected phase distortion using the Poisson-Boltzmann equation for a solution with an ionic strength of 2 mM. We find the phase change to be less than 10 degrees (Appendix Figure 5.5), which means that this change within the experimental phase uncertainty. The $\text{Im}[\chi^{(2)}]$ spectrum of an aqueous 2 mM SDS solution shows a negative and a positive peak centered at 1626 cm^{-1} and 1656 cm^{-1} , that we assigned to the dipolar and quadrupolar response of the water bending mode, respectively.¹²⁷ The negative sign of the dipolar contribution implies that the water molecules have a net orientation with their hydrogen atoms toward the surface, as a result of the negative charge of the surface imposed by the SDS surfactants.¹²⁷ In Figure 5.2 (c) we present the $\text{Im}[\chi^{(2)}]$ spectrum of an aqueous Dodecyltrimethylammonium bromide (DTAB) solution (dotted cyan) with a concentration of 2 mM and the $\text{Im}[\chi^{(2)}]$ spectrum of the same solution of DTAB containing 1 M of urea (solid dark cyan). The $\text{Im}[\chi^{(2)}]$ of DTAB shows a single positive peak centered at 1640 cm^{-1} that in comparison to the band observed in the $\text{Im}[\chi^{(2)}]$ spectrum of neat water shown in Figure 5.1 is enhanced, broadened and shifted ~ 10 wavenumbers to lower frequencies. This broad band can be separated in two frequency components centered at 1626 cm^{-1} and 1656 cm^{-1} , and assigned to the dipolar and quadrupolar response of the water bending mode, respectively.¹²⁷ in the case of the DTAB solution the dipolar contribution has a positive $\text{Im}[\chi^{(2)}]$ response, indicating a net orientation of the water molecules with their hydrogen atoms toward the bulk, as a result of the positive charge at the surface generated from the positively charged DTAB surfactants.

The presence of 1 M urea leads to a significant change of the $\text{Im}[\chi^{(2)}]$ spectra of the aqueous solutions of SDS and DTAB, as shown in Figure 5.2 (a,c). The resulting spectra (solid dark magenta and solid dark cyan) look very different from the $\text{Im}[\chi^{(2)}]$ of the aqueous solutions containing only SDS (dotted magenta) and only DTAB (dotted cyan). In Figure 5.2 (b) we have subtracted the $\text{Im}[\chi^{(2)}]$ response of the water bending mode from that of the solution containing 2 mM SDS and 1 M urea, and from that of the solution containing 2 mM DTAB and 1 M urea. The difference spectra show two distinct vibrational bands centered at 1590 cm^{-1} and 1660 cm^{-1} that we assign to mixed bands of the C=O stretch and NH_2 bend vibrations of the urea molecule. The mode at 1590 cm^{-1} is dominated by the NH_2 bending vibrations, and the band centered at 1660 cm^{-1} is dominated by the C=O stretch vibration.^{128,129} The band centered at 1660 cm^{-1} has a higher absolute amplitude than the peak at 1590 cm^{-1} , which can be explained from the larger transition dipole moment of the C=O stretch vibration. To confirm the above assignment of the vibrational modes of urea we also performed measurements with deuterated urea dissolved in D_2O . In deuterated urea the NH_2 groups of urea are exchanged by ND_2 groups leading to a significant redshift of the frequency of the bending vibration of these groups, and a decoupling from the C=O stretch vibration. Additionally, the bending vibration of D_2O is shifted to lower frequencies with respect to the bending mode of H_2O . For this system, we observe only a band

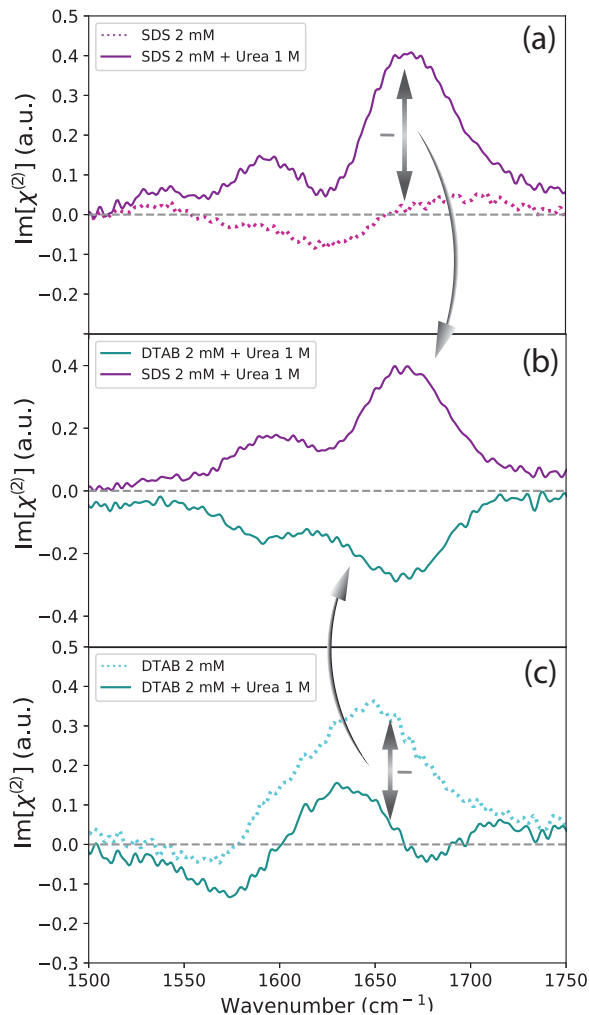


FIGURE 5.2. $\text{Im}[\chi^{(2)}]$ spectra of aqueous solutions of different surfactants and different concentrations of urea. (a) $\text{Im}[\chi^{(2)}]$ spectra of a solution with 2 mM SDS (dotted magenta), and of a solution with 2 mM SDS and 1 M urea (solid dark magenta). (c) $\text{Im}[\chi^{(2)}]$ spectra of a solution with 2 mM DTAB (dotted cyan), and of a solution with 2 mM DTAB and 1 M of urea (solid dark cyan). (b) The $\text{Im}[\chi^{(2)}]$ spectra of aqueous solutions containing 1 M urea and either 2mM SDS or 2mM DTAB, after subtraction of the response of the water bending mode.

at 1600 cm^{-1} that can be assigned to the nearly pure C=O stretching mode of the deuterated urea molecule (Appendix Figure 5.6), thus confirming the assignment of the 1590 cm^{-1} and 1660 cm^{-1} to bands of mixed C=O stretch and NH_2 bending vibration character.^{128,130}

Interestingly, the signs of the 1590 cm^{-1} and 1660 cm^{-1} bands in the $\text{Im}[\chi^{(2)}]$ spectra of Figure 5.2 (b) are governed by the sign of the charge at the surface. For a solution with 2 mM SDS and 1 M urea the two vibrational modes have a positive sign, which implies that the urea molecules near the surface orient with their NH_2 groups toward the negatively charged surface.¹³¹ For an aqueous solution with 2 mM DTAB and 1 M urea the two bands are negative, indicating that the urea molecules are pointing with their C=O group toward the positively charged surface. The strong dependence of the sign of the vibrational bands of urea on the nature of the surface charge, and the lack of any signal from urea for a neutral aqueous surface, show that the HD-VSFG response of urea results from an induced orientation of the urea molecules within the electric double layer (EDL) near the surface. Therefore this response can be described as an electric field induced $\chi_{Urea}^{(3)}$ effect, similar to the $\chi^{(3)}$ effect that has been observed previously for water molecules at charged interfaces.^{32,70,132}

$$E_{\text{VSFG}} \sim \chi_{\text{H}_2\text{O,quad}}^{(2)} N_{\text{H}_2\text{O}} + \left(\chi_{\text{H}_2\text{O,dip}}^{(3)} N_{\text{H}_2\text{O}} + \chi_{\text{urea,dip}}^{(3)} N_{\text{urea}} \right) E_{\text{DC,surf}} \quad (5.1)$$

Here E_{VSFG} is the VSFG response and $\chi^{(2)}$ is the second-order nonlinear susceptibility. $E_{\text{DC,surf}}$ represents the static electric field within the EDL and $N_{\text{H}_2\text{O}}$ and N_{urea} represent the number densities of water and urea, respectively. $\chi_{\text{H}_2\text{O,dip}}^{(3)}$ and $\chi_{\text{urea,dip}}^{(3)}$ are the responses resulting from the electric field induced orientation of water and urea molecules within the EDL. We find no indication for the presence of a quadrupolar $\chi^{(2)}$ contribution of urea molecules, suggesting that this contribution is negligible.

To study the properties of urea near aqueous surfaces in more detail, we measured the dependence of the spectra on the urea concentration. In Figure 5.3 we present the $\text{Im}[\chi^{(2)}]$ of aqueous (a) SDS and (b) DTAB solutions for different concentrations of urea in a range from 1 M to 6 M. The concentration of SDS and DTAB are kept constant at 2 mM. For all measurement results shown in Figure 5.3 the response of the water bending mode has been subtracted. For both the SDS and the DTAB solutions we observe that the absolute amplitudes of the bands at 1660 cm^{-1} and 1590 cm^{-1} increase with increasing urea concentration. This increase reflects an increased amount of oriented urea molecules. To study the concentration dependence of the amplitudes quantitatively, we decompose the responses measured at different concentrations of urea in two Lorentzian bands centered at 1660 cm^{-1} and 1590 cm^{-1} . In this decomposition routine we keep the central frequency and the width of the bands constant and we only allow the amplitude to vary with urea concentration. The fit results are shown in Figures 5.3 (a) and (b) with dashed lines and are shown in detail in the Appendix (Figures 5.7 and 5.8).

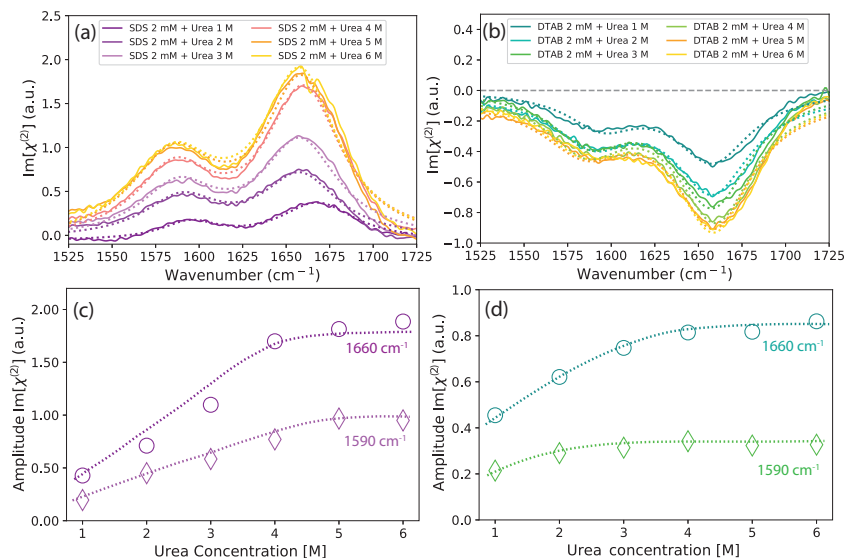


FIGURE 5.3. The $\text{Im}[\chi^{(2)}]$ spectra of aqueous solutions containing different concentrations of urea ranging from 1 M to 6 M, and (a) 2 mM SDS and (b) 2 mM DTAB. For all measurements the signature of the water bending mode is subtracted from the $\text{Im}[\chi^{(2)}]$ spectrum. Figures (c)-(d) show the absolute amplitude of the bands centered at 1660 cm^{-1} and 1590 cm^{-1} extracted from the fitting procedure as a function of the concentration of urea for (c) a solution containing 2 mM SDS, and (d) a solution containing 2 mM DTAB. The dotted lines are guides to the eye.

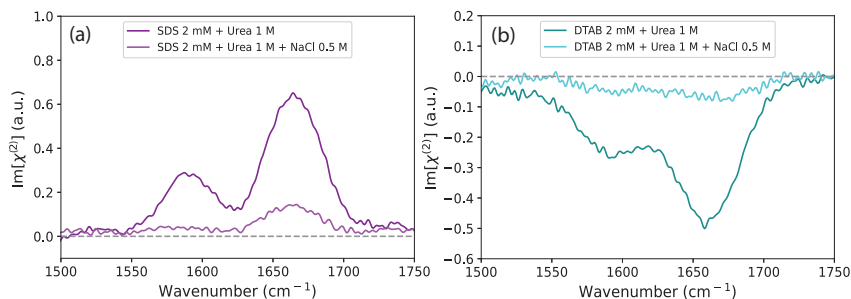


FIGURE 5.4. (a) The $\text{Im}[\chi^{(2)}]$ spectra of the 2 mM aqueous SDS solutions with 1 M of urea (dark magenta) and additional 0.5 M NaCl added to the solution (magenta). (b) The $\text{Im}[\chi^{(2)}]$ spectra of the 2 mM aqueous DTAB solutions with 1 M of urea (darkcyan) and additional 0.5 M NaCl added to the solution (cyan).

Figure 5.3 (c) and (d) show the amplitudes of the two vibrational modes extracted from the fitting procedure as a function of the urea concentration. For both SDS and DTAB the amplitude of the 1660 cm^{-1} and 1590 cm^{-1} modes first increases proportional to the urea concentration and then shows clear saturation, starting at a urea concentration of $\sim 4\text{ M}$. This saturation behavior can be explained from the dipole-dipole interactions between urea molecules close to the surface. With increasing urea concentration, the electric field experienced by a urea molecule will become increasingly screened by neighboring urea dipoles, thus leading to a decrease of the degree of orientation of all urea molecules.

In Figure 5.4 we study the effect of adding 0.5 M NaCl to a solution of 1 M urea and 2 mM SDS (a) and a solution of 1 M urea and of 2 mM DTAB (b). The spectra shown here are difference spectra of the spectra measured for solutions with and without 1 M of urea keeping the concentrations of SDS/DTAB and NaCl components of the solution the same, in order to remove the response from the water bending mode. For SDS and DTAB solutions, the response of the water bending mode is strongly affected by adding NaCl.¹²⁷ We observe that adding NaCl to the solution the amplitudes of the vibrational modes of urea substantially decrease. This decrease indicates that the net orientation of the urea molecules strongly decrease upon the addition of Na^+ and Cl^- ions. Previous studies of the responses of the OH stretch band of water and the dipolar contribution of the bending mode of water near charged surfaces showed a similar decrease in intensity upon the addition of sodium chloride.^{31,32,104} This decrease has been explained from the screening of the electric field in the EDL by the added ions, leading to a decrease of the degree of orientation of the water molecules.^{103,104} The observed decrease in the amplitudes of the vibrational bands of urea indicates that a similar effect occurs for urea, i.e. screening of the electric field of the surfactant molecules leads to a strong decrease of the net orientation of the urea molecules near the surface. The observed decrease in the signal of urea is similar to the one observed for the dipolar response of the bending mode of water.¹²⁷ This observation indicates that the orientation of urea and water molecules in a local electric field are highly correlated, which indicates that urea and water form a collective hydrogen-bond network. Application of an electric field induces a net orientation of this collective hydrogen-bond network, thus leading to a similar orientational effect on the responses of the urea and water molecules forming the network.

5.4 CONCLUSION

To conclude, we performed heterodyne-detected vibrational sum frequency generation (HD-VSFG) measurements on aqueous urea solutions and of aqueous urea solutions with ionic surfactants. We find that the HD-VSFG spectra of solutions only containing urea do not show characteristic vibrational signatures of urea, showing that urea has no distinct orientation in the region near a neutral aqueous surface. Charging the surface with ionic surfactants, leads to the observation of a high-frequency (1660 cm^{-1}) and a low-frequency (1590 cm^{-1})

band that can be assigned to urea vibrations of mixed C=O stretch and NH₂ bending character.

The signs and amplitudes of the vibrational bands of urea strongly depend on the sign and amplitude of the surface electric field, which implies that the response of urea is a field-induced $\chi_{Urea}^{(3)}$ effect, similar to the $\chi^{(3)}$ effect observed for the OH stretch vibration of water and the dipolar contribution of the bending vibration of water at charged aqueous surfaces. The $\chi_{Urea}^{(3)}$ effect is observed to saturate at a urea concentration of ~ 4 M, probably due to screening of the surface field by the urea molecules. We thus conclude that urea molecules constitute as an excellent probe of the interfacial electric field.

Finally, we find that the response of the urea molecules is strongly reduced when the surface electric field is screened by adding NaCl to the solution, similar to the effect observed for the OH stretch vibration of water and the dipolar response of the bending vibration of water. This observation shows that the orientations of urea and water molecules in a local electric field are highly correlated, which indicates that urea and water form a collective hydrogen-bond network.

5.5 APPENDIX

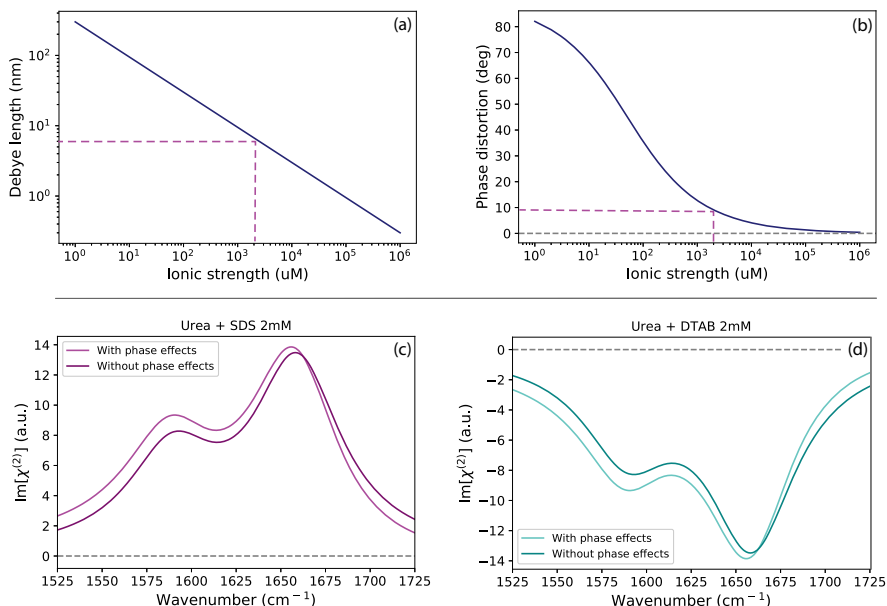


FIGURE 5.5. (a) The calculated Debye length and (b) the phase distortion in degree with respect to the Ionic strength located at the surface. The modeled $\text{Im}[\chi^{(2)}]$ spectra of the $\chi_{\text{urea,dip}}^{(3)}$ response in an aqueous solution of 2 mM of (c) SDS and (d) DTAB with and without the phase effects associated to the path length difference.

From literature it is known that a charged surface creates an electric double layer (EDL) in which dipolar molecules are oriented and can generate sum-frequency light.^{32,86} Depending on the thickness of the EDL, the sum-frequency light is thus generated by sources with different path lengths, which can lead to a phase change of the HD-VSFG spectrum.⁸⁷ We calculate the thickness of the EDL, denoted as the Debye length, using the linearized Poisson-Boltzmann distribution. In Figure 5.5 (a) we present the Debye length of a 1:1 electrolyte solution as a function of the ionic strength, and in Figure 5.5 (b) the resulting phase change in degrees as a function of the ionic strength. In Figure 5.5 (c) and 5.5 (d) we show the calculated $\text{Im}[\chi^{(2)}]$ due to the $\chi_{\text{urea,dip}}^{(3)}$ response for an aqueous solution with 2 mM of SDS and DTAB, with and without phase effects, respectively. For a 2 mM electrolyte solution, we find that the Debye length is ~ 4 nm and that the associated phase change of the SFG signal is $\sim 8^\circ$. The phase effects in our experiments due to EDL formation and associated path length variation of SFG are thus small, and within the experimental phase uncertainty.

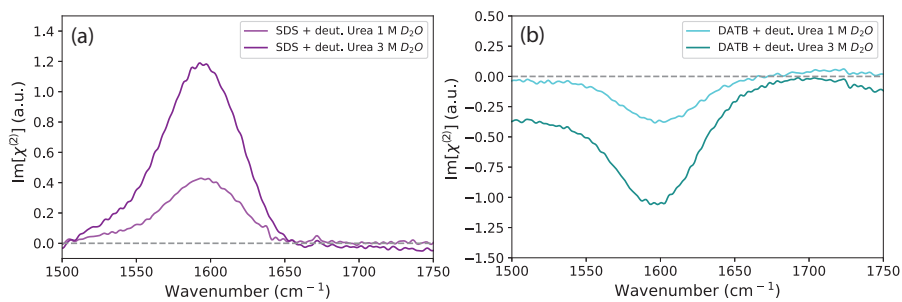


FIGURE 5.6. The $\text{Im}[\chi^{(2)}]$ spectra of a 2 mM (a) SDS and (b) DTAB solution with a concentration 1 M (magenta) and 3 M (dark magenta) of deuterated urea in D_2O .

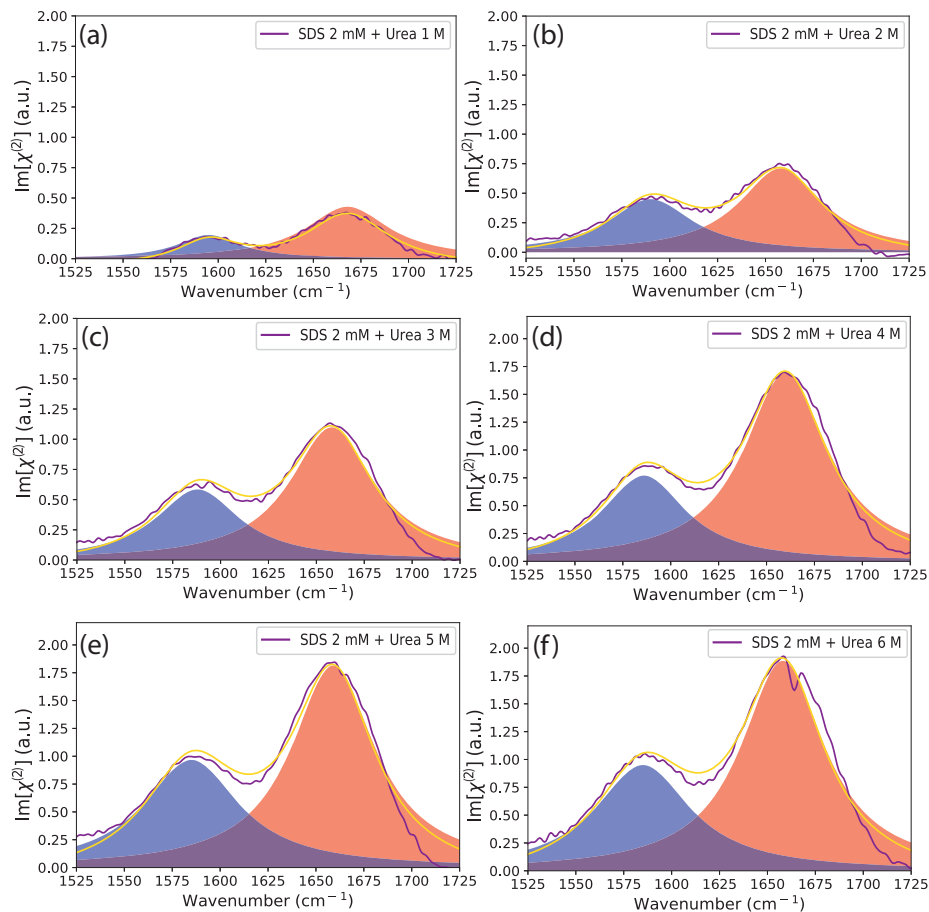


FIGURE 5.7. Spectral decomposition of experimental obtained $\text{Im}[\chi^{(2)}]$ spectra of the 2 mM SDS solution with urea at different concentrations (a) 1 M, (b) 2 M, (c) 3 M, (d) 4 M, (e) 5 M and (f) 6 M into two Lorentzian-shaped spectral components. The two Lorentzian-shaped spectral components are assigned to the mixed bands of the C=O stretch and NH_2 bending vibrations. The band centered at 1660 cm^{-1} has major contributions coming from the C=O stretch, while the mode at 1590 cm^{-1} has major contributions from NH_2 bending vibrations.

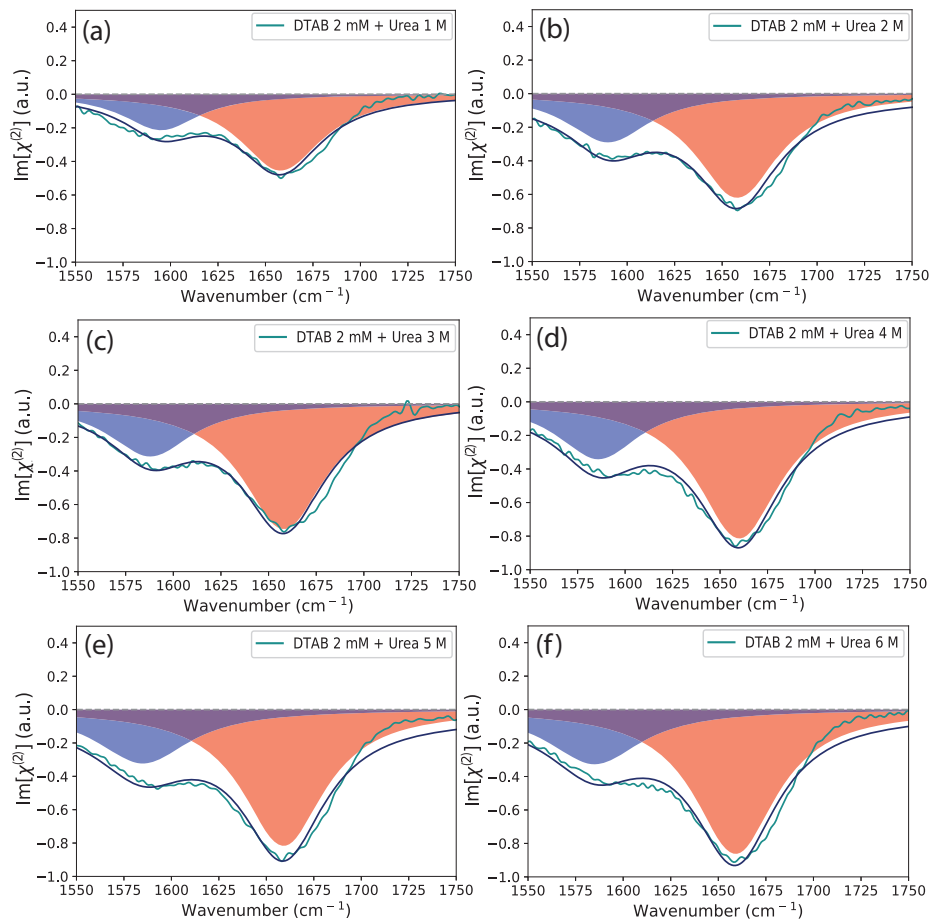


FIGURE 5.8. Spectral decomposition of experimental obtained $\text{Im}[\chi^{(2)}]$ spectra of the 2 mM DTAB solution with urea at different concentrations (a) 1 M, (b) 2 M, (c) 3 M, (d) 4 M, (e) 5 M and (f) 6 M into two Lorentzian-shaped spectral components. The two Lorentzian-shaped spectral components are assigned mixed bands of the C=O stretch and NH_2 bending vibrations. The band centered at 1660 cm^{-1} has major contributions coming from the C=O stretch, while the mode at 1590 cm^{-1} has major contributions from NH_2 bending vibrations.



6 MOLECULAR ORIENTATION OF SMALL CARBOXYLATES AT THE WATER-AIR INTERFACE

We study the properties of formate (HCOO^-) and acetate (CH_3COO^-) ions at the surface of water using heterodyne-detected vibrational sum-frequency generation (HD-VSFG) spectroscopy. For both ions we observe a response of the symmetric (ν_s) and antisymmetric (ν_{as}) vibrations of the carboxylate group. The spectra further show that for both formate and acetate the carboxylate group is oriented toward the bulk, with a higher degree of orientation for acetate than for formate. We find that increasing the formate and acetate bulk concentrations up to 4.5 m does not change the orientation of the formate and acetate ions at the surface and does not lead to saturation of the surface density of ions.

6.1 INTRODUCTION

Carboxylic acid (-COOH) and carboxylate (-COO⁻) groups are involved in many important interfacial processes, such as molecular recognition at biomembranes, protein folding, and energy conversion and storage.^{7-12,133,134} The chemical and physical properties of the carboxylate anion differ strongly from those of the conjugate carboxylic acid.¹³⁵⁻¹³⁷ Further, carboxylates form strong ionic bonds with different metal cations, giving rise to metal carboxylates as well as more elaborate structures such as carboxylate based metal organic frameworks.¹³⁸⁻¹⁴² Long-chain carboxylates are also frequently utilized as surfactants to solubilize hydrocarbons in fuel extraction.^{143,144} During the last decades, the pronounced surface activity of long-chain carboxylic acids and long-chain carboxylates inspired many studies of the acid/base equilibrium, the surface propensity, and the orientation properties of these systems in dependence on the chain length, the concentration and the pH.¹⁴⁵⁻¹⁴⁹ Surface-specific X-ray photoelectron spectroscopy (XPS) studies showed that the surface propensity increases with increasing chain length.¹⁵⁰ Furthermore, it has been shown that the carboxylic acid has a higher surface affinity compared than its conjugate carboxylate anion.¹⁵⁰ While many studies have been devoted to the properties of long-chain carboxylic acids and carboxylates at aqueous surfaces, much less attention has been given to the surface properties of small carboxylate ions, as acetate and formate. Surface tension measurements and MD simulations indicate that the propensity of formate and acetate to be located at the surface of water strongly differ: while the addition of formate does not significantly change the surface tension, adding acetate does lead to a substantial lowering of the surface tension compared to water.^{151,152} Up to now, this striking difference between formate and acetate has not been studied on the molecular scale.

In this work we perform HD-VSFG measurements to investigate the surface properties of aqueous sodium formate and sodium acetate solutions on the molecular scale with HD-VSFG spectroscopy. We compare our results with the results of surface tension measurements and MD simulations of the surfaces of aqueous solutions of formate and acetate. For both formate and acetate, we observe a vibrational surface response of the carboxylate group, and we can establish the net orientation of these ions at the solution surface.

6.2 EXPERIMENTAL METHODS

SAMPLE PREPARATION We prepared 1-5 molal (m) solutions of formate and acetate in D₂O by mixing of D₂O with the appropriate amount of salt in a vial. We used sodium formate ($\geq 99.0\%$, Fluka Analytical), sodium acetate (anhydrous, for molecular biology $\geq 99\%$, Sigma Aldrich) and D₂O (99.9% atom D, Aldrich) as received.

FTIR MEASUREMENTS The linear infrared absorption spectra were recorded with a commercial Bruker Vertex 80v Fourier-transform infrared spectrometer with a resolution of 2 cm^{-1} in transmission geometry. The samples were prepared by squeezing a droplet of the solution between a pair of circular 20 mm thick CaF_2 windows (Crystran) separated by a 5-25 μm thick PTFE spacer. The thickness of the spacers was adjusted such that the absorption of the carboxylate ions did not saturate. An empty cell with two identical CaF_2 windows was used for background measurements.

HETERODYNE-DETECTED VIBRATIONAL SUM-FREQUENCY GENERATION SPECTROSCOPY The VSG measurements described in this chapter are performed with the setup described in section 3.1.

6.3 RESULTS AND DISCUSSION

INFRARED ABSORPTION SPECTRA In Figure 6.1, we show the normalized FTIR spectra of solutions of 2.25 m sodium formate and sodium acetate in D_2O in the 6 μm region. The high-frequency band is assigned to the antisymmetric stretch vibration (ν_{as}) of the carboxylate group. For formate this band is centered at 1590 cm^{-1} and for acetate at 1565 cm^{-1} . The low-frequency band is assigned to the symmetric stretch vibration (ν_s) of the carboxylate group and is centered at 1352 cm^{-1} for formate and at 1417 cm^{-1} for acetate. For the formate solution an additional band at 1380 cm^{-1} is observed which has been assigned earlier to the in-plane CH bending vibration.¹⁵³ For acetate an additional band at 1350 cm^{-1} band is observed which can be assigned to the CH_3 deformation vibration. The symmetries of the CH vibrations and ν_s are different (A1 and B1 respectively) and hence mixing between these bands is formally not possible.¹⁵³⁻¹⁵⁶ To compare the absorption strengths of the different bands, we normalize the spectra on the maximum amplitudes of the ν_{as} vibrations. We observe that the ν_s vibration is almost twice as intense for acetate than for formate. We studied the concentration dependence of the bands (Figures 6.5 and 6.6 in the Appendix), and found that the ratio between the bending mode of D_2O ($\delta_{\text{D}_2\text{O}}$) and the ν_s of the carboxylate ions scales very well with the solute concentration. We also observe that both for formate and acetate the line shapes of the carboxylate stretch vibrations are quite independent of the concentration.

VSG SPECTRA Figure 6.2 presents the imaginary part of the HD-VSG spectra ($\text{Im}[\chi^{(2)}]$) of solutions of 2.25 m sodium formate (magenta) and sodium acetate (cyan) in D_2O in the frequency region of $1300 - 1650\text{ cm}^{-1}$. The $\text{Im}[\chi^{(2)}]$ spectra show a positive band at $1350\text{ cm}^{-1}/1410\text{ cm}^{-1}$, and a negative band at $1590\text{ cm}^{-1}/1550\text{ cm}^{-1}$ for formate/acetate. In line with the FTIR spectrum, we assign the low-frequency band to the ν_s vibration and the high-frequency band to the ν_{as} vibration of the carboxylate group. In SSP polarization combination only vibrational modes with a transition dipole moment (TD) component parallel to the surface normal can be observed. Hence, considering that the TD of the ν_{as} vibration of the carboxylate group is perpendicular to that of ν_s , only

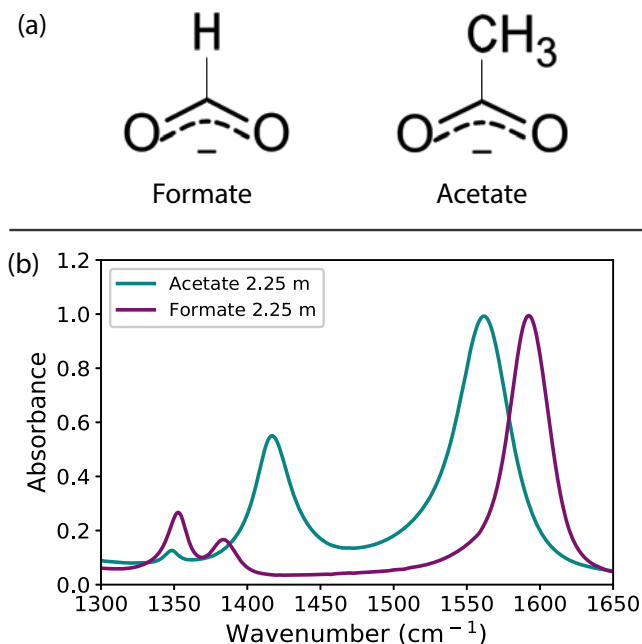


FIGURE 6.1. FTIR spectra of 2.25 m D_2O solutions of sodium formate (magenta) and sodium acetate (cyan) in the frequency region of $1300\text{--}1650\text{ cm}^{-1}$.

the latter vibration would have been detected in case the carboxylates would have their molecular c -axis parallel aligned with the surface normal. In earlier studies of long-chain carboxylates only the band of the ν_s vibration of the carboxylate group was observed in SSP polarization combination, indicating that for long-chain carboxylates the c -axis is indeed oriented parallel to the surface normal. For long-chain carboxylates the ν_{as} band could only be observed in SPS polarization configuration.^{148,149} Thus, the observation of the ν_{as} band in Figure 6.2 for formate and acetate shows that for these carboxylates the molecular c -axis is at a nonzero angle with respect to the surface normal.

We observe that for both carboxylate solutions the ν_s vibrational mode has a positive sign in the $\text{Im}[\chi^{(2)}]$ spectrum. As the transition dipole moment of the ν_s vibration is aligned parallel to the c -axis of the carboxylate group, this observation implies that formate and acetate orient with their carboxylate group toward the bulk. HD-VSFG measurements of formate and acetate solutions performed in the $3\ \mu\text{m}$ region support this assignment (Appendix Figure 6.7), as these measurements show a negative sign of the CH stretch vibration of the methine group of formate ($\nu_{CH,S}$) and the symmetric CH_3 stretch vibration of the methyl group of acetate ($\nu_{\text{CH}_3,S}$). These negative signs show that the CH bonds of the carboxylate anions have a net orientation pointing toward the air.³² To explain the negative sign of the ν_{as} of the carboxylate group, a more

detailed analysis of the hyperpolarizability tensor is required. In 2.3 we provide a brief description based on the analysis of a systems with C_{2v} symmetry, which represents the carboxylate group. Finally, we note that the in-plane CH bending vibration of formate, and the CH_3 deformation of acetate that are observed in the FTIR spectrum, are not observed in the HD-SFG spectrum.

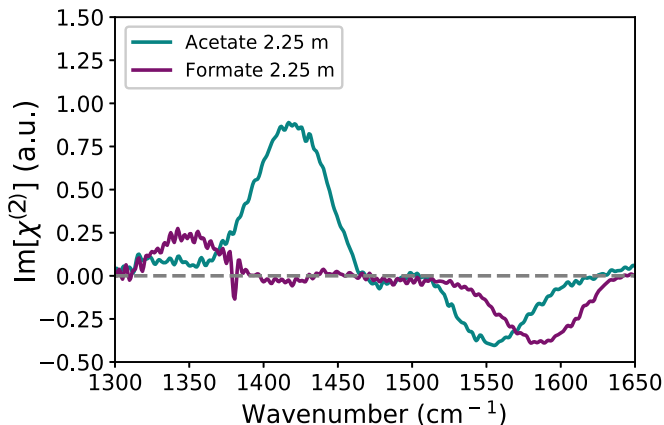


FIGURE 6.2. $\text{Im}[\chi^{(2)}]$ spectra of a solution of 2.25 m sodium formate (red) and sodium acetate (blue) in D_2O in the frequency region of 1300 -1650 cm^{-1} . The measurements are taken in SSP polarization configuration.

Comparing Figures 6.2 and 6.1, we observe that in the SFG spectrum the ν_{as} band is substantially weaker compared to the ν_s band than in the FTIR spectrum. This difference can be explained from two effects. The first effect is that the $\chi^{(2)}$ response measured in HD-VSFG is proportional to the product of the TD and the Raman transition matrix element. The ν_{as} vibration shows only weak Raman activity compared to the ν_s vibration¹⁵³, thus decreasing the SFG signal of the ν_{as} vibration relative to that of the ν_s vibration. A second effect is that the carboxylate ions are probably quite well oriented along the surface normal, which means that the transition dipole moment of the ν_{as} vibration will have a relatively small component along the surface normal, which decreases its SFG signal compared to that of the ν_s vibration. We observe in Figure 6.2 that the amplitudes of the ν_{as} bands of the sodium formate and sodium acetate solutions are almost the same. In previous surface-specific studies it was found that acetate has a quite high surface propensity, while formate was found to have a very low surface propensity.^{150,152}

In view of this difference in surface propensity, it is quite unexpected that the VSFG response of ν_{as} is about equal in amplitude for acetate and formate solutions. The effect of the higher surface propensity of acetate is probably compensated by a larger tilt angle of the c-axis with respect to the surface normal for formate. A larger tilt angle enhances the amplitude of the band of the ν_{as} vibration. In Figure 6.3 we show $\text{Im}[\chi^{(2)}]$ spectra of (a) sodium formate and (b) sodium acetate solutions at different concentrations in the range of 0.9 - 4.5 m. In Figure 6.3 (c,d) we show the amplitudes of the two vibrational

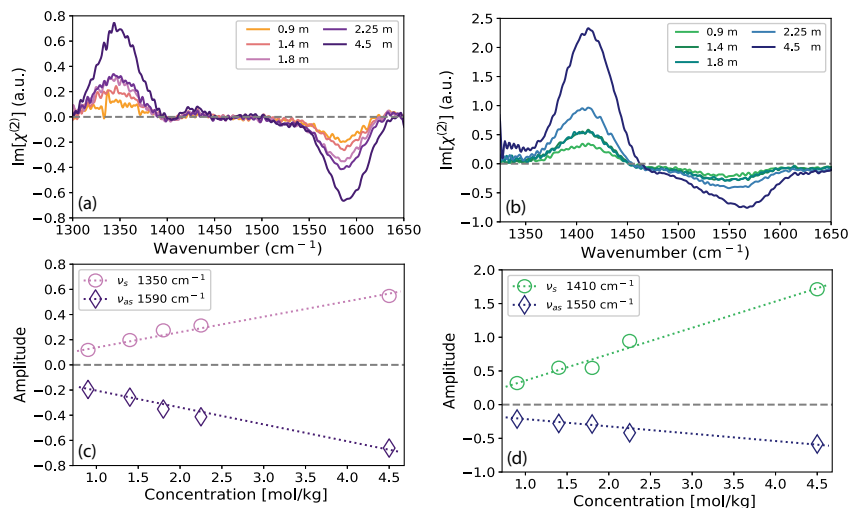


FIGURE 6.3. $\text{Im}[\chi^{(2)}]$ spectra of aqueous (a) sodium formate and (b) sodium acetate solutions in D_2O with different concentrations in the range of 0.9 - 4.5 m. (c)-(d) show the amplitudes of the bands of the ν_s and ν_{as} vibrations as a function of the carboxylate concentration.

modes as a function of the carboxylate concentration for formate and acetate. For both formate and acetate, we observe that the amplitudes of the ν_s and ν_{as} bands increase almost linearly with the bulk concentration. This result shows that the surface does not get saturated with formate/acetate ions up to bulk concentrations of 4.5 m.

The ratio of the amplitudes of ν_s and ν_{as} is independent of the concentrations, which implies that increasing the bulk concentration does not lead to a significant change of the orientation of the ions at the surface. We also observe that increasing the bulk concentration of formate/acetate leads to a shift of the vibrational bands to higher frequencies, and an increasing asymmetry of the band shape. This change of the spectral shape and position is most clearly seen for the ν_{as} band and can be explained by the change of the refractive index which in turn affects the Fresnel factors. We modeled the VSFG response of the ν_s and ν_{as} vibrations using a three-layer model, combined with a Lorentz model to calculate the change of the refractive index of the interfacial layer with increasing carboxylate concentration.^{70,157}

In Figure 6.4 we compare the experimental and calculated VSFG responses for an aqueous solution of sodium acetate at different concentrations. At high ion concentrations, the infrared refractive index and the Fresnel factor of the infrared light acquire a strong frequency dependence due to the vibrational resonances. This change of the Fresnel factor leads to an increase of the high-frequency wings of the responses of the ν_s vibrations and ν_{as} vibrations. As a result, the bands become asymmetric and the maxima shift to higher frequencies. It is also observed that the band of the ν_{as} vibration is more affected than

the band of the ν_s vibration. This can be explained from the higher infrared cross-section of the ν_{as} vibration, which induces a stronger frequency dependence of the refractive index and the Fresnel factor at frequencies close to this vibration.

We modeled the VSFG response of aqueous sodium acetate solutions at different concentrations also with the two-layer model, and we find that this model clearly overestimates the Fresnel effects on the VSFG spectrum (Appendix Figure 6.8). A detailed description of the two models and the determination of the Fresnel factors can be found elsewhere.^{70,73,157} We conclude that the three-layer model accounts very well for the experimentally observed changes in spectral shape and position. This means that these changes can be fully explained by Fresnel effects and are not caused by changes in the direct molecular environment of formate and acetate, e.g. changes in hydrogen-bond strength or configuration when increasing the carboxylate concentration.

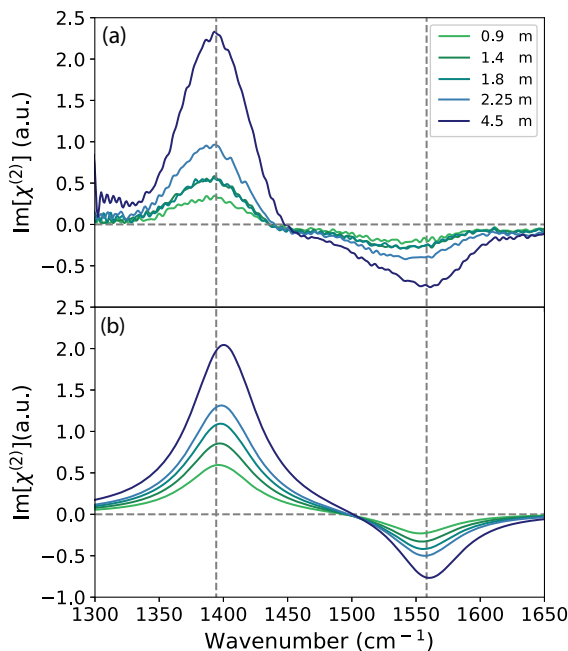


FIGURE 6.4. (a) Experimental and (b) calculated $\text{Im}[\chi^{(2)}]$ spectra of aqueous sodium acetate solutions for different concentrations in the concentration range of 0.9 - 4.5 m. The calculated $\text{Im}[\chi^{(2)}]$ spectra are obtained by accounting for the effect of acetate on the infrared Fresnel factors using the three-layer model, as described in the text and the Appendix.

Previous surface tension measurements by Minofar *et al.* show that for aqueous acetate solutions a clear decrease in surface tension is observed with increasing concentration, indicating that acetate is surface-active.^{151,152} These surface tension measurements are accompanied by MD simulations, yielding

the density profile of the carboxylate ion near the surface. For acetate it is found that the density is enhanced compared to that of water at the surface, meaning that this ion has a clear surface propensity.^{151,152} In addition, the MD simulations show that the acetate ions are oriented with their carboxylate groups pointing toward the bulk. Our observation of a strong positive ν_s band in the HD-VSFG spectrum of aqueous acetate, agrees well with the results of these previous surface tension measurements and MD simulations.^{151,152} Interestingly, in the same study it is found that the addition of sodium formate does not lead to a significant change of the surface tension.¹⁵² The accompanying MD simulations show that the density at the surface of formate is lower than that of water, and that the formate ions do not have a preferred orientation.¹⁵² The latter result is not in agreement with our observations.

The HD-VSFG spectrum of formate shown in Figure 6.2, in particular the positive ν_s vibrational band, show that formate has a clear net orientation of its carboxylate group toward the bulk, albeit that the degree of orientation is less than that of acetate. The fact that the addition of sodium formate does not significantly change the surface tension also indicates that formate is present at the surface, probably showing a very similar dependence of its density profile on the depth into the solution as water.

6.4 CONCLUSIONS

We performed Fourier Transform Infrared (FTIR) absorption and heterodyne-detected vibrational sum frequency generation (HD-VSFG) measurements of aqueous sodium formate and sodium acetate solutions. The HD-VSFG spectra contain responses of both the symmetric (ν_s) and the antisymmetric (ν_{as}) vibrations of the carboxylate group. The ν_s band has a positive sign which shows that formate and acetate both are oriented with their carboxylate group pointing toward the bulk. The observation of the ν_{as} band in the HD-VSFG spectrum of the formate and acetate solution shows that the c-axis of these ions is at a nonzero angle with respect to the surface normal. From the amplitudes of the ν_{as} bands it follows that this angle is smaller for acetate than for formate. We find that the amplitudes of both vibrational bands increase linearly with bulk concentration up to concentrations of 4.5 m. This observation implies that, even at these high bulk concentrations, the surface is not getting saturated with carboxylate ions, and that there is no significant change of the orientation angle of the formate and acetate ions. Finally, we found that at high carboxylate concentrations the ν_s and ν_{as} bands in the HD-VSFG spectrum become asymmetric and shift to higher frequencies, which can be quantitatively explained from the change of the Fresnel factor of the infrared beam.

6.5 APPENDIX

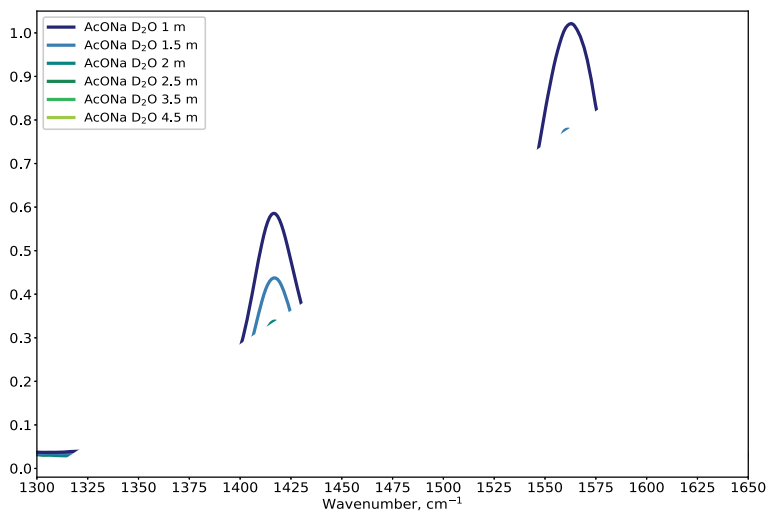


FIGURE 6.5. FTIR spectra in the frequency range $1300 - 1650 \text{ cm}^{-1}$ for different concentrations of sodium acetate in D_2O , in the range of 1.0 - 4.5 molal.

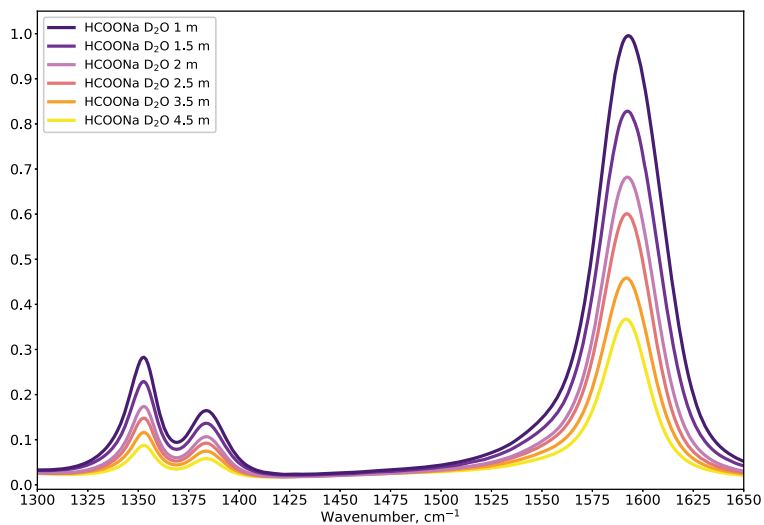


FIGURE 6.6. FTIR spectra in the frequency range $1300 - 1650 \text{ cm}^{-1}$ for different concentrations of sodium formate in D_2O , in the range of 1.0 - 4.5 molal.

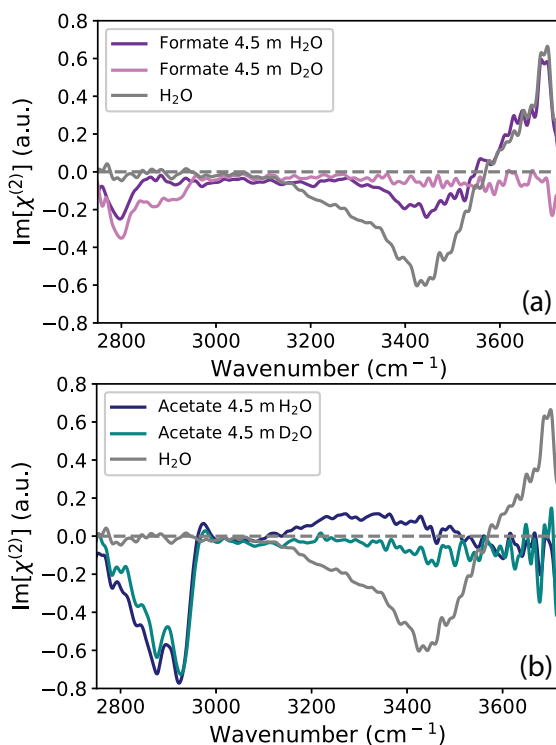


FIGURE 6.7. (a) $\text{Im}[\chi^{(2)}]$ spectra of neat water (gray) and aqueous formate solutions with a concentration of 4.5 m in H_2O (dark magenta) and D_2O (magenta) in the frequency range 2800 - 3720 cm^{-1} . (b) $\text{Im}[\chi^{(2)}]$ spectra of neat water surface (gray) and aqueous acetate solutions with a concentration of 4.5 m in H_2O (dark blue) and D_2O (cyan) in the frequency range 2800 - 3720 cm^{-1} . All measurements are taken in SSP polarization configuration.

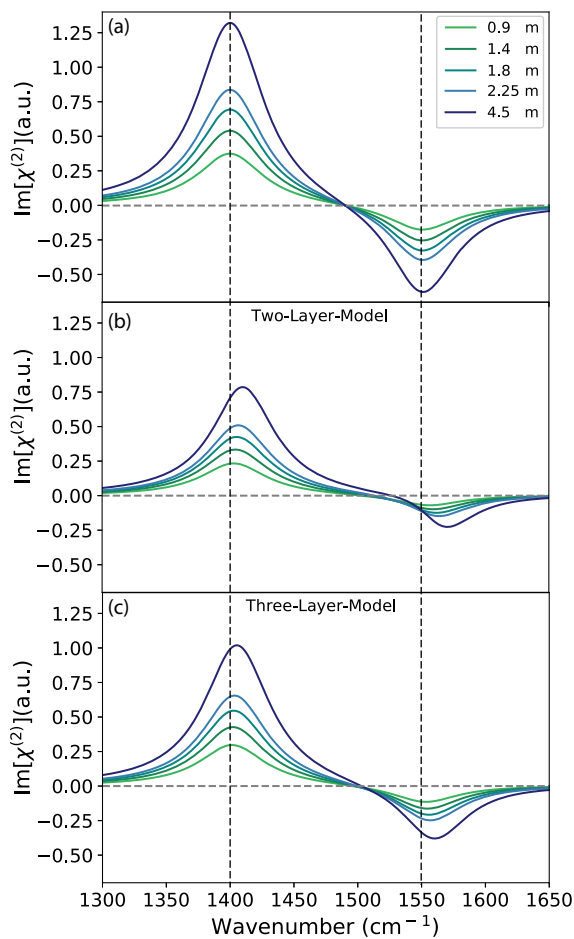


FIGURE 6.8. Calculated effect of the Fresnel factors on the $\text{Im}[\chi^{(2)}]$ spectra of ν_s and ν_{as} vibrations of the carboxylate group for different concentrations. Figure (a) represents the responses without Fresnel effects, Figure (b) the responses calculated with the two-layer model, and Figure (c) the responses calculated with the three-layer model.

We model the effect of the Fresnel factors on the measured $\text{Im}[\chi^{(2)}]$ responses of the ν_s and ν_{as} vibrations of the carboxylate group for acetate for different concentrations. We use two different models: the two-layer model and the three-layer model.^{70,157} Comparing the results of the two models with the experimental data we conclude that the two-layer model is overestimating the effects of the concentration- dependent Fresnel factors, while the three-layer model provided an accurate description of the experimentally observed shifts of the vibrational responses.



7 BULK RESPONSE OF CARBOXYLIC ACID SOLUTIONS OBSERVED WITH SURFACE SUM-FREQUENCY GENERATION SPECTROSCOPY

We study the molecular properties of aqueous acetic acid and formic acid solutions with heterodyne-detected vibrational sum-frequency generation spectroscopy (HD-VSFG). For acid concentrations up to ~ 5 M, we observe a strong increase of the responses of the acid hydroxyl and carbonyl stretch vibrations with increasing acid concentration, due to an increase of the surface coverage by the acid molecules. At acid concentrations > 5 M we observe first a saturation of these responses and then a decrease. For pure carboxylic acids we even observe a change of sign of the $\text{Im}[\chi^{(2)}]$ response of the carbonyl vibration. The decrease of the response of the hydroxyl vibration and the decrease and sign change of the response of the carbonyl vibration indicate the formation of cyclic dimers, that only show a quadrupolar bulk response in the HD-VSFG spectrum because of their anti-parallel conformation. We also find evidence for the presence a quadrupolar response of the CH vibrations of the acid molecules.

7.1 INTRODUCTION

Carboxylic acids have attracted significant attention in atmospheric chemistry in the past decades, as they are the most abundant oxygenated compounds in the atmosphere and form a major contributor to free acidity in precipitation.^{39,158} Interactions of atmospheric inorganic and organic species, including carboxylic acids, play a major role in many environmental processes and are thus important in the study of climate change. Furthermore, carboxylic acids are also commonly associated with atmospheric corrosion of metal surfaces. Within the corrosion process corrosive gases like formic acid (FA) and acetic acid (AA) penetrate a thin layer of water that covers the metal, and subsequently oxidize and damage the metal.^{159,160} Therefore, the understanding of chemical processes at surfaces, as the adsorption behavior of carboxylic acids is of great importance to atmospheric and surface chemistry.¹⁶¹ Beside surface tension measurements¹⁶², atomic force microscopy (AFM)¹⁶³, Raman scattering (SERS)¹⁶⁴ and X-ray photoelectron spectroscopy (XPS)¹⁶¹, vibrational sum frequency generation spectroscopy (VSFG) is a powerful tool as a probe for microscopic structures at interfaces.^{70,73} VSFG is highly surface sensitive and surface selective, because VSFG is based on the second-order polarization of the system, which is prohibited in centrosymmetric media and therefore in most bulk phases. Recently, many studies challenged this basic understanding of VSFG and demonstrated that sum-frequency light can also be generated by a bulk quadrupolar response.^{37,70,85,127,165} Clearly, the presence of such a response influences the surface selectivity and interpretation of VSFG spectra.^{70,85,165} Previous intensity VSFG measurements of aqueous FA and AA show that vibrational responses of the CH, OH and C=O vibration of acid molecules at the surface can already be observed at low concentrations (0.3 mol %).^{13,166,167} These studies also reported that these spectral responses change in shape upon increasing the concentration, which was explained from the formation of complexes of acid molecules, such as the hydrated monomer, the linear dimer, and the cyclic dimer. Here, we investigate the properties of FA and AA molecules at the surface of aqueous solutions with heterodyne detected vibrational sum-frequency generation (HD-VSFG). The signal measured with this technique is directly proportional to the complex second-order susceptibility $\chi^{(2)}$, whereas the signal probed in intensity VSFG is proportional to $|\chi^{(2)}|^2$. As a result, HD-VSFG provides unique information about the orientation of the molecular groups of the acid molecules at different concentrations and, as the signal is proportional to $\chi^{(2)}$ instead of $|\chi^{(2)}|^2$, enables the detection of low-concentration species that in intensity VSFG measurements are overwhelmed by the response of the dominant species. By varying the acid concentration, we demonstrate the presence of both a surface dipolar contribution and a bulk quadrupolar contribution to the responses of the C=O and CH vibrations.

7.2 EXPERIMENTAL METHODS

SAMPLE PREPARATION For all measurements we used water from a Millipore Nanopure system (18,2 M Ω cm). Acetic acid (99.8%) and formic acid (98%) are purchased from Sigma Aldrich and are used without further purification. The acid solutions were prepared by thorough mixing of H₂O with the appropriate amount of acid.

SPECTROSCOPY The VSFG measurements described in this chapter are performed with the setup described in section 3.1.

7.3 RESULTS AND DISCUSSION

In Figures 7.1 (a,b) and 7.2 (a,b) the experimental Im[$\chi^{(2)}$] spectra of aqueous AA and FA solutions at different concentrations in the frequency region 2850 - 3700 cm⁻¹ are presented. For AA the concentration ranges from 0.5 M to 17.5 M (pure) and for FA from 0.5 M to 26.5 M (pure). At all concentrations the Im[$\chi^{(2)}$] spectra of the AA solutions show a narrow negative feature at 2935 cm⁻¹ which we assign to the symmetric stretch vibration of the methyl group ($\nu_{CH_3,SS}$) of the AA molecule. In addition, the spectra show a narrow positive band at 2970 cm⁻¹ which we assign to the antisymmetric stretch vibration of the methyl group ($\nu_{CH_3,AS}$).^{13,168} For FA the Im[$\chi^{(2)}$] spectra show a single negative band in the CH region centered at 2910 cm⁻¹, which we assign to the stretch vibration of the methine group (ν_{CH}) of the FA molecule.¹⁶⁷ The signs of the Im[$\chi^{(2)}$] responses of the $\nu_{CH_3,SS}$ and $\nu_{CH_3,AS}$ vibrations of AA and the ν_{CH} of FA indicate that both molecules are oriented at the water surface with their CH bonds pointing toward the air phase.³² For pure FA we observe that the band of the methine group (ν_{CH}) is shifted ~ 15 cm⁻¹ to higher frequencies in comparison to aqueous solutions of FA, in agreement with the results of a previous study of Johnson *et al.*¹⁶⁷

The Im[$\chi^{(2)}$] spectra for the AA and the FA solutions further show a broad band between 3000 and 3700 cm⁻¹ that changes sign at a frequency of ~ 3450 cm⁻¹. In previous intensity VSFG studies this response has been assigned to a low-frequency band centered at ~ 3060 cm⁻¹ and a positive band centered at ~ 3600 cm⁻¹, which were assigned to the OH stretch vibrations of strongly hydrogen-bonded OH groups of the carboxylic acids, and to the OH stretch vibration of weakly hydrogen-bonded water molecules, respectively.¹³ The Im[$\chi^{(2)}$] spectra in Figure 7.1 (a,b) and 7.2 (a,b) show that in fact there exists a single broad distribution of OH stretch frequencies that gives rise to two separate bands in the intensity VSFG spectrum because of the zero-crossing at ~ 3450 cm⁻¹. The broad OH response represents OH stretch vibrations of both acid and water molecules.¹⁶⁸ These vibrations are likely mixed and delocalized, but it is to be expected that the low-frequency OH vibrations are dominated by strongly hydrogen-bonded OH groups of the acid molecules while the high-frequency OH vibrations show a dominant contribution of the OH stretch vibrations of weakly hydrogen-bonded water molecules.^{13,168} At low carboxylic acid concentrations in Figure 7.1 (a) and 7.2 (a) an additional negative band

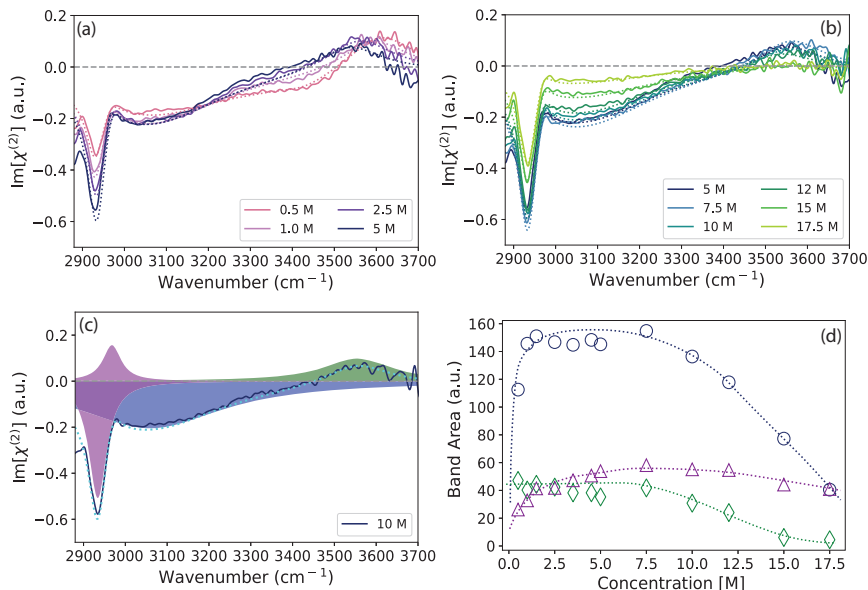


FIGURE 7.1. $\text{Im}[\chi^{(2)}]$ spectra of aqueous solutions containing different concentrations of AA (a) in the range of 0.5 M to 5 M and (b) in the range of 5 M to 17.5 M (pure AA) in the frequency region of 2850 - 3700 cm^{-1} . Figure (c) shows the decomposed spectra of a 10 M AA solution with four Lorentzian bands centered at 2935 cm^{-1} , 2970 cm^{-1} , 3060 cm^{-1} and 3600 cm^{-1} describing the symmetric ($\nu_{\text{CH}_3,SS}$) and antisymmetric ($\nu_{\text{CH}_3,AS}$) stretch vibrations (magenta), the OH stretch vibrations of the strongly (blue) hydrogen bonded AA molecules and the weakly hydrogen bonded water molecules (green), respectively. Figure (d) shows the absolute area of these bands extracted from the fitting procedure as a function of acid concentration.

centered at 3450 cm^{-1} is observed that vanishes with increasing acid concentration. This band is assigned to the OH stretch vibrations of hydrogen-bonded neat water molecules, in agreement with VSFG studies of the neat water surface.^{32,169–171} For FA at low acid-concentrations in Figure 7.2 (a) additionally a sharp feature at 3700 cm^{-1} is observed, which vanishes when the acid concentration is increased. This band is assigned to the OH stretch vibrations of non-hydrogen bonded OH groups of the neat water surface that stick out of the surface.^{16,172} Further, we observe for both AA and FA a positive response near $\sim 3600 \text{ cm}^{-1}$ that we assign to weakly hydrogen-bonded OH groups and that red-shifts with increasing acid concentration. This red-shift can be explained from the strengthening of the hydrogen bonds between the water and acid molecules with increasing acid concentration.

To analyze the $\text{Im}[\chi^{(2)}]$ quantitatively, we decompose the measured responses at different acid concentrations into several Lorentzian bands. For AA we decompose the $\text{Im}[\chi^{(2)}]$ into four Lorentzian bands centered at 2935 cm^{-1} , 2970 cm^{-1} , 3060 cm^{-1} and 3600 cm^{-1} , describing the symmetric ($\nu_{\text{CH}_3,SS}$) and antisymmetric ($\nu_{\text{CH}_3,AS}$) stretch vibration of the methyl group, and the low-

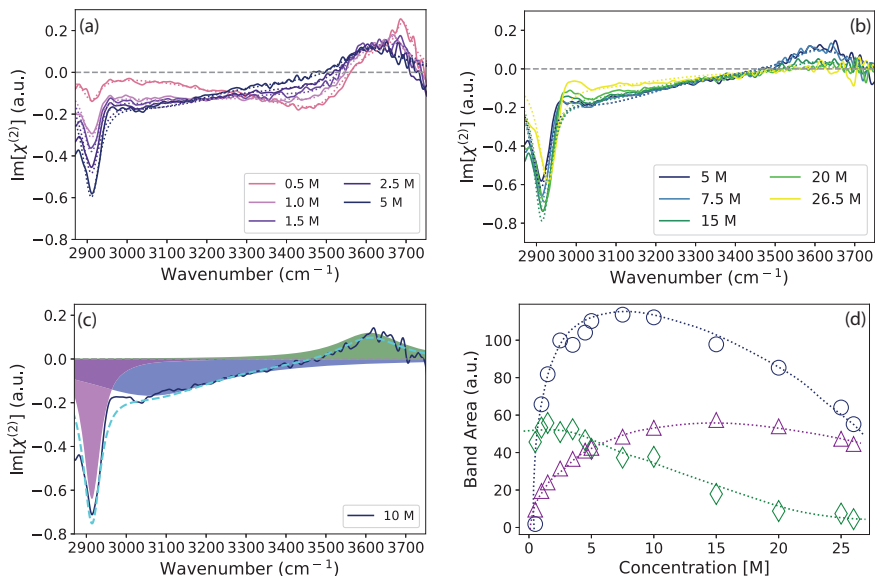


FIGURE 7.2. $\text{Im}[\chi^{(2)}]$ spectra of aqueous solutions containing different concentrations of FA (a) in the range of 0.5 M to 7.5 M and (b) in the range of 7.5 M to 26.5 M (pure FA) in the frequency region of 2850 - 3750 cm^{-1} . Figure (c) shows the decomposed spectra of FA with three Lorentzian bands centered at 2910 cm^{-1} , 3060 cm^{-1} and 3600 cm^{-1} describing the CH stretch vibration of the methine group (magenta) and the OH stretch vibrations of the strongly (blue) and weakly (green) hydrogen bonded FA molecules. Figure (d) shows the absolute area of these bands extracted from the fitting procedure as a function of acid concentration.

and high-frequency part of the OH stretch vibrations, respectively (Figure 7.1 (c,d)). For FA we decompose the $\text{Im}[\chi^{(2)}]$ spectra at different concentrations in three Lorentzian bands, centered at 2910 cm^{-1} , 3060 cm^{-1} and 3600 cm^{-1} , representing the stretch vibration of the methine group (ν_{CH}) and the low- and high-frequency part of the OH stretch vibrations, respectively (Figure 7.2 (c,d)). For both AA and FA we added an additional asymmetric Lorentzian curve centered at 3450 cm^{-1} to represent the response of the hydrogen-bonded OH stretch vibrations of the neat water surface. For FA we added further a narrow Lorentzian band centered at 3700 cm^{-1} representing the response of the OH stretch vibrations of non-hydrogen bonded OH groups of the neat water surface. In the decomposition we keep the widths of all Lorentzian bands constant and allow only the amplitudes of the bands to change with the acid concentration. The bands of the symmetric and antisymmetric vibrations of the methyl group of AA are highly correlated and we used a single parameter to represent their amplitudes in the fitting procedure. The resulting fits of the $\text{Im}[\chi^{(2)}]$ are shown in Figures 7.1 (a,b) and 7.2 (a,b) with dashed lines, and are presented in more detail in the Appendix (Figure 7.5(a-j) and Figure 7.6(a-j)). As an example we show in Figure 7.1 (c) and Figure 7.2 (c) the decomposition

of the $\text{Im}[\chi^{(2)}]$ spectrum of an AA and a FA solution with a concentration of 10 M.

In Figure 7.1 (d) and 7.2 (d) we present the areas of the vibrational modes extracted from the fitting procedure as a function of acid concentration. For the symmetric and antisymmetric vibrations of the methyl group of AA, the area shown is the sum of the absolute areas of the two bands. For both AA and FA we observe that the areas of the CH bands (magenta) increase with increasing concentration up to concentrations of 7.5 M for AA and 15 M for FA and then start to decrease. The initial increase of the areas of the CH bands can be well explained from the increasing surface coverage by the acid molecules. This interpretation is supported by surface tension measurements and calculations.^{162,166,173} For acetic acid solutions the surface tension strongly decreases with increasing acid concentration, which shows that the concentration of acetic acid molecules at the surface is enhanced in comparison to its bulk contribution. The surface mole fraction of acetic acid can be obtained from the concentration dependence of the surface tension and accounting for the surface areas of the water and acetic acid molecules.¹⁶⁶ The response of the CH vibrations saturates at a higher acid concentration for FA than for AA, which can be explained from the fact that the FA molecules are less hydrophobic than the AA molecules and therefore less surface active. For the low-frequency OH band we observe a steep increase up to a concentration of 5 M for AA and 7.5 M for FA. This increase also follows from the increasing accumulation of acid molecules at the surface. This accumulation enhances the average strength of the hydrogen-bond interactions due to the strong hydrogen-bond donating character of the acid hydroxyl group. In addition, the degree of orientation with respect to the surface normal of the strongly hydrogen-bonded OH groups will be enhanced with increasing concentration of acid molecules at the surface, as these acid molecules have a distinct preferential orientation of their OH groups toward the bulk. Above concentrations of 7.5 M for AA and 12 M for FA, the low-frequency OH band is observed to decrease with increasing acid concentration. The origin of this decrease will be discussed later. For both AA and FA the area of the high-frequency OH band (green) is constant up to a concentration of ~ 5 M, and then decreases until it completely vanishes for the pure acid. The fact that the area of the band remains constant up to ~ 5 M does not mean that the number density of high-frequency OH oscillators remains constant. For concentrations up to ~ 5 M the high-frequency OH band is also observed to shift to lower frequencies, which implies a strengthening of the hydrogen bonds of the OH groups. Hence, the constant area of this band while red-shifting in fact implies that the number density of high-frequency OH oscillators decreases. The high-frequency OH response is dominated by weakly hydrogen water molecules, and the decrease of the number density can thus be well explained from the decrease of the amount of water in the solution with increasing acid concentration.

To acquire a complete understanding of the molecular properties at the surface we also studied the response in the frequency region of the C=O stretch vibration of AA and FA. Figure 7.3 (a) and Figure 7.4 (a) show the experimental $\text{Im}[\chi^{(2)}]$ spectra (measured in SSP polarization configuration) of aqueous AA and FA solutions at different concentration in the frequency region of 1600

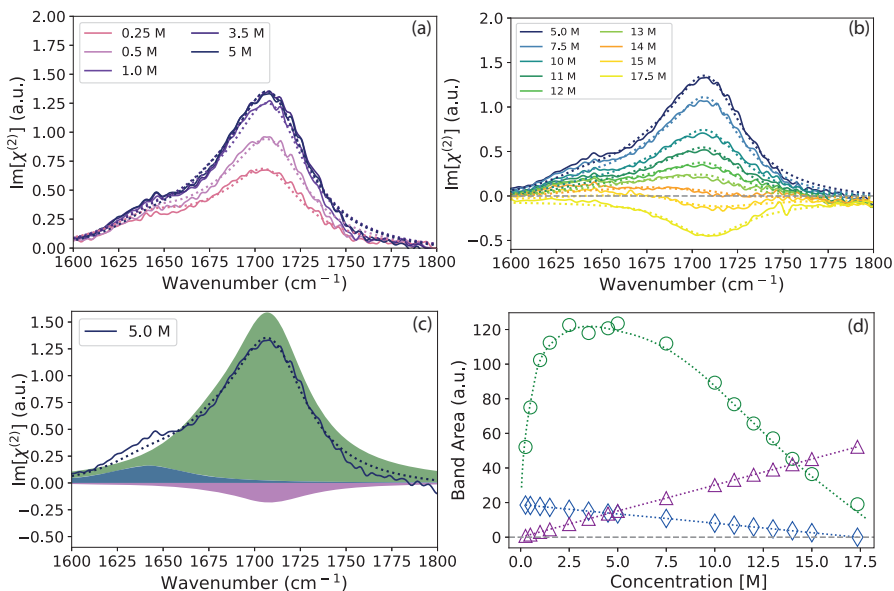


FIGURE 7.3. $\text{Im}[\chi^{(2)}]$ spectra of aqueous solutions containing different concentrations of AA (a) in the range of 0.5 M to 5 M and (b) in the range of 5 M to 17.5 M (pure AA) in the frequency region of 1600 - 1800 cm^{-1} . Figure (c) shows the decomposed spectra of AA with three Lorentzian bands centered at 1650 cm^{-1} , 1707 cm^{-1} , and 1712 cm^{-1} describing the water bending mode (blue), the dipolar response of the C=O vibration (green) and the quadrupolar response of the C=O vibration (magenta). Figure (d) shows the absolute area of these bands extracted from the fitting procedure as a function of acid concentration.

- 1800 cm^{-1} . For AA the concentration is ranging from 0.5 M to 5 M AA and for FA from 0.5 M to 7.5 M. For both AA and FA the $\text{Im}[\chi^{(2)}]$ spectrum shows a positive band centered at 1707 cm^{-1} with a shoulder centered at 1650 cm^{-1} . The band at 1707 cm^{-1} increases with increasing acid concentration and is assigned to the C=O stretch vibration of the acid molecules. The increase of the vibrational band of the C=O group is similar to the increase of the response of the CH vibrations shown in Figure 7.1 (a,b) and Figure 7.2 (a,b). The positive sign of the $\text{Im}[\chi^{(2)}]$ response of the C=O stretch vibration indicates that the positive charge of the C=O group is closer to the surface than the negative charge, which implies that the C=O group points with its oxygen atom toward the bulk.^{85,131,174} This finding is in agreement with the observation that the methyl group of AA and the methine group of FA are oriented toward the air. The $\text{Im}[\chi^{(2)}]$ spectrum of the neat water surface shows a vibrational response centered at 1650 cm^{-1} (Chapter 4) that is assigned to the water bending mode. Therefore, we explain the shoulder at 1650 cm^{-1} that is observed in the spectra of Figure 7.3 and 7.4, to the response of the water bending mode.^{33-35,37,127,167} The assignment is supported by measurements of AA and FA in D_2O solution that show that the band at 1650 cm^{-1} vanishes (Appendix Figure 7.7 and Fig-

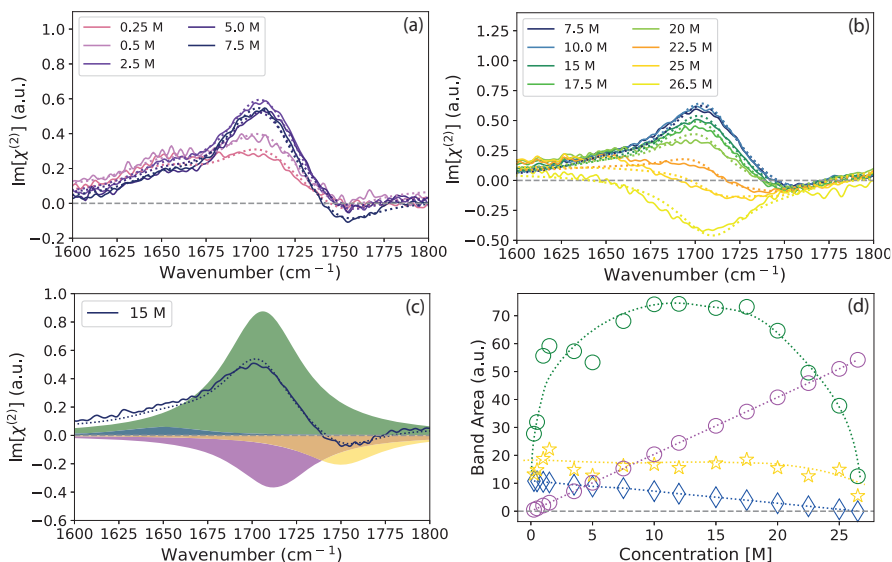


FIGURE 7.4. The $\text{Im}[\chi^{(2)}]$ spectra of aqueous solutions containing different concentrations of FA (a) in the range of 0.5 M to 7.5 M and (b) in the range of 7.5 M to 26.5 M (pure FA) in the frequency region of 1600 - 1800 cm^{-1} . Figure (c) shows the decomposed spectra of FA with four Lorentzian bands centered at 1650 cm^{-1} , 1707 cm^{-1} , 1712 cm^{-1} and the response of the linear FA dimers (yellow) describing the water bending mode (blue), the dipolar response of the C=O vibration (green), the quadrupolar response of the C=O vibrations (magenta) and the response of the linear FA dimers (yellow). Figure (d) shows the absolute area of these bands extracted from the fitting procedure as a function of acid concentration.

ure 7.8). With increasing acid concentration the band at 1650 cm^{-1} decreases due to the decrease in water content within the solution. For FA we observe an additional negative band centered at 1750 cm^{-1} , which we assign to the vibrational response of non-hydrogen bonded carbonyl groups.^{13,175–177} In Figure 7.3 (b) and Figure 7.4 (b) we present $\text{Im}[\chi^{(2)}]$ spectra of aqueous AA and FA solutions at even higher concentrations. The concentration of AA is ranging from 5 M to 17.5 M (pure AA), and the concentration of FA ranges from 7.5 M to 26.5 M (pure FA). We observe that in this concentration range the positive band of the C=O vibration decreases and changes sign.

To analyze the spectra quantitatively we decompose the $\text{Im}[\chi^{(2)}]$ spectra into Lorentzian bands. For AA we decompose the $\text{Im}[\chi^{(2)}]$ into three Lorentzian bands at 1650 cm^{-1} , 1707 cm^{-1} , and 1712 cm^{-1} (Figure 7.3 (c,d)). For FA we decompose the experimental $\text{Im}[\chi^{(2)}]$ spectra into four Lorentzian bands (Figure 7.4 (c,d)), representing the same responses as for AA and an additional band centered at 1750 cm^{-1} . We keep the widths of all Lorentzian bands constant and only allow the amplitude of the different contributions to change with acid concentration. The resulting fits are shown in Figure 7.3 (a,b) and Figure 7.4

(a,b) with dashed lines, and are presented in more detail in the Appendix (Figures 7.9 (a-j) and 7.10 (a-j)). As an example we show in Figure 7.3 (c) and Figure 7.4 (c) the fitted decomposition of the $\text{Im}[\chi^{(2)}]$ of an AA solution at a concentration of 11 M and of an FA solution at a concentration of 15 M. In Figures 7.3 (d) and 7.4 (d) we present the areas of the vibrational modes extracted from the fitting procedure as a function of the acid concentration. With increasing acid concentration the area of the response of the C=O vibration at 1707 cm^{-1} (green) first increases, for AA up to a concentration of 2.5 M and for FA up to a concentration of 7.5 M. Increasing the concentration further leads to a decrease of this band. The decrease and vanishing of the positive response of the C=O vibrations at higher concentrations is in good agreement with the results of Johnson *et al.*¹³, and can be explained by the formation of cyclic AA dimers.^{13,178} Cyclic dimers are centrosymmetric and therefore do not show a dipolar vibrational SFG response. This formation of cyclic dimers also explains why we observed a decrease of the low-frequency OH band at concentrations $>5\text{ M}$ for AA and $>7.5\text{ M}$ for FA.

The positive C=O band not only decreases but even changes sign at concentrations $>14\text{ M}$ for AA and $>22.5\text{ M}$ for FA. This sign change can be well accounted for by including in the fitting a negative band centered at 1712 cm^{-1} of which the amplitude increases with concentration. This band can be assigned to the quadrupolar response of the carbonyl vibration. This negative response becomes visible when the strong positive dipolar band of the carbonyl vibration vanishes as a result of the formation of cyclic dimers. In a cyclic dimer the two carbonyl vibrations have a nearly perfect anti-parallel arrangement, meaning that the dipolar response vanishes, thus leaving only the quadrupolar response of the C=O vibrations.⁸⁵ A detailed description of the quadrupolar response of molecular vibrations can be found in Refs.^{70,165,179–182} As the quadrupolar response of a particular vibration is not surface specific, its amplitude is expected to be proportional to the bulk concentration of that vibration. Therefore, in the fitting we assume that the amplitudes of the C=O band at 1712 cm^{-1} and the water bending mode at 1650 cm^{-1} , which also represents a quadrupolar response^{37,127}, are directly proportional to the (bulk) concentrations of acid and water molecules, respectively. The area of the band at 1750 cm^{-1} is more or less constant throughout the whole concentration series. This band has been assigned to the response of non-hydrogen-bonded carbonyl groups,^{13,175–177} and is probably associated with linear FA dimers, which would imply that the concentration of linear dimers would be independent from the FA concentration.

In view of the observations in the frequency region of the C=O vibrations showing the formation of cyclic dimers at higher acid concentration, it is surprising that the responses of the CH vibrations of the methyl group of AA and of the methine group of FA do not strongly decrease at high acid concentrations. In cyclic acid dimers the CH groups of the acid molecules are arranged in an anti-symmetric manner, which implies that the dipolar response of these vibrations is expected to vanish. There are two possible reasons why the response of the CH vibrations does not vanish due to the formation of cyclic dimers. The first is that even though the molecular structure of the cyclic dimers is centrosymmetric, the two aliphatic parts of the cyclic dimer can be in quite dif-

ferent molecular environments, one part being much closer to the surface than the other part. Hence, on the molecular scale the symmetry of the methyl and methine may still be broken which would imply that the dipolar response of the CH vibrations does not vanish.¹³ A second explanation is that the responses of the methyl and the methine groups show a quadrupolar bulk contribution that is not affected by the formation of cyclic dimers.^{165,180} Here, a clear difference with the carbonyl vibration is that for the CH vibrations the quadrupolar response is not of opposite sign to the dipolar response. As a result, for the CH vibrations the vanishing of the dipolar response only leads to a decrease of their $\text{Im}[\chi^{(2)}]$ response whereas for the C=O vibrations the vanishing of the dipolar response leads to a sign change of their $\text{Im}[\chi^{(2)}]$ response.

The central frequency of 1712 cm^{-1} of the quadrupolar response of the carbonyl vibration is slightly higher than the central frequency of 1707 cm^{-1} of the dipolar response of this vibration. This difference may be due to the difference in hydrogen-bond configuration between a cyclic dimer and a hydrated monomer. However, this frequency difference may also result from the change of the frequency-dependent refractive index of the solution upon increasing acid concentration, as this will lead to a change of the Fresnel factors. To investigate a potential effect of the concentration dependence of the Fresnel factors, we modeled the sum-frequency response of the carboxyl group using the three-layer-model combined with the Lorentz model to estimate the refractive index of the interfacial layer (Appendix Figure 7.11). A more detailed description of the model and the derivation of the Fresnel factors can be found elsewhere.^{70,73,157} We find that at higher acid concentrations the Fresnel factors of the infrared light become frequency dependent, resulting in an enhancement of the high-frequency wing of the response of the carbonyl vibration. Therefore, the frequency of the maximum of the carbonyl vibration will shift to higher frequencies with increasing acid concentration, even if the intrinsic vibrational frequency itself would not change. In the fitting procedure the optimal frequency of maximum response of the dipolar component will be dominated by the spectra measured at low acid concentrations, while the optimal frequency of maximum response of the quadrupolar response is governed by the spectra measured at high acid concentrations. Hence, the difference of $\sim 5\text{ cm}^{-1}$ between the central frequencies of the fitted dipolar and quadrupolar responses can indeed be due to the change of the Fresnel factors with acid concentration.

7.4 CONCLUSIONS

We performed heterodyne-detected vibrational sum frequency generation (HD-VSFG) measurements of aqueous acetic acid (AA) and formic acid (FA) solutions over a broad concentration range. In the frequency region from 2850 - 3700 cm^{-1} we find for both AA and FA solutions that the measured $\text{Im}[\chi^{(2)}]$ spectra show an increase of the bands in the CH region with increasing acid concentration, which can be explained from the increase in surface coverage by the acid molecules. The OH vibrations of the acid and the water molecules give rise to a broad response between 3000 cm^{-1} and 3700 cm^{-1} of which the $\text{Im}[\chi^{(2)}]$ response changes sign at a frequency of $\sim 3450 \text{ cm}^{-1}$. The amplitude of this band first increases with increasing acid concentration but starts to decrease for concentrations $>5 \text{ M}$ for AA and $>7.5 \text{ M}$ for FA, which can be explained from the formation of cyclic dimers. In cyclic dimers the vibrations of the acid monomers have a near-perfect anti-parallel arrangement which cancels the dipolar sum-frequency generation response of these vibrations. In the frequency region from 1600 - 1800 cm^{-1} we observe a similar initial increase and subsequent decrease for the C=O stretch vibration of AA and FA at 1707 cm^{-1} as for the broad O-H stretch vibrational response of these acids, which can be explained again from the formation of cyclic dimers. We observe that the band at 1707 cm^{-1} decreases and even changes sign at high acid concentrations. This sign change can be well explained from the presence of a band at 1712 cm^{-1} which has a negative $\text{Im}[\chi^{(2)}]$ response and that rises proportional to the bulk acid concentration. This band is assigned to the quadrupolar bulk response of the C=O stretch vibrations. The difference between the fitted frequency of maximum quadrupolar response and the fitted frequency of maximum dipolar response may originate from the difference in hydrogen-bond configuration between a cyclic acid dimer and a hydrated monomer, but can also be due to concentration-dependent Fresnel effects, as these effects enhance the high-frequency wing of the response at higher concentrations.

Finally, we find that at high acid concentrations the vibrational responses of the CH vibrations saturate but do not strongly decrease. This indicates that even in cyclic dimers the response of the CH groups of formic acid and acetic acid does not vanish because the two aliphatic parts of the cyclic acid dimer are in quite different molecular environments, or because the response of the CH vibrations contains a quadrupolar contribution that is of the same sign as the dipolar response. The present observation of a quadrupolar bulk component in the VSFG responses of the C=O vibration, and possibly in the VSFG response of the CH vibrations, implies that the probing of liquids via VSFG spectroscopy of these vibrations is likely not as surface specific as up to now has been assumed.

7.5 APPENDIX

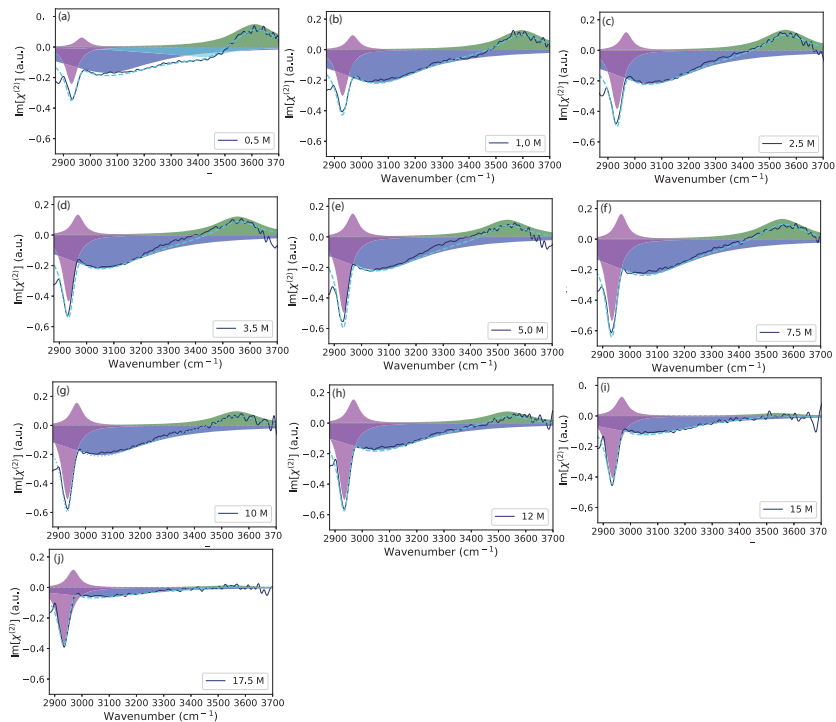


FIGURE 7.5. The decomposed $\text{Im}[\chi^{(2)}]$ spectra of aqueous AA solutions with different concentrations in the range of 0.5 M - 17.5 M. In (a) the $\text{Im}[\chi^{(2)}]$ spectra are decomposed in five Lorentzian bands centered at 2935 cm^{-1} , 2970 cm^{-1} , 3060 cm^{-1} , 3600 cm^{-1} and 3450 cm^{-1} describing the symmetric and antisymmetric stretch vibrations of the methyl group (magenta), the OH stretch vibrations of the strong hydrogen bonded AA molecules (blue), the weakly OH stretch vibrations of the water molecules (green) and the hydrogen-bonded OH stretch vibrations of the water molecules at the neat water surface (cyan), respectively. In Figure 7.5 (d-j) the $\text{Im}[\chi^{(2)}]$ spectra are decomposed in only four Lorentzian bands, as the vibrational response of the the hydrogen-bonded OH stretch water molecules of the neat water surface are vanishing.

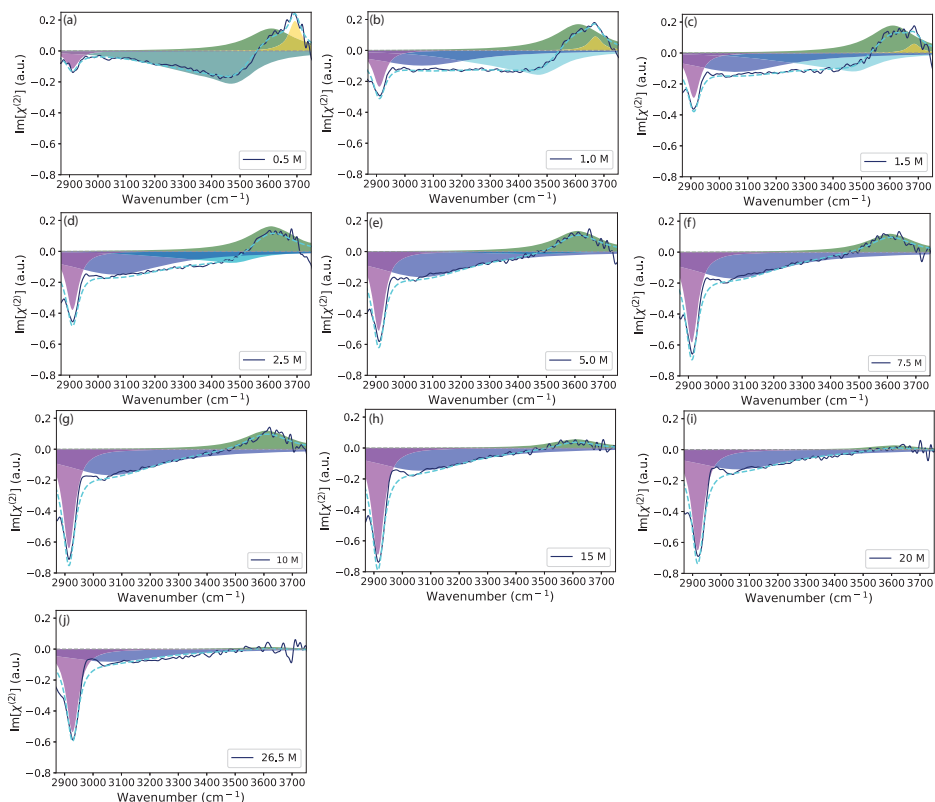


FIGURE 7.6. The decomposed $\text{Im}[\chi^{(2)}]$ spectra of FA with different concentrations in the range of 0.5 M - 26.5 M. In (a-d) the $\text{Im}[\chi^{(2)}]$ spectra are decomposed in five Lorentzian bands centered at 2910 cm^{-1} , 3060 cm^{-1} , 3600 cm^{-1} , 3450 cm^{-1} and 3700 cm^{-1} describing the stretch vibrations of the methine group (magenta), the OH stretch vibrations of the strong hydrogen-bonded OH groups of the acid molecules (blue) and of the weakly hydrogen-bonded water molecules (green), the OH stretch of the hydrogen-bonded (cyan) and the non hydrogen-bonded (yellow) water molecules of the neat water surface, respectively. In Figure 7.6 (b-j) the $\text{Im}[\chi^{(2)}]$ spectra are decomposed in only three Lorentzian bands, as the vibrational response of the hydrogen-bonded and the non hydrogen-bonded OH stretch vibrations of the water molecules at the neat water surface are vanishing.

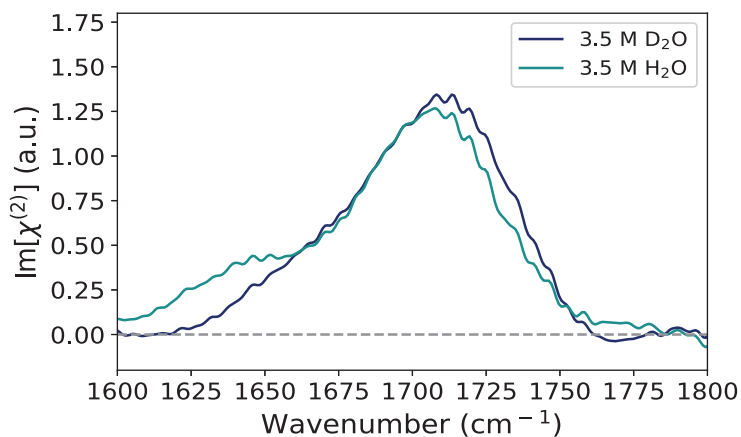


FIGURE 7.7. $\text{Im}[\chi^{(2)}]$ spectrum of aqueous AA solutions with a concentration of 3.5 M in D_2O and H_2O .

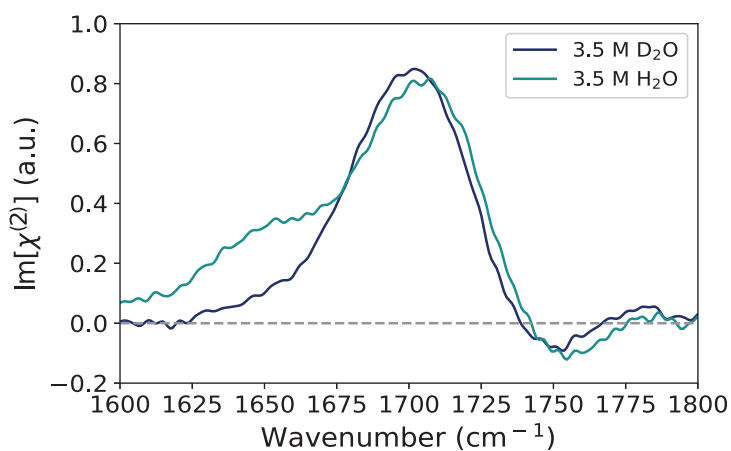


FIGURE 7.8. $\text{Im}[\chi^{(2)}]$ spectrum of aqueous FA solutions with a concentration of 3.5 M in D_2O and H_2O .

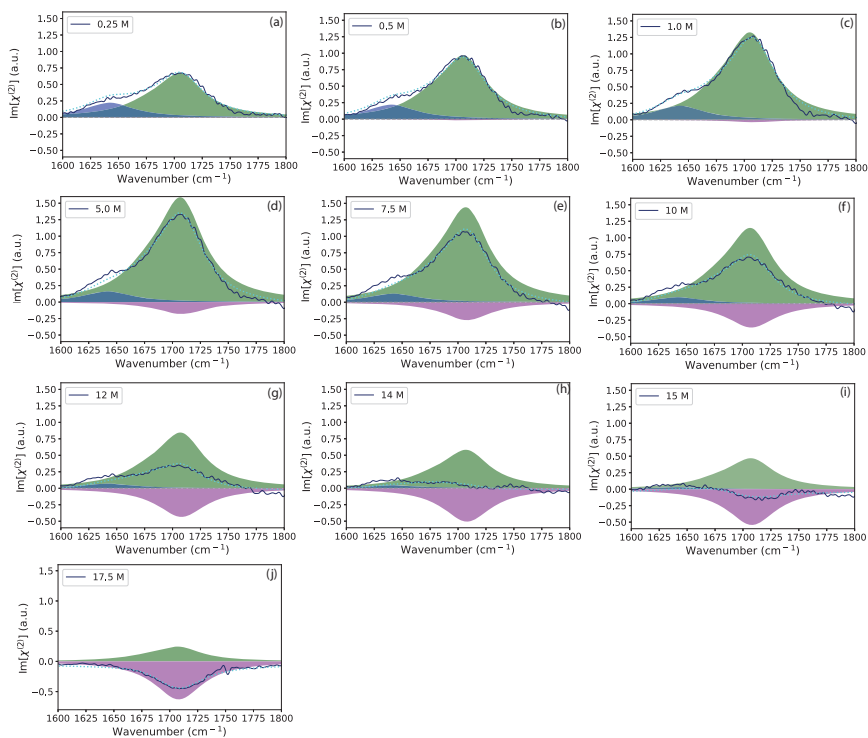


FIGURE 7.9. The decomposed spectra of aqueous AA solution with three Lorentzian bands centered at 1650 cm^{-1} , 1707 cm^{-1} and 1712 cm^{-1} at different concentrations describing the water bending mode (blue), the symmetric stretch vibrations of the C=O (green), the quadrupolar contribution of the C=O vibrations (magenta).

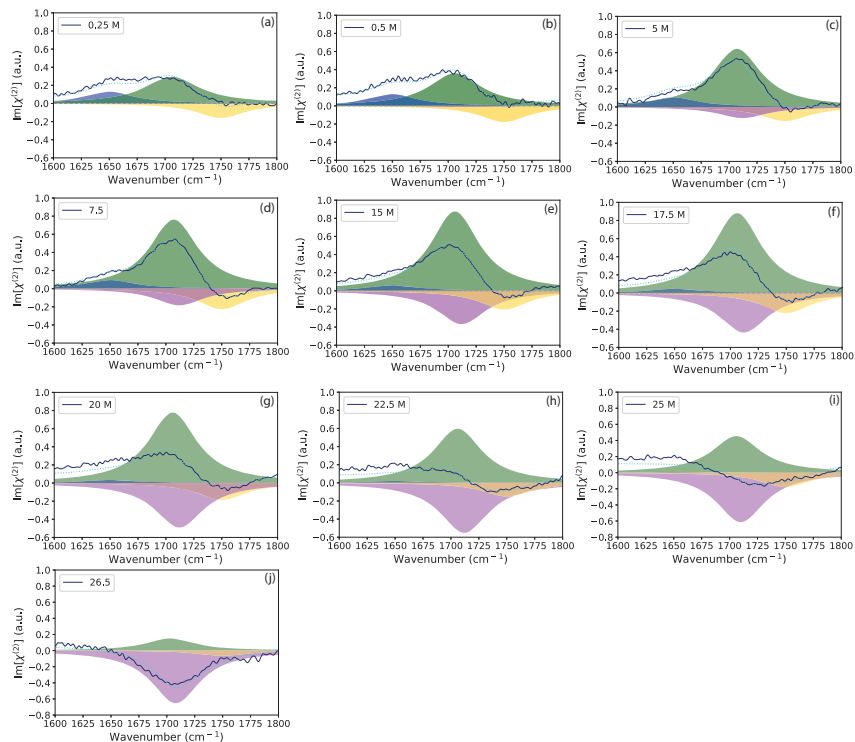


FIGURE 7.10. The decomposed spectra of FA with four Lorentzian bands centered at 1650 cm^{-1} , 1707 cm^{-1} , 1712 cm^{-1} and 1750 cm^{-1} at different concentrations describing the water bending mode (blue), the symmetric stretch vibrations of the C=O (green), the quadrupolar contribution of the C=O vibrations (magenta) and the response of the linear FA dimers (yellow).

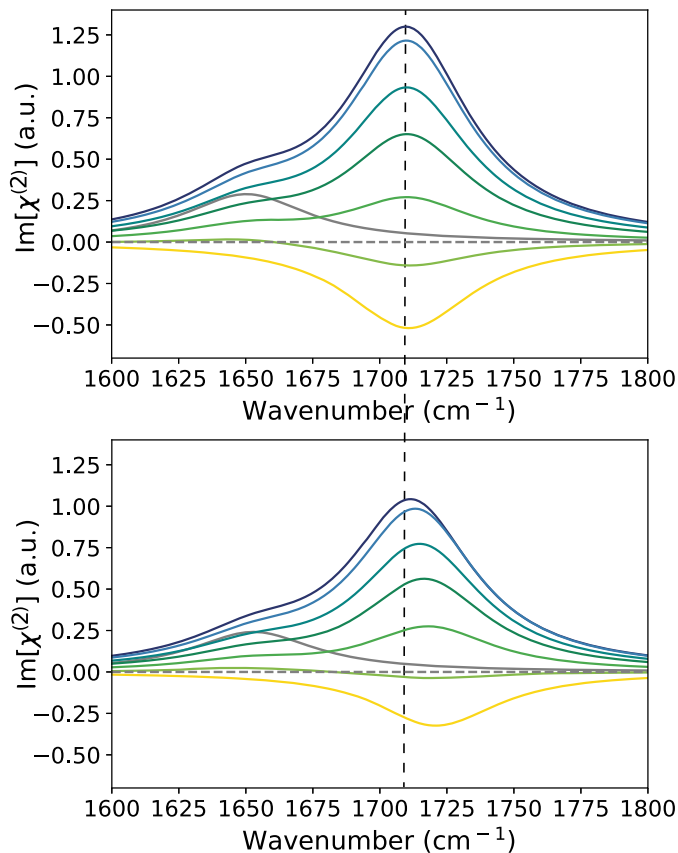


FIGURE 7.11. Modelling the effect of the Fresnel factors on the VSFG response of the carboxyl group for increasing concentrations including the water bending mode.

Here, we model the vibrational responses of the carboxyl group by implementing the effect of the Fresnel factors on the vibrational response at different concentrations using the three layer model combined with the Lorentz model to estimate the refractive index of the interfacial layer. Comparing the results of the model with the experimental data we conclude that the model is overestimating the effect on the frequency of the concentration dependent Fresnel factors slightly but gives a good impression that the change in the refractive index is responsible for the shift in frequency.



8 FREEZING OF AQUEOUS CARBOXYLIC ACID SOLUTIONS ON ICE

We study the properties of acetic acid and propionic acid solutions at the surface of monocrystalline ice with surface-specific vibrational sum-frequency generation (VSFG) and heterodyne-detected vibrational sum-frequency generation spectroscopy (HD-VSFG). When we decrease the temperature toward the eutectic point of the acid solutions, we observe the formation of a freeze concentrated solution (FCS) of the carboxylic acids that is brought about by a freeze-induced phase separation (FIPS). The freeze concentrated solution freezes on top of the ice surface as we cool the system below the eutectic point. We find that for freeze concentrated acetic acid solutions the freezing causes a strong decrease of the VSFG signal, while for propionic acid an increase and a blue-shift are observed. This different behavior points at a distinct difference in molecular-scale behavior when cooling below the eutectic point. We find that cooling of the propionic acid solution below the eutectic point leads to the formation of hydrogen-bonded dimers with an opposite alignment of the carboxylic acid OH groups.

8.1 INTRODUCTION

Carboxylic acids such as acetic acid (AA) or propionic acid (PA) are weak acids that consist of a hydrophilic carboxyl group and a hydrophobic alkyl chain. They are the most abundant oxygenated compounds in the atmosphere and form a major contributor to free acidity in precipitation.^{39,158} The interaction of atmospheric inorganic and organic species, including carboxylic acids with the surface of ice particles, plays an important role in the heterogeneous chemistry of clouds and is thus important in the study of climate change and other environmental issues. It is well-known that during freezing of atmospheric droplets, freeze-induced phase separation (FIPS) and the concomitant freeze concentration of the solutions (FCS) around ice particles occur. These phenomena have a great impact on the surface reactivity, on the physical and chemical properties of ice clouds, and therefore on the climate.^{183–186} Chemical processes occurring at ice surfaces are of great importance to atmospheric chemistry and have attracted significant attention in the past decade.^{39–42} Ice surfaces are known to act as sinks for pollutants, a process that considerably changes the properties of the ice surface.⁴³ Ice samples with impurities often contain a liquid solution phase that coexists with solid ice over a wide temperature range.^{183,187} It is important that at the interface of the ice surface and the liquid solution, chemical reactions and processes often show characteristics different from those seen in bulk liquid solutions.^{188,189} Here, we use conventional (VSFG) and heterodyne-detected vibrational sum-frequency generation spectroscopy (HD-VSFG) to investigate how atmospheric organic species such as AA and PA modify the structure and physical and chemical properties of the ice surface.

8.2 EXPERIMENTAL METHODS

SAMPLE PREPARATION The carboxylic acid solutions (40 wt %) are put on the ice surface by using a combination of a clean tissue and a plastic foil clamped in a tweezer. The tissue acts like a sponge to soak up the solution, and the plastic foil smooths the surface after the carboxylic acid is applied. With this technique, the AA and PA solutions are placed on the ice surface at temperatures of 265 K and 268 K, respectively. The applied layers have a thickness of several tens of nanometers, which implies that they are macroscopically thick on the molecular scale (containing many solution layers) but are sufficiently thin to avoid significant absorption and phase-change effects. To determine the influence of interference effects caused by the solution layer on top of the ice surface, we modeled the VSFG spectrum including these effects (Appendix Figure 8.7 (a–c)). From this modeling, we estimate the thickness of the AA solution on ice to be ~ 50 nm at 268 K and ~ 12 nm at 248 K. Similar values are obtained for the PA solution on ice. In addition, we used a cooling rate of ~ 1 K/min. Each measurement was taken 15 min after the temperature of interest was reached to allow the sample to equilibrate.

SPECTROSCOPY The VSFG measurements described in this chapter are performed with the setup described in section 3.1 and the preparation of the

monocrystalline ice samples is described in 3.3.

8.3 RESULTS

In Figure 8.1 we present the $|\chi^{(2)}|^2$ and the $\text{Im}[\chi^{(2)}]$ spectra of (a) aqueous 40 wt % AA and (b) PA solutions, measured with an ssp polarization configuration (s-SFG, s-VIS, p-IR). The presented $|\chi^{(2)}|^2$ spectra for AA and PA are in excellent agreement with the results obtained in previous studies.^{13,190,191} The $|\chi^{(2)}|^2$ spectrum of the AA solution spectrum shows a sharp peak at $\sim 2950\text{ cm}^{-1}$, which we assign to the symmetric methyl stretch vibration.¹³ The $|\chi^{(2)}|^2$ spectrum further shows a very broad signal with maxima at ~ 3080 and $\sim 3620\text{ cm}^{-1}$ that have been assigned to the OH stretch of the strong hydrogen-bonded OH groups of the carboxylic acids with the water molecules and to the OH stretch vibrations of weakly hydrogen-bonded water molecules, respectively.¹³ However, the $\text{Im}[\chi^{(2)}]$ spectrum reveals that in fact there exists only a single very broad distribution of OH stretch frequencies that appears as two separate responses in the $|\chi^{(2)}|^2$ spectrum because the sign of the signal changes at $\sim 3450\text{ cm}^{-1}$. The change of the sign within the broad band of OH stretch vibrations reveals that the orientation of the transition dipole moment, and therefore the orientation of the molecules, changes as a function of frequency. The PA solution spectrum looks very similar to the AA spectrum and only contains an additional signal at 2880 cm^{-1} that we assign to the CH stretch vibration of the methylene group.

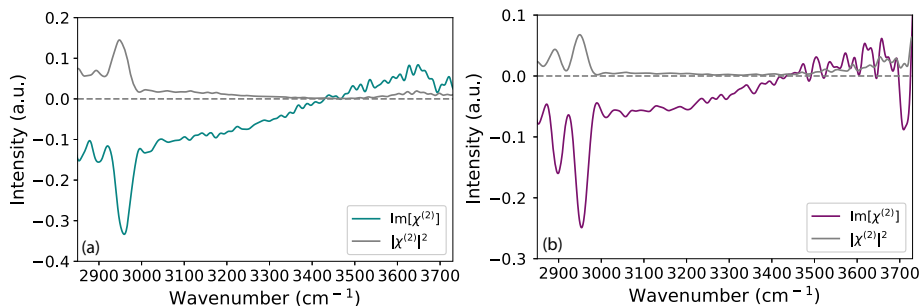


FIGURE 8.1. VSFG $\text{Im}[\chi^{(2)}]$ spectra of aqueous acetic acid (40 wt %, cyan) and propionic acid (40 wt %, magenta) at the solution–air interface. The corresponding intensity spectrum is shown in gray. All measurements were performed at room temperature (293 K) and in an ssp polarization configuration (s-SFG, s-VIS, p-IR).

In Figure 8.2 we show (a) the $|\chi^{(2)}|^2$ and (b) the $\text{Im}[\chi^{(2)}]$ VSFG spectra of a 40 wt % AA solution at the ice surface at temperatures ranging from 265 to 235 K. The $\text{Re}[\chi^{(2)}]$ spectra of these measurements can be found in the Appendix (Figure 8.9). We find that at 265 K the $|\chi^{(2)}|^2$ spectrum looks quite similar to that of an AA solution–air interface at room temperature. However, an important difference is that the VSFG spectrum of the AA solution on ice contains an additional weak broad band around $\sim 3160\text{ cm}^{-1}$. Decreasing the

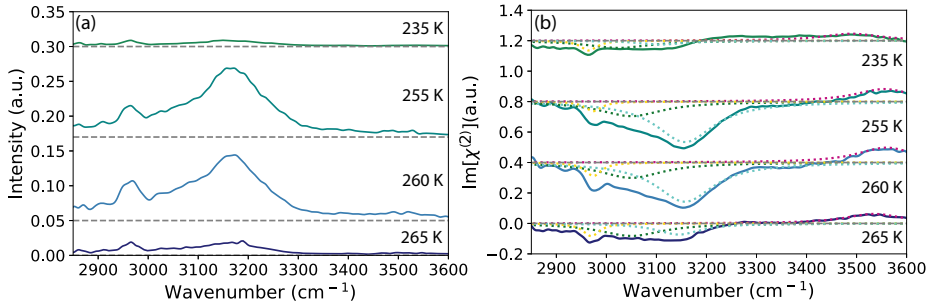


FIGURE 8.2. VSGF spectra of aqueous acetic acid (40 wt %) at the surface of ice at different temperatures. (a) The intensity VSGF spectra ($|\chi^{(2)}|^2$) and (b) the imaginary part of $\chi^{(2)}$. The colored dashed curves in (b) present the spectral decomposition of the $\text{Im}[\chi^{(2)}]$ spectra in Lorentzian components.

temperature to 255 K leads to the rise of the additional strong signal centered at $\sim 3160 \text{ cm}^{-1}$ that corresponds to both the response of OH stretch vibration of AA molecules and the ice surface underneath the AA solution. Decreasing the temperature also induces an increase of the band at 2950 cm^{-1} in the intensity VSGF spectra of Figure 8.2 (a). Comparison with the $\text{Im}[\chi^{(2)}]$ spectra at different temperatures of Figure 8.2 (b) shows that this increase in $|\chi^{(2)}|^2$ largely results from the constructive interference of the response of the CH methyl stretch vibration at 2950 cm^{-1} and the low-frequency wing of the broad OH signal that becomes stronger when the temperature is lowered.

Figure 8.3 presents the phase diagram for an aqueous solution of AA. According to this phase diagram, we expect that placing a 40 wt % AA solution at 265 K on the ice crystal will melt the top layers of the ice surface until a concentration of $\sim 22 \text{ wt } \%$ is reached. Lowering the temperature leads to freezing out of water from the AA solution and thus to an increase of the concentration AA. Upon lowering the temperature below the eutectic point of the solution (246 K), diffuse light scattering from the ice surface can be observed, which induces a significant decrease of the $|\chi^{(2)}|^2$ signal intensities at 2950 and 3160 cm^{-1} . This strong decrease of the OH stretch signals upon cooling below the eutectic point is reversible by increasing the temperature again above the eutectic point, as is demonstrated in Figure 8.10.

In Figure 8.4 we show the (a) $|\chi^{(2)}|^2$ and (b) the $\text{Im}[\chi^{(2)}]$ VSGF spectra of a 40 wt % PA solution placed on the surface of ice at temperatures between 268 and 235 K. The $\text{Re}[\chi^{(2)}]$ spectra of these measurements can be found in Figure 8.11. Figure 8.5 shows the phase diagram of water-PA mixtures. At 268 K, the VSGF spectrum looks similar to the VSGF spectrum of an aqueous PA solution at room temperature. As in the case of AA, we observe the rise of a strong signal at 3160 cm^{-1} when we lower the temperature to 255 K. This rise is accompanied by an increase of the CH signals at 2880 and 2950 cm^{-1} in the intensity VSGF spectra of Figure 8.4. Similar to the case of AA on ice, it is clear from the corresponding $\text{Im}[\chi^{(2)}]$ spectra (Figure 8.4 (b)) that this

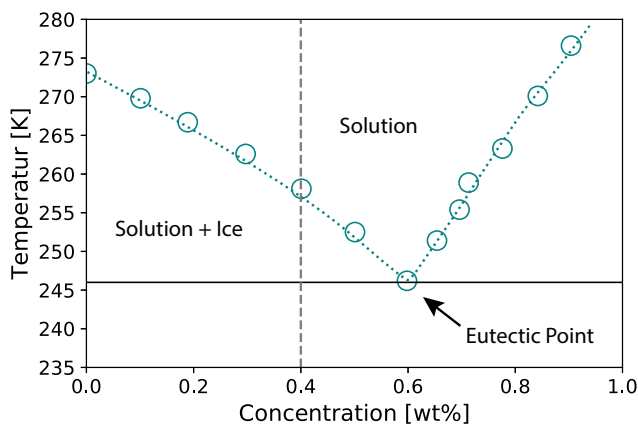


FIGURE 8.3. The phase diagram for aqueous solutions of AA. The data points were obtained by Barr et al.¹⁹²

increase results from enhanced constructive interference with the low-frequency wing of the increasing signal at $\sim 3160\text{ cm}^{-1}$. Lowering the temperature below the eutectic point of the PA solution ($\sim 245\text{ K}$) results in a further increase and blue-shift of the signal at 3160 cm^{-1} . The blue-shift of the VSGF signal at 3160 cm^{-1} upon cooling below the eutectic point of the mixture is reversible upon heating and cooling as shown in Figure 8.12. Lowering the temperature below the eutectic point also leads to a decrease of the CH signals at 2880 and 2950 cm^{-1} and a change in the ratio of the two signals in the intensity VSGF spectrum of Figure 8.4 (a). This change in ratio is not observed in the $\text{Im}[\chi^{(2)}]$ spectrum of Figure 8.4 (b), which implies that it merely reflects a change of the interference effect with the red wing of the broad OH signal.

We performed a spectral decomposition of the $\text{Im}[\chi^{(2)}]$ spectra of Figures 8.2 (b) and 8.4 (b) in Lorentzian-shaped spectral components curves. We use three components for the solution of AA on ice that we assign to the CH vibration of the CH_3 group (band at 2950 cm^{-1}), the OH vibration of strongly hydrogen-bonded carboxylic acid OH groups (3080 cm^{-1}), and the OH vibration of ice underneath the AA solution (band at 3160 cm^{-1}). This signal has a frequency position and spectral shape similar to those of the main component of the VSGF spectrum of the bare ice-air interface (Figure 3.6) and has been assigned to the bilayer-stitching OH stretch vibrations of water molecules in the top two bilayers of the ice crystal.^{92,193} We observe that the peak of the bilayer-stitching OH stretch vibrations of the ice is red-shifted in comparison to the bare ice surface. This indicates that the strength of the hydrogen bonds of the water molecules at the surface is increased, as has also been observed for other systems.¹⁹⁴ For the solution of PA on ice, we include an additional component representing the CH vibration of the CH_2 group (band at 2880 cm^{-1}). It should be noted that the studied solutions will contain ions as a result of acid dissociation. In the studied systems, the concentrations of ions will be low, in view of the pKa val-

ues ($\text{pKa} = 4.76$ for AA and $\text{pKa} = 4.87$ for PA¹⁹⁵). For a 40 wt % (=11.8 M) acetic acid [CH_3COOH] solution, the concentrations [H_3O^+] and [CH_3COO^-] are 14 mM. In case the acetate/propionate ions would have a propensity to accumulate at the interface of the ice crystal and the carboxylic acid solution, this would create a static electric field at the surface that orients the water molecules in the ice close to the surface, which will lead to a field-induced $\chi^{(3)}$ contribution to the SFG signal. This surface field-induced $\chi^{(3)}$ contribution has been studied in detail both theoretically and experimentally.^{87,102,193,196} In the studied systems, an electric field originating from the accumulation of acetate/propionate ions at the ice–solution interface would be short-range as it is effectively screened by protons that diffuse into the ice crystal. The screening by the protons diffused into the ice will be very effective as compared to Debye screening. In the case of Debye screening, the screening results from a difference in the distribution of the positive and negative ions in solution, with an associated energy penalty for their separation. In this case, this penalty is absent as only the positive ions will diffuse into the ice. For a solution of 14 mM of positive and negative ions, the Debye length is 2.5 nm. Hence, the length over which the protons screen the negative surface charge is expected to be shorter than 2.5 nm. The coherence length in SFG in reflection geometry is typically several tens of nanometers, corresponding to >100 layers of water molecules.¹⁹⁶ Hence, the depth over which water molecules may be oriented due to a surface electric field will be much smaller than the coherence length, which implies that the field-dependent $\chi^{(3)}$ contribution will be in phase with the $\chi^{(2)}$ contribution. This means that the VSFG signal of the ice–solution interface will not be distorted by this contribution. This latter notion is confirmed by our finding that we can decompose the observed VSFG spectra very well into a contribution of the solution–air interface and that of an ice surface with a response that is similar in shape to that of a bare ice–air interface. This indicates that the response of the ice is not distorted as a result of a field-dependent $\chi^{(3)}$ contribution. In Figure 8.6 we plot the areas of the bands as a function of temperature. We find that the band areas of the CH_3 and CH_2 vibrations are almost temperature independent. This result agrees with the results of Tyrode and co-workers for a solution of AA at room temperature.¹³ In this latter study, the CH_3 signal was observed to quickly saturate when the concentration of AA was increased. This saturation indicates that already at relatively low bulk concentrations the surface gets completely covered with AA molecules. According to the phase diagram shown in Figure 8.3, a liquid aqueous solution of AA at 265 K contains a concentration of ~ 22 wt % AA, which can be considered as a high concentration in comparison with the results of Tyrode and co-workers. Hence, already at 265 K the surface will be saturated with AA molecules, and decreasing the temperature toward the eutectic temperature will increase the concentration of AA in the bulk of the AA solution on top of the ice crystal, but not at the surface of the solution. The same effect occurs for the PA solution on the ice surface; already at 268 K the surface of the PA solution will be saturated with PA molecules, and decreasing the temperature will not further increase the surface concentration. This means that for temperatures above the eutectic point, the CH response of an acid solution on top of ice is similar to

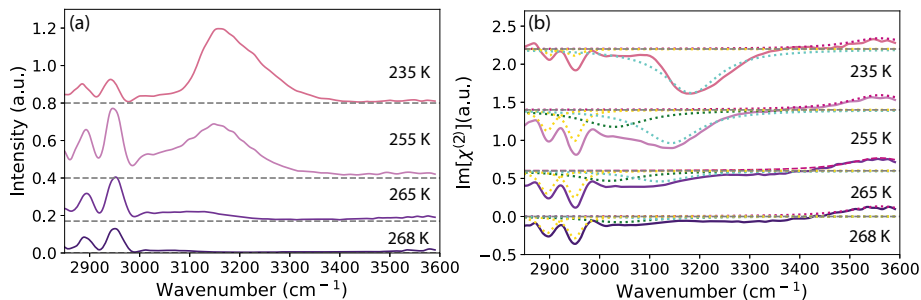


FIGURE 8.4. VSGF spectra of aqueous PA (40 wt %) at the surface of ice at different temperatures. (a) The intensity VSGF spectra ($|\chi^{(2)}|^2$) and (b) the imaginary part of $\chi^{(2)}$. The colored dashed curves in (b) present the spectral decomposition of the $\text{Im}[\chi^{(2)}]$ spectra in Lorentzian components.

that of an aqueous acid solution at room temperature. Cooling the systems below the eutectic point leads to a slight decrease in the band areas of the CH vibrations, which indicates a change in orientation of the AA and PA molecules when cooling below the eutectic point.

For both AA and PA, the band area of the OH stretch vibration of the carboxylic acid group increases with decreasing temperature in a temperature interval above the eutectic point. This observation indicates that the response of this vibration follows the bulk concentration of AA/PA in the solution on top of the ice surface that increases due to molecular freeze concentration. This result suggests that this response not only results from the (saturated) top molecular layer of the aqueous solution but also from layers underneath this layer and from layers close to the ice surface. When the temperature is lowered below the eutectic point, the amplitude of the OH vibration of the carboxylic acid group decreases somewhat for AA, whereas for PA this contribution completely vanishes, indicating a significant change of the interactions between the molecules for the latter system. The band area of the crystalline ice signal at 3160 cm⁻¹ strongly increases when the temperature is decreased, for solutions of both AA and PA on top of the ice crystal. This increase is also observed for the interface of bare ice and air and has been explained from the enhanced ordering of the water molecules in the top molecular layers of the ice crystal surface.¹⁹⁷ For the AA system, the crystalline ice signal at 3160 cm⁻¹ dominates the VSGF signal of the OH vibrations already at a temperature of 260 K. As a result, the OH VSGF signal has a temperature dependence that closely resembles that of a crystalline ice–air interface, showing a small red-shift when the temperature is decreased. For the PA system, the carboxylic acid group significantly contributes to the overall OH VSGF signal, probably because the PA solution on top of ice contains a higher mole fraction of carboxylic acid molecules than does a solution of AA on top of ice at the same temperature (Figures 8.3 and 8.5). With decreasing temperature, the amplitude of the carboxylic acid component increases less strongly than the crystalline ice component. As a result,

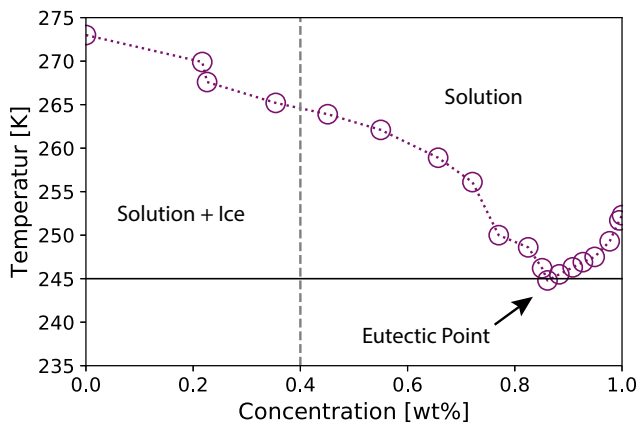


FIGURE 8.5. The phase diagram for aqueous solutions of PA. The data points were obtained by Barr et al.¹⁹²

for the PA system, the overall OH VSG signal undergoes a blue-shift when the temperature is decreased toward the eutectic point. There is a large difference between the AA and PA systems in how the OH VSG signal changes when the temperature is lowered below the eutectic point. For AA the signal decreases, while keeping the same shape. The surface above the eutectic point is smooth, and no scattering is observed. When we cool the AA system below the eutectic point, we observe that the surface starts to show diffuse light scattering, due to roughening of the surface. Furthermore, we observe an overall decrease of the intensity in all frequencies of the VSG spectrum, but no change of the shape of this spectrum. For PA we observe a further increase of the amplitude and an additional blue-shift when the temperature is lowered below the eutectic point.

From the analysis of the $\text{Im}[\chi^{(2)}]$ VSG spectrum of the PA solution on top of ice at 235 K (Figures 8.4 (b) and 8.6 (b)), it follows that the carboxylic acid contribution to the OH VSG signal vanishes completely below the eutectic point. As a result, the frequency and shape of the observed signal are almost identical to those of a pure ice–air interface at 245 K. We explain the intensity increase of the crystalline ice signal and vanishing of the carboxylic acid contribution from a phase separation of the water and propionic acid molecules upon freezing of the eutectic PA–water mixture.^{198,199} The vanishing of the VSG signal of the PA molecules suggests that these molecules cluster in hydrogen-bonded dimers with an opposite alignment of the carboxylic acid OH groups. As a result, the OH groups of the strongly hydrogen-bonded carboxylic acids no longer show a net orientation, and the VSG signal vanishes. This explanation is supported by previous work showing that PA indeed forms cyclic dimers upon crystallization.²⁰⁰

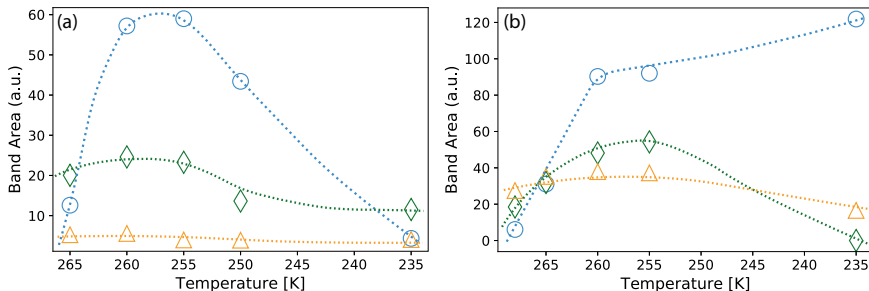


FIGURE 8.6. Areas of the different bands of the spectral decomposition of the temperature-dependent $\text{Im}[\chi^{(2)}]$ spectra of (a) AA and (b) PA. The different bands are assigned to the crystalline ice signal at $\sim 3160 \text{ cm}^{-1}$ (blue \circ), to strongly hydrogen-bonded OH groups of the carboxylic acid molecules at $\sim 3080 \text{ cm}^{-1}$ (green \diamond), to the CH-vibrations of the AA and PA (yellow \triangle). The solid lines are a guide to the eye.

8.4 CONCLUSION

We studied the properties of aqueous AA and PA acid solutions at the surface of ice at different temperatures using HD-VSFG spectroscopy. This technique allows us to determine $|\chi^{(2)}|^2$, $\text{Im}[\chi^{(2)}]$, and $\text{Re}[\chi^{(2)}]$. The VSFG spectra show resonances that can be assigned to the CH stretch vibration of the methyl group of acetic/propionic acid (2950 cm^{-1}), the CH stretch vibration of the methylene group of PA (2880 cm^{-1}), the OH vibration of the carboxylic acid group (3080 cm^{-1}), and the OH vibrations (3160 cm^{-1}) of the ice surface underneath the aqueous acetic/PA solution. Upon deposition of concentrated acid solutions on the basal surface of ice, the ice melts until a concentration is reached that is stable according to the phase diagram of the mixture. Lowering the temperature causes a freeze-induced phase separation (FIPS) into pure ice and a freeze concentrated acid solution (FCS) for both AA and PA. For the AA solution, lowering the temperature below the eutectic point leads to a decrease of the VSFG signal while retaining the shape of the spectrum, indicating a roughening of the surface of the frozen solution and enhanced diffuse scattering. Cooling of the PA solution on top of ice below the eutectic point leads to a strong VSFG signal that is highly similar to that of a pure ice–air interface at the same temperature. This observation indicates the formation of hydrogen-bonded dimers of PA molecules with an opposite alignment of their carboxylic acid OH groups, leading to a vanishing of the carboxylic acid contribution to the OH VSFG signal.

8.5 APPENDIX

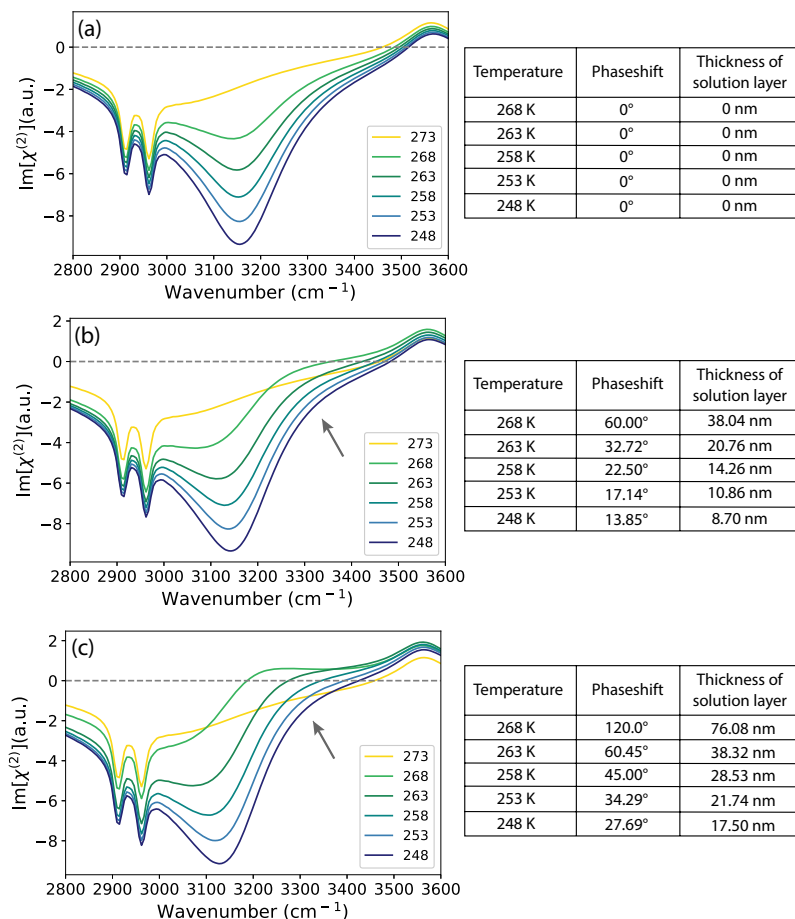


FIGURE 8.7. Modeling of interference effects induced by different thicknesses of the solution layer of PA.

In Figure 8.7 we modeled the effect of the thickness of the solution layer of PA on the spectral shape. In Figure 8.7 (a) we present the spectra obtained when the thickness of the solution layer is negligible. In this case no phase shift and thus no interference is observed. If we increase the thickness of the solution layer (Figure 8.7 (b,c)) the phase shift increases and interference effects arise, leading to a positive feature at $\sim 3250 \text{ cm}^{-1}$. This latter feature increases in amplitude with increasing thickness of the solution layer. Comparison of the modeled spectra with the measured spectra, reveals a small effect of interference at the highest measured temperature of 268 K. When the temperature is decreased the solution layer becomes thinner, and interference effects become negligible. In Figure 8.8 a measured spectrum of PA at the surface of ice is shown in which the most prominent effect of interference

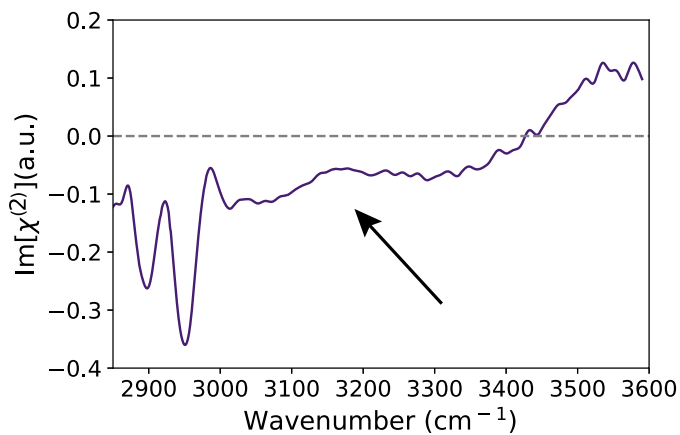


FIGURE 8.8. The $\text{Im}[\chi^{(2)}]$ spectrum of PA on the surface of ice at 268 K.

of the responses of the solution-air and ice-air interfaces is pointed out by an arrow. By comparing the modeled spectra with the measured spectra, we estimated that the solution layer has a maximum thickness of ~ 40 nm at 268 K.

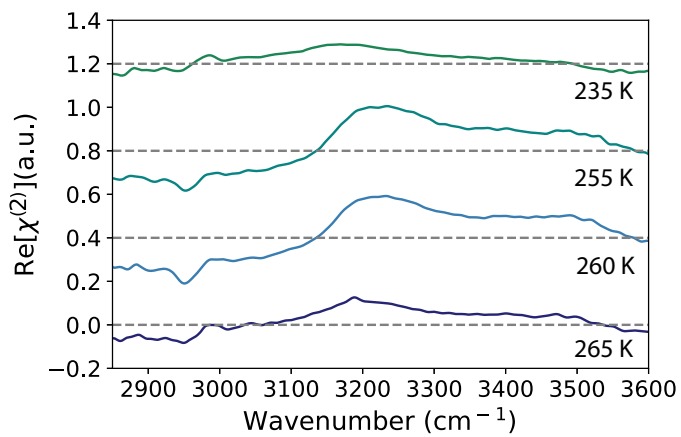


FIGURE 8.9. $\text{Re}[\chi^{(2)}]$ of aqueous AA (40 wt%) at the surface of ice at different temperatures.

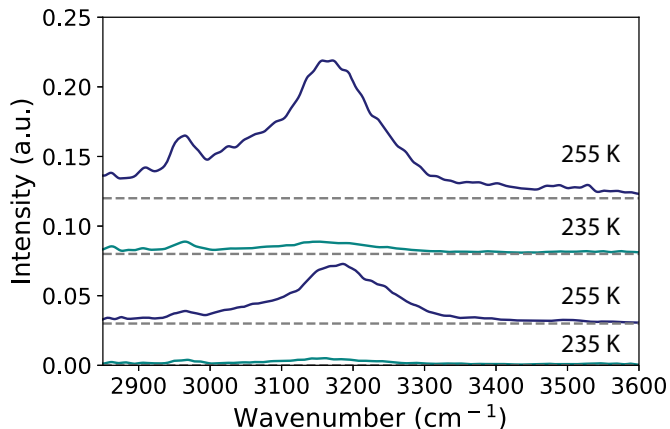


FIGURE 8.10. Reversibility of the VSFSG signals upon cooling below the eutectic point of AA.

The temperature was reduced from 255 K to 235 K, increased again to 255 K, and finally again reduced to 235 K. The waiting time between the measurements was 30 min to ensure that the temperature is fully adjusted. It is observed that the VSFSG spectra after the temperature cycle are not identical to the spectra of the first series. One possible reason is that the AA molecules would need more time to form the original configuration, another is that the experimental layout has slightly changed. An important observation is that the intensity of the OH stretch vibrations of the crystalline ice peak is increasing again after the system was cooled down below the eutectic point, which means that the eutectic crystallization of AA is reversible.

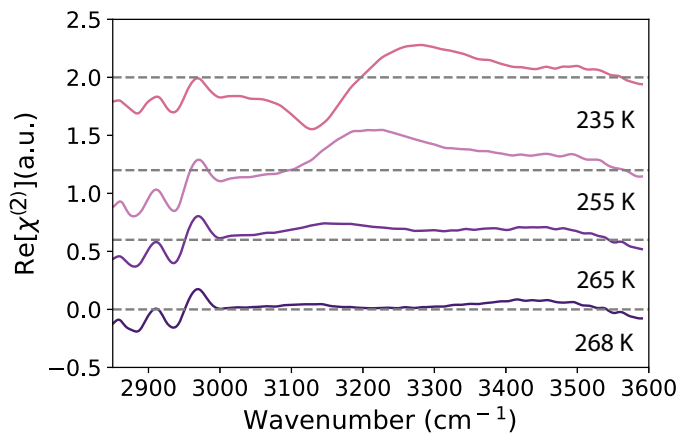


FIGURE 8.11. $\text{Re}[\chi^{(2)}]$ of aqueous PA (40 wt %) at the surface of ice at different temperatures.

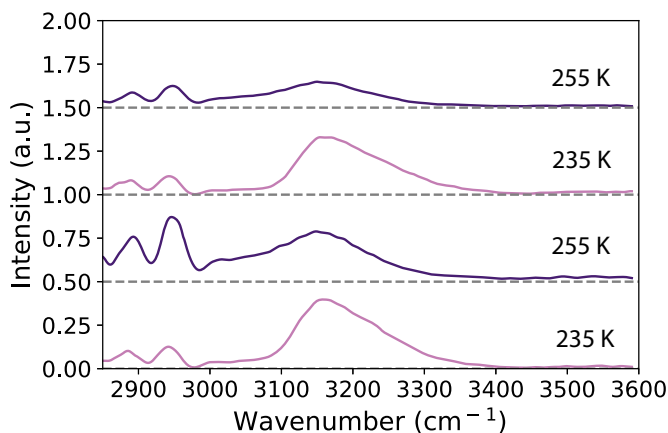


FIGURE 8.12. Reversibility of the VSGF signals upon cooling below the eutectic point of PA.

The measurement procedure is the same as for AA. The differences in intensity of the signals upon heating and cooling can be explained from small changes in the experimental configuration or the fact that the molecules need some time to rearrange. As mentioned above, the important point here is that the intensity of the OH stretch vibrations of the crystalline ice peak is increasing again after the system was cooled down below the eutectic point. Additionally, it can be observed that the blue-shift of the 3160 cm^{-1} peak is reversible too. This means that the continued FIPS of the PA and the anti-parallel dimer formation below the eutectic point are reversible.



9 MOLECULAR STRUCTURE OF HYPERACTIVE ANTIFREEZE PROTEIN ADSORBED TO ICE

Antifreeze proteins (AFPs) are a unique class of proteins that bind to ice crystal surfaces and arrest their growth. The working mechanism of AFPs is not well understood because, as of yet, it was not possible to perform molecular-scale studies of AFPs adsorbed to the surface of ice. Here, we study the structural properties of an AFP from the insect *Rhagium mordax* (RmAFP) adsorbed to ice with surface specific heterodyne detected vibrational sum-frequency generation spectroscopy and molecular dynamic simulations. We find that RmAFP, unlike other proteins, retains its hydrating water molecules upon adsorption to the ice surface. This hydration water has an orientation and hydrogen-bond structure different from the ice surface, thereby inhibiting the insertion of water layers in between the protein and the ice surface.

9.1 INTRODUCTION

Cold-adapted ectotherms living at subzero temperatures have evolved an elegant macromolecular solution to deal with the lethal threat of ice formation in their tissues. They produce antifreeze proteins (AFPs) that depress the freezing point of water in a non colligative manner.²⁰¹ They are of great interest for their use in antifreeze formulations for frozen food,⁴⁴ waterborne paints,⁴⁵ cryopreservation,⁴⁷ and other water-based materials.⁴⁶ The molecular details of the working mechanism of AFPs are poorly understood, which is mostly due to the fact that experimental studies of AFP-ice complexes are difficult.²⁰² Recent studies involving ice etching and the analysis of ice crystal growth morphology changes provided information on the ice plane specificity's of AFPs,^{203,204} but did not reveal the molecular-scale mechanisms by which AFPs bind to ice and by which they inhibit ice crystal growth. In particular, information on the ice surface, adsorbed AFPs, and the surrounding water would be of great value, as several simulation studies suggest a critical role of the hydration layers in the recognition and binding of AFPs to ice.^{205–208} Here, we use heterodyne-detected vibrational sum-frequency generation (HD-VSFG) spectroscopy to study AFP of *Rhagium mordax* (RmAFP) adsorbed to a monocrystalline, basal ice surface. We measure the real (Re) and imaginary (Im) part of the second-order susceptibility $\chi^{(2)}$ of the vibrations at the surface, which provides direct information on the absolute orientation of the surface-bound molecules.⁴ RmAFP is the most active AFP known and can bind to the basal and prism ice face. It is part of a large group of AFPs that possess an array of ordered threonine residues on a flat β -sheet region at their ice-binding site (Appendix Figure 9.5).^{209–212}

9.2 EXPERIMENTAL METHODS

SAMPLE PREPARATION All protein measurements were performed in a buffer solution (20 mM Na₃PO₄, 150 mM NaCl, pH 7.0). For the RmAFP samples with proven antifreeze activity, high purity samples were used, that were obtained by recombinant protein expression as described previously.²¹³ As control proteins α -lactalbumin, β -lactoglobulin and myoglobin were chosen. These proteins do not show antifreeze activity. Their sizes (\sim 14 kDa, \sim 18 kDa, \sim 16.7 kDa) and isoelectric points (IEP \sim 5, \sim 6, \sim 6.8) are comparable to that of RmAFP (\sim 12.4 kDa, IEP \sim 5). The samples were applied to the ice by using a combination of an ultraclean tissue and a plastic foil. The clean tissue acts as a sponge and the plastic foil smoothens the surface after the solution is deposited on the ice surface. Samples were applied at 265 K and the pure ice surface was always measured before applying samples to ensure that the ice surface was not contaminated. The procedure how to obtain and orient the monocrystalline ice samples is described in chapter 3.3.

HD-VSFG MEASUREMENTS The HD-VSFG measurements performed in this chapter are carried out with the setup described in section 3.1.

9.3 RESULTS AND DISCUSSION

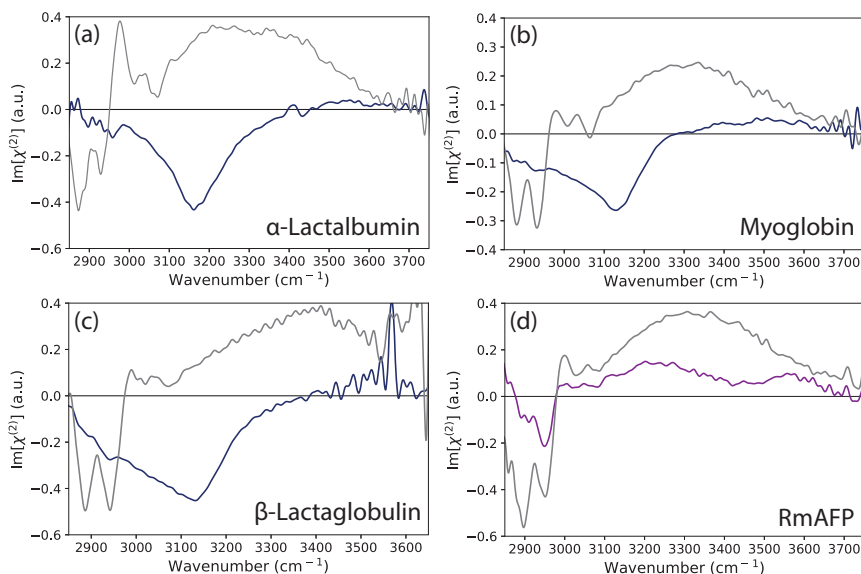


FIGURE 9.1. $\text{Im}[\chi^{(2)}]$ spectra of 15 μM solutions of (a) α -lactalbumin, (b) myoglobin, (c) β -lactoglobulin, and (d) RmAFP (20 mM NaPo_4 , 150 mM NaCl , and pH 7.0) at the solution-air interface and deposited on the basal face of monocrystalline ice. The HD-VSFG spectra of the aqueous protein solutions (gray) look similar with characteristic CH and OH stretch vibrations. The deposition of non-AFP solutions (a)–(c) on the surface of ice results in spectra with a dominant negative peak at $\sim 3150 \text{ cm}^{-1}$. With identical conditions, the deposition of an RmAFP solution shows a very different $\text{Im}[\chi^{(2)}]$ spectrum with a positive band centered at $\sim 3200 \text{ cm}^{-1}$. The measurements at the water surface (gray) were performed at 293 K, and those of the ice surface were performed at 255 K and with the SSP polarization configuration (s-SFG, s-VIS, p-IR).

In Figure 9.1 (a–d), we present $\text{Im}[\chi^{(2)}]$ spectra of α -lactalbumin, β -lactoglobulin, myoglobin, and RmAFP at the surfaces of water and ice. At the surface of water, the HD-VSFG spectra of the non-AFP and RmAFP solutions look very similar. All spectra show contributions from aliphatic CH stretch vibrations ($\sim 2880 \text{ cm}^{-1}$ and $\sim 2930 \text{ cm}^{-1}$) and aromatic ($\sim 3060 \text{ cm}^{-1}$) CH vibrations of the amino acid residues of the proteins. At frequencies $> 3100 \text{ cm}^{-1}$, all spectra show a broad positive band that we assign to the OH stretch vibrations of interfacial water molecules. The sign of $\text{Im}[\chi^{(2)}]$ is determined by the orientation of the vibrational transition dipole moment. In the case of well-defined local modes, the orientation of the transition dipole moment of

a vibration can be directly related to the orientation of the molecular group carrying that vibration. For pure liquid water and ice, the OH stretch vibrations are delocalized and thus the relation between the sign of $\text{Im}[\chi^{(2)}]$ and the orientation of the individual molecules is less straight forward. In this case, the sign of $\text{Im}[\chi^{(2)}]$ is determined by the dominant orientation of the transition dipole moments of the delocalized OH stretch vibrations. A positive sign indicates that there are more delocalized OH stretch vibrations involving OH groups for which the hydrogen atoms are pointing towards the air (up), while a negative sign of $\text{Im}[\chi^{(2)}]$ indicates that there are more delocalized OH vibrations involving OH groups for which the hydrogen atoms are pointing into the liquid (down). Hence, although for liquid water and ice $\text{Im}[\chi^{(2)}]$ cannot directly be related to particular hydrogenbonded OH groups, a positive sign of $\text{Im}[\chi^{(2)}]$ still implies that the interfacial water molecules have a preferential orientation with their OH groups pointing to the negatively charged proteins floating on the water surface.^{7,32,214}

The broad shape of the OH band observed for RmAFP on water indicates that the protein does not possess a pre-ordered hydration layer. Such a pre-ordered water layer has been observed experimentally for AFP III.⁶⁶ The absence of a pre-ordered hydration layer for RmAFP agrees with the results of recent molecular dynamics simulations.²⁰⁷ For α -lactalbumin, β -lactoglobulin, myoglobin, and RmAFP adsorbed to the ice surface the $\text{Im}[\chi^{(2)}]$ spectra again show the responses of the CH stretch vibrations of the proteins. For the non-AFPs, the $\text{Im}[\chi^{(2)}]$ spectra are dominated by a strong negative band centered at $\sim 3150\text{ cm}^{-1}$ that is similar to the signal that is observed at the bare ice-air interface (Figure 3.6). This band has been assigned to the bilayer-stitching OH stretch vibrations of the water molecules in the top two bilayers of the ice crystal.^{92,193} The negative sign indicates that these water molecules have a net orientation with their OH groups pointing away from the surface. This result shows that for non-AFPs, the hydrogen-bond structure and orientation of water molecules at and near the interface are completely determined by the mutual interactions of water molecules in ice. The $\text{Im}[\chi^{(2)}]$ spectrum of RmAFP at the surface of ice shows a positive signal centered at $\sim 3200\text{ cm}^{-1}$. This result shows that RmAFP remains hydrated with water molecules with an orientation that is determined by the RmAFP, even after adsorption of the protein to the ice surface. The spectral shape of the hydration water signal changes somewhat upon adsorption to the ice surface. We observe a shift in the center frequency from $\sim 3300\text{ cm}^{-1}$ at temperatures above the melting point to $\sim 3200\text{ cm}^{-1}$ at temperatures below the melting point, which indicates that the water molecules in the hydration layer of RmAFP become more strongly hydrogen-bonded upon adsorption of the protein to ice. The spectrum is broader and blueshifted compared to that of ice, showing that the hydrogen-bond structure of the hydration layer differs from that of ice. We further observe resonances at $\sim 2880\text{ cm}^{-1}$, $\sim 2930\text{ cm}^{-1}$, and 3060 cm^{-1} that we assign to CH vibrations of the protein and a signal at $\sim 3560\text{ cm}^{-1}$ that we assign to crystalline ice.⁹²

We explain the persistent presence of hydrating water molecules for RmAFP from the rigid, corrugated structure of the ice-binding surface (IBS) of RmAFP. The IBS consists of ridges with a high density of threonine residues that

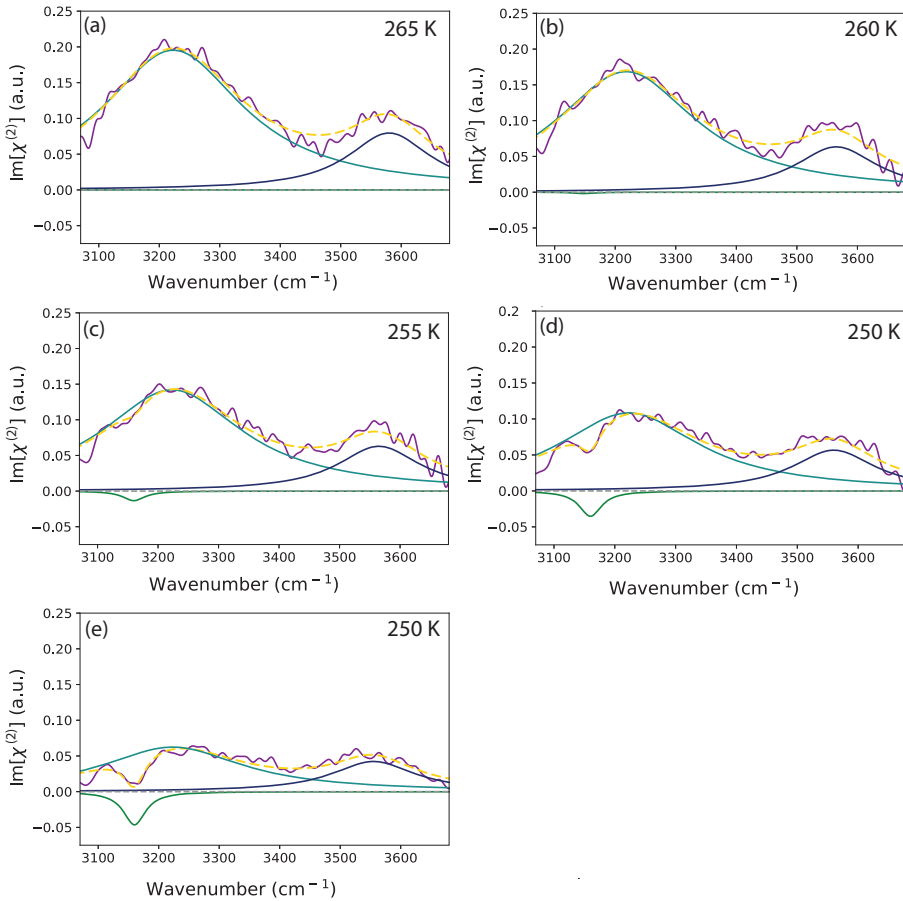


FIGURE 9.2. Imaginary $[\chi^{(2)}]$ spectra of RmAFP at the surface of basal ice at temperatures between 245 and 265 K. The spectra are fitted with three Lorentzian bands (darkcyan, blue, and green lines). The measured data are represented by the dark-magenta line and the fitted spectra by dashed yellow lines. Decreasing the temperature leads to a decrease of the $\sim 3200 \text{ cm}^{-1}$ signal and to an ingrowth of a signal at $\sim 3180 \text{ cm}^{-1}$.

strongly interact with the surface of ice. Such a corrugated motif of the IBS is common for insect and other hyperactive antifreeze proteins.²⁰⁷ In a previous study on the related hyperactive antifreeze protein from the beetle *Dendroides canadensis* (DAFP-1) at the water surface, it was shown that the valleys between these ridges contain hydrating water molecules.²¹⁵ Such “channel water molecules” were also observed in crystal structures and simulations of related AFPs.^{207,211,212} The present results indicate that the corrugated structure of RmAFP with ridges and valleys containing hydration water persists when the protein adsorbs to ice. Most other non-AFPs, including the proteins used in this

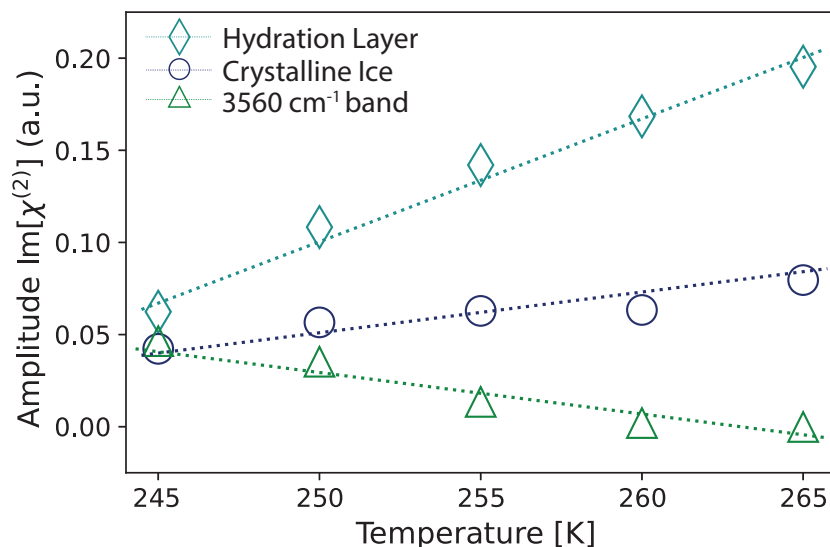


FIGURE 9.3. Amplitudes of the three different bands used in the spectral decomposition of the temperature-dependent $\text{Im}[\chi^{(2)}]$ spectra of Figure 9.2. The bands are assigned to crystalline ice signal at 3180 cm^{-1} (blue circles), the hydration shell of RmAFP at 3200 cm^{-1} (cyan diamonds), and a weaker crystalline ice signal at 3560 cm^{-1} (green triangles). The lines serve as guides to the eye.

study, do not possess such a rigid, corrugated surface and will likely unfold and stretch out on the ice surface. As a result, for these proteins, no protein-oriented water molecules in between the ice surface and the protein are observed. To corroborate the above explanation, molecular dynamics simulations of the adsorption of RmAFP and α -lactalbumin to the surface of ice using Groningen Machine for Chemical Simulations 4.5 (GROMACS 4.5) are performed. We find that for α -lactalbumin, a large fraction of the amino-acid residues are in direct contact with the ice surface, whereas for RmAFP, the interfacial region contains water molecules that hydrate the protein and are not associated with those in the ice crystal (Appendix Figure 9.6 and 9.7). These water domains between the IBS of the adsorbed RmAFP and the ice surface have a tetrahedrally coordinated arrangement, which is in excellent agreement with the observed center frequency of 3200 cm^{-1} in the $\text{Im}[\chi^{(2)}]$ spectrum of RmAFP adsorbed to ice. In Figure 9.2, we show $\text{Im}[\chi^{(2)}]$ spectra of RmAFP at the ice surface at different temperatures in the range between 265 K and 245 K. We find that the signals at $\sim 3200\text{ cm}^{-1}$ and $\sim 3560\text{ cm}^{-1}$ decrease when the temperature is lowered. We also observe an ingrowth of a negative band at $\sim 3180\text{ cm}^{-1}$ that we assign to the OH vibrations of crystalline ice. Further, we performed a spectral decomposition with Lorentzian-curves of the $\text{Im}[\chi^{(2)}]$ spectra to obtain quantitative information on the temperature dependence of the hydration-shell band and the

ice band. We in total decompose the $\text{Im}[\chi^{(2)}]$ spectra at different temperatures with six Lorentzian bands over the whole frequency region (Figure 9.8), while in Figure 9.2 we focus on the frequency region of the OH-stretch vibrations. In Figure 9.3, we plot the amplitude of these bands as a function of temperature. We explain the observed temperature dependence of the amplitude from the change in orientation and binding of the water molecules between the IBS of the adsorbed RmAFP and the ice surface. Decreasing the temperature causes the water domains to reorient away from the AFP and to join the ice lattice, thereby lowering the signal at $\sim 3200 \text{ cm}^{-1}$. The newly formed ice layers of the RmAFP solution give rise to the negative signal at $\sim 3180 \text{ cm}^{-1}$. The functioning of AFPs is intimately connected to the mechanism by which these proteins bind to ice and how they prevent further growth of the ice crystal at and near their adsorption sites. All AFPs are proposed to function according to the adsorption inhibition mechanism.²¹⁶ In this mechanism, ice can only grow in between the adsorbed AFPs, which results in a strongly curved ice surface with a high associated surface energy.²¹⁶ This so-called Kelvin effect explains the depression of the freezing point. We speculate that the different orientation and hydrogen-bond structure of the water molecules in the valleys between the ridges of the IBS will inhibit the intercalation of ice layers in between the adsorbed hyperactive AFP and the ice surface. As a result, the adsorbed hyperactive AFPs are not pushed away from the original ice surface, and ice can only grow in between the adsorbed RmAFPs, leading to a pronounced Kelvin effect. Hence, the water molecules between the ridges of the IBS of RmAFP are needed for the antifreeze mechanism of RmAFP and other hyperactive AFPs. The mechanism of adsorption of RmAFP to ice is schematically shown in 9.4.

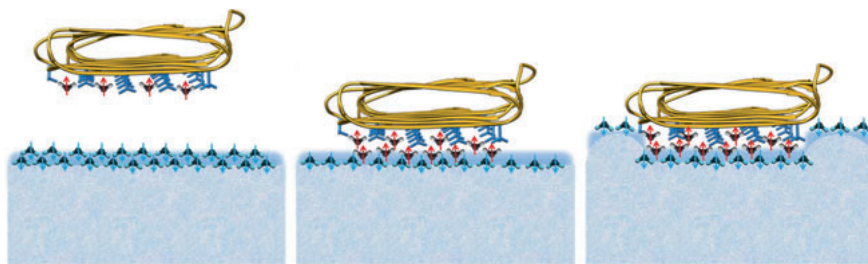


FIGURE 9.4. Schematic representation of the ice-binding and ice-crystal growth inhibition mechanism of AFPs. The ice surface contains a water layer, in which the water molecules have a net orientation with their OH groups pointing towards the ice. (I) RmAFP has water molecules in the valleys of the IBS that have an orientation towards the protein. (II) RmAFP accumulates at the interfacial region of ice and retains its hydrating water molecules at the IBS of which the orientation is determined by the protein and not by the ice surface. (III) Water molecules cannot intercalate between the hydration water and the surface, so that ice can only grow in between adsorbed AFPs, which results in a strongly curved ice surface with a high associated surface energy.

9.4 CONCLUSION

We studied the properties of the hydration layer of RmAFP, an antifreeze protein from the insect *Rhagium mordax*, using surface specific HD-VSFG spectroscopy and molecular dynamics simulations. We compare these properties with those of proteins that have no antifreeze activity. For all studied proteins, we find that the structure of the hydration layer of the protein in aqueous solution is determined by the interaction with the protein. In particular we observe that the net orientation of the hydrating water molecules is governed by the charge of the protein. However, when the studied non-AFPs adsorb to ice, we observe that the orientation of the water molecules in between the protein and the surface becomes independent of the protein charge and is completely determined by the mutual interactions of the water molecules in the top layers of the ice surface. In contrast, for RmAFP adsorbed to ice, the orientation of the water molecules in between the protein and the ice surface remains to be determined by the protein, indicating that the hydration layer at the ice-binding surface of RmAFP remains intact. MD-simulations agree with this observation by showing that the structure of the ice-binding surface (IBS) of RmAFP with ridges and valleys containing hydration water persists upon adsorption of the protein to ice. The orientation and hydrogen-bond structure of the water molecules in the valleys between the ridges of the IBS differ from that of the underlying ice layers, which inhibits the intercalation of ice layers in between the adsorbed hyperactive AFP and the ice surface. As a result, the ice crystal can only grow in between adsorbed RmAFPs, leading to a pronounced curvature of the ice surface and a depression of the freezing point (Kelvin effect).

9.5 APPENDIX

9.5.1 MOLECULAR DYNAMICS SIMULATIONS

Binding free energy calculations and equilibrium simulations were performed using the GROMACS 4.5 package^{217–219} with the OPLS/AA^{220–222} force field and the SPC/E²²³ water model. The details of the simulation protocol and the reasoning for the choice of the force-field and water model were described elsewhere.^{224,225}

9.5.2 MODELING OF RMAFP STRUCTURE

The 3-D crystal structure of RmAFP is unknown. We used the crystal structure of the antifreeze protein from *Rhagium inquisitor* (RiAFP; PDB: 4DT5) as a template to construct the structure of RmAFP using an iterative threading approach implemented in I-TASSER web-server.^{226,227} RiAFP and RmAFP are homologous proteins and share 76% sequence identity. The ice-binding surface of RiAFP contains an array of water molecules making hydrogen bonds with the threonine residues.²²⁸ These water molecules were considered during the modeling. The modeled RmAFP structure was minimized in vacuo using the steepest descent algorithm.

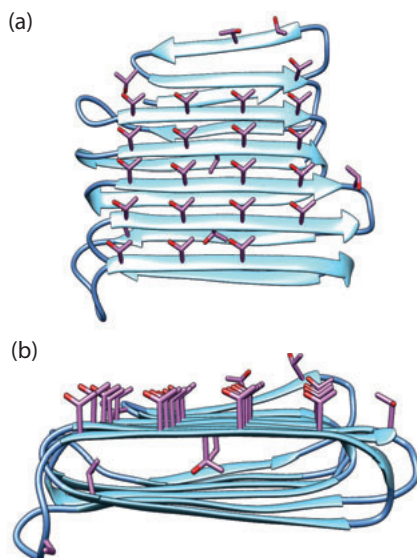


FIGURE 9.5. Model of the 3D structure of the RmAFP. The protein consists of a compressed β -helical fold with a relatively flat and hydrophobic threonine-rich ice-binding-surface. (a) Top view showing the flat threonine-rich ice-binding site. (b) Side view down the helix.

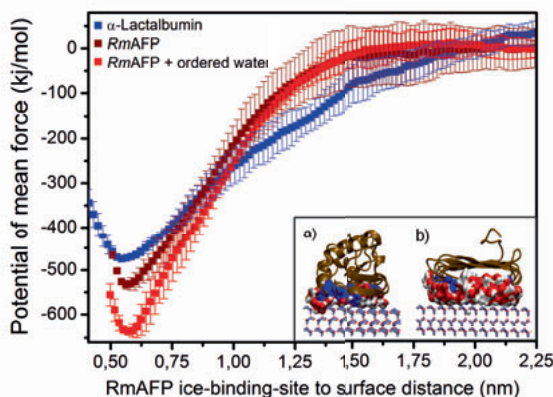


FIGURE 9.6. PMF profiles for the binding of RmAFP to the basal plane in presence of preordered water (red), in absence of preordered water (dark red) and α -lactalbumin to the basal plane (blue). Results are represented as Mean \pm S.D. ($n=2$). Structures corresponding to the PMF minima are shown in the inset for (a) α -lactalbumin and (b) RmAFP. Proteins are rendered as brown ribbon, ice binding residues are shown as blue vdW spheres and interfacial water molecules are shown in the surface representation with oxygen in red and hydrogen in white.

9.5.3 DOCKING OF RMAFP AND α -LACTALBUMIN TO THE BASAL PLANE

The structure of α -lactalbumin was obtained from the protein data base (PDB ID: 1A4V) and all hetero atoms were not considered. α -lactalbumin and optimized RmAFP were docked on the basal plane of ice using the PatchDock webserver.²²⁹ The top ranked docked complex was considered further. In case of the RmAFP the docking was carried out in the presence and absence of bound preordered water molecules next to the IBS.

9.5.4 CALCULATION OF THE BINDING FREE ENERGY FOR THE PROTEIN ADSORPTION TO THE BASAL PLANE

RmAFP-Ice docked complexes in the presence/absence of preordered water were aligned in such a way that the basal surface was along the X-Y plane. Both complexes were then solvated in a rectangular box of $80 \text{ \AA} \times 90 \text{ \AA} \times 80 \text{ \AA}$ with periodic boundary condition and using the SPC/E water model. Five sodium ions (Na^+) were added to neutralize the total charge of the system. The α -lactalbumin-Ice complex was solvated in a box of $100 \text{ \AA} \times 100 \text{ \AA} \times 90 \text{ \AA}$ dimension with periodic boundary condition. Seven sodium ions (Na^+) were added to neutralize the system. The box dimensions in all cases were chosen such that in the X and Y direction the ice slab did not collide with its image and in the Z-direction the box length is greater than double of the final pull distance between AFP and the basal plane center of

mass. Each system was initially minimized with 500 steps using a steepest descent algorithm. Then 1 ns position restrained dynamics were performed in each case in NVT ensemble at 225 K where the ice slab was kept frozen and protein atoms were restrained, but water molecules were allowed to move freely. The temperature was maintained using a *v*-rescale thermostat with a coupling constant of 0.1 ps. Finally 3 ns NVT simulations were performed for all the three AFP-ice docked complexes at 225 K in NVT ensemble. Electrostatic interactions were calculated using the particle mesh Ewald summation method. The umbrella sampling technique was used to construct the potential of mean force (PMF) profile for the RmAFP and α -lactalbumin adsorption on the basal ice plane. The center of mass distance along the Z-axis between the protein and basal ice slab was considered as the reaction co-ordinate. The docked protein was then pulled from the basal plane along the Z-direction with an interval of 0.1 nm. An umbrella force constant of $5000 \text{ kJ mol}^{-1} \text{ nm}^{-2}$ was used to keep the protein at desired position. 1 ns equilibration simulation followed by 2 ns production run in NVT ensemble was carried out in each umbrella window. Finally the PMF profile was obtained by using weighted histogram analysis method³⁹ implemented in GROMACS. Histogram analysis was performed in each case to ensure sufficient overlap among all the umbrella windows in each case. The final PMF profile was then rescaled on the basis of ice surface and ice binding surface of the protein distances. Docked structure corresponds to the PMF minimum in each cases was then subjected to equilibrium simulations at 225 K in NVT ensemble using V-rescale thermostat with a coupling constant of 0.1 ps. In the entire equilibrium simulations ice slab was kept frozen in all the three dimensions.

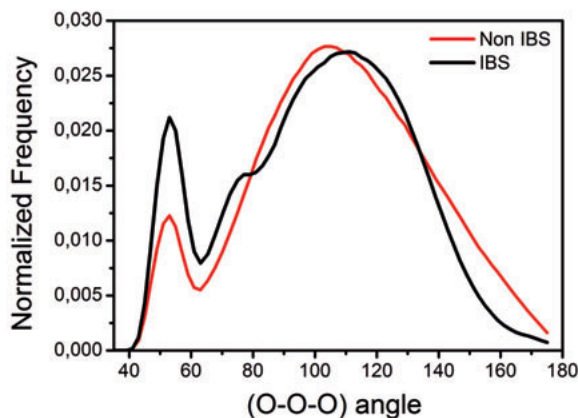


FIGURE 9.7. Hydration water within 4.0 \AA of the threonine methyl groups of the ice-binding site were considered (black) and bulk distribution was obtained by considering water within $10\text{-}12 \text{ \AA}$ of the threonine methyl groups of the non ice-binding sites.

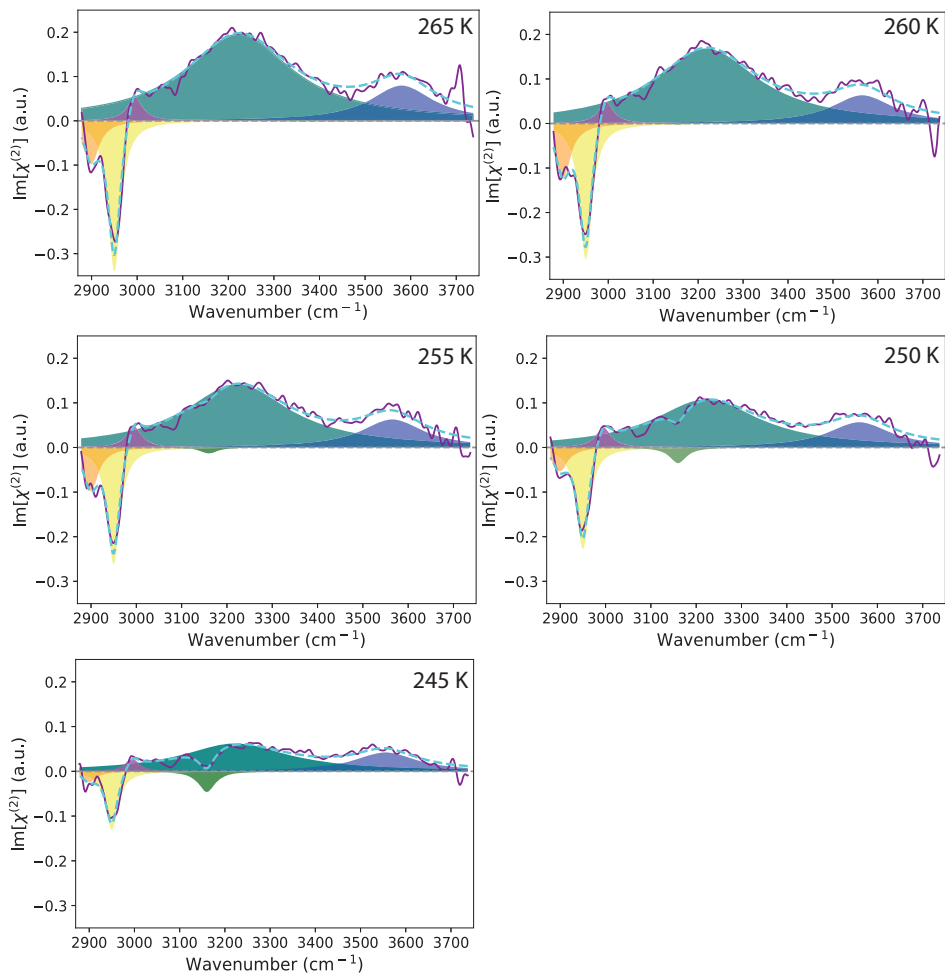


FIGURE 9.8. $\text{Im}[\chi^{(2)}]$ spectra of RmAFP at the surface of basal ice at temperatures between 245 and 265 K. The spectra are fitted with six Lorentzian bands. The measured data are represented by the dark magenta line and the fitted spectra by dashed cyan lines. Decreasing the temperature leads to a decrease of the $\sim 3200 \text{ cm}^{-1}$ signal and to an ingrowth of a signal at $\sim 3180 \text{ cm}^{-1}$.



10 THE MOLECULAR STRUCTURE AND SURFACE ACCUMULATION DYNAMICS OF HYALURONAN AT THE WATER/AIR INTERFACE

Hyaluronan is a biopolymer that is essential for many biological processes in the human body, like the regulation of tissue lubrication and inflammatory responses. Here we study the behavior of hyaluronan at aqueous surfaces using heterodyne-detected vibrational sum-frequency generation spectroscopy (HD-VSFG). Low-molecular weight hyaluronan (~ 150 kDa) gradually covers the water-air interface within hours, leading to a negatively charged surface and a reorientation of the interfacial water molecules. The rate of the surface accumulation strongly increases when the bulk concentration of low-molecular weight hyaluronan is increased. In contrast, high-molecular weight hyaluronan (>1 MDa) cannot be detected at the surface, even hours after addition of the polymer to the aqueous solution. The strong dependence on the polymer molecular weight can be explained from entanglements of the hyaluronan polymers. We also find that for low-molecular weight hyaluronan the migration kinetics of hyaluronan in aqueous media shows an anomalous dependence on the pH of the solution, which can be explained by the interplay of hydrogen-bonding and electrostatic interactions of the hyaluronan polymers.

10.1 INTRODUCTION

Glycosaminoglycans (GAGs) are charged biopolymers (polyelectrolytes), which play an important role in various biological processes in our body, ranging from anti-coagulation to immune response to external pathogens.²³⁰ Among all of the glycosaminoglycans, hyaluronan is arguably one of the most important and most studied. Hyaluronan is the structurally simplest GAG, and regulates biological functions like tissue lubrication and inflammatory responses.²³¹⁻²³⁴ New hyaluronan is constantly synthesized, and a defective regulation of hyaluronan production can lead to severe diseases. Alterations in the concentration and molecular weight of hyaluronan have for instance been linked to cancer initiation, metastasis, therapy resistance and arthritic diseases²³⁵⁻²³⁹. For example, it has been found that in healthy individuals the synovial fluid, which guarantees the correct lubrication between the knee cartilages, contains a concentration of 1.3 - 4 mg/ml of hyaluronic acid with a high molecular weight (HA_{HMW}) of 1.5 - 1.8 MDa.²³⁷ In the case of patients affected by arthritic diseases, the concentration of HA_{HMW} decreases to 0.1 - 1.3 mg/ml, whilst the concentration of low molecular weight hyaluronic acid (HA_{LMW} \sim 100 - 150 KDa) increases.²³⁷⁻²³⁹ Changing the ratio between HA_{HMW} and HA_{LMW} can influence the viscoelasticity of the synovial fluid, which can have drastic effects on the joint lubrication.²³⁷ Furthermore, because of its biocompatibility, hyaluronan is widely used in biomedicine to design hydrogels with tailored applications.²⁴⁰ The polymer, also forms important structural component of artificial tears, or eye drops, to facilitate the lubrication and hydration of contact lenses.^{241,242}

The outstanding physiological relevance and the wide application of hyaluronan have led to numerous studies of its microscopic and macroscopic properties in the bulk.^{62,64,243-248} Many of these studies were aimed at finding the connection between the macroscopic and molecular properties, which are dictated by molecular weight and concentration, and their impact on biological functions. However, up to now, the interfacial properties of hyaluronan have only been investigated by macroscopic surface tension measurements.^{249,250} Until now a detailed molecular picture of the surface of aqueous hyaluronan solutions is completely missing. A more detailed knowledge of these molecular-scale properties can be helpful in acquiring a better understanding of the special interfacial properties of aqueous hyaluronan solutions, like its lubrication behavior and its biochemical interactions.

We use conventional vibrational sum-frequency generation (VSFG) spectroscopy and heterodyne-detected vibrational sum-frequency generation (HD-VSFG) spectroscopy to study the surface propensity and molecular structure of aqueous HA solutions at the water/air interface. VSFG techniques are highly surface specific and, therefore, ideally suited for the study of the molecular-scale properties of polymers adsorbed at interfaces, providing information on the conformation and solvent interactions of the molecules of interest.^{4,251-253} We find that the kinetics of the adsorption process strongly depend on the

molecular weight and the bulk concentration, and shows an extremely strong and anomalous dependence on the ionic strength and the pH of the solution.

10.2 EXPERIMENTAL METHODS

SAMPLE PREPARATION The hyaluronic acid sodium salt in powder form from *Streptococcus equi* bacteria is purchased from Sigma Aldrich, Czech Republic (>1 MDa) and from Biomedical Lifecore (~ 150 kDa). In preparing HA solutions we use water from a Millipore Nanopure system (18.2 M Ω cm). Both types of HA are used without further purification. The HA solutions with low molecular weight and high molecular weight are prepared at room temperature at least two hours and 24 hours before the measurement, respectively, to ensure complete solvation of the biopolymer. The HA solutions are stored for at most 1 month at a temperature of 4°C . All HA solutions are mixed with a vortex once more directly before the measurement to ensure a uniform solution. In the concentration-dependent measurements we used a sodium phosphate buffer (137 mM NaCl, 10 mM Na_2HPO_4 and 2.7 mM KCl) as solvent to keep the pH constant at pH 7.4 and the ionic strength close to that of the synovial fluid, which contains 155 mM of sodium chloride.²⁵⁴ In the pH dependent measurements, the solution contained a constant concentration of 150 mM of NaCl, and the pH was regulated by adding NaOH and HCl to the solution. To perform measurements with different salt concentrations, we varied the NaCl concentration from 0 to 300 mM in the HA solution. Additionally, all measurements are taken in a custom-built sample cell covered by a calcium fluoride window to prevent solvent evaporation. The sample cell is made of Teflon and can hold a sample solution with a volume of up to 4 ml. A schematic picture of the sample cell can be found in the Appendix Figure 10.7. Since the sample cell has a diameter of 3.5 cm and the lateral spatial resolution of our measurement is 100 μm , we effectively have a flat air/liquid interface.

SPECTROSCOPY The VSGF measurements described in this chapter are performed with the setup described in section 3.1.

10.3 RESULTS AND DISCUSSION

In Figure 10.1, we present the comparison between the HD-VSGF spectra of pure water and low molecular weight hyaluronic acid ($\text{HA}_{\text{LMW}} \sim 100 - 150$ kDa) dissolved in buffer solution (pH=7.4), measured 60 min after placing the sample in the VSGF setup. The HA solution is mixed just before the measurement, therefore we can define for all of the reported measurements time zero as the time when the sample is positioned in the VSGF setup. The measurement is taken in SSP polarization configuration (s-SFG, s-VIS, p-IR). The presented $\text{Im}[\chi^{(2)}]$ spectrum of pure water is in excellent agreement with results obtained in previous studies.^{32,255,256} In the range between 3100 and 3550 cm^{-1} , the $\text{Im}[\chi^{(2)}]$ water spectrum shows a broad negative band originating from the OH stretch vibrations of water molecules that form hydrogen bonds to other water

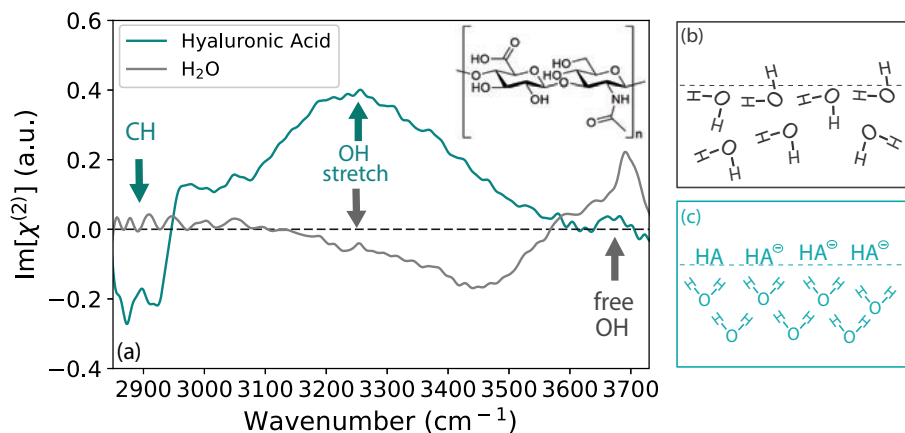


FIGURE 10.1. (a) $\text{Im}[\chi^{(2)}]$ spectra of pure water (gray) and a low molecular weight (100-150 kDa) hyaluronan solution (HA_{LMW} , 4.5 mg/ml, 60 min after placing the sample in the VSGF setup, cyan) at the water-air interface, measured in SSP polarization configuration (s-SFG, s-VIS, p-IR). The HA solutions have a pH of 7.4 regulated with a phosphate buffer, as described in the text. The inset shows a schematic of the repeating molecular structure of HA. Schematic of the orientation of water molecules (b) at the neat water surface and (c) at the surface of a hyaluronan solution.

molecules. Additionally, the spectrum shows a narrow peak at 3700 cm^{-1} . This highly surface specific feature at 3700 cm^{-1} is assigned to the OH stretch vibrations of non-hydrogen bonded OH-groups that stick out of the surface. The sign of the $\text{Im}[\chi^{(2)}]$ spectrum of the stretch vibration of water is directly related to the orientation of the vibrational transition dipole moment. A positive sign of $\text{Im}[\chi^{(2)}]$ of the OH stretch vibrations corresponds to a net orientation with the hydrogen atoms pointing toward the air (up), while a negative sign of $\text{Im}[\chi^{(2)}]$ corresponds to hydrogen atoms pointing into the liquid (down).

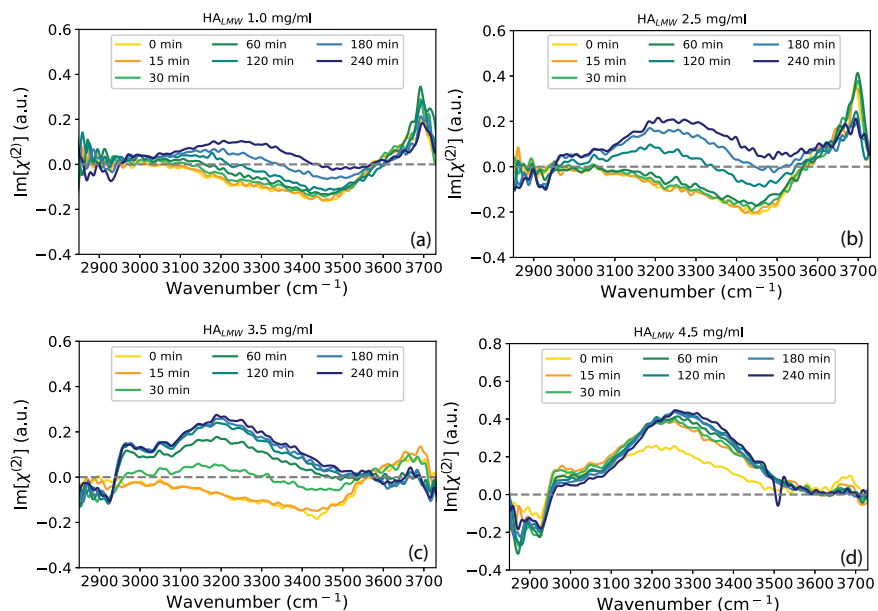


FIGURE 10.2. $\text{Im}[\chi^{(2)}]$ spectra of aqueous HA_{LMW} solutions with a concentration of (a) 1 mg/ml, (b) 2.5 mg/ml, (c) 3.5 mg/ml and (d) 4.5 mg/ml at the water-air interface in a time range of 0 min - 240 min. The measurements were taken in SSP polarization configuration (s-SFG, s-VIS, p-IR) and the pH is regulated with phosphate buffer to 7.4, as described in the text. For all HA_{LMW} solutions it can be observed that two signals in the CH region appear and the broad water band is changing sign. For low concentrations of hyaluronic acid (1 mg/ml and 2.5 mg/ml) the signal of the free OH at 3700 cm^{-1} decreases over time while for high concentrations (3.5 mg/ml and 4.5 mg/ml) it vanishes completely.

The $\text{Im}[\chi^{(2)}]$ spectrum of the HA solution differs strongly from the spectrum of pure water. In the region of 2850 cm^{-1} to 3000 cm^{-1} we find two narrow features that are associated with the CH vibrations of the HA molecules. Based on previous work we assign the two negative bands centered at 2880 cm^{-1} and 2940 cm^{-1} to the symmetric stretch vibration of the methyl group (ν_{CH_3}) and its Fermi resonance overlapping with the symmetric stretch vibration of the methylene group ($\nu_{\text{CH}_2, \text{SS}}$) respectively.^{32,251} The positive band at $\sim 2975 \text{ cm}^{-1}$ is assigned to the asymmetric stretch of the methylene group ($\nu_{\text{CH}_2, \text{AS}}$).^{32,257} The negative sign of the $\nu_{\text{CH}_2, \text{SS}}$ and the positive sign of $\nu_{\text{CH}_2, \text{AS}}$, show that the methylene groups have a net orientation with the CH bonds pointing toward the air phase. The negative sign of the ν_{CH_3} band suggests that the methyl groups are also pointing preferentially toward air.^{32,251} Between 3100 cm^{-1} and 3550 cm^{-1} we observe a broad signal that is associated with the OH stretch vibrations of interfacial water molecules. The positive sign of the broad OH stretch signal shows that the interfacial water molecules have a net orientation with the OH groups pointing toward the interface. The change in net orientation

of the water molecules compared to pure water, indicates that the surface is negatively charged³², as a result of the accumulation of HA molecules at the surface. Because of its pK_a of 2.9, hyaluronan is expected to be completely deprotonated in the bulk and thus negatively charged at pH 7.⁶⁴ In Figure 10.1 (b,c) we show a schematic that shows the orientation of water molecules for pure water and HA_{LMW} solution at the surface. The vanishing of the non hydrogen-bonded OH can be explained by the complete surface coverage by HA molecules.

It should be noted that HA_{LMW} only comes to the surface if a sufficient amount of ions are present in the solution (Appendix Figure 10.8 and 10.9). This observation can likely be explained from the competition between the ions and HA for the solvent molecules. Salt ions interact strongly with water molecules^{258,259}, thereby excluding the polymers from the bulk and pushing the polymer chains toward the surface. An additional effect may be the screening of the favorable interaction of the carboxylate anion groups of hyaluronan with water by the sodium ions.

10.3.1 EFFECT OF THE HYALURONAN CONCENTRATION ON ITS ACCUMULATION AT THE SURFACE

Figure 10.2 (a-d) shows the $Im[\chi^{(2)}]$ spectra of HA_{LMW} solutions with different concentrations in the time range of 0 min - 240 min. In Figure 10.2 (a), the $Im[\chi^{(2)}]$ spectra of a HA_{LMW} solution with a concentration of 1 mg/ml is presented. It can be observed that at 0 min the spectrum of the HA_{LMW} solution looks identical to that of a neat water surface. Over time we observe that the sign of the broad water OH stretch band at 3100 - 3550 cm^{-1} changes from negative to positive. This sign change reflects a change in the net orientation of the water molecules. At 0 min, the hydrogen atoms of the water molecules have a net orientation toward the bulk. Gradually, the water molecules are orienting more and more with their hydrogen atoms toward the surface, which is due to the accumulation of negatively charged HA molecules at the surface. For higher concentrations (Figure 10.2 (b,d)) of 2.5 mg/ml - 4.5 mg/ml we additionally observe that the response of the non hydrogen-bonded OH vibrations centered at 3700 cm^{-1} decreases and eventually vanishes completely, and that in the CH region two peaks appear that can be assigned to the methyl group (ν_{CH_3}) and the methylene group ($\nu_{CH_2,SS}$) of the HA molecules.^{32,251} We also find that the peak height of the non hydrogen-bonded molecules centered at 3700 cm^{-1} reduces to $\sim 65\%$ of its original value simultaneous with the first appearance of the CH vibrations of the polymer backbone. Hence, we conclude that to get a clear VSFG signal of the HA molecules, their surface coverage needs to be $\sim 35\%$, as the HD-VSFG signal is proportional to the surface density. The maximum studied bulk concentration is 4.5 mg/ml, which corresponds to $\sim 0.5\%$, which implies that the final surface concentration is much higher than the bulk concentration, showing that over time HA accumulates at the surface. The difference between the $Im[\chi^{(2)}]$ spectrum of HA_{LMW} solutions and that of pure water becomes more pronounced with increasing polymer concentration. Furthermore, it is observed that the spectral changes occur faster with

increasing HA_{LMW} concentration. Consistent with this notion is that increasing the bulk concentration of the HA_{LMW} solution, leads to faster mass transport diffusion²⁶⁰ and thus a faster accumulation of HA polymers at the surface.²⁶¹ We also performed surface tension measurements of HA_{LMW} in a sodium phosphate buffer (137 mM NaCl, 10mM Na_2HPO_4 , 2.7 mM KCl) with a pH of 7.4. As shown in Figure 10.10 and 10.11 of the Appendix, we observe no changes in the surface tension over time for solutions containing different concentrations of HA_{LMW} . It is more often observed that the surface tension of polyelectrolyte solutions is similar to that of water, even though the polyelectrolyte possesses a higher propensity at the surface than in the bulk.²⁶² The absence of an effect on the surface tension can be explained by the fact that the polyelectrolyte solution also contains counterions that often strongly interact with water, and that thus have an opposing effect on the surface tension. The advantage of VSFG in detecting the surface accumulation of HA is that this technique is highly selective in probing HA, and not affected by the other properties of the solution.

The spectral changes in the CH region indicate that, after diffusion to the surface, a rearrangement of the polymers takes place. The peak of the methylene group ($\nu_{\text{CH}_2, \text{SS}}$) overlapping with the Fermi resonance of the methyl group at 2940 cm^{-1} appears first, whereas at later times the signal of the symmetric stretch vibration of the methyl group at 2880 cm^{-1} becomes dominant (Appendix Figure 10.12). The observation of signals of CH_2/CH_3 suggests that the polymer backbone is aligned along the interfacial plane, with the hydrophobic groups pointing into the air and the negatively charged groups buried in the water, and thus pointing toward the bulk.^{263,264} This observation is in line with the formation of so-called *train* segments of polymers at interfaces.^{264,265}

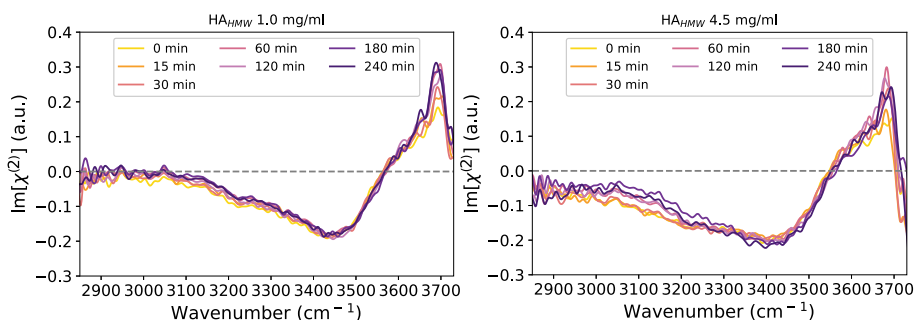


FIGURE 10.3. $\text{Im}[\chi^{(2)}]$ spectra of high molecular weight hyaluronan (HA_{HMW}) solutions with concentrations of (a) 1 mg/ml and (b) 4.5 mg/ml in a time frame of 0 min - 240 min. The HA solutions have a pH of 7.4 regulated with a phosphate buffer.

10.3.2 EFFECT OF HYALURONAN MOLECULAR WEIGHT ON ITS ACCUMULATION AT THE SURFACE

To study the effect of the molecular weight of the polymers on the surface accumulation, we also measured the adsorption kinetics of hyaluronic acid solutions with a high molecular weight ($\text{HA}_{\text{HMW}} \sim 1.5 - 1.8 \text{ MDa}$) at different concentrations, in a time frame of 0 min - 240 min. We observe in Figure 10.3 (a) that the HA_{HMW} solution shows a similar spectrum as a neat water-air interface. In contrast to HA_{LMW} , the spectra are observed to stay similar over time. Therefore, we conclude that HA_{HMW} molecules do not adsorb to the water surface, even at a concentration of 4.5 mg/ml (Figure 10.3 (b)). Similar results were obtained at concentrations of 2.5 mg/ml and 3.5 mg/ml, as shown in the Appendix (Figure 10.13).

The large difference in observed surface accumulation between HA_{LMW} and HA_{HMW} must be primarily due to a kinetic effect as the thermodynamics of these solutions are highly similar. Here, we cannot exclude the formation of intramolecular aggregates, but we can exclude that this would cause the observed difference in kinetics. The tendency to form intramolecular aggregates will be quite similar for LMW and HMW hyaluronan, as the two polymers are composed of exactly the same disugar units and both have chain lengths that are much longer than their persistence length. Hence, if there would be intramolecular aggregation this would occur similarly for HA_{LMW} and HA_{HMW} . The difference in kinetics for the surface accumulation of HA_{LMW} and HA_{HMW} likely follows from the following two effects.

In the first place HA_{LMW} diffuses faster than HA_{HMW} due to its ~ 10 times shorter chain length. A second effect, that becomes important at high concentrations, is the overlap and entanglement of HA_{HMW} molecules, which strongly restricts diffusive motion.²⁶⁶ The overlap concentration of HA_{LMW} of $\sim 10 \text{ mg/ml}$ is much higher than the overlap concentration of $\sim 1.5\text{-}2 \text{ mg/ml}$ of HA_{HMW} .^{267,268} Therefore, the shorter polymer chains have a much higher mobility than HA_{HMW} molecules. To support this argument further, we also measured the dynamics of a HA_{HMW} solution with an even higher concentration of 5.5 mg/ml. We find that very long waiting times HA_{HMW} does get adsorbed to the surface, and shows the same vibrational features as HA_{LMW} (Figure 10.14).). This finding indicates that HA_{LMW} also tends to accumulate at the surface, like HA_{LMW} , only the rate at which this happens is much lower.

10.3.3 EFFECT OF pH ON THE SURFACE ACCUMULATION OF HYALURONAN

In Figure 10.4 we show the $\text{Im}[\chi^{(2)}]$ spectra of a HA_{LMW} solution in the region of the OH stretch vibrations measured at pH 2 and a NaCl concentration of 150 mM. This pH value is below the isoelectric point of HA (2.5)¹³³, meaning that at this pH the HA polymers are no longer negatively charged. Surprisingly very little change between the spectra measured at different waiting times can

be observed in comparison to water. The rise of the CH peaks at later delay times shows that hyaluronan comes to the surface, but quite delayed and to a much lesser extent than at pH 7.4 (Figure 10.2). It is also seen that the arrival of hyaluronan at the surface does not lead to a change of the sign of the water OH band. This latter observation can be explained from the fact that at these low pH values 90 % of all carboxylate anion groups of hyaluronan⁶⁴, which has an isoelectric point of 2.5¹³³, will be protonated. Hence, hyaluronan will carry only 10 % negative charge, and the accumulation of hyaluronan at the surface does not induce a change of the orientation of the water OH groups from a net orientation to the bulk to a net orientation to the surface.⁶⁴

To study the pH dependence of the surface accumulation of HA in more detail, we performed intensity VSGF measurements of hyaluronan at different pH values in the frequency region of the carboxylate anion and carbonyl vibrations of hyaluronan (1300 - 1900 cm^{-1}). In Figure 10.5 we present intensity VSGF measurements of 4.5 mg/ml HA_{LMW} solutions in the frequency region of 1300 - 1900 cm^{-1} measured at different pH values in a time frame of 0 - 120 min. The pH was adjusted by adding HCl or NaOH to the solution. At all pH values the NaCl concentration was 150 mM. Figure 10.5 (a) shows the intensity VSGF spectra of a HA solution with pH 2. The spectra at different times all show a broad band around 1650 cm^{-1} , which can be assigned to the bending mode of water. The observed spectrum is similar to the spectrum observed in previous intensity VSGF measurements of the neat water surface (Appendix Figure 10.15).^{34,35} At pH 4.5 (Figure 10.5 (b)) we observe the same spectrum as at pH 2. For HA solutions with a pH above 7 (Figure 10.5 (c) and (d)), two prominent features appear in the spectra at 1420 and 1720 cm^{-1} . We assign the narrow peak at 1420 cm^{-1} to the symmetric stretch vibration of the carboxylate anion ($\nu_{\text{ss},\text{COO}^-}$) of HA, and the narrow peak at 1720 cm^{-1} to the carbonyl stretch vibration of the carboxylic acid group ($-\text{COOH}$) of HA.^{13,269} In view of the bulk

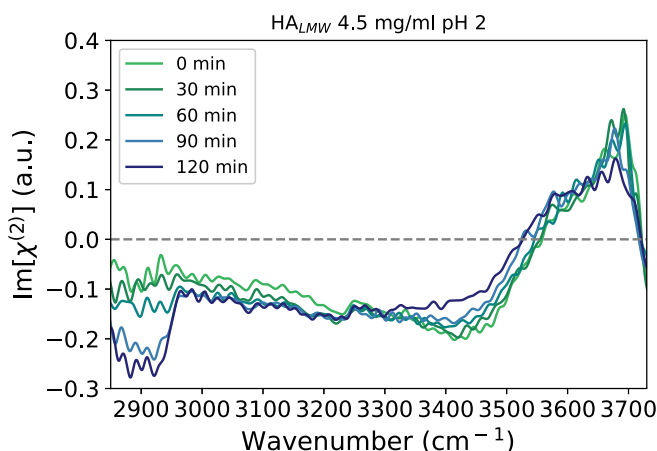


FIGURE 10.4. $\text{Im}[\chi^{(2)}]$ spectra of HA_{LMW} solutions with a concentration of 4.5 mg/ml at pH 2 in the time frame of 0 min - 90 min.

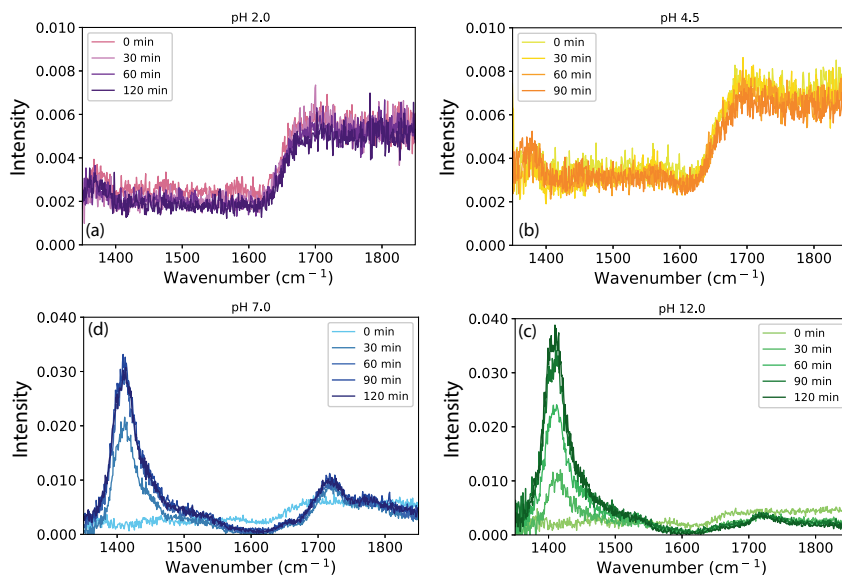


FIGURE 10.5. Intensity SFG spectra of 4.5 mg/ml HA_{LMW} solutions with different pH values of (a) 2 (magenta), (b) 4.5 (yellow), 7 (blue), and (d) 12 (green). The pH was adjusted using HCl and NaOH, while the salt concentration was constant at 150 mM of NaCl over all measurements

pK_a of HA, the presence of protonated carboxyl groups is unexpected at pH values above 6. However, in previous work it was found that the degree of acid dissociation at the surface can differ strongly from the degree of acid dissociation in the bulk.^{269,270} We observe that at pH=12 (Figure 10.5 (c)) the relative intensity of the COOH band is reduced compared to pH=7, indicating a further deprotonation of hyaluronan at the interface. This pH-dependence supports the assignment of the peak at 1720 cm^{-1} to the carbonyl stretch vibrations of the protonated carboxylic acid. Nevertheless, it is surprising that the feature at 1720 cm^{-1} does not vanish completely at pH 12, since one would expect HA_{LMW} to be completely deprotonated at this high pH, even at the surface. It could be that the surface contains a small amount of contaminations that gives rise to a small signal at 1720 cm^{-1} at all pH values, and that forms the only contribution to this signal at pH 12.

To quantify the effect of the solution pH on the surface accumulation of HA_{LMW} with a concentration of 4.5 mg/ml, we plot in Figure 10.6 the sum of the band areas below the COOH and COO^- peaks as function of the pH. The band areas were extracted from a fitting procedure using Lorentzian curves centered at 1720 cm^{-1} and 1420 cm^{-1} . The fitting procedure is illustrated in Figure 10.16 of the Appendix. Figure 10.6 clearly shows that the surface propensity strongly depends on the pH. For HA_{LMW} solutions at low pH the band areas at 1720 cm^{-1} and 1420 cm^{-1} are zero, while increasing the pH to 7 leads to a strong increase of the summed band areas, indicating that HA_{LMW}

molecules accumulate at the surface.

Previous measurements on polyacrylic acid (PAA) at water/air and water/oil interface also showed a high sensitivity of the degree of accumulation at the surface on the pH value.^{251,271-273} For PAA solutions, it was observed that increasing the bulk pH led to depletion of the polymers from the surface, because of the relative increase of carboxylate anion groups with respect to the COOH. In this context, it is remarkable and surprising that in the case of hyaluronan, depletion from the surface occurs upon lowering of the pH value. A possible explanation for this anomalous behavior of HA_{LMW} lies in the specific interchain interactions of HA that arises from low pH values. A special property of aqueous solutions of HA is that they form an elastic hydrogel near a pH value of 2.5.⁶⁴ In a recent study we showed that the formation of the hydrogel finds its origin in an enhanced interchain interaction of the HA polymer chains, in particular in the formation of interchain hydrogen bonds between amide groups and carboxylate anion groups, and between amide groups and carboxylic acid groups.⁶⁴ At high pH values these interchain hydrogen bonds do not form, because the polymer chains are strongly negatively charged and therefore repel each other. When the pH is lowered, carboxylate anion groups get protonated and the Coulombic repulsion between the polymers is decreased. As a result, the hyaluronan polymer chains will form interchain hydrogen bonds that continuously break and reform. This dynamic sticking of the hyaluronan polymers will strongly decrease their rate of diffusion, which provides an explanation why hyaluronan does not come to the surface even within a few hours at pH values <7. Here, it is important to mention that at low pH values <2.5 HA can also form aggregates which can cause a depletion from the surface.⁶⁴ In our measurements we can find that also at pH values of 4.5 and 5.5 HA_{LMW} is absent from the surface. Therefore, we suggest that the formation of interchain hydrogen bonds between the HA molecules is the main reason for the depletion of HA from the surface. At the bottom of Figure 10.6 we show a schematic drawing of the structure of the HA polymer chains in the two different pH regimes. The anomalous pH dependence of the accumulation at the surface of hyaluronan can thus be well explained from the special property of hyaluronan to show enhanced interchain interactions at low pH values.

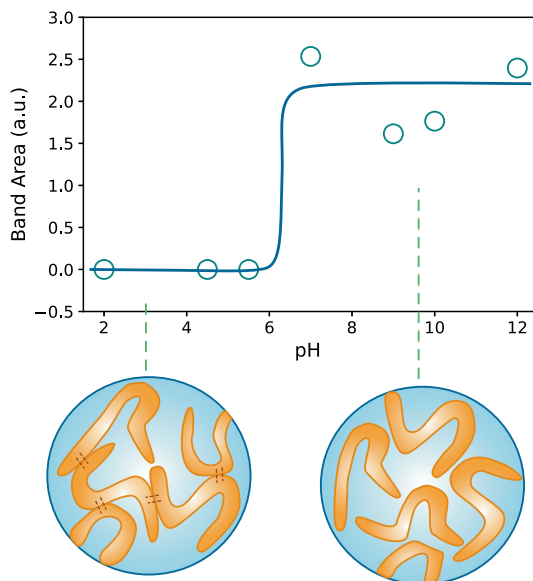


FIGURE 10.6. Sum of the band areas of the COOH and the COO⁻ peak of a 4.5 mg/ml HA_{LMW} solution at different pH values. The band areas were extracted from a fitting procedure using two Lorentzian curves. The solid line is a guide to the eye. Below the plot: Schematic pictures of hyaluronan polymers in solution in two different pH regimes, showing that for low pH value the HA polymer chains have enhanced interchain interaction, while diffusing freely in the solvent for high pH values.

10.4 CONCLUSIONS

We used vibrational sum-frequency generation (VSFG) and heterodyne-detected VSFG (HD-VSFG) to study the dependence of the surface accumulation and surface structure of hyaluronan polymers on the molecular weight and concentration of the polymers and the pH of the solution. The VSFG measurements show that at 1 mg/ml, low-molecular weight (~ 150 kDa) hyaluronan accumulates at the surface within a few hours, rendering the surface negatively charged due to the presence of carboxylate anion groups in the hyaluronan polymers. This rate strongly increases when the concentration of low-molecular weight hyaluronan increases. High molecular weight (~ 1000 kDa) hyaluronan does not accumulate at the surface within hours, which we explain from the much lower rate of diffusion of these polymers. The difference in observed surface accumulation between HA_{LMW} and HA_{HMW} is thus primarily due to kinetic effects. We find that the surface accumulation of hyaluronan strongly depends on the pH of the solution. A lowering of the pH of the solvent strongly decreases the degree of accumulation of hyaluronan at the surface, which we explain from the enhanced interchain interactions of the hyaluronan polymer chains and the consequent decrease of the rate of diffusion of the polymer chains. The present results show that the migration of hyaluronan to the surface shows

a strong and anomalous dependence on the polymer molecular weight and the properties of the solution, which can aid the understanding of some of the characteristic interfacial properties of these solutions, like its lubrication behavior and its biochemical interactions. It would be highly interesting to investigate the migration behavior and surface properties of hyaluronan also for other aqueous interfaces, and for varying solution properties, e.g. to study the effect of different salts on the rate of surface accumulation. We hope that the present work will stimulate experimental and theoretical work in this direction.

10.5 APPENDIX

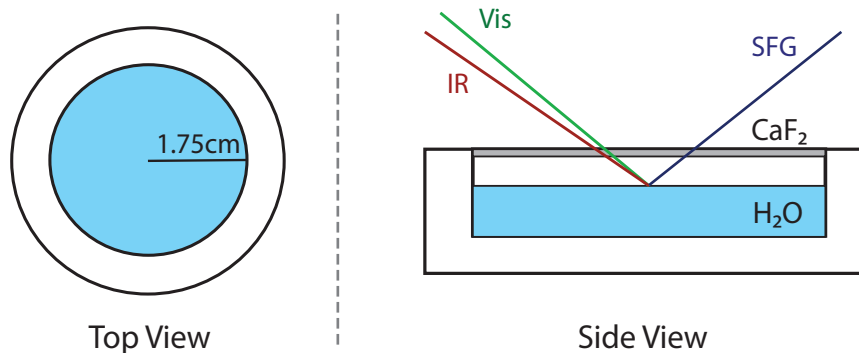


FIGURE 10.7. Schematic of the custom built sample cell made of Teflon and covered by a calcium fluoride window. The sample cell has a diameter of 3.5 cm and can hold a sample volume of 4 ml.

10.5.1 EFFECT OF THE SALT CONCENTRATION IN THE SOLVENT ON THE ACCUMULATION OF HYALURONAN AT THE SURFACE

In Figure 10.8 we show $\text{Im}[\chi^{(2)}]$ spectra in the region of the OH stretch vibrations of 4.5 mg/ml HA_{LMW} in pure water without salt added to the solution in a time range of 0 - 90 min with a pH of 7. It is seen that in the absence of salt, HA_{LMW} does not come to the surface. To confirm the depletion of HA_{LMW} from the surface by removing salt from the solvent, we performed additional measurements in the frequency region of the carboxylate anion and carbonyl vibrations of hyaluronan at 1350 cm^{-1} - 1850 cm^{-1} .

In Figure 10.9, we show intensity VSGF spectra of 4.5 mg/mL HA_{LMW} solutions with different concentrations of NaCl in a time frame of 0 - 90 min. Figure 10.9 (a) show the intensity VSGF spectra of HA_{LMW} without any additional salt added to the solution. The spectra show the response of the water bending mode at 1650 cm^{-1} that is identical to the line shape that is observed for a neat water surface (Figure 10.15).^{34,35} This observation confirms the observation of Figure 10.8 that HA polymers do not adsorb to the water/air interface if there is no salt present in the solution. When 150 mM NaCl is added to the 4.5 mg/ml HA_{LMW} solution, two prominent features are appear in the spectrum (Figure 10.9 (b)) at 1420 cm^{-1} and 1720 cm^{-1} , which we assign to the vibration of the symmetric mode of the COO⁻ group and to the vibration of the carbonyl mode of the COOH group, respectively.^{13,269} The presence of these two peaks indicates that for the salt containing solution, HA molecules are able to accumulate at the surface. Increasing the NaCl concentration further does not lead to additional changes in the adsorption process (Figure 10.9(c)). Figure 10.9 (b) and

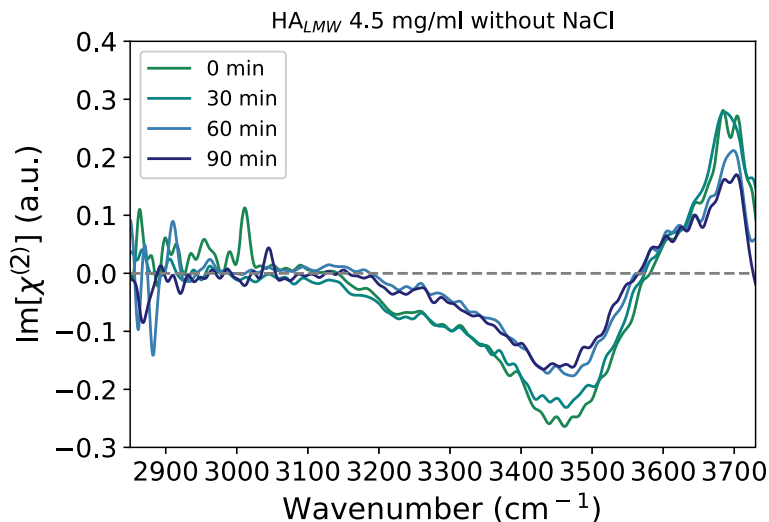


FIGURE 10.8. $\text{Im}[\chi^{(2)}]$ spectra of HA_{LMW} solutions with a concentration of 4.5 mg/ml with pH 7 and no NaCl added to the solution in the time frame of 0 min - 90 min.

(c) show that the peak height at 1420 cm^{-1} increases over time, while the peak at 1720 cm^{-1} stays more or less constant. The absence of a time-dependence of the $-\text{COOH}$ band can be explained by the higher surface propensity of the protonated carboxyl groups of the HA polymers. Previous surface tension studies showed that the surface activity for protonated fatty acids is higher than for their deprotonated analogues.²⁷⁰ It should be noted that the rise of the signal of HA coming to the surface in Figures 10.9 (b) and (c) is somewhat delayed compared to the result of Figure 10.2 (d) where we probed the signal of water for a highly similar solution containing salt and 4.5 mg/ml of HA_{LMW} . This difference can be explained by the fact that Figure 10.2 of the manuscript and Figure 10.9 represent experiments in different frequency regions and with different acquisition times. In the experiment of Figure 10.9 we used an infrared pulse centered at $6\ \mu\text{m}$ which yields a slightly different local temperature than the experiment of Figure 10.2 where we used a $3\ \mu\text{m}$ pulse that is much more strongly absorbed by water. In addition, Figure 10.9 represents an intensity VSFG experiment with a longer acquisition time than the HD-VSFG experiment of Figure 10.2. These differences do not affect the overall trend, being that for a solution containing 4.5 mg/ml of HA_{LMW} and a sufficient amount of salt, HA_{LMW} comes to the surface within ~ 30 min, but they do lead to differences in the observed early-time dynamics.

The enhanced surface accumulation of hyaluronan in the presence of salt can likely be explained from the competition of the ions with the solvent molecules. Salt ions interact strongly with water molecules,^{258,259} thereby excluding the polymers from the bulk and pushing the polymer chains toward the surface. This phenomenon was described before for proteins and is well known under the

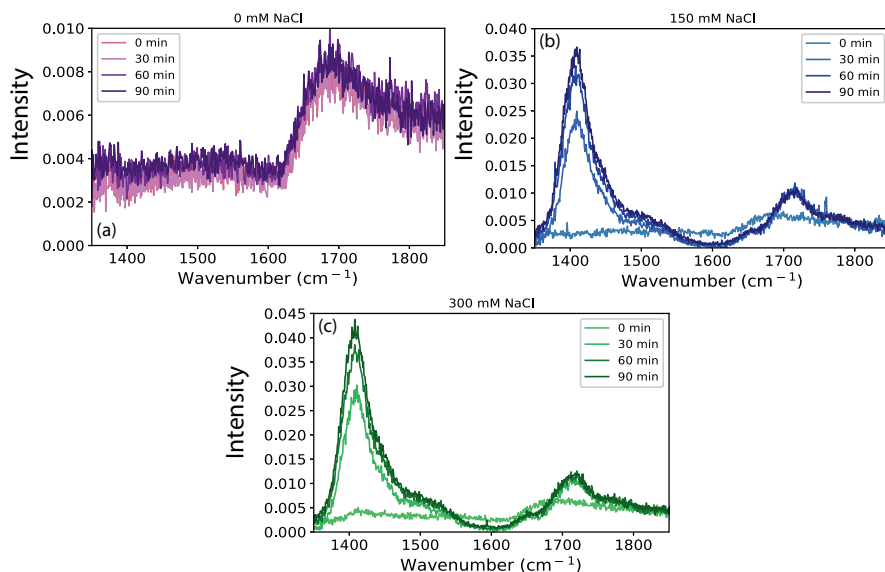


FIGURE 10.9. Intensity SFG spectra of 4.5 mg/ml HA_{LMW} solutions with different NaCl concentrations of (a) 0 mM (magenta), (b) 150 mM (blue) and (c) 300 mM (green).

name "salting up" effect.⁶⁷ An additional effect may be that the cations shield the negative charges of the carboxylate anion groups. As a result, these groups have a less strong interaction with water and the surface propensity increases. Hence, the presence of ions makes it more favorable for HA to accumulate at the surface. Without ions, the bulk-surface equilibrium is strongly shifted toward the bulk.

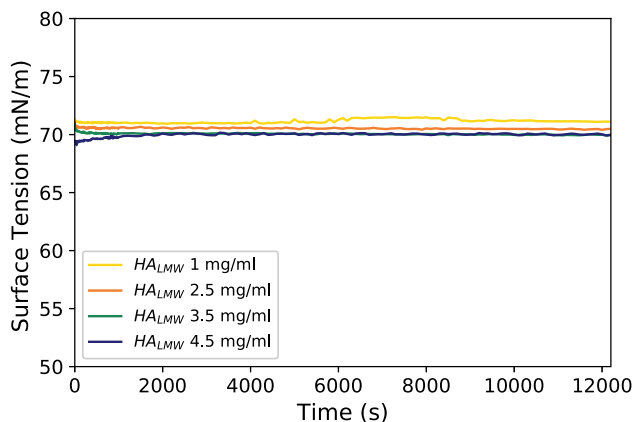


FIGURE 10.10. Surface tension measurements of HA_{LMW} in a sodium phosphate buffer (137 mM NaCl, 10 mM Na₂HPO₄, 2.7 mM KCl) with a pH of 7.4 for different concentrations of 1 mg/ml, 2.5 mg/ml, 3.5 mg/ml and 4.5 mg/ml.

10.5.2 SURFACE TENSION

The effect of hyaluronic acid on the water-air surface tension is measured with the pendant drop method. We performed the pendant drop measurements by using a DSA 30S drop shape analyzer (Kruss, Germany) and analyzed the measurements with the Kruss Advanced software. For each measurement, a 15 μ l droplet of hyaluronic acid solution is formed with a rate of 2 μ l per second using an automated dosing system from a hanging glass syringe with needle diameter of 1.060 mm (Hamilton). After the droplet reaches its final volume, images are taken over the course of four hours to follow the evolution of the droplet's shape. From these frames, the droplet contour is detected automatically and fitted with the Young-Laplace equation to yield the interfacial tension. All measurements are performed in a closed and humid environment to minimize water evaporation from the droplet.²⁷⁴

The surface tension measurement show that for HA_{LMW} in a sodium phosphate buffer (137 mM NaCl, 10 mM Na₂HPO₄, 2.7 mM KCl) with a pH of 7.4, the surface tension stays constant at a value of \sim 70 mN/m over a time frame of 240 min (Appendix Figure 10.10). This notion applies to all studied concentrations of 1 mg/ml, 2.5 mg/ml, 3.5 mg/ml and 4.5 mg/ml. Furthermore, we performed surface tension measurements for HA_{LMW} with a concentration of 4.5 mg/ml and 150 mM of NaCl at a pH of 2 (Appendix Figure 10.11). We again observe no change of the surface tension within 240 min. It should be noted that this does not mean that HA_{LMW} does not come to the surface. For a polyelectrolyte solution the tendency of the polyelectrolyte to come to the

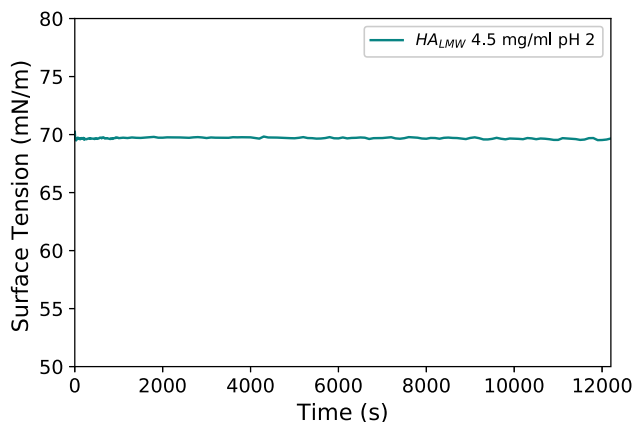


FIGURE 10.11. Surface tension measurements of HA_{LMW} with a concentration of 4.5 mg/ml and 150 mM of NaCl with a pH of 2.

surface is not necessarily associated with a decrease of the surface tension. A polyelectrolyte will have a quite favorable (Coulombic) interaction with water, so the gain in free energy of coming to the surface is much smaller for a polyelectrolyte surfactant than for instance for a neutral surfactant. In addition, a polyelectrolyte has counter-ions for which an increase of the surface area leads to a negative free-energy change, because a larger number of these ions is forced in the near surface area where the hydration interactions with these ions are less favorable. Hence, for a polyelectrolyte solution compared to pure water, an increase in surface has both a positive effect on the free energy in making more room for the polyelectrolyte, but also a negative effect in forcing more of the counter ions into the near surface region. These two opposing effects can compensate each other, with the result that the surface tension of a polyelectrolyte solution is similar to that of pure water and does not change when the concentration of the polyelectrolyte (and thus of its counterions) is increased.²⁶² The HD-VSFG measurements show very clearly that HA_{LMW} does come to the surface. An essential characteristic of HD-VSFG is that it measures the vibrational spectrum of the molecules at the surface, which constitutes a far more specific probe compared to the surface tension.

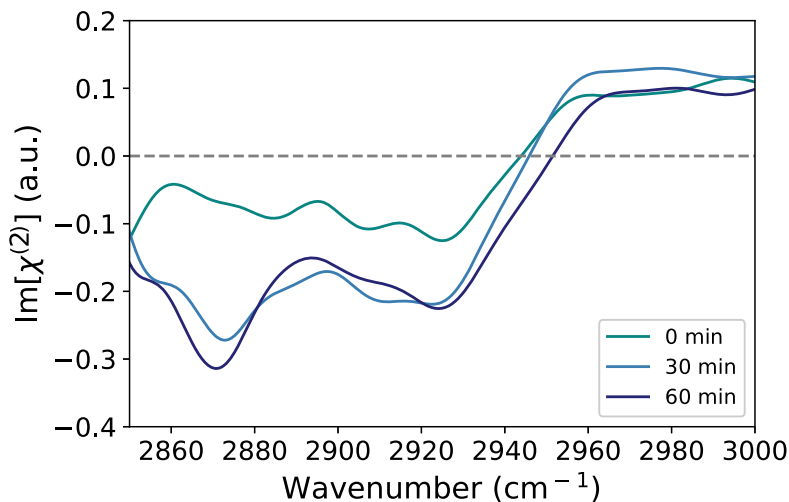


FIGURE 10.12. $\text{Im}[\chi^{(2)}]$ spectra of 4.5 mg/ml HA_{LMW} solutions measured over a time range of 0 - 60 min in the frequency region of the CH vibrations. The spectrum at 30 min shows the rise of the response of the symmetric stretch vibration of the methylene group ($\nu_{\text{CH}_2, \text{SS}}$) overlapping with the Fermi resonance of the methyl group at 2940 cm^{-1} . After 30 min the peak at 2880 cm^{-1} of the symmetric stretch vibration of the methyl group becomes dominating. This latter change of the spectrum indicates a reorganization of the HA molecules at the surface.

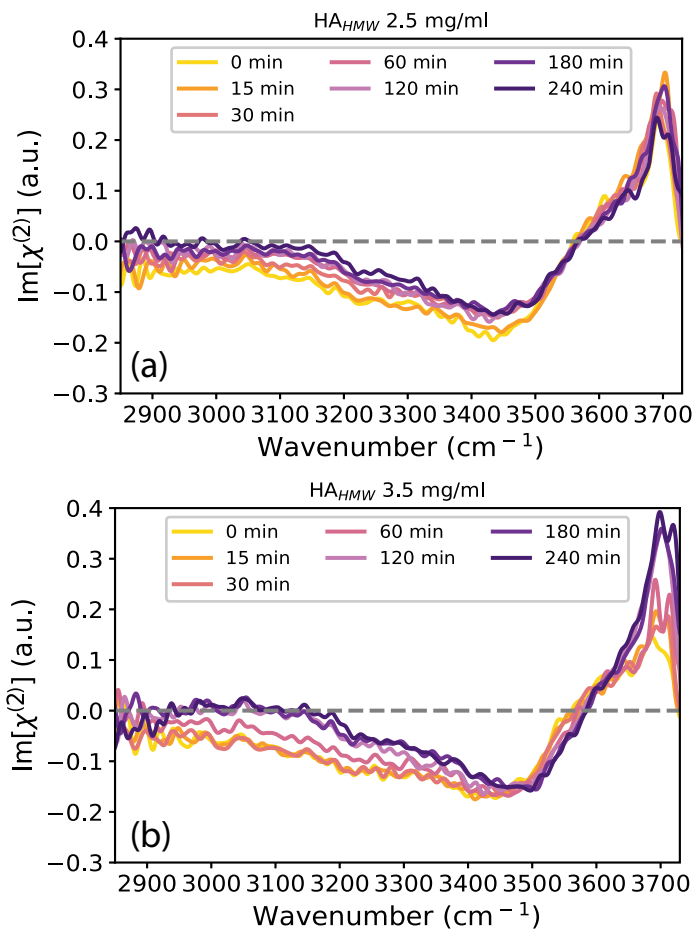


FIGURE 10.13. $\text{Im}[\chi^{(2)}]$ spectra of (a) 2.5 mg/ml and (b) 3.5 mg/ml HA_{HMW} solutions in a time frame of 0 - 240 min. For both concentrations the spectra are identical to the spectrum of a neat water surface. This means that HA_{HMW} does not accumulate at the solution surface within a time of 240 min for this concentrations.

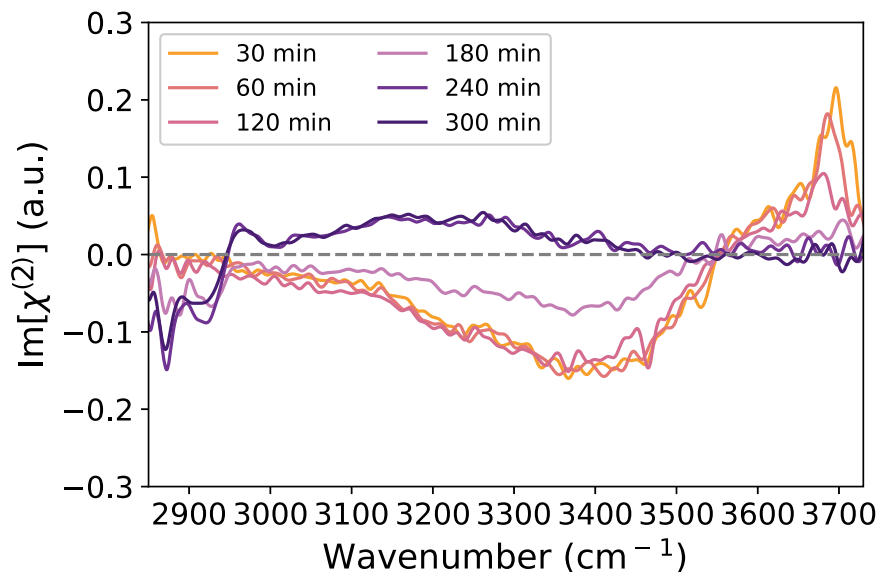


FIGURE 10.14. $\text{Im}[\chi^{(2)}]$ spectra of 5.5 mg/ml HA_{HMW} solutions in a time frame of 0 - 300 min. HA_{HMW} accumulates at the solution surface after very long waiting times of more than 240 min and shows the same vibrational features as HA_{LMW} . This measurement shows that the difference in surface accumulation of HA_{LMW} and HA_{HMW} is due to kinetic effects.

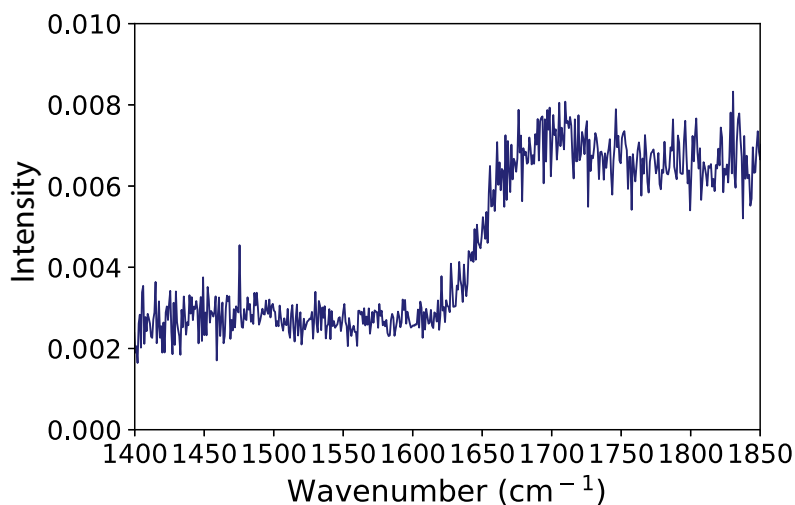


FIGURE 10.15. Intensity SFG spectra of a neat water surface in the frequency range of 1400 - 1850 cm^{-1} . The measurement was taken in SSP polarization configuration (s-SFG, s-VIS, p-IR).

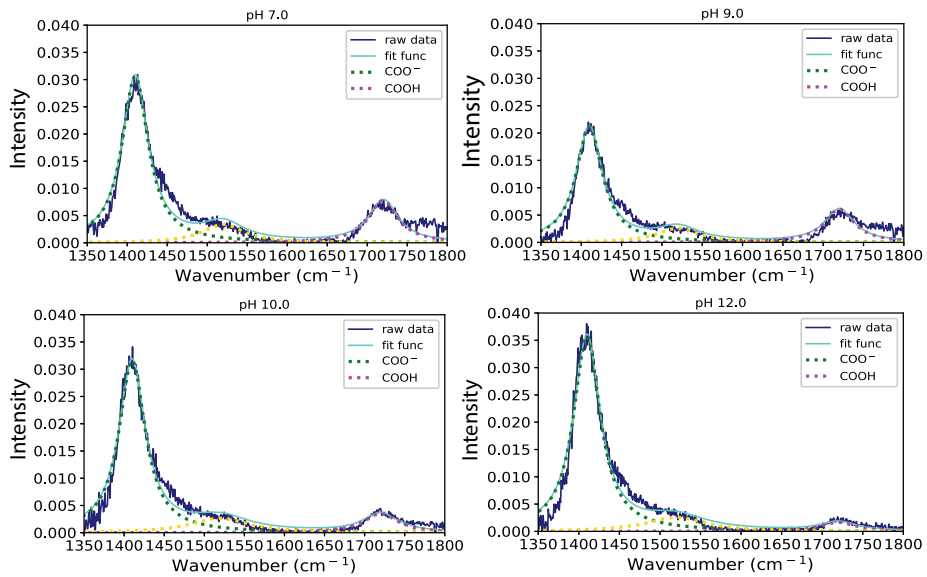


FIGURE 10.16. Shows the fitting procedure with lorentzian curves of the intensity VSFG spectra of HA_{LMW} with a concentration of 4.5 mg/ml at different pH values at 120 min.

In the Figure 10.16 the fitting procedure with Lorentzian curves of the intensity VSFG spectra of HA_{LMW} with a concentration of 4.5 mg/ml at different pH values at 120 min is shown. We fit the spectra with the sum of three different Lorentzian shape like curves centered at 1420 cm⁻¹, 1520 cm⁻¹ and 1720 cm⁻¹. The peak at 1420 cm⁻¹ is assigned to the symmetric stretch vibration of the carboxylate anion (ν_{ss,COO^-}) of HA, and the narrow peak at 1720 cm⁻¹ to the carbonyl stretch vibration of the carboxylic acid group (-COOH) of HA. In addition to the two dominant peaks at 1420 cm⁻¹ and 1720 cm⁻¹ we extract another peak centered at 1520 cm⁻¹. Here we suggest that this peak, that appears like a shoulder of the 1720 cm⁻¹ feature in the VSFG intensity spectra, can be assigned to the antisymmetric stretch vibrations of the carboxylate anion. To make a quantitative assessment about the surface propensity of HA_{LMW} at the surface we only take the sum of the vibrational modes of the stretch vibrations of the carboxylate anion (ν_{ss,COO^-}) and the carbonyl stretch vibration of the carboxylic acid group (-COOH).

BIBLIOGRAPHY

1. B. Lautrup, *Physics of Continuous Matter: Exotic and Everyday Phenomena in the Macroscopic World*. Boca Raton: CRC Press, 2011.
2. R. Garcia and R. Pérez, “Dynamic atomic force microscopy methods,” *Surface Science Reports*, vol. 47, no. 6, pp. 197–301, 2002.
3. G. Binnig, C. F. Quate, and C. Gerber, “Atomic Force Microscope,” *Physical Review Letters*, vol. 56, no. 9, pp. 930–933, 1986.
4. Y. R. Shen, “Surface properties probed by second-harmonic and sum-frequency generation,” *Nature*, vol. 337, pp. 519–525, 1989.
5. J. H. Hunt, P. Guyot-Sionnest, and Y. R. Shen, “Observation of C-H stretch vibrations of monolayers of molecules optical sum-frequency generation,” *Chemical Physics Letters*, vol. 133, no. 3, pp. 189–192, 1987.
6. S. K. Sinha, E. B. Sirota, S. Garoff, and H. B. Stanley, “X-ray and neutron scattering from rough surfaces,” *Physical Review B*, vol. 38, pp. 2297–2311, 1988.
7. S. Strazdaite, K. Meister, and H. J. Bakker, “Orientation of polar molecules near charged protein interfaces,” *Physical Chemistry Chemical Physics*, vol. 18, no. 10, pp. 7414–7418, 2016.
8. Y. C. Wen, S. Zha, X. Liu, S. Yang, P. Guo, G. Shi, H. Fang, Y. R. Shen, and C. Tian, “Unveiling Microscopic Structures of Charged Water Interfaces by Surface-Specific Vibrational Spectroscopy,” *Physical Review Letters*, vol. 116, no. 1, p. 016101, 2016.
9. P. Lo Nostro and B. W. Ninham, “Hofmeister phenomena: An update on ion specificity in biology,” *Chemical Reviews*, vol. 112, no. 4, pp. 2286–2322, 2012.
10. L. Zhang, Y. Yang, Y. T. Kao, L. Wang, and D. Zhong, “Protein hydration dynamics and molecular mechanism of coupled water-protein fluctuations,” *Journal of the American Chemical Society*, vol. 131, no. 30, pp. 10677–10691, 2009.
11. M. F. Toney, J. N. Howard, J. Richer, G. L. Borges, J. G. Gordon, O. R. Melroy, D. G. Wiesler, D. Yee, and L. B. Sorensen, “Voltage-dependent ordering of water molecules at an electrode-electrolyte interface,” *Nature Letters*, vol. 368, pp. 444–446, 1994.

12. C. Dutta, M. Mammetkuliyeu, and A. V. Benderskii, "Re-orientation of water molecules in response to surface charge at surfactant interfaces," *Journal of Chemical Physics*, vol. 151, no. 3, p. 034703, 2019.
13. C. M. Johnson, E. Tyrode, S. Baldelli, M. W. Rutland, and C. Leygraf, "A Vibrational Sum Frequency Spectroscopy Study of the Liquid - Gas Interface of Acetic Acid - Water Mixtures : 1 . Surface Speciation," *Journal of Physical Chemistry B*, vol. 109, no. 1, pp. 321–328, 2005.
14. A. K. Soper, "The radial distribution functions of water and ice from 220 to 673 K and at pressures up to 400 MPa," *Chemical Physics*, vol. 258, no. 2, pp. 121–137, 2000.
15. R. Kumar, J. R. Schmidt, and J. L. Skinner, "Hydrogen bonding definitions and dynamics in liquid water," *Journal of Chemical Physics*, vol. 126, no. 20, p. 204107, 2007.
16. Q. Du, R. Superfine, E. Freysz, and Y. R. Shen, "Vibrational spectroscopy of water at the vapor/water interface," *Physical Review Letters*, vol. 70, no. 15, pp. 2313–2316, 1993.
17. M. Moskovits and K. H. Michaelian, "A reinvestigation of the Raman spectrum of water," *The Journal of Chemical Physics*, vol. 69, no. 6, pp. 2306–2311, 1978.
18. D. M. Carey, "Measurement of the Raman spectrum of liquid water," *Journal of Chemical Physics*, vol. 108, no. 7, pp. 2669–2675, 1998.
19. A. Vasylieva, I. Doroshenko, Y. Vaskivskiy, Y. Chernolevska, and V. Pogorelov, "FTIR study of condensed water structure," *Journal of Molecular Structure*, vol. 1167, pp. 232–238, 2018.
20. Y. R. Shen, "Phase-Sensitive Sum-Frequency Spectroscopy," *Annual Review of Physical Chemistry*, vol. 64, pp. 129–150, 2013.
21. N. Ji, V. Ostroverkhov, C.-Y. Chen, and Y.-R. Shen, "Phase-Sensitive Sum-Frequency Vibrational Spectroscopy and Its Application to Studies of Interfacial Alkyl Chains," *Journal of the American Chemical Society*, vol. 129, no. 33, pp. 10056–10057, 2007.
22. N. Ji, V. Ostroverkhov, C. S. Tian, and Y. R. Shen, "Characterization of vibrational resonances of water-vapor interfaces by phase-sensitive sum-frequency spectroscopy," *Physical Review Letters*, vol. 100, no. 9, p. 096102, 2008.
23. K. ichi Inoue, M. Ahmed, S. Nihonyanagi, and T. Tahara, "Reorientation-induced relaxation of free OH at the air/water interface revealed by ultrafast heterodyne-detected nonlinear spectroscopy," *Nature Communications*, vol. 11, no. 1, 2020.

24. J. Kubota and K. Domen, "Study of the dynamics of surface molecules by time-resolved sum-frequency generation spectroscopy," *Analytical and Bioanalytical Chemistry*, vol. 388, no. 1, pp. 17–27, 2007.
25. K.-i. Inoue, T. Ishiyama, S. Nihonyanagi, S. Yamaguchi, A. Morita, and T. Tahara, "Efficient Spectral Diffusion at the Air/Water Interface Revealed by Femtosecond Time-Resolved Heterodyne-Detected Vibrational Sum Frequency Generation Spectroscopy," *The Journal of Physical Chemistry Letters*, vol. 7, no. 10, pp. 1811–1815, 2016.
26. M. Bonn, H. J. Bakker, A. Ghosh, S. Yamamoto, M. Sovago, and R. K. Campen, "Structural Inhomogeneity of Interfacial Water at Lipid Monolayers Revealed by Surface-Specific Vibrational Pump-Probe Spectroscopy," *Journal of the American Chemical Society*, vol. 132, no. 42, pp. 14971–14978, 2010.
27. A. Ghosh, M. Smits, J. Bredenbeck, N. Dijkhuizen, and M. Bonn, "Femtosecond time-resolved and two-dimensional vibrational sum frequency spectroscopic instrumentation to study structural dynamics at interfaces," *Review of Scientific Instruments*, vol. 79, no. 9, pp. 0–9, 2008.
28. K.-I. Inoue, P. C. Singh, S. Nihonyanagi, S. Yamaguchi, and T. Tahara, *Ultrafast Vibrational Dynamics of Water at a Zwitterionic Lipid/Water Interface Revealed by Two-Dimensional Heterodyne-Detected Vibrational Sum Frequency Generation (2D HD-VSFG)*. Okinawa: Springer Proceedings in Physics, 2015.
29. C. J. Tainter, Y. Ni, L. Shi, and J. L. Skinner, "Hydrogen bonding and oh-stretch spectroscopy in water: Hexamer (Cage), liquid surface, liquid, and ice," *Journal of Physical Chemistry Letters*, vol. 4, no. 1, pp. 12–17, 2013.
30. C. Tian, S. J. Byrnes, H. L. Han, and Y. R. Shen, "Surface propensities of atmospherically relevant ions in salt solutions revealed by phase-sensitive sum frequency vibrational spectroscopy," *Journal of Physical Chemistry Letters*, vol. 2, no. 15, pp. 1946–1949, 2011.
31. C. S. Tian and Y. R. Shen, "Structure and charging of hydrophobic material/water interfaces studied by phase-sensitive sum-frequency vibrational spectroscopy," *Proceedings of the National Academy of Sciences of the United States of America*, vol. 106, no. 36, pp. 15148–15153, 2009.
32. S. Nihonyanagi, S. Yamaguchi, and T. Tahara, "Direct evidence for orientational flip-flop of water molecules at charged interfaces: A heterodyne-detected vibrational sum frequency generation study," *Journal of Chemical Physics*, vol. 130, no. 20, 2009.
33. Y. Ni and J. L. Skinner, "IR and SFG vibrational spectroscopy of the water bend in the bulk liquid and at the liquid-vapor interface, respectively," *Journal of Chemical Physics*, vol. 143, no. 1, p. 014502, 2015.

34. M. Vinaykin and A. V. Benderskii, "Vibrational sum-frequency spectrum of the water bend at the air/water interface," *Journal of Physical Chemistry Letters*, vol. 3, no. 22, pp. 3348–3352, 2012.
35. Y. Nagata, C. S. Hsieh, T. Hasegawa, J. Voll, E. H. Backus, and M. Bonn, "Water bending mode at the water-vapor interface probed by sum-frequency generation spectroscopy: A combined molecular dynamics simulation and experimental study," *Journal of Physical Chemistry Letters*, vol. 4, no. 11, pp. 1872–1877, 2013.
36. T. Seki, S. Sun, K. Zhong, C. C. Yu, K. Machel, L. B. Dreier, E. H. Backus, M. Bonn, and Y. Nagata, "Unveiling Heterogeneity of Interfacial Water through the Water Bending Mode," *Journal of Physical Chemistry Letters*, vol. 10, no. 21, pp. 6936–6941, 2019.
37. A. Kundu, S. Tanaka, T. Ishiyama, M. Ahmed, K. I. Inoue, S. Nihonyanagi, H. Sawai, S. Yamaguchi, A. Morita, and T. Tahara, "Bend Vibration of Surface Water Investigated by Heterodyne-Detected Sum Frequency Generation and Theoretical Study: Dominant Role of Quadrupole," *Journal of Physical Chemistry Letters*, vol. 7, no. 13, pp. 2597–2601, 2016.
38. J. Russo, K. Akahane, and H. Tanaka, "Water-like anomalies as a function of tetrahedrality," *Proceedings of the National Academy of Sciences*, vol. 115, no. 15, pp. E3333–E3341, 2018.
39. R. W. Talbot, J. E. Dibb, B. L. Lefer, E. M. Scheuer, J. D. Bradshaw, S. T. Sandholm, S. Smyth, D. R. Blake, N. Blake, G. W. Sachse, J. E. Collins, and G. L. Gregory, "Large-scale distributions of tropospheric nitric, formic, and acetic acids over the western Pacific basin during wintertime," *Journal of Geophysical Research*, vol. 102, pp. 28,303–28,313, 1997.
40. R. A. Cox, M. A. Fernandez, A. Symington, A. Ullerstam, and A. Abbatt, "A kinetic model for uptake of hno₃ and hcl on ice in a coated wall flow system.," *Physical Chemistry Chemical Physics*, no. 7, pp. 3434–3442, 2005.
41. A. M. Grannas, C. Bogdal, K. J. Hageman, C. Halsall, T. Harner, H. Hung, R. Kallenborn, P. Klan, J. Klanova, R. W. Macdonald, T. Meyer, and F. Wania, "The role of the global cryosphere in the fate of organic contaminants," *Atmospheric Chemistry and Physics*, vol. 13, pp. 3271–3305, 2013.
42. P. von Hessberg, N. Pouvesle, A. K. Winkler, G. Schuster, and J. N. Crowley, "Interaction of formic and acetic acid with ice surfaces between 187 and 227 K . Investigation of single species- and competitive adsorption," *Physical Chemistry Chemical Physics*, vol. 10, pp. 2345–2355, 2008.
43. A. Steffen, T. Douglas, M. Amyot, P. Ariya, K. Aspö, T. Berg, J. Bottenheim, S. Brooks, F. Cobbett, A. Dastoor, A. Dommergue, R. Ebinghaus, C. Ferrari, K. Gardfeldt, M. E. Goodsite, D. Lean, A. J. Poulain,

- C. Scherz, H. Skov, J. Sommar, and C. Temme, "A synthesis of atmospheric mercury depletion event chemistry in the atmosphere and snow," *Atmospheric Chemistry and Physics*, vol. 8, pp. 1445–1482, 2008.
44. M. Hassas-Roudsari and H. D. Goff, "Ice structuring proteins from plants: Mechanism of action and food application," *Food Research International*, vol. 46, no. 1, pp. 425–436, 2012.
45. A. P. Esser-Kahn, V. Trang, and M. B. Francis, "Incorporation of antifreeze proteins into polymer coatings using site-selective bioconjugation," *Journal of the American Chemical Society*, vol. 132, no. 38, pp. 13264–13269, 2010.
46. H. J. Kim, J. H. Lee, Y. B. Hur, C. W. Lee, S. H. Park, and B. W. Koo, "Marine antifreeze proteins: Structure, function, and application to cryopreservation as a potential cryoprotectant," *Marine Drugs*, vol. 15, no. 2, 2017.
47. G. Amir, L. Horowitz, B. Rubinsky, B. S. Yousif, J. Lavee, and A. K. Smolinsky, "Subzero nonfreezing cryopresevation of rat hearts using antifreeze protein I and antifreeze protein III," *Cryobiology*, vol. 48, no. 3, pp. 273–282, 2004.
48. Y. Levy and J. N. Onuchic, "Water mediation in protein folding and molecular recognition," *Annual Review of Biophysics and Biomolecular Structure*, vol. 35, no. 1, pp. 389–415, 2006.
49. H. Khesbak, O. Savchuk, S. Tsushima, and K. Fahmy, "The Role of Water H-Bond Imbalances in B-DNA Substate Transitions and Peptide Recognition Revealed by Time-Resolved FTIR Spectroscopy," *Journal of the American Chemical Society*, vol. 133, no. 15, pp. 5834–5842, 2011.
50. M. S. Bretscher, "The molecules of the cell membrane," *Scientific American*, vol. 253, no. 4, pp. 100–109, 1985.
51. D. Michalska, B. Morzyk, D. C. Bienko, and W. Wojciechowski, "Glutarimide: a carrier transporting drug through cell membranes," *Medical Hypotheses*, vol. 54, no. 3, pp. 472–474, 2000.
52. P. J. Quinn, "Effects of temperature on cell membranes," *Symposia of the Society for Experimental Biology*, vol. 42, pp. 237–258, 1988.
53. S. J. Singer and G. L. Nicolson, "The Fluid Mosaic Model of the Structure of Cell Membranes," *Science*, vol. 175, no. 4023, pp. 720–731, 1972.
54. G. Saulis, M. S. Venslauskas, and J. Naktinis, "Kinetics of pore resealing in cell membranes after electroporation," *Journal of Electroanalytical Chemistry and Interfacial Electrochemistry*, vol. 321, no. 1, pp. 1–13, 1991.
55. P. I. Haris and F. Severcan, "FTIR spectroscopic characterization of protein structure in aqueous and non-aqueous media," *Journal of Molecular Catalysis B: Enzymatic*, vol. 7, no. 1, pp. 207–221, 1999.

56. S. A. Tatulian, *Structural Characterization of Membrane Proteins and Peptides by FTIR and ATR-FTIR Spectroscopy*. Totowa, NJ: Humana Press, 2013.
57. A. C. Williams, H. G. M. Edwards, and B. W. Barry, "Raman spectra of human keratotic biopolymers: Skin, callus, hair and nail," *Journal of Raman Spectroscopy*, vol. 25, no. 1, pp. 95–98, 1994.
58. R. C. Lord, "Strategy and tactics in the raman spectroscopy of biomolecules," *Applied Spectroscopy*, vol. 31, no. 3, pp. 187–194, 1977.
59. A. Rygula, K. Majzner, K. M. Marzec, A. Kaczor, M. Pilarczyk, and M. Baranska, "Raman spectroscopy of proteins: A review," *Journal of Raman Spectroscopy*, vol. 44, no. 8, pp. 1061–1076, 2013.
60. T. A. Hanafy, K. Elbanna, S. El-Sayed, and A. Hassen, "Dielectric relaxation analysis of biopolymer poly(3-hydroxybutyrate)," *Journal of Applied Polymer Science*, vol. 121, no. 6, pp. 3306–3313, 2011.
61. M. Wolf, R. Gulich, P. Lunkenheimer, and A. Loidl, "Relaxation dynamics of a protein solution investigated by dielectric spectroscopy," *Biochimica et Biophysica Acta (BBA) - Proteins and Proteomics*, vol. 1824, no. 5, pp. 723–730, 2012.
62. E. P. van Dam, G. Giubertoni, F. Burla, G. H. Koenderink, and H. J. Bakker, "Hyaluronan biopolymers release water upon pH-induced gelation," *Physical Chemistry Chemical Physics*, vol. 22, no. 16, pp. 8667–8671, 2020.
63. C. C. M. Groot and H. J. Bakker, "Proteins Take up Water Before Unfolding," *The Journal of Physical Chemistry Letters*, vol. 7, no. 10, pp. 1800–1804, 2016.
64. G. Giubertoni, F. Burla, C. Martinez-Torres, B. Dutta, G. Pletikapic, E. Pelan, Y. L. Rezus, G. H. Koenderink, and H. J. Bakker, "Molecular Origin of the Elastic State of Aqueous Hyaluronic Acid," *Journal of Physical Chemistry B*, vol. 123, no. 14, pp. 3043–3049, 2019.
65. A. M. Alperstein, J. S. Ostrander, T. O. Zhang, and M. T. Zanni, "Amyloid found in human cataracts with two-dimensional infrared spectroscopy," *Proceedings of the National Academy of Sciences*, vol. 116, no. 14, pp. 6602–6607, 2019.
66. K. Meister, S. Strazdaite, A. L. DeVries, S. Lotze, L. L. C. Olijve, I. K. Voets, and H. J. Bakker, "Observation of ice-like water layers at an aqueous protein surface," *Proceedings of the National Academy of Sciences*, vol. 111, no. 50, pp. 17732–17736, 2014.
67. Y. Li, M. Shrestha, M. Luo, I. Sit, M. Song, V. H. Grassian, and W. Xiong, "Salting up of Proteins at the Air/Water Interface," *Langmuir*, vol. 35, no. 43, pp. 13815–13820, 2019.

-
68. G. Ma, J. Liu, L. Fu, and E. C. Y. Yan, "Probing water and biomolecules at the air-water interface with a broad bandwidth vibrational sum frequency generation spectrometer from 3800 to 900 cm^{-1} ," *Applied Spectroscopy*, vol. 63, no. 5, pp. 528–537, 2009.
 69. R. W. Boyd, *Nonlinear Optics*. Academic Press, 2003.
 70. A. Morita, *Theory of Sum Frequency Generation Spectroscopy*. Singapore: Springer, 2018.
 71. Y. R. Shen, *The principles of nonlinear optics*. New York: John Wiley Sons, 1984.
 72. S. Mukamel, *Principles of nonlinear optical spectroscopy*. New York: Oxford University Press, 1999.
 73. Y. R. Shen, *Fundamentals of Sum-Frequency Spectroscopy*. Cambridge: Cambridge University Press, 2016.
 74. C. Hirose, N. Akamatsu, and K. Domen, "Formulas for the analysis of surface sum-frequency generation spectrum by CH stretching modes of methyl and methylene groups," *The Journal of Chemical Physics*, vol. 96, no. 2, pp. 997–1004, 1992.
 75. H. Goldstein, *Classical Mechanics*. Addison-Wesley, 3rd edition ed., 2002.
 76. X. Wei, P. B. Miranda, and Y. R. Shen, "Surface vibrational spectroscopic study of surface melting of ice," *Physical Review Letters*, vol. 86, no. 8, pp. 1554–1557, 2001.
 77. D. P. Chong and S. R. Langhoff, "Theoretical study of polarizabilities and hyperpolarizabilities of ne, hf, f^- , and oh^- ," *The Journal of Chemical Physics*, vol. 93, no. 1, pp. 570–578, 1990.
 78. R. Lu, W. Gan, B.-h. Wu, Z. Zhang, Y. Guo, and H.-f. Wang, "Ch stretching vibrations of methyl, methylene and methine groups at the vapor/alcohol ($n = 1$ to 8) interfaces," *The Journal of Physical Chemistry B*, vol. 109, no. 29, pp. 14118–14129, 2005.
 79. H. Wu, W.-k. Zhang, W. Gan, and et al., "An empirical approach to the bond additivity model in quantitative interpretation of sum frequency generation vibrational spectra," *The Journal of Chemical Physics*, vol. 125, no. 13, p. 133203, 2006.
 80. H. F. Wang, W. Gan, R. Lu, Y. Rao, and B. H. Wu, "Quantitative spectral and orientational analysis in surface sum frequency generation vibrational spectroscopy (SFG-VS)," *International Reviews in Physical Chemistry*, vol. 24, no. 2, pp. 191–256, 2005.
 81. J. D. Jackson, *Classical electrodynamics*. New York: John Wiley Sons, 1998.

82. R.-r. Feng, Y. Guo, R. Lü, L. Velarde, and H.-f. Wang, "Consistency in the sum frequency generation intensity and phase vibrational spectra of the air/ neat water interface," *The Journal of Physical Chemistry A*, vol. 115, no. 23, pp. 6015–6027, 2011.
83. S. Kovalenko, "Descartes-Snell law of refraction with absorption," *Semiconductor Physics, Quantum Electronics and Optoelectronics*, vol. 4, no. 3, pp. 214–218, 2001.
84. M. Ahmed, S. Nihonyanagi, A. Kundu, S. Yamaguchi, and T. Tahara, "Resolving the Controversy over Dipole versus Quadrupole Mechanism of Bend Vibration of Water in Vibrational Sum Frequency Generation Spectra," *The Journal of Physical Chemistry Letters*, vol. 11, no. 21, pp. 9123–9130, 2020.
85. L. Wang, W. Mori, A. Morita, M. Kondoh, M. Okuno, and T.-a. Ishibashi, "Quadrupole Contribution of CO Vibrational Band in Sum Frequency Generation Spectra of Organic Carbonates," *The Journal of Physical Chemistry Letters*, vol. 11, no. 20, pp. 8527–8531, 2020.
86. G. Gonella, C. Lütgebaucks, A. G. F. De Beer, and S. Roke, "Second harmonic and sum-frequency generation from aqueous interfaces is modulated by interference," *Journal of Physical Chemistry C*, vol. 120, no. 17, pp. 9165–9173, 2016.
87. P. E. Ohno, H. F. Wang, and F. M. Geiger, "Second-order spectral line-shapes from charged interfaces," *Nature Communications*, vol. 8, no. 1, pp. 1–9, 2017.
88. D. E. Gragson and G. L. Richmond, "Investigations of the Structure and Hydrogen Bonding of Water Molecules at Liquid Surfaces by Vibrational Sum Frequency Spectroscopy," *The Journal of Physical Chemistry B*, vol. 102, no. 20, pp. 3847–3861, 1998.
89. A. Eftekhari-Bafrooei and E. Borguet, "Effect of Electric Fields on the Ultrafast Vibrational Relaxation of Water at a Charged Solid–Liquid Interface as Probed by Vibrational Sum Frequency Generation," *The Journal of Physical Chemistry Letters*, vol. 2, no. 12, pp. 1353–1358, 2011.
90. R. E. Pool, J. Versluis, E. H. Backus, and M. Bonn, "Comparative study of direct and phase-specific vibrational sum-frequency generation spectroscopy: Advantages and limitations," *Journal of Physical Chemistry B*, vol. 115, no. 51, pp. 15362–15369, 2011.
91. H. W. Fairbrain, *Structural petrology of deformed rocks*. Addison-Wiley, 1954.
92. W. J. Smit, F. Tang, Y. Nagata, M. A. Sánchez, T. Hasegawa, E. H. Backus, M. Bonn, and H. J. Bakker, "Observation and identification of a new oh stretch vibrational band at the surface of ice," *Journal of Physical Chemistry Letters*, vol. 8, no. 15, pp. 3656–3660, 2017.

-
93. S. Nihonyanagi, S. Yamaguchi, and T. Tahara, "Ultrafast Dynamics at Water Interfaces Studied by Vibrational Sum Frequency Generation Spectroscopy," *Chemical Reviews*, vol. 117, no. 16, pp. 10665–10693, 2017.
 94. J. A. McGuire and Y. R. Shen, "Ultrafast Dynamics at Water Interfaces," *Science*, vol. 313, pp. 1945–1948, 2006.
 95. J. D. Cyran, E. H. G. Backus, Y. Nagata, and M. Bonn, "Structure from Dynamics: Vibrational Dynamics of Interfacial Water as a Probe of Aqueous Heterogeneity," *The Journal of Physical Chemistry B*, vol. 122, no. 14, pp. 3667–3679, 2018.
 96. S. Strazdaite, J. Versluis, E. H. G. Backus, and H. J. Bakker, "Enhanced ordering of water at hydrophobic surfaces," *The Journal of Chemical Physics*, vol. 140, no. 5, p. 54711, 2014.
 97. X. Chen, T. Yang, S. Kataoka, and P. S. Cremer, "Specific Ion Effects on Interfacial Water Structure near Macromolecules," *Journal of the American Chemical Society*, vol. 129, no. 40, pp. 12272–12279, 2007.
 98. W. Xiong, J. E. Laaser, R. D. Mehlenbacher, and M. T. Zanni, "Adding a dimension to the infrared spectra of interfaces using heterodyne detected 2D sum-frequency generation (HD 2D SFG) spectroscopy," *Proceedings of the National Academy of Sciences*, vol. 108, no. 52, pp. 20902–20907, 2011.
 99. C.-S. Hsieh, M. Okuno, J. Hunger, E. H. G. Backus, Y. Nagata, and M. Bonn, "Aqueous Heterogeneity at the Air/Water Interface Revealed by 2D-HD-SFG Spectroscopy," *Angewandte Chemie International Edition*, vol. 53, no. 31, pp. 8146–8149, 2014.
 100. E. Tyrode, S. Sengupta, and A. Stoeber, "Identifying Eigen-like hydrated protons at negatively charged interfaces," *Nature Communications*, vol. 11, no. 493, 2020.
 101. P. C. Singh, S. Nihonyanagi, S. Yamaguchi, and T. Tahara, "Interfacial water in the vicinity of a positively charged interface studied by steady-state and time-resolved heterodyne-detected vibrational sum frequency generation," *The Journal of Chemical Physics*, vol. 141, no. 18, p. 18C527, 2014.
 102. P. E. Ohno, H. F. Wang, F. Paesani, J. L. Skinner, and F. M. Geiger, "Second-Order Vibrational Lineshapes from the Air/Water Interface," *Journal of Physical Chemistry A*, vol. 122, no. 18, pp. 4457–4464, 2018.
 103. S. Nihonyanagi, S. Yamaguchi, and T. Tahara, "Counterion Effect on Interfacial Water at Charged Interfaces and Its Relevance to the Hofmeister Series," *Journal of the American Chemical Society*, vol. 136, no. 17, pp. 6155–6158, 2014.
 104. M. M. Sartin, W. Sung, S. Nihonyanagi, and T. Tahara, "Molecular mechanism of charge inversion revealed by polar orientation of interfacial water molecules: A heterodyne-detected vibrational sum frequency generation study," *Journal of Chemical Physics*, vol. 149, no. 2, p. 024703, 2018.

105. L. B. Dreier, Y. Nagata, H. Lutz, G. Gonella, J. Hunger, E. H. Backus, and M. Bonn, "Saturation of charge-induced water alignment at model membrane surfaces," *Science Advances*, vol. 4, no. 3, pp. 1–9, 2018.
106. H. S. Frank and F. Franks, "Structural approach to the solvent power of water for hydrocarbons; Urea as a structure breaker," *The Journal of Chemical Physics*, vol. 48, no. 10, pp. 4746–4757, 1968.
107. Y. L. A. Rezus and H. J. Bakker, "Effect of urea on the structural dynamics of water," *Proceedings of the National Academy of Sciences*, vol. 103, no. 49, pp. 18417–18420, 2006.
108. W. Bruning and A. Holtzer, "The effect of urea on hydrophobic bonds: The critical micelle concentration of n-dodecyltrimethylammonium bromide in aqueous solutions of urea," *Journal of the American Chemical Society*, vol. 83, no. 23, pp. 4865–4866, 1961.
109. P. O. Åstrand, A. Wallqvist, and G. Karlström, "Molecular dynamics simulations of 2 m aqueous urea solutions," *Journal of Physical Chemistry*, vol. 98, no. 33, pp. 8224–8233, 1994.
110. J. F. Brandts and L. Hunt, "The Thermodynamics of Protein Denaturation. III. The Denaturation of Ribonuclease in Water and in Aqueous Urea and Aqueous Ethanol Mixtures," *Journal of the American Chemical Society*, vol. 89, no. 19, pp. 4826–4838, 1967.
111. L. B. Sagle, Y. Zhang, V. A. Litosh, X. Chen, Y. Cho, and P. S. Cremer, "Investigating the hydrogen-bonding model of urea denaturation," *Journal of the American Chemical Society*, vol. 131, no. 26, pp. 9304–9310, 2009.
112. P. J. Rossky, "Protein denaturation by urea: Slash and bond," *Proceedings of the National Academy of Sciences of the United States of America*, vol. 105, no. 44, pp. 16825–16826, 2008.
113. M. Auton and D. W. Bolen, "Predicting the energetics of osmolyte-induced protein folding unfolding," *Proceedings of the National Academy of Sciences*, vol. 102, no. 42, pp. 15065–15068, 2005.
114. U. Kaatze, H. Gerke, and R. Pottel, "Dielectric relaxation in aqueous solutions of urea and some of its derivatives," *Journal of Physical Chemistry*, vol. 90, no. 21, pp. 5464–5469, 1986.
115. A. K. Soper, E. W. Castner, and A. Luzar, "Impact of urea on water structure: A clue to its properties as a denaturant?," *Biophysical Chemistry*, vol. 105, no. 2-3, pp. 649–666, 2003.
116. E. G. Finer, F. Franks, and M. J. Tait, "Nuclear Magnetic Resonance Studies of Aqueous Urea Solutions," *Journal of the American Chemical Society*, vol. 94, no. 13, pp. 4424–4429, 1972.

-
117. A. Idrissi, M. Gerard, P. Damay, M. Kiselev, Y. Puhovsky, E. Cinar, P. Lagant, and G. Vergoten, "The effect of urea on the structure of water: A molecular dynamics simulation," *Journal of Physical Chemistry B*, vol. 114, no. 13, pp. 4731–4738, 2010.
118. G. E. Walrafen, "Raman spectral studies of the effects of urea and sucrose on water structure," *The Journal of Chemical Physics*, vol. 44, no. 10, pp. 3726–3727, 1966.
119. S. Funkner, M. Havenith, and G. Schwaab, "Urea, a Structure Breaker? Answers from THz Absorption Spectroscopy," *The Journal of Physical Chemistry B*, vol. 116, no. 45, pp. 13374–13380, 2012.
120. A. Shimizu, K. Fumino, K. Yukiyasu, and Y. Taniguchi, "NMR studies on dynamic behavior of water molecule in aqueous denaturant solutions at 25 °C: Effects of guanidine hydrochloride, urea and alkylated ureas," *Journal of Molecular Liquids*, vol. 85, no. 3, pp. 269–278, 2000.
121. S. Halonen, T. Kangas, M. Haataja, and U. Lassi, "Urea-Water-Solution Properties: Density, Viscosity, and Surface Tension in an Under-Saturated Solution," *Emission Control Science and Technology*, vol. 3, pp. 161–170, 2017.
122. A. Terzis, E. Sauer, G. Yang, J. Groß, and B. Weigand, "Characterisation of acid–base surface free energy components of urea–water solutions," *Colloids and Surfaces A: Physicochemical and Engineering Aspects*, vol. 538, pp. 774–780, 2018.
123. M. C. Stumpe and H. Grubmüller, "Aqueous urea solutions: Structure, energetics, and urea aggregation," *Journal of Physical Chemistry B*, vol. 111, no. 22, pp. 6220–6228, 2007.
124. D. Bandyopadhyay, S. Mohan, S. K. Ghosh, and N. Choudhury, "Molecular dynamics simulation of aqueous urea solution: Is urea a structure breaker?," *Journal of Physical Chemistry B*, vol. 118, no. 40, pp. 11757–11768, 2014.
125. R. Breslow and T. Guo, "Surface tension measurements show that chaotropic salting-in denaturants are not just water-structure breakers," *Proceedings of the National Academy of Sciences of the United States of America*, vol. 87, no. 1, pp. 167–169, 1990.
126. X. Chen, L. B. Sagle, and P. S. Cremer, "Urea Orientation at Protein Surfaces," *Journal of the American Chemical Society*, vol. 129, no. 49, pp. 15104–15105, 2007.
127. C. J. Moll, J. Versluis, and H. J. Bakker, "Direct Evidence for a Surface and Bulk Specific Response in the Sum-Frequency Generation Spectrum of the Water Bend Vibration," *Physical Review Letters*, vol. 127, no. 11, p. 116001, 2021.

128. P. G. Puranik and L. Sirdeshmukh, "Vibrational spectra, force constants and meanamplitudes of vibrations of urea and deuterated urea," *Proceedings of the National Academy of Sciences of the United States of America*, vol. 67, pp. 99–108, 1966.
129. J. E. Stewart, "Infrared Absorption Spectra of Urea, Thiourea, and Some Thiourea-Alkali Halide Complexes," *The Journal of Chemical Physics*, vol. 26, no. 2, pp. 248–254, 1957.
130. J. K. Carr, L. E. Buchanan, J. R. Schmidt, M. T. Zanni, and J. L. Skinner, "Structure and Dynamics of Urea/Water Mixtures Investigated by Vibrational Spectroscopy and Molecular Dynamics Simulation," *The Journal of Physical Chemistry B*, vol. 117, no. 42, pp. 13291–13300, 2013.
131. M. Okuno, S. Yamada, T. Ohto, H. Tada, W. Nakanishi, K. Ariga, and T. A. Ishibashi, "Hydrogen Bonds and Molecular Orientations of Supramolecular Structure between Barbituric Acid and Melamine Derivative at the Air/Water Interface Revealed by Heterodyne-Detected Vibrational Sum Frequency Generation Spectroscopy," *Journal of Physical Chemistry Letters*, vol. 11, no. 7, pp. 2422–2429, 2020.
132. J. A. Mondal, S. Nihonyanagi, S. Yamaguchi, and T. Tahara, "Structure and orientation of water at charged lipid monolayer/water interfaces probed by heterodyne-detected vibrational sum frequency generation spectroscopy," *Journal of the American Chemical Society*, vol. 132, no. 31, pp. 10656–10657, 2010.
133. I. Gatej, M. Popa, and M. Rinaudo, "Role of the pH on hyaluronan behavior in aqueous solution," *Biomacromolecules*, vol. 6, no. 1, pp. 61–67, 2005.
134. G. Kocak, C. Tuncer, and V. Bütün, "PH-Responsive polymers," *Polymer Chemistry*, vol. 8, no. 1, pp. 144–176, 2017.
135. M. V. Fedotova and S. E. Kruchinin, "Hydration of acetic acid and acetate ion in water studied by 1D-RISM theory," *Journal of Molecular Liquids*, vol. 164, no. 3, pp. 201–206, 2011.
136. T. Hajari and N. F. Van Der Vegt, "Solvation thermodynamics of amino acid side chains on a short peptide backbone," *Journal of Chemical Physics*, vol. 142, no. 14, 2015.
137. J. P. Bruce, K. Zhang, S. G. Balasubramani, A. R. Haines, R. P. Galhenage, V. K. Voora, F. Furche, and J. C. Hemminger, "Exploring the Solvation of Acetic Acid in Water Using Liquid Jet X-ray Photoelectron Spectroscopy and Core Level Electron Binding Energy Calculations," *The Journal of Physical Chemistry B*, 2021.
138. M. N. Ahamad, M. S. Khan, M. Shahid, and M. Ahmad, "Metal organic frameworks decorated with free carboxylic acid groups: Topology, metal

- capture and dye adsorption properties,” *Dalton Transactions*, vol. 49, no. 41, pp. 14690–14705, 2020.
139. X. Wang, L. Zhai, Y. Wang, R. Li, X. Gu, Y. D. Yuan, Y. Qian, Z. Hu, and D. Zhao, “Improving Water-Treatment Performance of Zirconium Metal-Organic Framework Membranes by Postsynthetic Defect Healing,” *ACS Applied Materials and Interfaces*, vol. 9, no. 43, pp. 37848–37855, 2017.
140. H. Li, K. Wang, Y. Sun, C. T. Lollar, J. Li, and H. C. Zhou, “Recent advances in gas storage and separation using metal-organic frameworks,” *Materials Today*, vol. 21, no. 2, pp. 108–121, 2018.
141. S. Shirase, S. Tamaki, K. Shinohara, K. Hirose, H. Tsurugi, T. Satoh, and K. Mashima, “Cerium(IV) Carboxylate Photocatalyst for Catalytic Radical Formation from Carboxylic Acids: Decarboxylative Oxygenation of Aliphatic Carboxylic Acids and Lactonization of Aromatic Carboxylic Acids,” *Journal of the American Chemical Society*, vol. 142, no. 12, pp. 5668–5675, 2020.
142. Y. Devi, I. Ang, F. E. Soetaredjo, S. P. Santoso, W. Irawaty, M. Yuliana, A. E. Angkawijaya, S. B. Hartono, P. L. Tran-Nguyen, S. Ismadji, and Y. H. Ju, “An iron-carboxylate-based metal-organic framework for Furosemide loading and release,” *Journal of Materials Science*, vol. 55, no. 28, pp. 13785–13798, 2020.
143. G. Alvarez Jürgenson, C. Bittner, V. Kurkal-Siebert, G. Oetter, and J. Tinsley, “Alkyl ether carboxylate surfactants for chemically enhanced oil recovery in harsh field conditions,” *Society of Petroleum Engineers - SPE Asia Pacific Enhanced Oil Recovery Conference, EORC 2015*, pp. 288–298, 2015.
144. J. Lu, C. Britton, S. Solairaj, P. J. Liyanage, D. H. Kim, S. Adkins, G. W. Arachchilage, U. Weerasooriya, and G. A. Pope, “Novel large-hydrophobe alkoxy carboxylate surfactants for enhanced oil recovery,” *SPE Journal*, vol. 19, no. 6, pp. 1024–1034, 2014.
145. S. Roy and J. A. Mondal, “Kosmotropic Electrolyte (Na_2CO_3 , NaF) Perturbs the Air/Water Interface through Anion Hydration Shell without Forming a Well-Defined Electric Double Layer,” *The Journal of Physical Chemistry B*, vol. 125, no. 16, pp. 3977–3985, 2021.
146. E. M. Adams, B. A. Wellen, R. Thiriaux, S. K. Reddy, A. S. Vidalis, F. Paesani, and H. C. Allen, “Sodium-carboxylate contact ion pair formation induces stabilization of palmitic acid monolayers at high pH,” *Physical Chemistry Chemical Physics*, vol. 19, no. 16, pp. 10481–10490, 2017.
147. M. C. Soule, P. G. Blower, and G. L. Richmond, “Effects of atmospherically important solvated ions on organic acid adsorption at the surface of aqueous solutions,” *Journal of Physical Chemistry B*, vol. 111, no. 49, pp. 13703–13713, 2007.

148. C. Y. Tang, Z. Huang, and H. C. Allen, "Binding of Mg^{2+} and Ca^{2+} to palmitic acid and deprotonation of the cooh headgroup studied by vibrational sum frequency generation spectroscopy," *Journal of Physical Chemistry B*, vol. 114, no. 51, pp. 17068–17076, 2010.
149. E. Tyrode and R. Corkery, "Charging of Carboxylic Acid Monolayers with Monovalent Ions at Low Ionic Strengths: Molecular Insight Revealed by Vibrational Sum Frequency Spectroscopy," *Journal of Physical Chemistry C*, vol. 122, no. 50, pp. 28775–28786, 2018.
150. N. Ottosson, E. Wernersson, J. Söderström, W. Pokapanich, S. Kaufmann, S. Svensson, I. Persson, G. Öhrwall, and O. Björneholm, "The protonation state of small carboxylic acids at the water surface from photoelectron spectroscopy," *Physical Chemistry Chemical Physics*, vol. 13, no. 26, pp. 12261–12267, 2011.
151. B. Minofar, R. Vácha, A. Wahab, S. Mahiuddin, W. Kunz, and P. Jungwirth, "Propensity for the air/water interface and ion pairing in magnesium acetate vs magnesium nitrate solutions: Molecular dynamics simulations and surface tension measurements," *Journal of Physical Chemistry B*, vol. 110, no. 32, pp. 15939–15944, 2006.
152. B. Minofar, P. Jungwirth, M. R. Das, W. Kunz, and S. Mahiuddin, "Propensity of formate, acetate, benzoate, and phenolate for the aqueous solution/vapor interface: Surface tension measurements and molecular dynamics simulations," *Journal of Physical Chemistry C*, vol. 111, no. 23, pp. 8242–8247, 2007.
153. K. Ito and H. J. Bernstein, "the Vibrational Spectra of the Formate, Acetate, and Oxalate Ions," *Canadian Journal of Chemistry*, vol. 34, no. 2, pp. 170–178, 1956.
154. S. E. Cabaniss and I. F. McVey, "Aqueous infrared carboxylate absorbances: aliphatic monocarboxylates," *Spectrochimica Acta Part A: Molecular and Biomolecular Spectroscopy*, vol. 51, no. 13, pp. 2385–2395, 1995.
155. N. J. Nicholas, G. V. Franks, and W. A. Ducker, "Selective adsorption to particular crystal faces of ZnO ," *Langmuir*, vol. 28, no. 18, pp. 7189–7196, 2012.
156. S. Hosseinpour, C. M. Johnson, and C. Leygraf, "Alkanethiols as Inhibitors for the Atmospheric Corrosion of Copper Induced by Formic Acid: Effect of Chain Length," *Journal of The Electrochemical Society*, vol. 160, no. 6, pp. C270–C276, 2013.
157. L. Wang, R. Murata, K.-i. Inoue, S. Ye, and A. Morita, "Dispersion of Complex Refractive Indices for Intense Vibrational Bands . II . Implication to Sum Frequency Generation Spectroscopy," *Journal of Physical Chemistry B*, vol. 125, no. 34, pp. 9804–9810.

-
158. A. Chebbi and P. Calier, "Carboxylic Acids in the Troposphere , Occurrence , Sources , and Sinks : A Review," *Atmospheric Environment*, vol. 30, no. 24, pp. 4233–4249, 1996.
159. Y. Fukuda, T. Fukushima, A. Sulaiman, I. Musalam, L. C. Yap, L. Chotimongkol, S. Judabong, A. Potjanart, O. Keowkangwal, K. Yoshihara, and M. Tosa, "Indoor corrosion of copper and silver exposed in japan and ASEAN¹ countries," *Journal of The Electrochemical Society*, vol. 138, no. 5, p. 1238, 1991.
160. C. Leygraf, I. O. Wallinder, J. Tidblad, and T. Graedel, *Atmospheric Corrosion*. New Jersey: John Wiley Sons, 2016.
161. A. Křepelová, T. Bartels-Rausch, M. A. Brown, H. Bluhm, and M. Ammann, "Adsorption of Acetic Acid on Ice Studied by Ambient-Pressure XPS and Partial-Electron-Yield NEXAFS Spectroscopy at 230–240 K," *The journal of physical chemistry. A*, vol. 117, pp. 401–409, 2013.
162. E. Álvarez, G. Vázquez, M. Sánchez-Vilas, B. Sanjurjo, and J. M. Navaza, "Surface tension of organic acids and water binary mixtures from 20°C to 50°C," *Journal of Chemical and Engineering Data*, vol. 42, no. 5, pp. 957–960, 1997.
163. S. Sugiyama, T. Yoshino, H. Kanahara, M. Shichiri, D. Fukushi, and T. Ohtani, "Effects of acetic acid treatment on plant chromosome structures analyzed by atomic force microscopy," *Analytical Biochemistry*, vol. 324, no. 1, pp. 39–44, 2004.
164. J. T. Young and F. J. Boerio, "Surface-enhanced raman scattering as an in-situ probe of polyimide/silver interphases," *MRS Proceedings*, vol. 304, 1993.
165. W. Mori, L. Wang, Y. Sato, and A. Morita, "Development of quadrupole susceptibility automatic calculator in sum frequency generation spectroscopy and application to methyl C–H vibrations," *The Journal of Chemical Physics*, vol. 153, no. 17, p. 174705, 2020.
166. E. Tyrode, C. M. Johnson, S. Baldelli, and M. W. Rutland, "A Vibrational Sum Frequency Spectroscopy Study of the Liquid/Gas Interface of Acetic Acid/Water Mixtures: 2. Orientation Analysis," *Journal of Physical Chemistry B*, vol. 109, pp. 329–341, 2005.
167. C. M. Johnson, E. Tyrode, A. Kumpulainen, and C. Leygraf, "Vibrational sum frequency spectroscopy study of the liquid/vapor interface of formic acid/water solutions," *Journal of Physical Chemistry C*, vol. 113, no. 30, pp. 13209–13218, 2009.
168. C. J. Moll, K. Meister, J. Versluis, and H. J. Bakker, "Freezing of Aqueous Carboxylic Acid Solutions on Ice," *The Journal of Physical Chemistry B*, vol. 124, no. 25, pp. 5201–5208, 2020.

169. P. A. Pieniazek, C. J. Tainter, and J. L. Skinner, "Interpretation of the water surface vibrational sum-frequency spectrum," *Journal of Chemical Physics*, vol. 135, no. 4, p. 044701, 2011.
170. T. Ishiyama and A. Morita, "Vibrational spectroscopic response of intermolecular orientational correlation at the water surface," *Journal of Physical Chemistry C*, vol. 113, no. 37, pp. 16299–16302, 2009.
171. S. Nihonyanagi, R. Kusaka, K. I. Inoue, A. Adhikari, S. Yamaguchi, and T. Tahara, "Accurate determination of complex χ (2) spectrum of the air/water interface," *Journal of Chemical Physics*, vol. 143, no. 12, 2015.
172. A. Morita and J. T. Hynes, "A theoretical analysis of the sum frequency generation spectrum of the water surface," *Chemical Physics*, vol. 258, no. 2-3, pp. 371–390, 2000.
173. A. Bagheri and K. Alizadeh, "How do temperature and chemical structure affect surface properties of aqueous solutions of carboxylic acids?," *Colloids and Surfaces A: Physicochemical and Engineering Aspects*, vol. 467, pp. 78–88, 2015.
174. C. J. Moll, J. Versluis, and H. J. Bakker, "Direct observation of the orientation of urea molecules at charged interfaces," *The Journal of Physical Chemistry Letters*, vol. 12, no. 44, pp. 10823–10828, 2021.
175. E. Spinner, "Comment on 'A simple method for the matrix isolation of monomeric and dimeric carboxylic acids'. Possible implications of findings, in regard to liquid formic acid," *Spectrochimica Acta - Part A: Molecular and Biomolecular Spectroscopy*, vol. 55, no. 9, pp. 1819–1825, 1999.
176. M. Lim and R. M. Hochstrasser, "Unusual vibrational dynamics of the acetic acid dimer," *Journal of Chemical Physics*, vol. 115, no. 16, pp. 7629–7643, 2001.
177. H. M. Gantenberg, M. and W. Sander, "Dimerization of Formic Acid-An Example of a "Noncovalent" Reaction Mechanism," *Chemistry European Journal*, vol. 6, pp. 1865–1869, 2000.
178. J. E. Bertie and K. H. Michaelian, "The Raman spectra of gaseous formic acid -h₂ and -d₂," *The Journal of Chemical Physics*, vol. 76, no. 2, pp. 886–894, 1982.
179. K. Shiratori and A. Morita, "Theory of Quadrupole Contributions from Interface and Bulk in Second-Order Optical Processes," *Bulletin of the Chemical Society of Japan*, vol. 85, no. 10, pp. 1061–1076, 2012.
180. K. Matsuzaki, S. Nihonyanagi, S. Yamaguchi, T. Nagata, and T. Tahara, "Vibrational Sum Frequency Generation by the Quadrupolar Mechanism at the Nonpolar Benzene/Air Interface," *The Journal of Physical Chemistry Letters*, vol. 4, no. 10, pp. 1654–1658, 2013.

181. S. Yamaguchi, K. Shiratori, A. Morita, and T. Tahara, "Electric quadrupole contribution to the nonresonant background of sum frequency generation at air/liquid interfaces," *The Journal of Chemical Physics*, vol. 134, no. 18, p. 184705, 2011.
182. Y. R. Shen, "Revisiting the basic theory of sum-frequency generation," *Journal of Chemical Physics*, vol. 153, no. 18, p. 180901, 2020.
183. A. Bogdan and M. J. Molina, "Physical Chemistry of the Freezing Process of Atmospheric Aqueous Drops," *Journal of Physical Chemistry A*, vol. 121, no. 16, pp. 3109–3116, 2017.
184. A. Bogdan, M. J. Molina, H. Tenhu, E. Mayer, and T. Loerting, "Formation of mixed-phase particles during the freezing of polar stratospheric ice clouds," *Nature Chemistry*, vol. 2, pp. 197–201, 2010.
185. A. Bogdan, "Ice Clouds: Atmospheric Ice Nucleation Concept versus the Physical Chemistry of Freezing Atmospheric Drops," *Journal of Physical Chemistry A*, vol. 122, no. 39, pp. 7777–7781, 2018.
186. A. Bogdan and M. J. Molina, "Aqueous aerosol may build up an elevated upper tropospheric ice supersaturation and form mixed-phase particles after freezing," *Journal of Physical Chemistry A*, vol. 114, no. 8, pp. 2821–2829, 2010.
187. A. Bogdan, M. J. Molina, M. Kulmala, H. Tenhu, and T. Loerting, "Solution coating around ice particles of incipient cirrus clouds," *Proceedings of the National Academy of Sciences of the United States of America*, vol. 110, no. 27, p. E2439, 2013.
188. A. Waldner, L. Artiglia, X. Kong, F. Orlando, T. Huthwelker, M. Ammann, and T. Bartels-Rausch, "Pre-melting and the adsorption of formic acid at the air – ice interface at 253 K as seen by NEXAFS and XPS," *Physical Chemistry Chemical Physics*, vol. 20, pp. 24408–24417, 2013.
189. E. Anim-Danso, Y. Zhang, and A. Dhinojwala, "Freezing and melting of salt hydrates next to solid surfaces probed by infrared visible sum frequency generation spectroscopy," *Journal of American Chemical Society*, vol. 135, pp. 8496–8499, 2013.
190. I. R. Hill and I. W. Levin, "Vibrational spectra and carbon-hydrogen stretching mode assignments for a series of n-alkyl carboxylic acids," *The Journal of Chemical Physics*, vol. 70, no. 2, pp. 842–851, 1979.
191. E. Tyrode, C. M. Johnson, S. Baldelli, and M. W. Rutland, "A Vibrational Sum Frequency Spectroscopy Study of the Liquid/Gas Interface of Acetic Acid/Water Mixtures: 2. Orientation Analysis," *Journal of Physical Chemistry B*, vol. 109, pp. 329–341, 2005.
192. R. S. Barr and D. M. T. Newsham, "Freezing Temperatures of Water, Alkanolic Acids and their Mixtures," *The chemical Engineering Journal*, vol. 33, pp. 79–86, 1986.

193. Y. Otsuki, T. Sugimoto, T. Ishiyama, A. Morita, K. Watanabe, and Y. Matsumoto, "Unveiling subsurface hydrogen-bond structure of hexagonal water ice," *Physical Review B*, vol. 90, p. 115405.
194. K. Meister, C. J. Moll, S. Chakraborty, B. Jana, A. L. DeVries, H. Ramløv, and H. J. Bakker, "Molecular structure of a hyperactive antifreeze protein adsorbed to ice," *The Journal of Chemical Physics*, vol. 150, no. 13, p. 131101, 2019.
195. G. A. Saracino, R. Improta, and V. Barone, "Absolute pKa determination for carboxylic acids using density functional theory and the polarizable continuum model," *Chemical Physics Letters*, vol. 373, no. 3-4, pp. 411–415, 2003.
196. S. K. Reddy, R. Thiriaux, B. A. Wellen Rudd, L. Lin, T. Adel, T. Joutsuka, F. M. Geiger, H. C. Allen, A. Morita, and F. Paesani, "Bulk Contributions Modulate the Sum-Frequency Generation Spectra of Water on Model Sea-Spray Aerosols," *Chem*, vol. 4, no. 7, pp. 1629–1644, 2018.
197. W. J. Smit and H. J. Bakker, "The Surface of Ice Is Like Supercooled Liquid Water," *Angewandte Chemie*, vol. 129, no. 49, pp. 15746–15750, 2017.
198. A. Bogdan, M. J. Molina, H. Tenhu, E. Mayer, E. Bertel, and T. Lörting, "Different freezing behavior of millimeter- and micrometer-scaled $(\text{NH}_4)_2\text{SO}_4/\text{H}_2\text{O}$ droplets," *Journal of Physics Condensed Matter*, vol. 23, no. 3, p. 035103, 2011.
199. A. Bogdan, "Double freezing of $(\text{NH}_4)_2\text{SO}_4/\text{H}_2\text{O}$ droplets below the Eutectic Point and the crystallization of $(\text{NH}_4)_2\text{SO}_4$ to the ferroelectric phase," *Journal of Physical Chemistry A*, vol. 114, no. 37, pp. 10135–10139, 2010.
200. W. Sander and M. Gantenberg, "Aggregation of acetic and propionic acid in argon matrices - A matrix isolation and computational study," *Spectrochimica Acta - Part A: Molecular and Biomolecular Spectroscopy*, vol. 62, no. 4-5, pp. 902–909, 2005.
201. A. L. DeVries, "Glycoproteins as Biological Antifreeze Agents in Antarctic Fishes Abstract.," *Science*, vol. 172, no. 6, pp. 1152–1155, 1971.
202. K. A. Sharp, "A peek at ice binding by antifreeze proteins," *Proceedings of the National Academy of Sciences of the United States of America*, vol. 108, no. 18, pp. 7281–7282, 2011.
203. C. A. Knight, C. C. Cheng, and A. L. DeVries, "Adsorption of alpha-helical antifreeze peptides on specific ice crystal surface planes," *Biophysical Journal*, vol. 59, no. 2, pp. 409–418, 1991.
204. M. Bar, Y. Celik, D. Fass, and I. Braslavsky, "Interactions of β -helical antifreeze protein mutants with ice," *Crystal Growth and Design*, vol. 8, no. 8, pp. 2954–2963, 2008.

-
205. M. J. Kuiper, C. J. Morton, S. E. Abraham, and A. Gray-Weale, "The biological function of an insect antifreeze protein simulated by molecular dynamics," *eLife*, vol. 4, 2015.
206. S. Chakraborty and B. Jana, "Molecular Insight into the Adsorption of Spruce Budworm Antifreeze Protein to an Ice Surface: A Clathrate-Mediated Recognition Mechanism," *Langmuir*, vol. 33, no. 28, pp. 7202–7214, 2017.
207. A. Hudait, N. Odendahl, Y. Qiu, F. Paesani, and V. Molinero, "Ice-Nucleating and Antifreeze Proteins Recognize Ice through a Diversity of Anchored Clathrate and Ice-like Motifs," *Journal of the American Chemical Society*, vol. 140, no. 14, pp. 4905–4912, 2018.
208. D. R. Nutt and J. C. Smith, "Dual function of the hydration layer around an antifreeze protein revealed by atomistic molecular dynamics simulations," *Journal of the American Chemical Society*, vol. 130, no. 39, pp. 13066–13073, 2008.
209. E. Kristiansen, H. Ramløv, P. Højrup, S. A. Pedersen, L. Hagen, and K. E. Zachariassen, "Structural characteristics of a novel antifreeze protein from the longhorn beetle *Rhagium inquisitor*," *Insect Biochemistry and Molecular Biology*, vol. 41, no. 2, pp. 109–117, 2011.
210. E. Kristiansen, C. Wilkens, B. Vincents, D. Friis, A. B. Lorentzen, H. Jenssen, A. Løbner-Olesen, and H. Ramløv, "Hyperactive antifreeze proteins from longhorn beetles: Some structural insights," *Journal of Insect Physiology*, vol. 58, no. 11, pp. 1502–1510, 2012.
211. A. Hakim, J. B. Nguyen, K. Basu, D. F. Zhu, D. Thakral, P. L. Davies, F. J. Isaacs, Y. Modis, and W. Meng, "Crystal structure of an insect antifreeze protein and its implications for ice binding," *Journal of Biological Chemistry*, vol. 288, no. 17, pp. 12295–12304, 2013.
212. Y. C. Liou, A. Tocilj, P. L. Davies, and Z. Jia, "Mimicry of ice structure by surface hydroxyls and water of a β -helix antifreeze protein," *Nature*, vol. 406, pp. 322–324, 2000.
213. D. S. Friis, E. Kristiansen, N. Von Solms, and H. Ramløv, "Antifreeze activity enhancement by site directed mutagenesis on an antifreeze protein from the beetle *Rhagium mordax*," *FEBS Letters*, vol. 588, no. 9, pp. 1767–1772, 2014.
214. S. Devineau, K. I. Inoue, R. Kusaka, S. H. Urashima, S. Nihonyanagi, D. Baigl, A. Tsuneshige, and T. Tahara, "Change of the isoelectric point of hemoglobin at the air/water interface probed by the orientational flip-flop of water molecules," *Physical Chemistry Chemical Physics*, vol. 19, no. 16, pp. 10292–10300, 2017.

215. K. Meister, S. Lotze, L. L. Olijve, A. L. DeVries, J. G. Duman, I. K. Voets, and H. J. Bakker, "Investigation of the ice-binding site of an insect antifreeze protein using sum-frequency generation spectroscopy," *Journal of Physical Chemistry Letters*, vol. 6, no. 7, pp. 1162–1167, 2015.
216. J. A. Raymond and A. L. DeVries, "Adsorption inhibition as a mechanism of freezing resistance in polar fishes," *Proceedings of the National Academy of Sciences of the United States of America*, vol. 74, no. 6, pp. 2589–2593, 1977.
217. H. J. C. Berendsen, D. van der Spoel, and R. van Drunen, "GROMACS: A message-passing parallel molecular dynamics implementation," *Computer Physics Communications*, vol. 91, no. 1, pp. 43–56, 1995.
218. S. Pronk, S. Páll, R. Schulz, P. Larsson, P. Bjelkmar, R. Apostolov, M. R. Shirts, J. C. Smith, P. M. Kasson, D. Van Der Spoel, B. Hess, and E. Lindahl, "GROMACS 4.5: A high-throughput and highly parallel open source molecular simulation toolkit," *Bioinformatics*, vol. 29, no. 7, pp. 845–854, 2013.
219. D. Van Der Spoel, E. Lindahl, B. Hess, G. Groenhof, A. E. Mark, and H. J. Berendsen, "GROMACS: Fast, flexible, and free," *Journal of Computational Chemistry*, vol. 26, no. 16, pp. 1701–1718, 2005.
220. G. A. Kaminski, R. A. Friesner, J. Tirado-rives, and W. L. Jorgensen, "Evaluation and Reparametrization of the OPLS-AA Force Field for Proteins via Comparison with Accurate Quantum Chemical Calculations on Peptides†," *Journal of Physical Chemistry B*, vol. 105, pp. 6474–6487, 2001.
221. W. L. Jorgensen and J. Tirado-Rives, "The OPLS Potential Functions for Proteins. Energy Minimizations for Crystals of Cyclic Peptides and Crambin," *Journal of the American Chemical Society*, vol. 110, no. 6, 1988.
222. W. L. Jorgensen, D. S. Maxwell, and J. Tirado-Rives, "Development and testing of the OPLS all-atom force field on conformational energetics and properties of organic liquids," *Journal of the American Chemical Society*, vol. 118, no. 45, pp. 11225–11236, 1996.
223. H. J. Berendsen, J. R. Grigera, and T. P. Straatsma, "The missing term in effective pair potentials," *Journal of Physical Chemistry*, vol. 91, pp. 6269–6271, 1987.
224. T. Bryk and A. D. Haymet, "Ice 1h/water interface of the SPC/E model: Molecular dynamics simulations of the equilibrium basal and prism interfaces," *Journal of Chemical Physics*, vol. 117, no. 22, pp. 10258–10268, 2002.
225. S. Chakraborty and B. Jana, "Conformational and hydration properties modulate ice recognition by type i antifreeze protein and its mutants,"

-
- Physical Chemistry Chemical Physics*, vol. 19, no. 18, pp. 11678–11689, 2017.
226. Y. Zhang, “I-TASSER server for protein 3D structure prediction,” *BMC Bioinformatics*, vol. 9, p. 40, 2008.
227. J. Yang, R. Yan, A. Roy, D. Xu, J. Poisson, and Y. Zhang, “The I-TASSER Suite: protein structure and function prediction,” *Nature Methods*, vol. 12, pp. 7–8, 2015.
228. D. Schneidman-Duhovny, Y. Inbar, R. Nussinov, and H. J. Wolfson, “Patchdock and symmdock: servers for rigid and symmetric docking,” *Nucleic Acids Research*, vol. 33, pp. W363–W367, 2005.
229. J. S. Hub, B. L. de Groot, and D. van der Spoel, “g_wham—A Free Weighted Histogram Analysis Implementation Including Robust Error and Autocorrelation Estimates,” *Journal of Chemical Theory and Computation*, vol. 6, no. 12, pp. 3713–3720, 2010.
230. A. Onishi, K. St Ange, J. S. Dordick, and R. J. Linhardt, “Heparin and anticoagulation,” *Frontiers in Bioscience - Landmark*, vol. 21, no. 7, pp. 1372–1392, 2016.
231. G. Kogan, L. Soltes, R. Stern, and P. Gemeiner, “Hyaluronic acid : a natural biopolymer with a broad range of biomedical and industrial applications,” *Biotechnology Letters*, vol. 29, pp. 17–25, 2007.
232. Z. Zhang and G. F. Christopher, “The nonlinear viscoelasticity of hyaluronic acid and its role in joint lubrication,” *Soft Matter*, vol. 11, no. 13, pp. 2596–2603, 2015.
233. O. Chaudhuri, L. Gu, D. Klumpers, M. Darnell, S. A. Bencherif, J. C. Weaver, N. Huebsch, H. P. Lee, E. Lippens, G. N. Duda, and D. J. Mooney, “Hydrogels with tunable stress relaxation regulate stem cell fate and activity,” *Nature Materials*, vol. 15, no. 3, pp. 326–334, 2016.
234. M. Litwiniuk, A. Krejner-Bienias, M. Speyrer, A. Gauto, and T. Grzela, “Hyaluronic acid in inflammation and tissue regeneration,” *Wounds*, vol. 28, pp. 78–88, 2016.
235. B. P. Toole, “Hyaluronan: from extracellular glue to pericellular cue,” *Nature Reviews Cancer*, vol. 4, pp. 528–539, jul 2004.
236. X. Tian, J. Azpurua, C. Hine, A. Vaidya, M. Myakishev-Rempel, J. Ablava, Z. Mao, E. Nevo, V. Gorbunova, and A. Seluanov, “High-molecular-mass hyaluronan mediates the cancer resistance of the naked mole rat,” *Nature*, vol. 499, pp. 346–349, 2013.
237. J. J. Kwiecinski, S. G. Dorosz, T. E. Ludwig, S. Abubacker, M. K. Cowman, and T. A. Schmidt, “The effect of molecular weight on hyaluronan ’s

- cartilage boundary lubricating ability alone and in combination with proteoglycan 4,” *Osteoarthritis and Cartilage*, vol. 19, no. 11, pp. 1356–1362, 2011.
238. D. C. Florian Wieland and Patrick Degen and Thomas Zander and Sören Gayer and Akanksha Raj and Junxue An and Andra Dédinaité, P. Claesson, and R. Willumeit-Römera, “Soft Matter effects of molecular weight and ion composition ,” *Royal Society of Chemistry*, vol. 12, pp. 729–740, 2016.
239. M. M. Temple-wong, S. Ren, P. Quach, B. C. Hansen, A. C. Chen, A. Hasegawa, D. D. D. Lima, J. Koziol, K. Masuda, M. K. Lotz, and R. L. Sah, “Hyaluronan concentration and size distribution in human knee synovial fluid : variations with age and cartilage degeneration,” *Arthritis Research & Therapy*, pp. 1–8, 2016.
240. A. Singh, M. Corvelli, S. A. Unterman, K. A. Wepasnick, P. McDonnell, and J. H. Elisseeff, “Enhanced lubrication on tissue and biomaterial surfaces through peptide-mediated binding of hyaluronic acid,” *Nature Materials*, vol. 13, pp. 988–995, 2014.
241. M. J. Rah, “A review of hyaluronan and its ophthalmic applications,” *Optometry - Journal of the American Optometric Association*, vol. 82, no. 1, pp. 38–43, 2011.
242. J. J. Nichols and L. T. Sinnott, “Tear film, contact lens, and patient-related factors associated with contact lens-related dry eye,” *Investigative Ophthalmology and Visual Science*, vol. 47, no. 4, pp. 1319–1328, 2006.
243. G. Giubertoni, G. H. Koenderink, and H. J. Bakker, “Direct Observation of Intrachain Hydrogen Bonds in Aqueous Hyaluronan,” *Journal of Physical Chemistry A*, vol. 123, no. 38, pp. 8220–8225, 2019.
244. F. Burla, J. Tauber, S. Dussi, J. van der Gucht, and G. H. Koenderink, “Stress management in composite biopolymer networks,” *Nature Physics*, vol. 15, pp. 549–553, 2019.
245. X. Chen and R. P. Richter, “Effect of calcium ions and pH on the morphology and mechanical properties of hyaluronan brushes,” *Interface Focus*, vol. 9, no. 2, 2019.
246. E. A. Balazs and J. Cui, “The story of hyaluronan putty,” *Bioactive Carbohydrates and Dietary Fibre*, vol. 2, no. 2, pp. 143–151, 2013.
247. P. H. Weigel and P. L. DeAngelis, “Hyaluronan synthases: A decade-plus of novel glycosyltransferases,” *Journal of Biological Chemistry*, vol. 282, no. 51, pp. 36777–36781, 2007.
248. L. Martin-Alarcon and T. A. Schmidt, “Rheological effects of macromolecular interactions in synovial fluid,” *Biorheology*, vol. 53, no. 2, pp. 49–67, 2016.

-
249. K. Vorvolakos, J. C. Coburn, and D. M. Saylor, "Dynamic interfacial behavior of viscoelastic aqueous hyaluronic acid: Effects of molecular weight, concentration and interfacial velocity," *Soft Matter*, vol. 10, no. 13, pp. 2304–2312, 2014.
250. W. Ribeiro, L. Mata, and B. Saramago, "Effect of Concentration and Temperature on Surface Tension of Sodium Hyaluronate Saline Solutions," *Langmuir*, vol. 23, no. 13, pp. 7014–7017, 2007.
251. P. Balzerowski, K. Meister, J. Versluis, and H. J. Bakker, "Heterodyne-detected sum frequency generation spectroscopy of polyacrylic acid at the," *Physical Chemistry Chemical Physics*, vol. 18, no. 2, pp. 2481–2487, 2015.
252. X. Lu, C. Zhang, N. Ulrich, M. Xiao, Y. H. Ma, and Z. Chen, "Studying Polymer Surfaces and Interfaces with Sum Frequency Generation Vibrational Spectroscopy," *Analytical Chemistry*, vol. 89, no. 1, pp. 466–489, 2017.
253. D. Hu and K. C. Chou, "Re-Evaluating the Surface Tension Analysis of Polyelectrolyte-Surfactant Mixtures Using Phase-Sensitive Sum Frequency Generation Spectroscopy," *Journal of American Chemical Society*, vol. 136, no. 43, pp. 15114–15117, 2014.
254. A. Maroudas, "Balance between swelling pressure and collagen tension in normal and degenerate cartilage," *Nature*, vol. 260, pp. 808–809, 1976.
255. C. S. Tian and Y. R. Shen, "Isotopic dilution study of the water/vapor interface by phase-sensitive sum-frequency vibrational spectroscopy," *Journal of the American Chemical Society*, vol. 131, no. 8, pp. 2790–2791, 2009.
256. X. Chen, W. Hua, Z. Huang, and H. C. Allen, "Interfacial water structure associated with phospholipid membranes studied by phase-sensitive vibrational sum frequency generation spectroscopy," *Journal of the American Chemical Society*, vol. 132, no. 32, pp. 11336–11342, 2010.
257. J. C. Conboy, M. C. Messmer, and G. L. Richmond, "Dependence of alkyl chain conformation of simple ionic surfactants on head group functionality as studied by vibrational sum-frequency spectroscopy," *Journal of Physical Chemistry B*, vol. 101, no. 34, pp. 6724–6733, 1997.
258. R. Cota, N. Ottosson, H. J. Bakker, and S. Woutersen, "Evidence for Reduced Hydrogen-Bond Cooperativity in Ionic Solvation Shells from Isotope-Dependent Dielectric Relaxation," *Physical Review Letters*, vol. 120, no. 21, pp. 1–5, 2018.
259. R. Buchner, "What can be learnt from dielectric relaxation spectroscopy about ion solvation and association?," *Pure and Applied Chemistry*, vol. 80, no. 6, pp. 1239–1252, 2008.

260. J. Zhang and R. Pelton, "The dynamic behavior of poly(N-isopropylacrylamide) at the air/water interface," *Colloids and Surfaces A: Physicochemical and Engineering Aspects*, vol. 156, no. 1-3, pp. 111–122, 1999.
261. V. G. Babak, E. A. Skotnikova, I. G. Lukina, S. Pelletier, P. Hubert, and E. Dellacherie, "Hydrophobically associating alginate derivatives: Surface tension properties of their mixed aqueous solutions with oppositely charged surfactants," *Journal of Colloid and Interface Science*, vol. 225, no. 2, pp. 505–510, 2000.
262. H. Yim, M. Kent, A. Matheson, R. Ivkov, S. Satija, J. Majewski, and G. S. Smith, "Adsorption of poly(styrenesulfonate) to the air surface of water by neutron reflectivity," *Macromolecules*, vol. 33, no. 16, pp. 6134–6139, 2000.
263. D. Hu, Z. Yang, and K. C. Chou, "Interactions of Polyelectrolytes with Water and Ions at Air/Water Interfaces Studied by Phase-Sensitive Sum Frequency Generation Vibrational Spectroscopy," *The Journal of Physical Chemistry C*, vol. 117, no. 30, pp. 15698–15703, 2013.
264. Q. Chen, D. Zhang, G. Somorjai, and C. R. Bertozzi, "Probing the surface structural rearrangement of hydrogels by sum-frequency generation spectroscopy," *Journal of the American Chemical Society*, vol. 121, no. 2, pp. 446–447, 1999.
265. R. R. Netz and D. Andelman, "Neutral and charged polymers at interfaces," *Physics Reports*, vol. 380, no. 1-2, pp. 1–95, 2003.
266. J. R. van der Maarel, *Introduction to biopolymer physics*. World Scientific, 2007.
267. S. L  lu and A. Pluen, "Characterization of composite networks made of type I collagen, hyaluronic acid and decorin," *Macromolecular Symposia*, vol. 256, no. 1, pp. 175–188, 2007.
268. A. Borzacchiello and L. Ambrosio, "Network formation of low molecular weight hyaluronic acid derivatives," *Journal of Biomaterials Science, Polymer Edition*, vol. 12, no. 3, pp. 307–316, 2001.
269. S. Strazdaite, K. Meister, and H. J. Bakker, "Reduced Acid Dissociation of Amino-Acids at the Surface of Water," *Journal of the American Chemical Society*, vol. 139, no. 10, pp. 3716–3720, 2017.
270. B. A. Wellen, E. A. Lach, and H. C. Allen, "Surface pK_a of octanoic, nonanoic, and decanoic fatty acids at the air-water interface: Applications to atmospheric aerosol chemistry," *Physical Chemistry Chemical Physics*, vol. 19, no. 39, pp. 26551–26558, 2017.
271. D. K. Beaman, E. J. Robertson, and G. L. Richmond, "Ordered polyelectrolyte assembly at the oil-water interface," *Proceedings of the National Academy of Sciences of the United States of America*, vol. 109, no. 9, pp. 3226–3231, 2012.

-
272. E. J. Robertson and G. L. Richmond, "Molecular insights in the structure and layered assembly of polyelectrolytes at the oil/water interface," *Journal of Physical Chemistry C*, vol. 118, no. 49, pp. 28331–28343, 2014.
273. D. K. Beaman, E. J. Robertson, and G. L. Richmond, "Metal ions: Driving the orderly assembly of polyelectrolytes at a hydrophobic surface," *Langmuir*, vol. 28, no. 40, pp. 14245–14253, 2012.
274. J. D. Berry, M. J. Neeson, R. R. Dagastine, D. Y. Chan, and R. F. Tabor, "Measurement of surface and interfacial tension using pendant drop tensiometry," *Journal of Colloid and Interface Science*, vol. 454, pp. 226–237, 2015.

SUMMARY

Surfaces are omnipresent in nature, therefore in the past numerous theoretical and experimental techniques were developed to get a fundamental understanding of important interfacial processes. As water is one of the most abundant molecules in nature undoubtedly many important interfacial processes take place at aqueous interfaces. In this thesis we use surface-specific vibrational sum-frequency generation spectroscopy (VSFG) to study surfaces at a molecular level ranging from relatively simple surfaces like the neat water/air interface (Chapter 4) to more complex surfaces like the ice surface with adsorbed antifreeze proteins (Chapter 9). Briefly, VSFG is a surface selective technique in which an infrared (IR) beam and a visible beam (VIS) overlap spatially and temporally at the interface and generate light at their sum frequency. Therefore, the VSFG response is dependent on the incoming electric fields, the IR and visible beam, and on the nonlinear second-order susceptibility ($\chi^{(2)}$) of the probed material. The sum-frequency light is enhanced if the IR beam is in resonance with a vibration of the molecules of the studied system. A detailed description of the theoretical background of the origin of VSFG can be found in chapter 2, while in chapter 3 we introduce the experimental methods. Here, we also introduce a technique to measure the phase of the generated sum-frequency light: heterodyne-detected vibrational sum-frequency generation (HD-VSFG).

CHAPTER 4: DIRECT EVIDENCE FOR A SURFACE AND BULK SPECIFIC VSFG RESPONSE OF THE WATER BEND VIBRATION First, we report on HD-VSFG measurements of the surfaces of pure water and of charged aqueous surfaces. By comparing the responses measured for differently charged water surfaces, we identify the presence of a surface-specific dipolar response of the water bending mode centered at 1626 cm^{-1} . This response changes sign when the sign of the surface charge changes, and increases with increasing surface charge, i.e. by increasing the concentration of an ionic surfactant. In addition to this dipolar contribution, we observe the presence of a quadrupolar bulk contribution of the bending mode centered at 1656 cm^{-1} . This contribution is not surface-charge dependent and dominates the response of (charge-neutral) neat water in the frequency region of the bending mode. We thus demonstrate that HD-VSFG involving the bending mode of the water molecules can provide important information on the hydrogen-bond structure of both the surface and the bulk of aqueous solutions. With these findings we resolve the controversy on the origin of the response of the water bending mode measured in previous vibrational SFG studies. Our findings also open up the way to use HD-VSFG in the frequency region of the bending mode of the water molecules to study the hydrogen-bond structure of both the surface and the bulk of a wide variety of aqueous systems, as presented in chapter 5 - 7.

CHAPTER 5: DIRECT OBSERVATION OF THE ORIENTATION OF UREA MOLECULES AT CHARGED INTERFACES Aqueous urea solutions have most striking properties and play an important role in many biological processes. Thus, a fundamental understanding of the interfacial properties of aqueous urea solutions is of strong general importance. In this chapter, we study the properties of urea molecules at charged aqueous interfaces. We find that the net orientation of the urea molecules is highly correlated to that of the directly surrounding water molecules, showing the same dependence on the sign of the charge at the surface and a similar reduction of the degree of net orientation upon screening of the surface electric field by adding ions to the solution. These observations indicate that urea and water form a robust hydrogen-bond network near the interface that governs their collective molecular dynamics. We further conclude that beside water, urea molecules serve as an excellent probe for the interfacial electric field.

CHAPTER 6: MOLECULAR ORIENTATION OF SMALL CARBOXYLATES AT THE WATER-AIR INTERFACE Many interfacial processes involve the deprotonated carboxylate group ($-\text{COO}^-$), which is ubiquitous in nature. Here, we probe the surface and bulk properties of aqueous sodium formate and sodium acetate, using Fourier Transform Infrared and HD-VSFG spectroscopy. We find that in aqueous solutions sodium formate and sodium acetate give rise to responses of the symmetric stretch vibration (ν_s) and the antisymmetric stretch vibration ν_{as} of the two CO groups of the carboxylate group. From these responses, we deduce that formate as well as acetate anions are present at the surface. Additionally, we obtain information about the orientation of the carboxylates at the surface and observe that for both formate and acetate the main molecular axis is at a nonzero angle with respect to the surface normal. We can further observe that the surface response increases with increasing carboxylate concentration in the bulk solution, due to accumulation of the carboxylates at the surface. Finally we found, that in the explored concentration range the vibrational response of carboxylates is modulated by the Fresnel factors that are dependent on the carboxylate concentration, leading to a shift toward higher frequencies and an asymmetry of the vibrational bands.

CHAPTER 7: BULK RESPONSE OF CARBOXYLIC ACID SOLUTIONS OBSERVED WITH SURFACE SUM-FREQUENCY GENERATION SPECTROSCOPY In the past decades carboxylic acids have attracted significant attention in the research field of atmospheric chemistry. Therefore, we study the interfacial properties of aqueous acetic and formic acid solutions with different concentrations. We find that by increasing the bulk concentration of the acid solutions the surface response of the hydroxyl and carbonyl stretch vibrations increases, due to accumulation of the acid molecules at the surface. A further increase of the acid concentration leads to a saturation and subsequently to a decrease in intensity of these responses. At very high carboxylic acid concentrations even a change in sign of the $\text{Im}[\chi^{(2)}]$ response of the carbonyl vibration can be observed, indicating the formation of cyclic dimers, which only show a quadrupolar bulk response in the HD-VSFG spectrum because of the antiparallel orientation of

the carboxyl groups in these dimers. This quadrupolar response is of opposite sign in comparison to the dipolar response of monomeric carboxylic acids. In the CH region we find that by increasing the concentration the response of the CH vibrations saturates instead of decreasing. This indicates that either the centrosymmetry regarding the CH groups of formic acid and acetic acid is broken directly at the surface or that the response of the CH vibrations also contains a quadrupolar contribution that is of the same sign as the dipolar response. Further, formic acid shows an additional negative band throughout the whole concentration range which indicates the presence of linear dimers, in addition to cyclic dimers. In this chapter the observation of quadrupolar bulk components in the SFG responses of the CH and C=O vibrations implies that the probing of liquids via SFG spectroscopy of these vibrations is likely not as surface specific as up to now has been assumed.

CHAPTER 8: FREEZING OF AQUEOUS CARBOXYLIC ACID SOLUTIONS ON ICE

The properties of carboxylic acids not only at the water surface but also at the surface of ice plays an important role in atmospheric chemistry. In particular the interaction of carboxylic acids with the surface of ice particles, plays a crucial role in the heterogeneous chemistry of clouds and is thus important in the study of climate change and other environmental issues. Therefore, we study the freezing of carboxylic acid solutions on the surface of ice. If we decrease the temperature toward the eutectic point of the acid solutions, we observe the formation of a freeze concentrated solution (FCS) of the carboxylic acids that is brought about by a freeze-induced phase separation (FIPS). As we cool the system below the eutectic point the freeze concentrated solution freezes on top of the ice surface. In the case of the freeze concentrated acetic acid solutions we find that the freezing causes a strong decrease of the VSFG signal, while in the case of propionic acid an increase and a blue-shift are observed. This different behavior points at a distinct difference in molecular-scale behavior upon freezing acetic and propionic acid solutions on the surface of ice.

CHAPTER 9: MOLECULAR STRUCTURE OF HYPERACTIVE ANTIFREEZE PROTEIN ADSORBED TO ICE

Ice surfaces play also a crucial role for biological systems as for instance in their interaction with antifreeze proteins (AFPs), a unique class of proteins that bind to the surfaces of ice crystals and that arrest their growth. To understand the working mechanism of these proteins is of great interest for the medicine, pharmacy and industry. In this chapter, we study the structural properties of the hydration layer of an AFP from the insect *Rhagium mordax* (RmAFP) adsorbed to ice. We find that RmAFP, unlike other proteins, retains its hydrating water molecules upon adsorption to the ice surface. This hydration water has an orientation and hydrogen-bond structure different from the ice surface, thereby inhibiting the insertion of water layers in between the protein and the ice surface.

CHAPTER 10: THE MOLECULAR STRUCTURE AND SURFACE ACCUMULATION DYNAMICS OF HYALURONAN AT THE WATER/AIR INTERFACE

Hyaluronan is a biopolymer that is essential for many biological processes in the human body. Furthermore, because of its biocompatibility, hyaluronan is widely used

in biomedicine to design hydrogels with tailored applications. The outstanding physiological relevance and the wide range of applications of hyaluronan have led to numerous studies of its microscopic and macroscopic properties, while the interfacial properties are poorly understood. Therefore, we investigate the dependence of the surface accumulation and surface structure of hyaluronan polymers on the molecular weight and concentration of the polymers, and the pH of the solution. We find that low-molecular weight (~ 150 kD) hyaluronan accumulates at the water/air interface within a few hours, rendering the surface negatively charged due to the presence of carboxylate anion groups in the hyaluronan polymers. This rate strongly increases when the concentration of low-molecular weight hyaluronan increases. Surprisingly, high molecular weight (>1 MDa) hyaluronan cannot be detected at the surface, even hours after addition of the polymer to the aqueous solution. This low rate of diffusion to the surface probably finds its origin in the entanglement of the long polymer chains of high molecular weight hyaluronan. Furthermore, we find that the surface accumulation of hyaluronan shows an anomalous dependence on the pH of the solution. A lowering of the pH strongly decreases the degree of accumulation of hyaluronan at the surface, which can be explained by the interplay of hydrogen-bonding and electrostatic interactions of the hyaluronan polymers.

SAMENVATTING

Oppervlaktes zijn alomtegenwoordig in de natuur, daarom zijn in het verleden vele theoretische en experimentele technieken ontwikkeld om een fundamenteel begrip te krijgen van belangrijke processen op grensvlakken. Omdat water een van de meest voorkomende moleculen is in de natuur, vinden vele belangrijke processen plaats op grensvlakken van water. In dit proefschrift gebruiken we oppervlakte-specifieke vibrationele som-frequentie generatie spectroscopie (VSFG) voor het bestuderen van oppervlaktes op moleculair niveau, variërend van relatief simpele oppervlaktes zoals het puur water/lucht grensvlak (hoofdstuk 4), tot complexere oppervlaktes zoals het ijsoppervlak met geadsorbeerde antivrieseiwitten (hoofdstuk 9). VSFG is een oppervlakte selectieve techniek waarbij een infrarood (IR) bundel en een zichtbare bundel (VIS) in tijd en ruimte met elkaar overlappen op een grensvlak, en licht genereren met een frequentie die de som is van de IR en VIS frequenties. De sterkte van de VSFG-respons is afhankelijk van de elektrische velden van de IR en de zichtbare bundel, en van de niet-lineaire tweede order susceptibiliteit ($\chi^{(2)}$) van het te onderzoeken materiaal. Het som-frequentie licht wordt intenser als de IR bundel in resonantie is met een vibratie van de moleculen in het bestudeerde systeem. Een gedetailleerde beschrijving van de theoretische achtergrond van de oorsprong van VSFG wordt gegeven in hoofdstuk 2. In hoofdstuk 3 introduceren we de experimentele methodes. Hierin introduceren we ook een techniek om de fase te meten van het gegenereerde som-frequentie licht: heterodyne-gedetecteerde vibrationele som-frequentie generatie (HD-VSFG).

HOOFDSTUK 4: DIRECT BEWIJS VOOR EEN OPPERVLAKTE EN BULK SPECIFIEKE VSFG RESPONS VAN DE WATER BUIGVIBRATIE Als eerste rapporteren we HD-VSFG metingen van de oppervlakte van puur water en geladen water oppervlaktes, Door het vergelijken van de respons gemeten voor oppervlaktes met verschillende ladingen, identificeren we de aanwezigheid van een oppervlakte-specifiek dipolair response van de water buigvibratie, gecentreerd rond 1626 cm^{-1} . Deze respons verandert van teken wanneer het teken van de oppervlaktelading verandert, en neemt toe met toenemende oppervlaktelading, wat bereikt kan worden door de concentratie van een ionische surfactant te verhogen. Naast deze dipolaire contributie, observeren we de aanwezigheid van een quadropolaire bulk contributie van de buigvibratie bij 1656 cm^{-1} . Deze contributie is niet oppervlaktelading afhankelijk en domineert de respons van (neutraal geladen) puur water. Hierdoor demonstreren we dat HD-VSFG van de buigvibratie van water moleculen belangrijke informatie kan leveren over de waterstofbrugstructuur van zowel het oppervlakte als de bulk van waterige oplossingen. Met deze bevindingen lossen we de controverse op over de oorsprong van de respons van de water buigvibratie gemeten in voorgaande vi-

brationele SFG studies. Onze bevindingen openen ook de weg om HD-SFG te gebruiken in het frequentiegebied van de buigvibratie van watermoleculen voor het bestuderen van de waterstofbrugstructuur van zowel de oppervlakte als de bulk voor een grote verscheidenheid van waterige systemen zoals getoond in hoofdstuk 5-7.

HOOFDSTUK 5: DIRECTE OBSERVATIE VAN DE ORIËNTATIE VAN UREUM MOLECULEN AAN GELADEN GRENSVLAKKEN Waterige ureumoplossingen hebben zeer opvallende eigenschappen en spelen een belangrijke rol in vele biologische processen. Het is daarom van groot algemeen belang om een fundamenteel begrip te verkrijgen van de grensvlak eigenschappen van waterige ureum oplossingen. In dit hoofdstuk bestuderen we de eigenschappen van ureummoleculen aan geladen waterige grensvlakken. We vinden dat de netto oriëntatie van de ureummoleculen sterk gecorreleerd is aan die van de watermoleculen in de directe omgeving, met dezelfde afhankelijkheid van het teken van de lading aan het oppervlak en een vergelijkbare afname van de graad van netto oriëntatie wanneer het elektrisch veld van het oppervlak wordt afgeschermd door het toevoegen van ionen aan de oplossing. Deze observaties geven aan dat ureum en water een robuust waterstofbrug netwerk vormen in de buurt van het grensvlak, dat hun collectieve moleculaire dynamica bepaalt. Verder concluderen we dat net als water, ureum een uitstekende probe zijn voor het interfaciale elektrische veld.

HOOFDSTUK 6: VIBRATIONEEL RESPONS VAN KLEINE CARBOXYLATEN AAN HET WATER-LUCHT GRENSVLAK Vele grensvlakprocessen hebben betrekking op de gedeprotoneerde carboxylaatgroep ($-\text{COO}^-$), die alomtegenwoordig is. Hier bestuderen we de oppervlakte en bulk eigenschappen van waterig natriumformiaat en natriumacetaat, door middel van Fourier Transformatie Infrarood en HD-VSFG spectroscopie. We vinden dat in waterige oplossingen natriumformiaat en natriumacetaat een respons geven van de symmetrische strekvibratie (ν_s) en de antisymmetrische strekvibratie (ν_{as}) van de twee CO groepen van de carboxylaatgroep. Uit deze responsen deduceren we dat formiaat en acetaat zich beiden aan het oppervlak bevinden. Daarnaast verkrijgen we informatie over de oriëntatie van de carboxylaten aan het oppervlak en zien we dat voor zowel formiaat als acetaat de moleculaire hoofdas niet loodrecht op het oppervlak staat. We kunnen verder waarnemen dat de respons aan het oppervlak toeneemt met toenemende carboxylaatconcentratie in de bulkoplossing, als gevolg van accumulatie van de carboxylaten aan het oppervlak. Tenslotte vonden we dat in het onderzochte concentratiebereik de vibrationele respons van carboxylaten gemoduleerd wordt door de Fresnel factoren die afhankelijk zijn van de carboxylaatconcentratie, wat leidt tot een verschuiving naar hogere frequenties en asymmetrie van de vibrationele banden.

HOOFDSTUK 7: BULK RESPONS VAN CARBONZUROPLOSSINGEN GEBESERVEERD MET OPPERVLAKTE SOM-FREQUENTIE GENERATIE SPECTROSCOPIE In de afgelopen decennia hebben carbonzuren veel aandacht gekregen in onderzoek op het gebied van de atmosferische chemie. Daarom bestuderen we de interfaciale eigenschappen van waterige azijnzuur- en mierenzuuroplossingen

met verschillende concentraties. We vinden dat door het verhogen van de bulkconcentratie van de zuuroplossingen, de oppervlakte respons van de hydroxyl en carbonyl strekvibraties toeneemt, wat wijst op accumulatie van de zuurmoleculen aan het oppervlak. Een verdere verhoging van de concentratie leidt tot een verzadiging en vervolgens tot een afname van de intensiteit van deze respons. Bij zeer hoge carbonzuurconcentraties wordt zelfs een verandering in het teken van de $\text{Im}[\chi^{(2)}]$ respons van de carbonylvibratie waargenomen, wat wijst op de vorming van cyclische dimeren die alleen een quadrupolaire bulk respons in het HD-VSFG-spectrum vertonen vanwege de antiparallelle oriëntatie van de carboxylgroepen in deze dimeren. Deze quadrupolaire respons is van tegengesteld teken in vergelijking met de dipolaire respons van carbonzuur monomeren. In het CH gebied zien we dat bij verhoging van de concentratie de respons van de CH vibraties verzadigt in plaats van afneemt. Dit wijst erop dat ofwel de centrosymmetrie met betrekking tot de CH groepen van mierenzuur en azijnzuur direct aan het oppervlak wordt verbroken, of dat de respons van de CH-trillingen ook een quadrupolaire bijdrage bevat die van hetzelfde teken is als de dipolaire respons. Verder vertoont mierenzuur een extra negatieve band over het gehele concentratiebereik, wat wijst op de aanwezigheid van lineaire dimeren naast de cyclische dimeren. In dit hoofdstuk impliceert de waarneming van de quadrupolaire bulk componenten in de SFG responsen van de CH en C=O vibraties dat het onderzoeken van vloeistoffen met behulp van SFG spectroscopie waarschijnlijk niet zo oppervlakte specifiek is als tot nu toe werd aangenomen.

HOOFDSTUK 8: BEVRIEZEN VAN WATERIGE CARBONZUROPLOSSINGEN OP IJS
De eigenschappen van carbonzuren spelen niet alleen aan het wateroppervlak, maar ook aan het oppervlak van ijs een belangrijke rol in de atmosferische chemie. In het bijzonder speelt de interactie van carbonzuren met het oppervlak van ijsdeeltjes een cruciale rol in de heterogene chemie van wolken, en is derhalve belangrijk voor klimaatverandering en milieuvraagstukken. Daarom bestuderen we het bevriezen van carbonzuuroplossing aan het oppervlak van ijs. Als we de temperatuur verlagen naar het eutectische punt van de carbonzuuroplossingen, zien we de vorming van een vriesgeconcentreerde oplossing (FCS) van de carbonzuren, die tot stand komt door bevriezing geïnduceerde fasescheiding (FIPS). Wanneer we het systeem afkoelen tot onder het eutectische punt, bevriest de vriesgeconcentreerde oplossing bovenop het ijsoppervlak. In het geval van vriesgeconcentreerde azijnzuuroplossingen zien we dat het bevriezen een sterke afname van het VSFG signaal veroorzaakt, terwijl in het geval van propionzuur een toename en een blauwverschuiving van het VSFG signaal worden waargenomen. Dit verschillende gedrag wijst op een duidelijk verschil op moleculaire schaal bij het bevriezen van azijnzuur- en propionzuuroplossingen aan het oppervlak van ijs.

HOOFDSTUK 9: MOLECULAIRE STRUCTUUR VAN HYPERACTIEF ANTIVRIESEI-WIT GEADSORBEERD AAN IJS
Ijsoppervlakken spelen ook een cruciale rol voor biologische systemen, zoals bijvoorbeeld in hun interactie met antivrieseiwitten (AFP's), een unieke klasse van eiwitten die zich binden aan de oppervlakken

van ijskristallen en hun groei kunnen stoppen. Het begrijpen van het werkingsmechanisme van deze eiwitten is van groot belang voor de geneeskunde, de farmacie en de industrie. In dit hoofdstuk bestuderen we de structurele eigenschappen van de hydratatielaag van een AFP van het insect *Rhagium mordax* (RmAFP) geadsorbeerd aan ijs. We nemen waar dat RmAFP, in tegenstelling tot andere eiwitten, zijn hydratatiemoleculen behoudt na adsorptie aan het ijsoppervlak. Dit hydratatiewater heeft een oriëntatie en waterstofbrugstructuur die afwijkend is van het ijsoppervlak, waardoor het zorgt voor een remming van het invoegen van waterlagen tussen het eiwit en het ijsoppervlak.

HOOFDSTUK 10: DE MOLECULAIRE STRUCTUUR EN OPPERVLAKTEACCUMULATIE DYNAMICA VAN HYALURONAN OP HET GRENSVLAK VAN WATER/LUCHT
Hyaluronan is een biopolymeer dat essentieel is voor vele biologische processen in het menselijk lichaam. Bovendien, wegens zijn biocompatibiliteit, wordt hyaluronan veel gebruikt in de biogeneeskunde om hydrogels met aangepaste toepassingen te ontwerpen. De buitengewone fysiologische relevantie en het brede gebied aan toepassingen van hyaluronan hebben geleid tot talrijke studies van zijn microscopische en macroscopische eigenschappen, terwijl de interfaciale eigenschappen slecht begrepen zijn. Daarom onderzoeken wij de oppervlakteaccumulatie en oppervlaktestructuur in afhankelijkheid van het moleculaire gewicht en de concentratie van de hyaluronan polymeren, en de zuurgraad van de oplossing. We ontdekten dat laag moleculair gewicht (~ 150 kDa) hyaluronan zich binnen enkele uren ophoopt aan het water/lucht grensvlak, waardoor het oppervlak negatief geladen wordt, als gevolg van de carboxylaataniongroepen in de hyaluronan polymeren. Deze snelheid neemt sterk toe wanneer de concentratie van laagmoleculair gewicht hyaluronzuur toeneemt. Verassend is dat hyaluronan met een hoog molecuulgewicht (>1 MDa) niet aan het oppervlak wordt gedetecteerd, zelfs uren na toevoeging van het polymeer aan de waterige oplossing. Deze lage diffusiesnelheid naar het oppervlak vindt waarschijnlijk zijn oorsprong in de verstrengeling van de lange polymeerketens van hyaluronan met een hoog moleculair gewicht. Bovendien vonden we dat de accumulatie van hyaluronan een onverwachte afhankelijkheid vertoont van de pH van de oplossing. Een verlaging van de pH verlaagt de negatieve lading waardoor je in eerste instantie zou verwachten dat hyaluronan sneller naar het oppervlak zou komen. We meten echter een sterke afname van de mate van accumulatie van hyaluronan aan het oppervlak, wat verklaard kan worden uit het samenspel van de waterstofbruggen en elektrostatistische interacties van de hyaluronan polymeren.

ACKNOWLEDGEMENTS

*When calls the heart...*most of you make fun of me because of my love for absolute predictable love stories with a little bit of drama. If this predictable love story would be your life, would it be so predictable?

If I look back over the last 4 years, a lot of events were not predictable and came with a lot of frustration and heartbreak, but as many events came with a lot of love, happiness, and success. And for everyone who was not part of my life, I can assure you there was also a lot of drama =) The last chapter I would like to dedicate to everyone who played part in my little Ph.D. telenovela and without this thesis would have not been possible.

First, I would like to thank my supervisor Huib for giving me the opportunity to continue the research, that I started in my Master's internship at AMOLF over another four years. Besides this, you gave me the freedom of exploring many different research projects, from which seven ended in this book. You helped me to develop my scientific mind and made me a "stubborn" scientist, who does not believe everything only because it is written in a high-impact journal. And at last, thank you for having so much patience in helping me to structure and write all the projects down and for helping me to answer any kind of nasty reviewer comments. Second, I would like to thank Konrad who is not only my Co-promotor but was also my daily supervisor during my Master's internship and in the first month of my Ph.D.. Thank you for never giving up on me although my writing and English skills needed much improvement. I will never forget when you told me to stop all my measurements to introduce me to the Dutch tradition of 'borrels'. You have taught me that the way to the perfect measurement is to sometimes take a break, drink a glass of gin tonic with a good friend to clear your head, and start fresh again the next day. I would also like to thank the Doctorate Committee, prof. dr. Wybren Jan Buma, prof. dr. Ellen Backus, prof. dr. Wim Noorduyn, prof. dr. Poul Petersen, dr. Monique van der Veen and prof. dr. Ilja Voets for accepting to be part of my committee and taking the time to read and evaluate my thesis. Further, I would like to thank Gijsje Koenderink for sharing her expertise and knowledge about hyaluronic acid and for making chapter 10 possible.

Furthermore, I would like to thank Jan, there is not one word to describe what you are doing at AMOLF and what you have done for me. I guess the term LASER MAGICIAN would be close, but it leaves out all the scientific knowledge you have and share. Besides fixing, saving, or better healing the lasers you helped me to interpret and model my data. You are not only a

really good scientist but also a very kind and motivating person. I will miss our passionate discussions in the hallway about new data, bikes, and life. I am very grateful that I have met and got to know you. You helped me through the last two not-so-easy years and made me keep my love for science. I would also like to thank Hincó, you are not only an amazing technician who was essential for making all my projects happen but also the heart of our research group. You always have an open ear and were there for us when we needed you the most. You listen to all our struggles inside and outside the office. If we need help you never say no and always try to help us. Besides that, you are a very welcoming, funny and warm person and you make a fantastic Stew =)

Next, I would like to thank my two amazing paranymphs Eliane and Roberto, without whom that journey would have been more difficult, maybe even impossible, and way less fun. Eliane, I have to say when I met you the first time, I was a bit intimidated by your direct Dutch personality, but it took not long that I started to love that part of you and learned that there is much more to you than being the bossy in the group. You are an amazing, honest, funny, talented, considerate, and kind friend, office mate, and scientist. I could not imagine a better person to "steal" Christmas trees with, dance on the table at summer barbeques, plan the dress that we are going to wear at the Christmas lunch and keep each other awake during late-night measurements. When you moved to Germany, I missed you a lot in the office, even though sometimes it seemed like you never left the Netherlands cause of all the supporting text messages helping me through highs and lows in the last year of my Ph.D. Roberto, I am still impressed that you were able to finish your Ph.D. thesis in an office with Eliane and me chatting for hours ("only scientific discussion of course"). I guess it was an advantage to have good headphones =) You were the calm and positive person that balanced the emotions in the office. Thank you for all the times you were there for me with a hug and a beer, when I had a difficult time in and outside of the office. Thank you for the positive and happy energy you brought into the office and to many parties. Thanks for all the guacamole that made my life so much better. To both of you thank you for all the scientific and hilarious discussions, all the support and motivation, all the Party boards and drinks we shared. I am looking forward to sharing more happy and slightly dramatic moments with both of you and to having you both by my side at the defense and many other events, travels, and parties.

Laura my clumsy lovely friend, the first time we met you dropped red wine on my shirt...and it was not the last time. Who could have imagined that such a great friendship would come out of some drops of red wine, that lasts even though we do not live in the same country? You are such a wonderful, caring, funny, generous, and creative person. I cannot express in words how happy I am that we met. Thank you for giving me a push when I needed it and showing me that the world is there to explore it. Do not stop to light up the world with your amazing and beautiful smile. Alexander in the last years we shared way more than just one chapter of this thesis. Thanks for all the help and support in the lab and the office. Thank you for accepting me in "your" office after

Aleksandr left (I guess it was quite a change). With your calm, kind and caring personality you made me feel always comfortable and less lonely. Thank you for listening to all my stories without getting annoyed, for all the discussions in the office, after-work snacks and drinks, dances in the lab, and hugs. Next, I would like to thank Aleksandr! You are the perfect example for a person with a hard (or in your case dark) shell and a softcore. Once I got to know you, I saw you are not only a really smart, persistent, and talented but also a very kind and supportive person. I missed all your dark jokes in the group meetings the last year. You will probably hate me for writing this, but you have a wonderful smile, and I am happy you shared that with me a couple of times. Many thanks to the both of you for introducing me to Russian and Ukrainian traditions (рюмка водки на столе) and the out of body experiences that came with it. Giulia, everyone in our group always called you Mama Giulia, because of your supporting, caring, and selfless personality. You helped and worked with almost everyone in the group together on a project. You are an incredible and enthusiastic scientist and I hope that you will get everything that you are dreaming of in science. Thank you for never letting me down even in the hard times in and outside of AMOLF. Further, I would like to thank Balázs for all the sweets in the office. I think the sugar definitely made some days happier, but also almost gave me diabetes. Thank you for all your efforts to cheer me up or distract me with some Nintendo games in the hard times. Do not forget to turn it up to eleven and the rest of your Ph.D. and life will be a success.

Johannes besides Konrad you were the first person I worked with in AMOLF, you taught me all the basics I had to know to work with the optical setups. I had so much fun working with you in the lab and celebrating special measurements after work. If you ever reach a limit in life, remember “Re-scale B*****”. Sanghamitra you have such a cheerful personality and with your laugh, you light up AMOLF. I am very happy that we met in the US at the conference, where we not only discussed science but also connected on a personal level (thanks to all the wine and the pool table). You are a fantastic scientist and a wonderful addition to the group. I hope that soon you can start your own group and share your devotion and enthusiasm with the rest of the scientific world. Even though we just shared a short time at AMOLF thank you Gökçen for sharing your own Ph.D. writing experience with me and celebrating every little step in the last month with a proper glass of gin tonic. Marloes, it is inspiring how much enthusiasm and devotion you put in everything you start. Thank you for all the positive and creative energy you shared with me and the rest of the group. Alexandra thank you for all the weird conversations we had, it is always good to see the world from a different perspective. Harmen, thank you for all the time helping me to fix the laser when Jan was on vacation and for the interesting, but long group meeting presentations which not only fried my brain. Furthermore, I would like to thank all the other group members Rahul, Aditi, Biplab, Carien, Wilbert, Andrea, Bart, Simona, Oleg, Yves, Sabine for all the scientific discussion and the support during the time we spent together at AMOLF. Teresa, your cheerful and happy personality is encouraging and makes AMOLF a better place to work. Thank you for always being under-

standing and organizing all the meetings as fast as possible although it was not always easy. Next, I want to thank Niels for all the nice chats and for supporting me in the moments when Hinco was not available. Dion thank you for getting me started producing ice and for all your efforts trying to teach me a bit of Dutch.

Furthermore, I would like to thank all the support departments, the workshop, facilities, communications, ICT, Finance, the Library, Purchase, HR, Health and Safety, the secretary office, the Electronics and the Mechanical Engineering a department who made AMOLF such an amazing and shiny place to work at. Without all of you, a lot of measurements and thus this thesis would have not been possible. Here, I would like to thank especially Tom B., Marco S., Dirk Jan S., and Henk-Jan who build the fantastic ice sample cell and created its measurement programs. Thanks also to Wessel for a wonderful dance at the Christmas lunch, I think we were extraordinarily good. Thanks to Mark for always having a bandage for fixing small wounds and helping me order chemical compounds more than one time. Next, I would like to thank the PV for organizing all the awesome outings, Christmas lunches, Borrels, and many more events!

Outside work I would like to thank all the people that made AMOLF a wonderful place to be. Lucie, we started not only our Master's thesis together at AMOLF at the same time, but also submitted our Ph.D. thesis on the same day (Submission Sisters)! Apart from that, we shared so many more amazing moments, including many glasses of wine, dances on tables, picnics in Flevopark, more than one Veldhoven conference (party), Christmas lunches, and raclette evenings. You are such a nice, friendly and lovely person and your beautiful smile is making everyone feel better. Mareike, I am so happy that we did the presenting course together and I got to know you better. You made the course a really fun experience although I think it would have been slightly nicer without the creepy choleric guy. After that, we shared many more beautiful moments from an impromptu candlelight dinner at a random but very nice Italian restaurant to cocktail evenings and dress-up parties. I am looking forward to having many more girls' evenings with you. Nasim, when I read the acknowledgments about me in your thesis, I had tears in my eyes. I think you are a person who always sees the good in people and that is a part of your personality that makes you beautiful and unique. Thank you so much for all the smiles during my Ph.D. and random chats in the park. Jenny your laugh can break walls and I mean that in a good way. You are a person that enters a room and it is difficult not to become your friend. I am so happy that I have met you at AMOLF and for all the evenings we spent together. Besides that, you were a considerate and nice neighbor. Susan thank you for accepting me together with Lucie and Nasim in your sect. It was so much fun dreaming and planning a life outside of AMOLF.

Andrea C., besides the Ph.D. we also did our Mastern Internship together, thanks for all the crazy parties in DUWO and the funny and nice discussions at AMOLF. Lukas, thank you for all the freshly baked bread, the Feuerzangen-

bowle in the dark and cold winter nights, the crazy Lukas parties, and all the hugs when I needed them. Thank you for being an amazing, kind, caring, and unique friend. Thank you for all the nice dinners together and all the times you helped with annoying heating systems and stubborn washing machines. Hans, thank you for the good, happy, and cheerful atmosphere you created around you in AMOLF. It was infectious. Thank you, Yarik, for all the nice and motivating chats, while I was getting liquid nitrogen and you were smoking outside. Anna you have such a sweet, welcoming, and open personality, thank you for all the open-minded chats about everything. Agustin, you are such a colorful and at the same time calm and kind person, thanks for making my days at AMOLF better with your constant smile. Federica, thanks for being always such a welcoming, friendly and nice person. Thanks for all the nice evenings with a glass of wine and thanks for all the discussions about hyaluronic acid.

Ale, thanks for all the times we spent together at the gym and for all the drinks afterward, the morning croissants with orange juice, and all the pizza evenings before I went on a long trip. Thank you for all the times you have been my Baymax. Marco, thanks for always giving me a reason to bake cakes, for all the after-gym beers, all the fantastic self-cooked dinners. Thank you for all the pan di stelle you imported for me from Italy, for always answering all my text messages as stupid they might be, and for being there for me with a piece of chocolate when I needed it. Thank you, Giorgio, for smiling at me from day one I entered AMOLF you are such a nice, funny and caring person. Thanks for supporting me and having a chat with me when the days at and outside of AMOLF were not so shiny. I enjoyed the “many” times we spent together at the gym and the beers we had together with the others afterward. I am looking forward to many more fantastic, parties, picnics, barbeques, aperitivi, and yet to execute Mole evening ;-). Ele, I liked having you around in Amsterdam even though it was not so often. Thank you for being such a kind, friendly and sweet person and for all the encouraging text messages you have sent me. Judith there is no better and nicer person I would like to lay the floor with than you. Thank you for all your help moving and assembling furniture and all the nice aperitivi and evenings with Giulia. Lorenzo, thank you for always being such a welcoming, friendly and funny host. Katya, thanks for all the nice and fun moments we spent together, if on the boat in Amsterdam or at an abandoned beach in New Zealand. Andrea, thank you for being such a nice, cheerful, and colorful friend and for all the homemade sweets you bring for any occasion. Thank you Florian and Ivonne for all the beers, negroni and fun conversations and to Florian for pushing my monster of washing machine up the stairs.

Further, I would like to thank Magda, Mario, Olga, Nicola, Christian, Ruslan, Imme S., Kevin, Parisa, Robin, Ruslan, Ariane, Moritz F., Moritz S., Said, Rene, Roel, Dario, and Anastasia for the many nice chats, discussions, and coffee breaks at AMOLF. In those days when AMOLF appeared to be a little too green and I needed a change of scenery, the lovely people from ARCNL welcomed me with open arms. Here, I would like to thank especially Ruben (for all the chats in front of the elevator at DUWO), **Stephen** (thanks for all the

wine in the backyard of DUWO, while watching late-night canal swimmers), and Vanessa (for all the nice beers at the windmill). Besides that, I would like to thank Ale T., Fiona, Victor, Mengqi, Randy, Christina, John, Lukas P. for all the nice coffee breaks, Werewolf games, borrels, and picnics in Flevopark. Further, I would like to thank Arjun, you were such a good neighbor and I miss you in Oost a lot. Thanks for showing me the best kebab places in Javastraat and for all the homemade Indian food and chairs. I enjoyed our long walks and the discussion about life and science. Thanks, for being such a good, outgoing, lovely, and caring friend. Hannah, thanks for all the Wednesday dinners with Arjun and all the nice chats in Flevopark.

Neben meinen Freunden in Amsterdam würde ich mich gerne auch bei meinen Freunden aus Deutschland bedanken, die mir auf unterschiedliche Weise immer wieder geholfen haben. Lisa R., deine ruhige Ausstrahlung hat es mir immer einfach gemacht mich bei dir zu Hause zu fühlen. Lisa S., du bist eine wundervolle, fröhliche und positive Person und ich bin froh, dass wir so viel mehr als die Tartanbahn teilen! Sabine, ohne dich hätte ich die Schulzeit bestimmt nicht überlebt und hätte zwangsläufig nicht meinen PhD gemacht. Lili, danke für all die wundervollen Autofahrten zum Training und für die süße Unterstützung mit Tofffee über die letzten Jahre. Ein ganz besonderer Dank gilt meinen Mädels vom Studium: Imme (I will always love you), Beate, Lea, Stella und Kathi, ohne eure Unterstützung wäre diese Arbeit nicht möglich gewesen. Danke für alle Lernsessions, Sauna-Tage, kleinen Urlaube und WG-Feiern, die das Studium so viel schöner gemacht haben. Neben den Mädels sollte ich natürlich auch Erdi nicht vergessen, danke für die vielen tollen Momente während des Studiums und auch danach. Chris, danke, dass du dir immer Zeit genommen hast, wenn ich mal wieder in der „Hood“ war und für die vielen angeheiterten Gespräche auf den Spielplätzen in Holzheim. Tatjana, danke, dass du mich mit Konrad und Gijsje in Kontakt gebracht hast, ohne dich wäre ich nie in Amsterdam gelandet. Danke, für die Unterstützung außerhalb der Arbeit, Shisha-Abende und die Autofahrten zurück nach Deutschland. Götz, danke für deine Hilfe mit all meinen Computer und MATLAB Problemen. Ihr beide habt mein erstes Jahr am AMOLF so viel einfacher gemacht. Markus und Melanie, danke für all die Freitag Abende, die ihr für mich geopfert habt. Danke für die Mathenachhilfe und die Verpflegung mit Zitronentee ohne die ich mein Studium und so auch meinen PhD nie geschafft hätte. Guido, danke dafür, dass du mir geholfen hast mich wiederzufinden, für all die aufmunternden Telefonate und für all die positive Energie über die letzten Monate.

Am Ende würde ich mich gerne bei meiner Familie bedanken, ohne deren Unterstützung diese Arbeit ausgeschlossen wäre: Ewald, dem besten Patenonkel der Welt, Doris, meinem lustigen Onkel Felix, Bine, meinem Cousin Florian, meiner Cousine Lotta und meinem Trainer Frank. Danke, dass ihr immer für mich da wart und mich über die letzten Jahre auf unterschiedliche Weisen unterstützt habt. Weiter möchte ich mich auch bei Ulrike bedanken, du hast mich und meine Familie unterstützt als wir dich am meisten gebraucht haben. Richard, danke, dass du mich immer für neue Dinge begeisterst, dein Enthusi-

asmus neue Dinge zu entwickeln und zu verstehen ist ansteckend.

Moritz, Janna, Mama und Papa, es gibt nicht genügend Seiten und Worte die ausdrücken wie dankbar ich für eure Unterstützung in den letzten Jahren bin. Ich habe euch unendlich lieb! Janna, besonders in den letzten Monaten habe ich meine große Schwester mehr als einmal gebraucht und du warst für mich da, wenn ich am Rande des Verzweifeln war oder einfach mal kurz mit jemandem reden musste. Markus, ich freue mich, dass ich jetzt auch einen großen Bruder habe und dass du immer für Bier bei euch sorgst ;-). Moritz, ich denke im AMOLF kennt fast jeder deinen Namen, weil ich so stolz bin deine Tante zu sein. Danke für deine Umarmungen, wenn ich sie gebraucht habe, die selbstgemalten Bilder und all die wunderschönen Blödsinn Momente. Danke euch dreien für die wunderschönen Besuche in Amsterdam und am Strand. Mama, danke für all die Momente als ich nach Hause gekommen bin und du mich nicht nur mit deinen Kochkünsten verwöhnt hast. Danke, für die Mama-Caro Abende und „Dümpeltage“ an denen ich mich entspannen und wieder Kraft tanken konnte. Danke, für deine aufmunternden Karten und Pakete, die mir das Gefühl von zu Hause gegeben haben. Papa, ohne dich hätte ich es an meinem ersten Tag nicht ans AMOLF geschafft, danke, dass du mich nach Amsterdam "geflogen" hast. Danke dafür, dass du immer für mich da bist, wenn ich mal wieder mein Handy in die Waschmaschine gesteckt habe oder das Badezimmer unter Wasser gesetzt habe. Du hast mich aufgelesen, wenn ich auf der Tartanbahn gefallen bin oder im Studium nicht an mich geglaubt habe. Danke auch für die wunderschönen Bilder, die diese Arbeit verschönern! Als letztes würde ich mich gerne bei meinen unglaublich starken, eigensinnigen, wundervollen und liebenswerten Omas bedanken. Ich habe viel von euch gelernt und vermisse euch so sehr!!! Danke Omi Resi (+06.08 2020) und Omi Karla (+07.08 2021).

As my Dad always told me: " Life is a journey not a destination." Thank you AMOLF, I had an amazing and fun time!

